Méthodes multi-échelles (VMS) pour la stabilisation des écoulements Stokes-Darcy couplés dans des milieux poreux subissant des grandes déformations : application aux procédés d'infusion pour la fabrication des matériaux composites.

Lara Abou Orm

NNT : *Communiqué le jour de la soutenance*

THÈSE

présentée par

Lara ABOU ORM

pour obtenir le grade de
Docteur de l'École Nationale Supérieure des Mines de Saint-Étienne

Spécialité : Mécanique et Ingénierie

VMS (Variational MultiScale) stabilization for Stokes-Darcy coupled flows in porous media undergoing finite deformations: application to infusion-based composite processing.

soutenue à Saint-Etienne, le 27 septembre 2013

Membres du jury

Président :	Xxxxx XXX	Établissement, Ville
Rapporteurs :	M.Ramon Codina	Pr, Universitat Politècnica de Catalunya. BarcelonaTech, Barcelone
	M.Christian Geindreau	Pr, Université Joseph Fourier,Grenoble
Examinateurs :	M.Luisa Silva	Associate professor, CEMEF – ENSMP, Sophia-Antipolis
	M.Christophe Binetruy	Professor, École centrale de Nantes, Nantes
Directeur de thèse :	M.Sylvain Drapier	Pr, ENSMSE, Saint-Étienne
Co-directeur de thèse :	M.Julien Bruchon	Dr,ENSMSE, Saint-Étienne
Co-encadrant de thèse :	M.Nicolas Moulin	Dr,ENSMSE, Saint-Étienne

Spécialités doctorales :	Responsables :
SCIENCES ET GENIE DES MATERIAUX	K. Wolski Directeur de recherche
MECANIQUE ET INGENIERIE	S. Drapier, professeur
GENIE DES PROCEDES	F. Gruy, Maître de recherche
SCIENCES DE LA TERRE	B. Guy, Directeur de recherche
SCIENCES ET GENIE DE L'ENVIRONNEMENT	D. Graillot, Directeur de recherche
MATHEMATIQUES APPLIQUEES	O. Roustant, Maître-assistant
INFORMATIQUE	O. Boissier, Professeur
IMAGE, VISION, SIGNAL	JC. Pinoli, Professeur
GENIE INDUSTRIEL	A. Dolgui, Professeur
MICROELECTRONIQUE	Ph. Collot, Professeur

EMSE : Enseignants-chercheurs et chercheurs autorisés à diriger des thèses de doctorat (titulaires d'un doctorat d'État ou d'une HDR)

AVRIL	Stéphane	MA	Mécanique & Ingénierie	CIS
BATTON-HUBERT	Mireille	MA	Sciences & Génie de l'Environnement	Fayol
BENABEN	Patrick	PR 1	Sciences & Génie des Matériaux	CMP
BERNACHE-ASSOLLANT	Didier	PR 0	Génie des Procédés	CIS
BIGOT	Jean-Pierre	MR	Génie des Procédés	SPIN
BILAL	Essaïd	DR	Sciences de la Terre	SPIN
BOISSIER	Olivier	PR 1	Informatique	Fayol
BORBELY	Andras	MR	Sciences et Génie des Matériaux	SMS
BOUCHER	Xavier	MA	Génie Industriel	Fayol
BRODHAG	Christian	DR	Sciences & Génie de l'Environnement	Fayol
BURLAT	Patrick	PR 2	Génie industriel	Fayol
COLLOT	Philippe	PR 1	Microélectronique	CMP
COURNIL	Michel	PR 0	Génie des Procédés	SPIN
DARRIEULAT	Michel	IGM	Sciences & Génie des Matériaux	SMS
DAUZERE-PERES	Stéphane	PR 1	Génie industriel	CMP
DEBAYLE	Johan	CR	Image, Vision, Signal	CIS
DELAFOSSE	David	PR1	Sciences & Génie des Matériaux	SMS
DESRAYAUD	Christophe	MA	Mécanique & Ingénierie	SMS
DOLGUI	Alexandre	PR 1	Génie Industriel	Fayol
DRAPIER	Sylvain	PR 1	Mécanique & Ingénierie	SMS
FEILLET	Dominique	PR 2	Génie Industriel	CMP
FOREST	Bernard	PR 1	Sciences & Génie des Matériaux	CIS
FORMISYN	Pascal	PR 1	Sciences & Génie de l'Environnement	Fayol
FRACZKIEWICZ	Anna	DR	Sciences & Génie des Matériaux	SMS
GARCIA	Daniel	MR	Sciences de la terre	SPIN
GIRARDOT	Jean-Jacques	MR	Informatique	Fayol
GOEURIOT	Dominique	MR	Sciences & Génie des Matériaux	SMS
GRAILLOT	Didier	DR	Sciences & Génie de l'Environnement	Fayol
GROSSEAU	Philippe	MR	Génie des Procédés	SPIN
GRUY	Frédéric	MR	Génie des Procédés	SPIN
GUY	Bernard	MR	Sciences de la Terre	SPIN
GUYONNET	René	DR	Génie des Procédés	SPIN
HAN	Woo-Suck	CR		SMS
HERRI	Jean-Michel	PR 2	Génie des Procédés	SPIN
INAL	Karim	PR 2	Microélectronique	CMP
KLÖCKER	Helmut	DR	Sciences & Génie des Matériaux	SMS
LAFOREST	Valérie	CR	Sciences & Génie de l'Environnement	Fayol
LERICHE	Rodolphe	CR CNRS	Mécanique et Ingénierie	SMS
LI	Jean-Michel	EC (CCI MP)	Microélectronique	CMP
MALLIARAS	George Grégory	PR 1	Microélectronique	CMP
MOLIMARD	Jérôme	PR2	Mécanique et Ingénierie	SMS
MONTHEILLET	Frank	DR 1 CNRS	Sciences & Génie des Matériaux	SMS
PERIER-CAMBY	Laurent	PR 2	Génie des Procédés	SPIN
PIJOLAT	Christophe	PR 1	Génie des Procédés	SPIN
PIJOLAT	Michèle	PR 1	Génie des Procédés	SPIN
PINOLI	Jean-Charles	PR 0	Image, Vision, Signal	CIS
ROUSTANT	Olivier	MA		Fayol
STOLARZ	Jacques	CR	Sciences & Génie des Matériaux	SMS
SZAFNICKI	Konrad	MR	Sciences & Génie de l'Environnement	Fayol
TRIA	Assia		Microélectronique	CMP
VALDIVIESO	François	MA	Sciences & Génie des Matériaux	SMS
VIRICELLE	Jean-Paul	MR	Génie des procédés	SPIN
WOLSKI	Krzysztof	DR	Sciences & Génie des Matériaux	SMS
XIE	Xiaolan	PR 1	Génie industriel	CIS

ENISE : Enseignants-chercheurs et chercheurs autorisés à diriger des thèses de doctorat (titulaires d'un doctorat d'État ou d'une HDR)

FORTUNIER	Roland	PR	Sciences et Génie des matériaux	ENISE
BERGHEAU	Jean-Michel	PU	Mécanique et Ingénierie	ENISE
DUBUJET	Philippe	PU	Mécanique et Ingénierie	ENISE
LYONNET	Patrick	PU	Mécanique et Ingénierie	ENISE
SMUROV	Igor	PU	Mécanique et Ingénierie	ENISE
ZAHOUANI	Hassan	PU	Mécanique et Ingénierie	ENISE
BERTRAND	Philippe	MCF	Génie des procédés	ENISE
HAMDI	Hédi	MCF	Mécanique et Ingénierie	ENISE
KERMOUCHE	Guillaume	MCF	Mécanique et Ingénierie	ENISE
RECH	Joël	MCF	Mécanique et Ingénierie	ENISE
TOSCANO	Rosario	MCF	Mécanique et Ingénierie	ENISE
GUSSAROV Andrey	Andrey	Enseignant contractuel	Génie des procédés	ENISE

Glossaire :

PR 0	Professeur classe exceptionnelle	Ing.	Ingénieur
PR 1	Professeur 1ère classe	MCF	Maître de conférences
PR 2	Professeur 2ème classe	MR(DR2)	Maître de recherche
PU	Professeur des Universités	CR	Chargé de recherche
MA(MDC)	Maître assistant	EC	Enseignant-chercheur
DR	Directeur de recherche	IGM	Ingénieur général des mines

Centres :

SMS	Sciences des Matériaux et des Structures
SPIN	Sciences des Processus Industriels et Naturels
FAYOL	Institut Henri Fayol
CMP	Centre de Microélectronique de Provence
CIS	Centre Ingénierie et Santé

Dernière mise à jour le : 02 avril 2012

Contents

List of Figures

List of Tables

Introduction

The use of composite materials has spread during the last decade, especially in aeronautics and automotive. The best known example is probably the Airbus A380 aircraft, of which about 25 % of the mass is composed of composite materials. Composite materials considered here, are obtained by a combination of an organic matrix, which ensures the cohesion of the material, and fiber reinforcement (fibers of carbon, glass fibers, etc..) that gives the material its mechanical properties . The advantage of composite materials is that they have high properties weight ratio compared with metals. Composite materials take part in the reduction of the weight of the structures, allowing the reduction of the energy transportation costs. In addition, composite pieces can be tailored in such a way that their reinforcement direction permit to deal with the multi-directional mechanical sollicitations.

However, several obstacles may affect the use of composite materials, their costs and more generally their development. Usually, we distinguish two types of manufacturing processes: wet processes and dry processes. In wet processes, fiber reinforcements are sold pre-impregnated with resin. This makes easier the development of the piece, and provides a good control of the fiber fraction, which is of paramount importance in composite materials performance. However, these processes are expensive because they require refrigerated storage of pre-impregnated reinforcements and heavy hand costs. To reduce this cost, wet processes have been developed in the last years. They consist in infusing the resin into fibrous preforms during the manufacturing process. However, the control of these processes is more difficult, it is hard to control the most critical properties related to the final piece like the volume fraction of fibers. For this reason, this work is conducted to propose a numerical methodology to simulate the resin infusion process which will help to control them and therefore to tune the process parameters to control the final piece geometrical as well as physical properties

Especially, we are interested in manufacturing large pieces. In this case, the resin is fed over the preforms (not impregnated yet) in a fluid distribution medium of a very high permeability. Then, under the action of mechanical pressure, exerted by the atmosphere when the vacuum is pulled, the resin is infused in the thickness of preforms. The complete modelling of this process is very complex and involves several physical phenomena. First, the dry preforms are compacted, and undergoing also large deformations. The thermoset resin flows then in the fluid distribution medium then into preforms. During its infusion, the resin undergoes, during

its infusion thermochemical transformations that affect its viscosity. The pressure applied by the resin into fibers network causes the inflation of preforms which modifies their porosity and therefore their permeability. This phenomenon is observed when coupling solid and fluid mechanics.

Moreover, one should take into consideration the cooling phase, during the development of internal stress. However, in this work, we have isothermal conditions and the resin is considered as Newtonian incompressible fluid with constant viscosity. We model the flow of resin into the fluid distribution medium using Stokes' equations. The flow of resin into preforms is described by Darcy's equations with low permeability of order $10^{-14}\mathrm{m}^2$. The deformations of wet and dry preforms are considered with an elastic non linear law.

An important part of this work is dedicated to solve, using the finite element method, Stokes-Darcy coupled problem. This work is based on the work of Guillaume Pacquaut which defended his phd at École Nationale des Mines de Saint-Étienne in december 2010. Following this work, we adopted a monolithic approach for the Stokes-Darcy coupled problem, which means that we use one single mesh for Stokes and Darcy. The interface which separates these two domains is represented by the isovalue zero of a level set function ϕ defined as a distance function to the interface. The coupled problem is classically solved by formulating first a mixed velocity-pressure problem. It is known, relatively to Brezzi-Babũska theory that the pair of the chosen interpolations should mainly satisfy two conditions (V_0 ellipticity of a and the *inf-sup* condition on b in their classical notations) which conducts to a discrete problem well-posed (existence and unicity of the solution). The difficulty of the choice of stable elements for Stokes-Darcy coupled problem is that the stable elements for Stokes are not stable for Darcy and vice versa. Therefore, the *inf-sup* condition presents a problem in the choice of the pair of elements in Stokes, especially in the choice of pressure space while the problem in Darcy is the V_0 ellipticity condition and the control of the divergence of the velocity. Briefly, it does not exist a standard stable finite element pair for both Stokes and Darcy. The choice of different stable pairs (defined in two different discretized spaces) succeeds in decoupled approach where every domain is represented by a mesh independently from the other domain. However, in a monolithic approach, this is not possible because it conducts to a loss of consistency of the solution and oscillations around the interfaces. This is the limitation of the approach proposed by Guillaume Pacquaut which relies on the MINI-element in Stokes (linear elements for velocity and pressure, the velocity is enriched by a bubble function) and a linear element for pressure and

velocity in Darcy stabilized with a Variational MultiScale method (Hughes Variational MultiScale). This pair of elements (P1+/P1-HVM) does not ensure the continuity of the normal velocity on the interface (consistency error) and leads to oscillations of velocity on the interface.

In this work, velocity and pressure fields, in Stokes and Darcy are approximated by linear and continuous functions per element (triangle or tetrahedron). The pair $P_1 - P_1$ (linear-linear) is not stable for Stokes and Darcy. For this reason, we modify the discrete variational formulation of the problem by adding additionnal terms depending on the size of mesh and residual finite elements to make them stable. In addition, we use stabilization methods called "Variational MultiScale". Developed twenty years ago, these methods offer a generic and formal framework for the stabilization of the finite elements formulations. They consist in decomposing the unknown and the test functions of the problem into two components: one corresponding to the unresolvable scale which is not captured by the mesh and another one corresponding to the resolvable scale which is the finite element solution. After this step, we establish fine scale problem and coarse scale problem (finite element problem). The approximation of the fine scale problem is injected in the finite element problem which allows the generation of stabilization terms.

When the Stokes-Darcy coupled problem is solved, we use it for the simulation of resin infusion processes, where the thickness of the fluid distribution medium is very low relatively to the thickness of the piece, and the permeability of fibrous reinforcement is small. The second level set function is used to describe the moving flow front, this function is initially defined by hyperbolic tangent form of the signed distance function to the resin front, and is constant outside a neighbourhood of this front. We adopt an Updated Lagrangian approach to solve the solid mechanics problem, *i.e* the deformation of dry preforms under their compaction due to a mechanical pressure and the deformation of wet preforms due to the pressure of the infused resin. The coupling between the resin flow and the deformation of preforms is carried out incrementally via the pressure of the resin in the expression of the wet preforms mechanical response, then via the porosity and the permeability which is a parameter present in Darcy's equations.

Our manuscript is organized as follow:

– The **first chapter** introduces the definition of composite materials with organic matrix and their manufacturing processes. Then, we concentrate on the description and the

modelling of the process that we take into consideration which is "LRI" (Liquid Resin Infusion)

- The **second chapter** is an essential bibliographic study concerning the mixed finite elements used to solve Stokes'and Darcy's equations and then Stokes-Darcy coupled problem. We introduce the theoretical framework of Brezzi-Babũska which allows to establish the conditions of existence, unicity and stability of the solutions of both the discrete and continuous problem.
- The **third chapter** presents the method that we choose to couple Stokes and Darcy in a single approach: the finite element formulation is stabilized by using Variational MultiScale method called "ASGS" method (Algebraic SubGrid Scale). An analysis about the constants of stabilization which appear in this method is carried out.
- The **fourth chapter** is dedicated to the numerical validation of Stokes-Darcy coupled problem using ASGS method in the conditions imposed by LRI process. Different tests are conducted to validate the coupling conditions on the interface, such as a flow perpendicular to the interface, a flow parallel to the interface, and we use the manufactured solution method to study the order of convergence. In addition, we compare the obtained results with those obtained by another monolithic approach and by a decoupled approach.
- The **fifth chapter** is made up of two distinct parts. In the first part, we present a bibliographic study of the numerical methods of interface capturing. After this, we detail the method chosen to model the fluid front, the level set method combined with a hyperbolic tangent filter. In the second part of this chapter, we deal with the deformation of preforms. We introduce the theoretical context of large deformations, then we formulate the mechanical problem with a Lagrangian Updated approach. Finally, we formulate the coupling between the deformations of preforms and the flow of the resin into preforms
- The **sixth chapter** proposes some simulations of resin injection (Stokes-Darcy and level set) then the infusion of resin (Stokes-Darcy, level set and deformation of preforms). 2D and 3D simulations are considered on simple cases, and then on complex pieces presenting curvatures and thickness. A comparison with existing experimental results is proposed on a simple geometry.

Chapter 1

Composite materials, LCM processes and their modelling

Contents

1.1 Introduction

Composite materials consist of a combination of materials that are mixed together to achieve specific structural properties. A composite material is made of a reinforcement material embedded in a resin matrix. The properties of the composite material are superior to the properties of the individual materials from which it is constructed. The main advantages of composite materials are their high strength and stiffness, combined with low density, when compared with bulk materials, allowing for a weight reduction in the finished part. Composite materials have gained popularity (despite their high cost) in high performance products that need to be lightweight and "strong" enough such as aerospace structures, tails, wings, fuselages, bicycle frames and racing car body (Figure 1.1). In the first part of this chapter, we will introduce composite materials properties and their manufacturing processes. Then, we will detail the resin infusion processes that we will model and show the difficulties related to their modelling. In the second part of this chapter, we will present the modelling of resin infusion processes taking into consideration the coupling between different physical phenomena occuring in resin infusion processes.

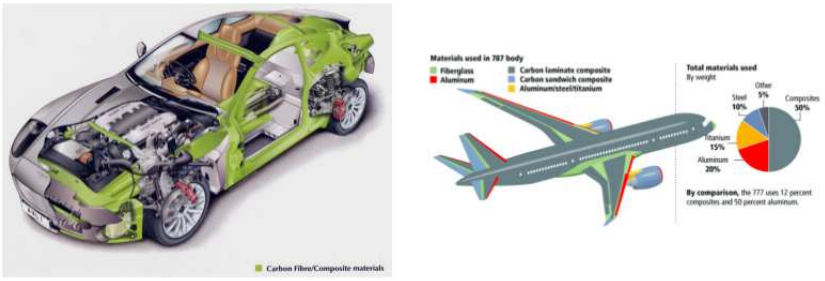

Figure 1.1: Composite materials products: (a) GD - Aston Martin V12 Vanquish, (b) HP - Boeing 787 Dreamliner

1.2 Composite materials constituents

1.2.1 Matrix

Synthetic resins are used as matrix materials in organic composites. Resins are generally either thermoplastic resins or thermosetting resins.
Thermosetting resins are the most diverse and widely used of all man-made materials. They are linked together by tight bounds of a chemical nature. After their polymerization by ap-

plying heat in the presence of a catalyst, these resins lead to geometric structure that can be destroyed only by a considerable application of thermal energy. For this reason, thermosetting resins have high thermomecanical properties. The principal thermosetting resins used in manufacturing composite materials are polyethanes, polyester and epoxy. Epoxy resins are the most widely used in high-performance composites. Polyester resins are the most widely used because of their low production cost, their flexibility and their stiffness.
In thermoplastic resins, macromolecular chains are linked together by weak bonds of physical nature. The advantage of thermoplastic resins lies in their low cost and recyclability. Nevertheless, this low cost is associated with low thermomechanical and mechanical properties. Their mechanical applications include helicopter rotor blades, and fairing panels on civil aircrafts. The most commonly used contemporary compounds are polyethylene, polyester and polycarbonate.

1.2.2 Reinforcements

Reinforcements bring to the composite material its mechanical properties [Berthelot 2005]. They are commercialized in the form of preforms of various architectures which can be dry or pre-impregnated with resin. Fibers are the most commonly used reinforcements. There are different types of fibers: Carbon, Glass fibers and Aramid fibers which can be purchased in various formats (chapped fibers, long fibers, fiber tows $\cdots$).

Glass fibers and Aramid fibers

Glass fibers are often used for helicopter rotor blades, for secondary structure on aircraft such as fairings and wings tips. Glass fibers have lower cost than other fibers. Composite materials made up by Glass fibers are available as a dry fabric or prepreg material. There are several types of Glass fibers: E-glass,D-glass,C-glass, R or S glass.

- E-glass accounts for 90 % of the glass fiber market and is used mainly in a polyester matrix and it has good electrical properties.
- D-glass has high dielectric properties.
- C-glass has good chemical resistance.
- R-glass or S glass has high mechanical resistance.

Aramid fibers are light weight, strong and tough [Dursapt 2007]. Aramid fibers have high resistance to impact damage, however, they are weak in compression due to the interface weakness. The most well-known and used aramid fibers is Kevlar.

Carbon fibers

Carbon fibers are the dominant advanced composite materials for aerospace, automobile, sporting goods due to their high strength, high modulus, low density and reasonable cost. There are several types of Carbon fibers: fiber with high resistance (HR), fiber with intermediate modulus (IM) and fiber with high modulus (HM). Table 1.1 allows to compare the characteristics of the different types of fibers.

Preforms architecture

The diameter of fibers is small, for this reason, preforms are commercialized in different forms of products which contain million of fibers, architectured in different forms. Several types of fibers architecture can be used depending on the number of directions occupied by fibers: Unidirectional (UD), bidirectional and multidirectional. Figure 1.2 shows the different types of preforms architecture.

Characteristics	E-glass	R-glass	Carbon HR	Carbon HM	Aramide
Young modulus E (GPa)	73	85	240	400	135
Tensile strength R (MPa)	3500	4500	3800	1600	3100
Compressive strength	Medium	Medium	Good	Good	Bad
Shock resistance	Medium	Medium	Weak	Weak	Excellent
Sensibility to humidity	Yes	Yes	No	No	Yes
Density	2,6	2,6	1,75	1,9	1,5
Expansion coefficient (10^{-6}mm/mm/C)	5	4	1	1	0
Relative price	1	4	30	60	10

Table 1.1: Comparison of different types of fibers [Dursapt 2007].

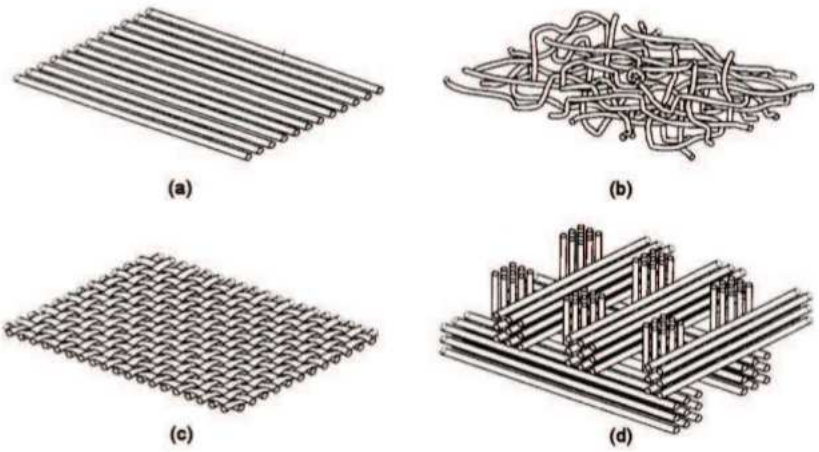

Figure 1.2: Different types of preforms architecture

1.3 Manufacturing processes of composite materials

Manufacturing processes for composite materials are numerous. They can be classified into two categories: dry route processes and wet route processes.

1.3.1 Dry route processes

Dry processes correspond to processes where composite material is formed by stacking "prepregs". Prepregs are composite reinforcements (glass fibers, carbon fiber, aramid, etc.) that are pre-impregnated with resin. Dry processes have the advantage of convenient use and can easily master the final properties of the final product especially the volume fraction of fibers. The stacking of "Prepregs" is then placed in a mould for manufacturing the composite material. Prepreg materials are cured with an elevated temperature within an autoclave, oven or heat blanket. These processes allow to obtain composite pieces with excellent mechanical properties resulting from a low porosity and a high volume fiber fraction. However, the cost of storage is high because Prepreg material must be stored in a freezer at a temperature below 0° C to delay the curing process.

1.3.2 Wet route processes

These processes appear to reduce the costs with performance and properties identical to those obtained with dry processes. Wet processes are used for the development of composite materials in aeronautics, automative and shipbuilding.
There are two main types of processes. First there are processes based on injection of the resin into a mould like RTM (Resin Transfer Molding), VARTM (Vacuum Assisted Resin Transfer Molding) and ICRTM (Injection Compression Resin Transfer Molding).
Second, to solve the problems of filling met in manufacturing large pieces without high costs, infusion processes appeared twenty five years ago. The most known processes based on infusion of the resin are VARI (Vacuum Assisted Resin infusion), RIFT (Resin infusion under Flexible film infusion), LRI (Liquid Resin Infusion) and RFI (Resin Film Infusion). Below, we will describe RTM processes in the field of processes based on injection, LRI and RFI processes in the field of processes based on infusion.

1.3.2.1 RTM processes

Resin Transfer molding (RTM) is a composite manufacturing process in which fibrous preforms one placed in a closed mold, then a viscous resin is injected into the mold to fill the empty spaces between the network of fibers. Then a cycle of temperature is applied to allow the reticulation of resin taking place. The injection of resin occurs mainly in the plane of preforms. The pieces obtained with this process can be complex with a well controlled final thickness. However, it is important to achieve a large filling of the mold for large pieces. In this process, the vent location is one of the most important variable in process design, it has a great impact on mold filling time and resin flow pattern, which increases the process efficiency and the quality of products.

1.3.2.2 RFI (Resin Film Infusion)

RFI processes consist in depositing fibrous preforms under a layer of solid resin (Figure 1.3). A punched mold can be placed on the top of stacking to improve efficient finishing of the surface. The bleeder and a vacuum bag are placed on top of the assembly. Bleeder absorbs the mass of excess resin. First, a cycle of temperature is applied to maintain the resin in its liquid state and to allow the infusion of the resin through the preforms under the action of pressure cycle. Then, at the end of infusion, a cycle of temperature and pressure is applied again to lead to the crosslinking of the resin.

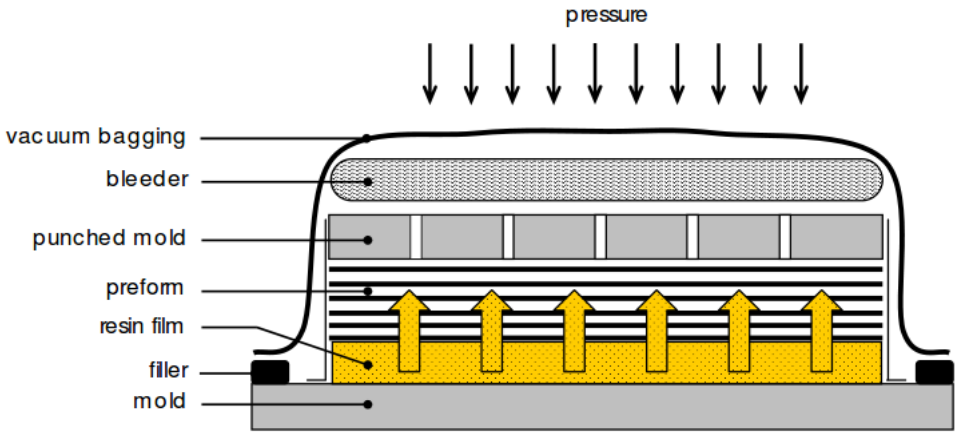

Figure 1.3: Resin Film Infusion (RFI) schematic

1.3.2.3 LRI processes (Liquid Resin Infusion)

In LRI processes, a resin bed is formed through a highly permeable fluid distribution medium placed on the top of fiber preforms. The deformation of the fluid medium is assumed to be negligible compared with the deformations into preforms due to its high stiffness distribution. A punched mold can be placed on the top of the stacking of preforms to improve the finishing of the surface which is not in contact with the mould (Figure 1.4). A vacuum bag is then placed, and vacuum is pulled out to compact the stack of preforms. This also serves as a driving force for infusing the resin across the preforms. Indeed, the difference of pressure between the resin inlet, located in the fluid distribution medium, and the vacuum vent, set on the base of the preform, causes the infusion of resin into the fluid medium then across the thickness of preforms. When the infusion is complete, a cycle of pressure and temperature is applied to realize the crosslinking of the resin.

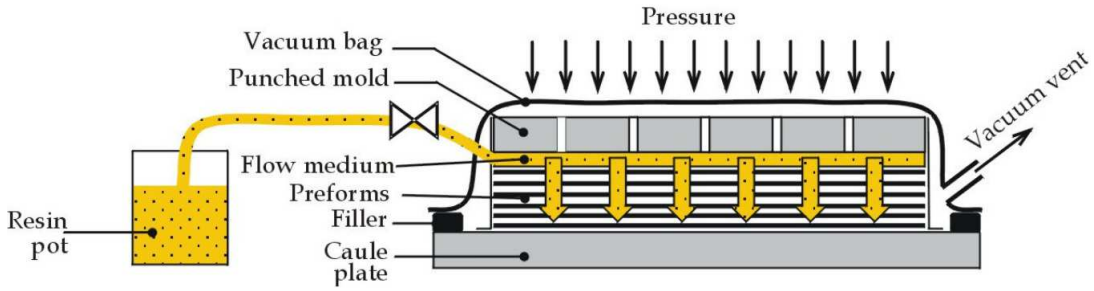

Figure 1.4: Liquid Resin infusion process principle [Wang *et al.* 2010]

1.4 Industrial context

Resin infusion processes have been developed in recent years. They show an advantage relatively to "Prepregs" processes which have high storage costs and are limited to small pieces. Resin infusion processes allow a manufacturing of large pieces because they consist in infusing resin across the thickness of preforms rather then in their plane. Distances travelled by resin are small compared with the distances that are involved in processes by injection (RTM) and a good impregnation of resin is ensured which permits to obtain pieces with good mechanical properties. However, in LRI processes, some mechanical (thickness of preforms) and geometrical properties (fiber-volume fraction) are not well controlled. Numerical simulation will allow a better understanding of the influence of the LRI process parameters (pressure, temperature, viscosity, permeability) onto the final piece characteristics. This will lead to drastic reduction in turning these promissing manufacturing processes, and eventually to optimize the industrial process configurations.

1.5 Challenges and motivation of this work

Numerical simulation is necessary to optimize process promotion to reach infusion time and to master, above all, thickness and fibers volume fraction. Infusion process is a very complex problem to solve, it must rely on general model which couples all the mechanical (solid-fluid) and thermochemical phenomena. Decoupled representation of each phenomenon does not represent the physical reality. The difficulties met in this work is to model the isothermal flow of resin into preforms undergoing large deformations through two coupled mechanisms: the flow of resin (developed in chapter 2) and the deformation of preforms (developed in chapter 5). The second difficulty is the conservation of the fluid mass and the capture of moving flow fronts. To represent the moving flow front, we have two approaches. Lagrangian approaches where the moving flow front is presented by marks which correspond to the nodes of the boundary of the mesh. These marks change their position over the time with a velocity equal to the velocity of the resin. Eulerian approaches where the mesh is fixed. The front of the resin passes through the mesh and is represented by a function computed in the domain. In this case, we have to solve transport equation to detect the evolution of the resin flow front. Consequently, to simulate the resin infusion processes taking into consideration all the physical problems already cited, one has to propose a numerical multi-physical model able to describe the flow of resin into preforms undergoing large deformations. To this day, two models exist, one developed by Celle [Celle *et al.* 2008] and one developed by Pacquaut [Pacquaut 2009]. Celle uses a decoupled

approach which consists in using two different meshes matching at the interface which separate the resin (fluid) and the preforms (porous). Pacquaut uses a monolithic approach which consists in using one single mesh for resin and preforms and represents the interface between porous and fluid domains with a level set function. The numerical model developed by Pacquaut presents some accuracy problems such as consistensy errors and oscillations of velocity in severe cases corresponding to physical reality (complex geometries, curved interfaces and low permeabilities). The aim of this work, based on the work from Pacquaut is to propose a robust numerical multi-physical model to simulate resin infusion processes in an industrial context by using one mesh for resin and preforms. This model will be able to deal with physical and numerical problems met in literature [Pacquaut 2009] and to deal with severe cases matching with industrial reality.

Conclusions

We introduced in this first part, composite material and their manufacturing processes. In addition, we presented resin infusion processes which are hard to control (thickness of preforms, fiber-volume fraction). The numerical simulation will allow to understand this process and to reduce the costs of experimental turning. To understand the simulation methods, we will introduce in the next part the ways of modelling resin infusion processes.

1.6 Modelling scales

Composite materials are heterogenous materials consisting of fibers and resin. The first step implied to model these materials is to choose the scale of description of the physical mechanisms. In general, the more the modelling scale is low, the more we get close to the fundamental physical problem and the less we have to determine experimental parameters. However, the lower the modelling scale, the more we must have local meshes and inducing higher computational costs. There are several possible approaches: microscopic, mesoscopic and macroscopic approaches. Figure 1.5 illustrates these different scales in the case of a flow of resin through a fiber bed.

1.6.1 Microscopic scale

The microscopic scale corresponds to the scale where one is able to describe the flow of resin between the filaments (Figure 1.5). Due to the large difference between the diameter of a fiber ($7 - 10\,\mu m$) and the dimensions of a composite piece (of the order of a meter), this scale is usually not considered in simulation methods. In this approach, we use a representative

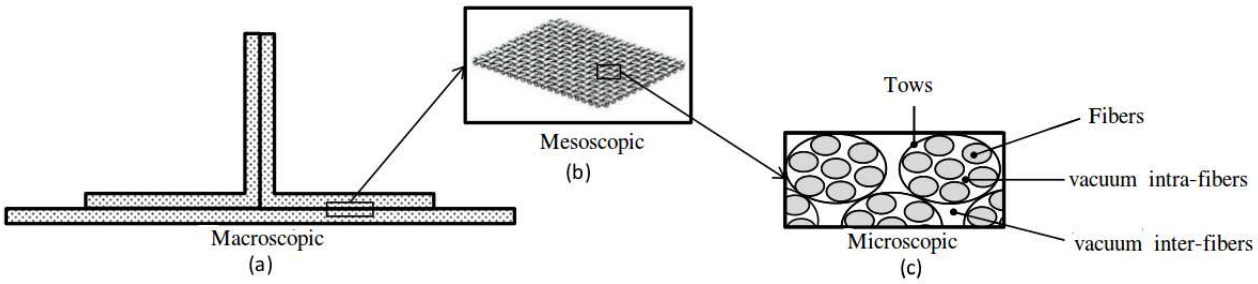

Figure 1.5: The different modelling scales of resin infusion processes

elementary volume (VER). This approach allows an accurate characterization of the behavior of fibers and resin because it consists in studying separatly their behavior using local models. However, this approach is difficult to implement in the case of industrial applications since the computation time associated with such models is prohibitive.

1.6.2 Mesoscopic scale

The mesoscopic scale is the scale where one is able to describe the flow of resin between the tows (Figure 1.5). The working scale corresponds to the tow dimension, typically one to several millimetres.

1.6.3 Macroscopic scale

The macroscopic scale corresponds to the scale of the piece, the tows are not represented and the stacking of tows is considered as a homogeneous equivalent medium (Figure 1.5). This approach is more convenient for the industrial cases. Indeed, the time of computation associated with these models is generally lower than the time associated with microscopic models. However, the physical characteristics of the enviromnent are complex to characterize and difficult to observe. To study the influence of process parameters (pressure, temperature) on the final piece characteristics, we will use macroscopic approach to model resin infusion process through reinforcements represented as equivalent homogeneous medium.

1.7 Multi-domain modelling

Taking into account, the description of LRI process, we will adopt Multi-domain modelling described in Figure 1.6 where we decompose our domain into three different zones corresponding to:

– The fluid distribution medium corresponding to the draining fabrication so-called "Stokes zone".

– Preforms impregnated with resin (wet preforms).

– Preforms not impregnated yet with resin (dry preforms).

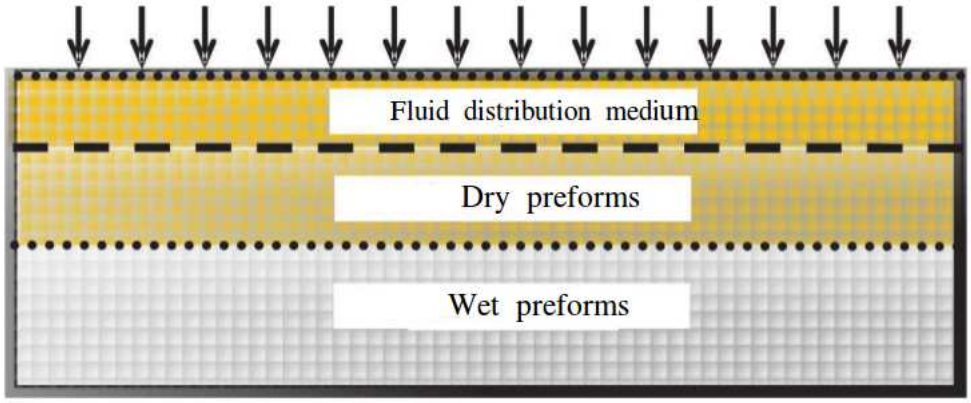

Figure 1.6: Representation of the domain decomposition into three zones during the modelling of resin infusion processes: fluid distribution medium with resin, dry preforms and wet preforms

1.8 Multi-phyiscal modelling

Resin infusion processes involve several complex physical phenomena. In reality, resin infusion process modelling consists in modelling and coupling four physical problems: fluid mechanics problem, solid mechanics problem, thermal problem, and resin cross-linking problem. Figure 1.7 illustrates the different physical phenomena and the interactions between these phenomena.

Fluid mechanics problem corresponds to the flow of resin in the fluid distribution medium and into preforms. This problem is coupled with the thermal transfer and the cross-linking kinetics. The cross-linking of resin affects the viscosity, then it affects the flow. This problem is coupled with the solid mechanics problem because it influences the deformation of preforms due to the pressure of the resin inside the pores. On the other hand, the solid mechanics problem influences the flow of resin because it changes the permeability of preforms *i.e* the capability of the preforms to be infused by the resin. Thermal and cross-linking problems are

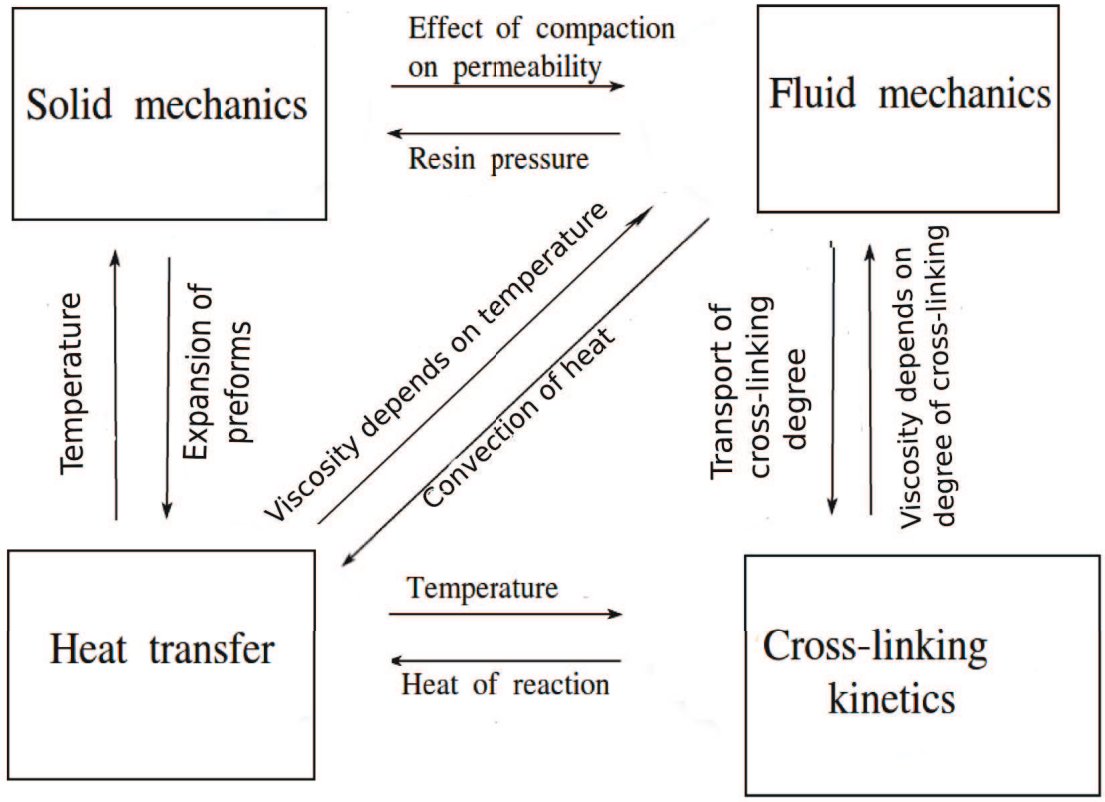

Figure 1.7: Physical phenomena occuring in the modelling of resin infusion processes

also important to model. The cross-linking changes the viscosity, then it affects the resin flow. In addition, cross-linking influences the thermal transfer because it produces heat during the resin exothermal polymerization. Converse, thermal transfer influences the cross-linking kinetic because the temperature is essential for the activation of the resin polymerization reaction. The temperature has also an effect on the resin flow because it changes the viscosity and affects the deformation of preforms by expansion.

In this work, we will concentrate on fluid mechanics and solid mechanis without taking into consideration thermal and cross-linking aspects. In chapter 2, we will develop the modelling of fluid mechanical problem and in chapter 5, we will develop the modelling of solid mechanics problem.

1.9 Conclusions

In this chapter, composite materials and their manufacturing processes were briefly described to define the general context of our work. Then, we presented the numerical simulation considered as an essential way to control resin infusion processes, especially the impregnation of resin into deformable preforms, which will allow to reduce the costs in turning composites materials manufacturing. In addition, we described briefly the bibliographic study of the modelling of resin infusion processes, taking into consideration all the physical phenomena included in this modelling. In the next chapter, we will describe the physical and mathematical models to describe the flow of resin in the fluid distribution medium and preforms, and the different stabilized methods used to discretize the associated mathematical model using finite element methods.

Chapter 2

Stabilized finite element methods for Stokes, Darcy and Stokes-Darcy coupled problem

Contents

2.1 Introduction

In this chapter, we will present the modelling of the resin flow, the resin being considered as an incompressible fluid. It consists on modelling the resin into the fluid distribution medium and into preforms. We present separately Stokes equations and Darcy equations. Then, we present the discretized finite element method used for Stokes and Darcy, and the different stabilized methods used in the literature which lead to stabilize the Galerkin's formulation of Stokes and Darcy's equations. Then, we present the "unified" and "decoupled" strategies used in coupling Stokes and Darcy flows and the way to choose compatible finite elements for both Stokes and Darcy in the coupling problem.

2.2 Stokes-Darcy coupled problem: strong and weak formulations

In this section, we will present the modelling of the fluid. For that we first introduce Stokes' equations and their weak formulation. Then, we present the modelling of the resin flow into preforms. For this we introduce Darcy's equations and their weak formulation. Finally, we present the Stokes-Darcy coupled problem and its weak formulation.

2.2.1 Modelling of the fluid part

2.2.1.1 Incompressible Newtonian fluid

The first assumption is related to the resin which is classically considered as a Newtonian incompressible fluid:

$$\sigma_s \quad = \quad 2\mu\dot{\varepsilon}(\mathbf{v_s}) - p_s\, I \tag{2.1}$$

where $\sigma_\mathbf{s}$ is the cauchy stress tensor, $\dot{\boldsymbol{\varepsilon}}(\mathbf{v_s})$ is the strain rate tensor which is defined by $\dot{\boldsymbol{\varepsilon}}(\mathbf{v_s}) = \frac{1}{2}(\nabla\mathbf{v_s} + \nabla\mathbf{v_s}^T)$, $\mathbf{v_s}$ is the resin velocity, p_s is the hydrostatic pressure, μ is the viscosity and I is the second order identity tensor.

2.2.1.2 Stokes equations

Let us consider Ω_s the region occupied by the fluid, the motion of which is described by both the momentum and mass balance equations. We consider $\partial\Omega_s$ the boundary of Ω_s that can be split into two distinct parts, $\partial\Omega_s = \Gamma_{s,D} \cup \Gamma_{s,N}$ with $\Gamma_{s,D} \cap \Gamma_{s,N} = \emptyset$, corresponding to two different kinds of boundary conditions: Dirichlet or essential condition, Neumann or

natural condition. The velocity is enforced over $\Gamma_{s,D}$ (Dirichlet condition), while the normal stress is enforced over $\Gamma_{s,N}$ (natural condition). The Stokes system, which expresses momentum and mass balances when inertia effect is neglected, is written as: find the velocity $\mathbf{v_s}$ and the pressure p_s fields defined by:

$$\begin{array}{rcll} -div(2\mu\dot{\boldsymbol{\varepsilon}}(\mathbf{v_s})) + \nabla p_s &=& \mathbf{f_s} & \text{in } \Omega_s \\ div\,\mathbf{v_s} &=& h_s & \text{in } \Omega_s \\ \mathbf{v_s} &=& \mathbf{v}^1 & \text{on } \Gamma_{s,D} \\ \boldsymbol{\sigma_{n,s}} &=& -p_{ext,s}.\mathbf{n_s} & \text{on } \Gamma_{s,N} \end{array} \tag{2.2}$$

where $\mathbf{f_s}$ is the volume force, $\mathbf{v^1}$ is the velocity prescribed on the boundary $\Gamma_{s,D}$, $\mathbf{n_s}$ is the unit vector normal to the boundary of Ω_s and $\boldsymbol{\sigma_{n,s}}$ is the normal stress prescribed on $\Gamma_{s,N}$ to be equal to $-p_{ext,s}.\mathbf{n_s}$. If the fluid is incompressible then $h_s = 0$.

2.2.1.3 Weak formulation of Stokes equations

In order to solve Stokes equations by the finite element method, the weak formulation has to be established. We introduce some spaces that we will use for the velocity, pressure and test functions in the weak formulation of Stokes equations:

$$Q_s = L^2(\Omega_s) = \{u : \Omega_s \to R \,|\, \int_{\Omega_s} u^2 d\Omega < \infty\} \tag{2.3}$$

$$H^1(\Omega_s)^m = \{\mathbf{u} \in L^2(\Omega_s)^m \mid \nabla\mathbf{u} \in L^2(\Omega_s)^{m\times m}\} \tag{2.4}$$

$$V_s = H^1_{\Gamma_{s,D}}(\Omega_s)^m = \{\mathbf{u} \in H^1(\Omega_s)^m \mid \mathbf{u} = \mathbf{u^1} \text{ on } \Gamma_{s,D}\} \tag{2.5}$$

$$V_s{}^0 = H^{1,t}_{\Gamma_{s,D}}(\Omega_s)^m = \{u \in H^1(\Omega_s)^m \mid \mathbf{u} = 0 \text{ on } \Gamma_{s,D}\} \tag{2.6}$$

$L^2(\Omega_s)$ is the Lebesgue space of square integrable functions and $H^1_{\Gamma_{s,D}}(\Omega_d)^m$ is the Sobolev space where m is the dimension of the problem ($m = 2$ or 3).
In the entire chapter, we note $\|.\|_0$ and $\|.\|_1$ the L^2 and H^1 norms defined by:

$$\|q\|_0 = (\int_{\Omega_s} q^2 d\Omega_s)^{1/2}$$

$$\|w\|_1 = (\|w\|_0^2 + \sum_{j=1}^{m} \|\frac{\partial w}{\partial x_j}\|_0^2)^{1/2}$$

The weak formulation of Stokes problem is obtained by multiplying the Stokes Equation (2.2) by weighting functions $\mathbf{w_s} \in V_s^0$ and $q_s \in L^2(\Omega_s)$ and then by integrating by parts on the domain Ω_s. For the sake of simplicity, $< .,. >$ denotes the scalar product of functions in $L^2(\Omega_s)$.

The integration by part of the first term of the Stokes equation gives (Equation(2.2)):

$$\begin{aligned} - < div(2\mu\dot{\boldsymbol{\varepsilon}}(\mathbf{v_s})), \mathbf{w_s} > &= < 2\mu\dot{\boldsymbol{\varepsilon}}_{\boldsymbol{ij}} \frac{\partial w_{s,i}}{\partial x_j} > - < 2\mu\dot{\boldsymbol{\varepsilon}}_{\boldsymbol{ij}} n_j, w_{s,i} >_{\Gamma_{s,N}} \\ &= < 2\mu\dot{\boldsymbol{\varepsilon}}(\mathbf{v_s}) : \dot{\boldsymbol{\varepsilon}}(\mathbf{w_s}) > - < (2\mu\dot{\boldsymbol{\varepsilon}}(\mathbf{v_s}).\mathbf{n_s}), \mathbf{w_s} >_{\Gamma_{s,N}} \end{aligned} \tag{2.7}$$

Note: The integral $< -2\mu\dot{\boldsymbol{\varepsilon}}(\mathbf{v_s}).\mathbf{n_s}, \mathbf{w_s} >_{\Gamma_s}$ reduces to $< -2\mu\dot{\boldsymbol{\varepsilon}}(\mathbf{v_s}).\mathbf{n_s}, \mathbf{w_s} >_{\Gamma_{s,N}}$ because the test function $\mathbf{w_s}$ vanishes on $\Gamma_{s,D}(\mathbf{w}_{|\Gamma_{s,D}} = 0)$.

The integration by parts of the second term of Equation (2.2) gives:

$$< \nabla p_s, \mathbf{w_s} >= - < p_s, div\mathbf{w_s} > + < p_s, \mathbf{w_s}.\mathbf{n_s} >_{\Gamma_s}$$

with

$$< p_s, \mathbf{w_s}.\mathbf{n_s} >_{\Gamma_s} = < p_s, \mathbf{w_s}.\mathbf{n_s} >_{\Gamma_{s,N}}$$

since $\mathbf{w}_{|\Gamma_{s,D}} = 0$.

Consequently, we obtain the weak formulation of Stokes equations:

Find $[\mathbf{v_s}, p_s] \in V_s \times Q_s$ such as:

$$< 2\mu\dot{\boldsymbol{\varepsilon}}(\mathbf{v_s}) : \dot{\boldsymbol{\varepsilon}}(\mathbf{w_s}) > - < p_s, div\mathbf{w_s} >= < -p_{ext,s}.\mathbf{n_s}, \mathbf{w_s} >_{\Gamma_{s,N}} + < \mathbf{f_s}, \mathbf{w_s} > \tag{2.8}$$

The weak formulation of Stokes equations can be written as:

Find $\mathbf{v_s} \in V_s$ and $p_s \in Q_s$ such that:

$$B_s([\mathbf{v_s}, p_s], [\mathbf{w_s}, q_s]) = L_s([\mathbf{w_s}, q_s]),\ \forall \mathbf{w_s} \in {V_s}^0,\ \forall q_s \in Q_s \tag{2.9}$$

The bilinear form B_s and the linear form L_s are defined by:

$$B_s([\mathbf{v_s}, p_s], [\mathbf{w_s}, q_s]) = 2\mu < \dot{\boldsymbol{\varepsilon}}(\mathbf{v_s}) : \dot{\boldsymbol{\varepsilon}}(\mathbf{w_s}) > - < p_s, div\mathbf{w_s} > + < div\mathbf{v_s}, q_s > \tag{2.10}$$

$$L_s([\mathbf{w_s}, q_s]) =< \mathbf{f_s}, \mathbf{w_s} > + < h_s, q_s > - < p_{ext,s}.\mathbf{n_s}, \mathbf{w_s} >_{\Gamma_{s,N}} \quad (2.11)$$

Let us note that this formulation corresponds to the dual weak formulation of Stokes equations.

2.2.2 Flow of resin into preforms

Ω_d is the region occupied by the preforms. To model the infiltration of resin into preforms in a macroscopic approach, one represents classically the preforms as an equivalent homogeneous porous medium. Consequently, the laws used to describe the flow into preforms are these from the mechanics of porous media, the classical laws proposed by Darcy [Darcy 1856] and Brinkman [Brinkman 1947]. The Reynolds number R_e is the dimensionless number which allows to simplify the modelling and measures the importance of the inertial forces compared with the viscous forces. It is written as $R_e = \frac{|\mathbf{v_d}|\, d\, \rho}{\mu}$ where d is the average pore diameters, $|\mathbf{v_d}|$ is the fluid velocity in the pores and ρ is the fluid density. The flow is considered as laminar if the Reynolds number is much smaller than 1. Sometimes, it is difficult to know with precision the average pore diameter d. This is why some authors prefer to consider the root of the permeability [1], denoted by $\sqrt{k}$ instead of d [Bear 1990]. In this case, the Reynolds number can be written as: $R_e = \frac{\mathbf{v_d}\sqrt{k}\rho}{\mu}$. For more typical values corresponding to the case considered in this work, $\mathbf{v_d} = 1m/s$, $\mu = 0.1Pa.s$, $k = 10^{-14}\mathrm{m}^2$, $\rho = 10^3 Kg/m^3$ the Reynolds number is equal to 10^{-3}. Hence, the inertial forces are negligible compared with the viscous forces.

2.2.2.1 Darcy's law

The Darcy's law is a derived constitutive equation that describes the flow of a fluid through a porous medium. The law was formulated by Henry Darcy [Darcy 1856], it is a simple first gradient proportional relationship between the volume flux (m/s) and the pressure change per unit length of the porous media. If the flow is one dimensional, the gradient of pressure is $\frac{dp}{dx}$, the Darcy's law is $q = \frac{k}{\mu}\frac{dp}{dx}$. k is the permeability (m^2), μ is the viscosity (Pa.s).

This law is convenient for a low Reynolds number ($R_e << 1$), which is the case where viscous forces dominate inertial forces. In this case, the gradient of pressure is proportional to the velocity of the fluid flow. This Darcy's law can be generalized as [Hassanizadeh 1983]:

$$\mathbf{v_d} = -\frac{\mathbf{k}}{\mu}\boldsymbol{\nabla} p_d$$

with p_d the pressure, $\mathbf{k}$ is the second order permeability tensor and $\mathbf{v_d}$ the average of the ve-

1. Permeability describes the ability of a porous medium to be penetrated by a fluid

locity. To compute the actual fluid velocity in the pores, one has to divide $\mathbf{v_d}$ by the porosity ψ which is the ratio between the volume of pores and the total volume. Then, the real velocity denoted by $\mathbf{v_r}$ is

$$\mathbf{v_r} = \frac{\mathbf{v_d}}{\psi}$$

2.2.2.2 Brinkman's law

An increasing number of articles use Brinkman's equations in place of Darcy's equation for describing flows in porous media. Brinkman's law introduced in [Brinkman 1947] proposes to describe the flow into porous media by generalizing Navier-Stokes equations. This isotropic law for the flow of a Newtonian fluid through a swarm of fixed particles is in the form:

$$\nabla p_d = -\tfrac{\mu}{k}\mathbf{v_d} + \mu^e \Delta \mathbf{v_d} \tag{2.12}$$

where μ^e is the effective viscosity (sometimes called "apparent viscosity"). The practical advantage of Equation (2.12) stands in the fact that it is a slight modification of Stokes equations. Theoretical investigations of the domain of validity of Brinkman equation yield to $\mu^e = \mu$ [Vernescu 1990] and it is estimated that the effective viscosity μ^e goes to μ as the porosity increases to 1 which corresponds to important permeability while in resin infusion processes, on the contrary we have small permeabilities ($10^{-8}\mathrm{m}^2 \leq k \leq 10^{-15}\mathrm{m}^2$).

Both Darcy's law and Brinkman's law are valid at a large scale compared with the pore scale. It means they correspond to a macroscopic approach of the resin flow into preforms. In this manuscript, we will use Darcy's equations considering the permability that we will use for preforms is typically between $10^{-8}\mathrm{m}^2$ and $10^{-15}\mathrm{m}^2$.

2.2.2.3 Darcy's equations

Let us consider Ω_d the region occupied by the preforms. We consider $\partial\Omega_d$ the boundary of Ω_d that can be split into two distinct parts $\partial\Omega_d = \Gamma_{d,D} \cup \Gamma_{d,N}$, corresponding to the two different kinds of boundary conditions: Dirichlet and Newman. Respectively, the Darcy's equations are then expressed as:

Find the velocity $\mathbf{v_d}$ and pressure p_d such as:

$$\begin{array}{lcllll} \frac{\mu}{\mathrm{k}}\mathbf{v_d} + \nabla p_d & = & \mathbf{f_d} & \text{in} & \Omega_d & \\ div\,\mathbf{v_d} & = & h_d & \text{in} & \Omega_d & \\ \mathbf{v_d}.\mathbf{n_d} & = & g_d & \text{on} & \Gamma_{d,D}\,\text{(dual)} \quad \text{or} & \Gamma_{d,N}\,\text{(primal)} \\ p_d & = & p_{ext,d} & \text{on} & \Gamma_{d,N}\,\text{(dual)} \quad \text{or} & \Gamma_{d,D}\,\text{(primal)} \end{array} \tag{2.13}$$

where k is the permeability reduced to a scalar in the isotropic case considered here, $p_{ext,d}$ is a pressure to be prescribed on $\Gamma_{d,N}$, $\mathbf{n_d}$ is the outward unit vector normal to the boundary of Ω_d and $\mathbf{f_d}$ is the volume force. If the fluid is incompressible then $h_d = 0$.

2.2.2.4 Weak formulation of Darcy equations

In order to solve Darcy problem by a finite element method, the weak formulation has to be established. The general spaces of velocity, pressure and test functions are defined by:

$$\begin{array}{lcl} Q_d = L^2(\Omega_d) & = & \{q_d : \Omega_d \longrightarrow \mathrm{R} \,|\, \displaystyle\int_{\Omega_d} \mathbf{q}^2 d\Omega < \infty\} \\ H(div, \Omega_d) & = & \{\mathbf{u} \in L^2(\Omega_d)^m \,|\, div(\mathbf{u}) \in L^2(\Omega_d)\} \\ V_d & = & \{\mathbf{u} \in H(div, \Omega_d) \,|\, \mathbf{u}.\mathbf{n} = u^2 \text{ on } \Gamma_{d,D}\} \\ V_d^0 & = & \{\mathbf{u} \in H(div, \Omega_d) \,|\, \mathbf{u}.\mathbf{n} = 0 \text{ on } \Gamma_{d,D}\} \end{array} \tag{2.14}$$

We have two weak formulations of the Darcy problem: the dual formulation and the primal formulation.

Dual weak formulation

The dual weak formulation for Darcy's equations is obtained by multiplying Equations (2.13) by the weighting functions $\mathbf{w_d} \in V_0^d$ and $q_d \in Q_d$ and then by integrating by parts the term of pressure in the first equation. Then the dual weak formulation of Darcy is:
Find $\mathbf{v_d} \in V_d$ and $p_d \in Q_d$ such that:

$$\begin{array}{rcl} B_d([\mathbf{v_d}, p_d], [\mathbf{w_d}, q_d]) & = & L_d([\mathbf{w_d}, q_d]) \\ \forall \mathbf{w_d} \in V_d^0,\, \forall q_d \in Q_d & & \end{array} \tag{2.15}$$

where the bilinear form B_d and the linear form L_d are defined in Darcy by:

$$\begin{aligned} B_d([\mathbf{v_d}, p_d], [\mathbf{w_d}, q_d]) &= \tfrac{\mu}{k} < \mathbf{v_d}, \mathbf{w_d} > \\ &\quad - < p_d, div\, \mathbf{w_d} > \\ &\quad + < q_d, div\, \mathbf{v_d} > \\ &\quad + < p_d, \mathbf{w_d}.\mathbf{n_d} >_{\Gamma_{d,N}} \end{aligned} \tag{2.16}$$

$$\begin{aligned} L_d([\mathbf{w_d}, q_d]) &= < \mathbf{f_d}, \mathbf{w_d} > \\ &\quad + < h_d, q_d > \\ &\quad + < p_{ext,d}\mathbf{n}, \mathbf{w_d} >_{\Gamma_{d,N}} \end{aligned} \tag{2.17}$$

Primal weak formulation

The primal weak formulation of Darcy problem is obtained by multiplying Equations (2.13) by the weighting functions $\mathbf{w_d} \in L^2(\Omega_d)^m$ and $q_d \in H^1_{\Gamma_{d,D}}(\Omega_d)$ and then by integrating by parts the mass conservation equation. Then, the primal weak formulation of Darcy problem writes: Find $\mathbf{v_d} \in L^2(\Omega_d)^m$ and $p_d \in Q_d$ such that:

$$\begin{aligned} B_d([\mathbf{v_d}, p_d], [\mathbf{w_d}, q_d]) &= L_d([\mathbf{w_d}, q_d]) \\ \forall \mathbf{w_d} \in L^2(\Omega_d)^m \text{ and } q_d \in H^{1,t}_{\Gamma_{d,D}}(\Omega_d) & \end{aligned} \tag{2.18}$$

The bilinear form B_d is defined by:

$$\begin{aligned} B_d([\mathbf{v_d}, p_d], [\mathbf{w_d}, q_d]) &= \tfrac{\mu}{k} < \mathbf{v_d}, \mathbf{w_d} > \\ &\quad + < \nabla p_d, \mathbf{w_d} > \\ &\quad - < \mathbf{v_d}, \nabla q_d > \\ &\quad + < q_d, \mathbf{v}.\mathbf{n_d} >_{\Gamma_{d,N}} \end{aligned} \tag{2.19}$$

In our approach, we will use the dual formulation of Darcy's equations in order to have the same finite elements for pressure and velocity in Stokes and Darcy. This will be detailed later.

2.2.3 Stokes-Darcy coupled problem

The "Stokes-Darcy" coupled problem has been studied by many researchers in many fields of engineering. The main strategies found in the literature to solve the coupling problem are either "decoupled" strategies or "unified" strategies. The decoupled approach consists in using two different discrete spaces to solve Stokes' and Darcy's equations [Riviere & I.Yotov 2005]. Conversely, the monolithic approach consists in using the same finite element spaces [E.Burmana & P.Hansbob 2007], [T.Karper *et al.* 2009], [Arbogast & Brunson 2007]. The originality of

our approach is to use the "unified" approach for coupling Stokes-Darcy in a multi-physics framework in severe transient regimes. Now, we will present the coupling between Stokes and Darcy equations. Let us define $\Omega \subset \mathrm{R^m}$ ($m = 2$ or $m = 3$) a bounded domain made up by two non overlapping subdomains Ω_s and Ω_d separated by a surface $\Gamma = \partial\Omega_s \cap \partial\Omega_d$ (Figure 2.1). Index s is used to denote everything that concerns the purely fluid domain (Stokes), and index d for porous medium (Darcy domain). Γ is the interface between Stokes and Darcy. We note $\mathbf{v}$ the velocity and p the pressure. When coupling Stokes and Darcy, the velocity and pressure in Stokes are noted by $\mathbf{v_s} = \mathbf{v}_{|\Omega_s}$, $p_s = p_{|\Omega_s}$. The velocity and pressure in Darcy are denoted by $\mathbf{v_d} = \mathbf{v}_{|\Omega_d}$ and $p_d = p_{|\Omega_d}$. Conditions have to be considered on the interface Γ of normal $\mathbf{n} = \mathbf{n_s}$. These conditions are:

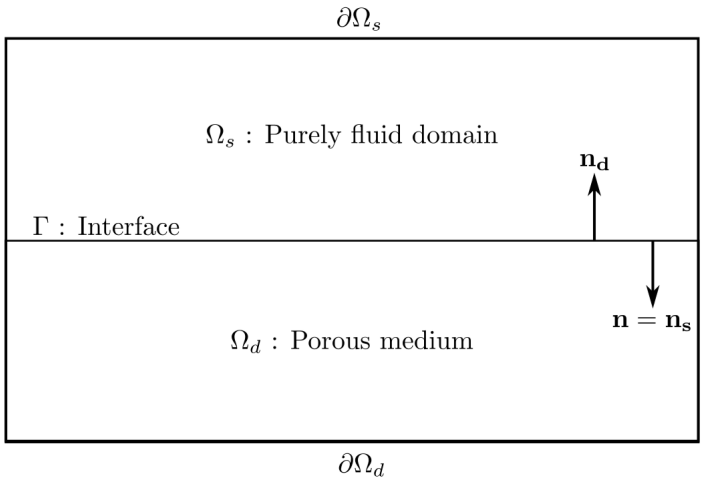

Figure 2.1: Computational domain

Continuity of normal velocity

The mass conservation through the interface Γ is expressed by the continuity of the normal velocity field $\mathbf{v}$ across Γ.

$$\mathbf{v_s}.\mathbf{n_s} + \mathbf{v_d}.\mathbf{n_d} = 0 \quad \text{on } \Gamma \tag{2.20}$$

By considering $\mathbf{n} = \mathbf{n_s} = -\mathbf{n_d}$, Equation (2.20) can be written as

$$\mathbf{v_s}.\mathbf{n} = \mathbf{v_d}.\mathbf{n} \text{ on } \Gamma \tag{2.21}$$

Continuity of the fluid normal stress

The continuity of normal stress over the interface Γ is expressed by

$$\mathbf{n}.\boldsymbol{\sigma_n}.\mathbf{n} \quad = \quad \mathbf{n}.\boldsymbol{\sigma_d}.\mathbf{n} \text{ on } \Gamma \tag{2.22}$$

The stress in Stokes is defined in Equation (2.1) by $\boldsymbol{\sigma_s} = (2\mu\dot{\boldsymbol{\varepsilon}}(\mathbf{v_s}) - p_s\mathbf{I})$ and the stress in porous media is $\boldsymbol{\sigma_d} = -p_d\mathbf{I}$ [Layton *et al.* 2003]. Then, this condition becomes:

$$p_s - 2\mu\mathbf{n}.\dot{\boldsymbol{\varepsilon}}(\mathbf{v_s}).\mathbf{n} = p_d \text{ on } \Gamma \tag{2.23}$$

Beaver-Joseph-Saffman condition

The Beaver Joseph Saffman condition allows the tangential velocity to be specified on the interface Γ. For an isotropic permeability, the interface condition can be written as

$$2\mathbf{n}.\dot{\varepsilon}(\mathbf{v_s}).\boldsymbol{\tau_j} \quad = \quad -\frac{\alpha}{\sqrt{k}}(\mathbf{v_s}.\boldsymbol{\tau_j}), \quad j = 1, 2 \tag{2.24}$$

where α is a dimensionless parameter, so-called slip coefficient, and $\boldsymbol{\tau_j}$ are the tangentiel vectors on the interface.

2.2.3.1 Weak formulation in pressure and velocity for the coupled problem

In order to solve the Stokes-Darcy coupled problem by a finite element method, the weak formulation has to be established. The weak formulation of Stokes-Darcy coupled problem is obtained by summing up both weak formulations of Stokes and Darcy [J.M.Urquiza *et al.* 2008]. We will rewrite the weak formulation of Stokes problem detailed in Section 2.2.1.3 and the weak formulation of Darcy's equations detailed in Section 2.2.2.4 to show how we can take interface conditions into consideration in these formulations.

2.2.3.2 Weak formulation of Stokes equations

By multiplying the Stokes Equations (2.2) by weighting functions $\mathbf{w_s} \in V_s^0$ and $q_s \in Q_s$ and then by integrating by parts on the domain Ω_s, we obtain:

$$\begin{aligned} < 2\mu\,\dot{\boldsymbol{\varepsilon}}(\mathbf{v_s}) : \dot{\boldsymbol{\varepsilon}}(\mathbf{w_s}) >_{\Omega_s} \quad &- \quad < \left(2\mu\,\mathbf{n_s}.\dot{\boldsymbol{\varepsilon}}(\mathbf{v_s}).\mathbf{n_s}\right), (\mathbf{w_s}.\mathbf{n_s}) >_{\Gamma} - < \left(2\mu\,\mathbf{n_s}.\dot{\boldsymbol{\varepsilon}}(\mathbf{v_s}).\boldsymbol{\tau}\right), (\mathbf{w_s}.\boldsymbol{\tau}) >_{\Gamma} \\ &- \quad < p_s, div\,\mathbf{w_s} >_{\Omega_s} + < p_s, \mathbf{w_s}.\mathbf{n_s} >_{\Gamma} = < \boldsymbol{t_s}, \mathbf{w_s} >_{\Gamma_{s,N}} + < \mathbf{f_s}, w_s >_{\Omega_s} \end{aligned} \tag{2.25}$$

$$< q_s,\, div\,\mathbf{v_s} >_{\Omega_s} = < h_s, q_s >_{\Omega_s} \tag{2.26}$$

Using the continuity of the normal stress (2.22) and the BJS interface condition (2.24), we obtain the weak formulation of the Stokes equations:

Find $\mathbf{v_s} \in V_s$ and $p_s \in Q_s$, such that

$$B_s([\mathbf{v_s}, p_s], [\mathbf{w_s}, q_s]) \quad = \quad L_s([\mathbf{w_s}, q_s]) \quad \forall \mathbf{w_s} \in V_s^0, \forall q_s \in Q_s \tag{2.27}$$

with the bilinear form B_s and the linear form L_s defined in Stokes by:

$$\begin{aligned} B_s([\mathbf{v_s}, p_s][\mathbf{w_s}, q_s]) &= 2\mu < \dot{\boldsymbol{\varepsilon}}(\mathbf{v_s}) : \dot{\boldsymbol{\varepsilon}}(\mathbf{w_s}) >_{\Omega_s} - < p_s, div\mathbf{w_s} >_{\Omega_s} + < div\mathbf{v_s}, q_s >_{\Omega_s} \\ &\quad + \underbrace{< p_d, \mathbf{w_s}.\mathbf{n_s} >_{\Gamma}}_{A} + < \frac{\alpha\eta}{\sqrt{k}}(\mathbf{v_s}.\boldsymbol{\tau}), (\mathbf{w_s}.\boldsymbol{\tau}) >_{\Gamma} \\ L_s([\mathbf{w_s}, q_s]) &= < \mathbf{f_s}, \mathbf{w_s} >_{\Omega_s} + < h_s, q_s >_{\Omega_s} + < \mathbf{t_s}, \mathbf{w_s} >_{\Gamma_{s,N}} \end{aligned}$$

2.2.3.3 Weak formulation of Darcy's equations

The weak formulation of Darcy is obtained by multiplying the equations of Darcy (2.13) by the weighting functions defined in V_d^0 and $q_d \in Q_d$ and then, by integrating by part on the domain Ω_d:

$$\begin{array}{ccccccc} < \frac{\mu}{K}\mathbf{v_d}, \mathbf{w_d} >_{\Omega_d} & - & < p_d,\, div\, \mathbf{w_d} >_{\Omega_d} & - & < p_d,\, \mathbf{w_d}.\mathbf{n_s} >_{\Gamma_d} & & \\ & & & = & < \mathbf{f_d}, \mathbf{w_d} >_{\Omega_d} & & \\ & - & < div\mathbf{v_d}, q_d >_{\Omega_d} & = & < h_d, q_d >_{\Omega_d} & & \end{array} \tag{2.28}$$

with $\mathbf{n} = \mathbf{n_s} = -\mathbf{n_d}$.

Using the fact that $\mathbf{w_d}.\mathbf{n_d}$ vanishes on $\Gamma_{d,D}$ and that the weighting functions are in the same spaces ($\mathbf{w_s} \equiv \mathbf{w_d}$), we obtain the so-called dual weak formulation of the Darcy equations which is:
Find $\mathbf{v_d} \in V_d$ and $p_d \in Q_d$, such that

$$B_d([\mathbf{v_d}, p_d], [\mathbf{w_d}, q_d]) \quad = \quad L_d([\mathbf{w_d}, q_d]),\, \forall\, \mathbf{w_d} \in V_d^0,\, \forall q_d \in Q_d \tag{2.29}$$

The bilinear form B_d and the linear form L_d are defined in Darcy by:

$$\begin{aligned} B_d([\mathbf{v_d}, p_d][\mathbf{w_d}, q_d]) &= \frac{\mu}{k} < \mathbf{v_d}, \mathbf{w_d} >_{\Omega_d} - < p_d, div\mathbf{w_d} >_{\Omega_d} \\ &\quad - < q_d, div\mathbf{v_d} >_{\Omega_d} - \underbrace{< p_d,\, \mathbf{w_s}.\mathbf{n_s} >_{\Gamma}}_{B} \\ L_d([\mathbf{w_d}, q_d]) &= < \mathbf{f_d}, \mathbf{w_d} >_{\Omega_d} + < h_d, q_d >_{\Omega_d} + < p_{ext}, \mathbf{w_d} >_{\Gamma_{d,N}} \end{aligned} \tag{2.30}$$

2.2.3.4 Mixed weak formulation of Stokes-Darcy coupled problem

The mixed weak formulation of Stokes-Darcy is obtained by summing up Equations (2.28) and (2.30) and taking into consideration the conditions imposed on the Stokes-Darcy interface described in Section 2.2.3. The terms denoted by A and B in Equations (2.28), (2.30) respectively vanish when summing up these two formulations. The integrals over Ω_s and Ω_d have to be redefined. For this, we introduce the Heaviside function H_i (equal to 1 in the domain i ($i = s \,\text{or}\, d$) and vanishing elsewhere), and we have:

$$\int_{\Omega_i} (\ ) = \int_{\Omega} (\ ) H_i d\Omega$$

Hence, the variational formulation of the Stokes-Darcy coupled problem consists in finding $[\mathbf{v}, p] \in V_c \times Q_c$ such that:

$$B_c([\mathbf{v}, p], [\mathbf{w}, q]) = L_c([\mathbf{w}, q])$$

$$\forall [\mathbf{w}, q] \text{ defined in } V_c^0 \times Q_c$$

.

$$V_c = V_s \times V_d$$

$$V_c^0 = V_s^0 \times V_d^0$$

$$Q_c = Q_s \times Q_d$$

The bilinear form B_c and the linear form L_c are defined by:

$$\begin{aligned} B_c([\mathbf{v}, q], [\mathbf{w}, q]) \;=\; & < 2\mu\dot{\boldsymbol{\varepsilon}}(\mathbf{v}) : \dot{\boldsymbol{\varepsilon}}(\mathbf{w}) H_s >_\Omega + < \frac{\mu}{k}\, \mathbf{v}, \mathbf{w}\, H_d >_\Omega \\ & - < p\,, div\, \mathbf{w} >_\Omega + < q,\, div \mathbf{v} >_\Omega \\ & + < \frac{\alpha\mu}{\sqrt{k}}\, \mathbf{v}\,, \mathbf{w} >_\Gamma \end{aligned} \tag{2.31}$$

$$L_c([\mathbf{v}, p], [\mathbf{w}, q]) \;=\; < \mathbf{f}, \mathbf{w} >_\Omega + < h, q >_\Omega + < \mathbf{t_s}, \mathbf{w} >_{\Gamma_{s,N}} + < p_{ext}, \mathbf{w} >_{\Gamma_{d,N}} \tag{2.32}$$

($\mathbf{f}$, h) are defined by ($\mathbf{f_d}$,h_d) in Darcy and ($\mathbf{f_s}$,h_s) in Stokes.

2.3 Stability of the mixed continuous and discretized problems

2.3.1 Stability of the mixed continuous problem

Some problems can not be solved using the Lax–Milgram theorem enunciated in Appendix A. To allow a better understanding of the theorems mentioned before, we will take the Stokes' problem as an example:

$$\begin{array}{rcll} -\mu\Delta\mathbf{v_s} + \nabla p_s & = & \mathbf{f_s} & \text{in } \Omega_s \\ div\,\mathbf{v_s} & = & h_s & \text{in } \Omega_s \\ \mathbf{v_s} & = & \mathbf{v}^1 & \text{on } \Gamma_{s,D} \\ \boldsymbol{\sigma_n} & = & -p_{ext,s}.\mathbf{n_s} & \text{on } \Gamma_{s,N} \end{array} \tag{2.33}$$

Then, the weak formulation associated with the Stokes system defined in Equation (2.33) is: Find $[\mathbf{v_s}, p_s]$ such that:

$$B_s([\mathbf{v_s}, p_s], [\mathbf{w_s}, q_s]) = L_s([\mathbf{w_s}, q_s] \tag{2.34}$$
$$\forall [\mathbf{w_s}, q_s] \in V_s^0 \times Q_s$$

where the bilinear form $B_s([\mathbf{v_s}, p_s], [\mathbf{w_s}, q_s])$ and the linear form $L_s([\mathbf{w_s}, q_s])$ are defined by:

$$\begin{array}{rcl} B_s([\mathbf{v_s}, q_s], [\mathbf{w_s}, q_s]) & = & 2\mu < \nabla\mathbf{v_s}, \nabla\mathbf{w_s} >_{\Omega_s} \\ & & - < p_s, div\mathbf{w_s} >_{\Omega_s} \\ & & + < div\mathbf{v_s}, q_s >_{\Omega_s} \end{array} \tag{2.35}$$

$$\begin{array}{rcl} L_s([\mathbf{w_s}, q_s]) & = & < \mathbf{f_s}, \mathbf{w_s} >_{\Omega_s} \\ & & + < p_{ext,s}.\mathbf{n_s}, \mathbf{w_s} >_{\Gamma_{s,N}} \end{array} \tag{2.36}$$

To make an attempt at proving the coercivity of $B_s(.,.)$ one computes:

$$B_s([\mathbf{v_s}, p_s], [\mathbf{v_s}, p_s]) = \int_{\Omega_s} |\nabla\mathbf{v_s}|^2 d\Omega \tag{2.37}$$

Equation (2.37) cannot be lower bounded by $|||[\mathbf{v_s}, p_s]|||$ since $||p_s||_0$ is absent in the identity above (2.37).Then, the mixed formulation cannot be studied in the usual framework of the **Lax-Miligram** theorem.

In this section, we will enunciate two theorems used to prove the existence and uniqueness of the solution for this type of problems. The first theorem is dedicated to the mixed problems written in their abstract form (**P**). Let us consider the following problem (**P**):

Find $\mathbf{v}$ and p such that:

$$(P)\begin{cases} a(\mathbf{v},\mathbf{w})+b(\mathbf{v},p) &= L(\mathbf{w})\ \forall \mathbf{w}\in V \\ b(\mathbf{w},q) &= F(q)\ \forall q\in M \end{cases} \tag{2.38}$$

V and M are Hilbert spaces. a and b are bilinear continuous forms, L and F are linear continuous forms.
We remark that for all $\mathbf{w}\in V$, the application: $\mathbf{w}\longrightarrow a(\mathbf{v},\mathbf{w})$ is linear and continuous (because of the bilinearity of $a(.,.)$). Then, by using the Riesz representation, it exists a unique vector Av such that:

$$a(\mathbf{v},\mathbf{w})=(Av,\mathbf{w})_V\ \forall\,\mathbf{w}\in V$$

In addition, we do the same with b which is also bilinear and continuous from $V\times M$ to $\mathbb{R}$, we introduce $B\in\mathcal{L}(V,M)$ and its adjoint $B^{'}\in\mathcal{L}(M,V)$ ($\mathcal{L}$ is the set of the linear forms) such that:

$$\forall\mathbf{w}\in V,\forall q\in M, b(\mathbf{w},q)=(B\mathbf{w},q)_M=(\mathbf{w},B^{'}q)_V$$

We can do the same thing with the vectors $l\in V$ and $f\in M$ such that:

$$\begin{aligned} \forall\mathbf{w}\in V, L(\mathbf{w}) &= (l,\mathbf{w})_V \\ \forall q\in M, F(q) &= (\mathbf{f},q)_M \end{aligned} \tag{2.39}$$

Using the operators introduced before, the problem can be written as:

Find $\mathbf{v}\in V$ and $p\in M$ such that :

$$\begin{aligned} Av+B^{'}p &= l \\ Bv &= f \end{aligned} \tag{2.40}$$

Let us note,

$$Z=\{\mathbf{w}\in V\,\text{such that}\,B(\mathbf{w},q)=0,\forall q\in M\}=\{\mathbf{w}\in V\,\text{such that}\,\mathbf{Bw}=0\}=Ker\mathbf{B}$$

and

$$Z_f=\{\mathbf{w}\in V\ \text{such that}\ b(\mathbf{w},q)=F(q),\forall q\in M\}=\{\mathbf{w}\in V\,\text{such that}\,\mathbf{Bw}=f\}$$

The initial problem (P) can be associated with $(P^{'})$ such that:

$$(P') \begin{cases} \text{Find } \mathbf{v} \in Z_f \in M & \text{such that} \\ a(\mathbf{v}, \mathbf{w}) = L(\mathbf{w}) \, \forall \mathbf{w} \in Z \end{cases} \tag{2.41}$$

If we suppose that Z_f is not empty, then $\exists \mathbf{v_0} \in Z_f$ such that $\mathbf{v_1} = \mathbf{v} - \mathbf{v_0}$, the problem $(P^{'})$ is equivalent to the following problem (Q):

$$(Q) \begin{cases} \text{Find } \mathbf{v_1} \in Z & \text{such that} \\ a(\mathbf{v_1}, \mathbf{w}) = L(\mathbf{w}) - a(\mathbf{v_0}, \mathbf{w}) \, \forall \mathbf{w} \in Z \end{cases} \tag{2.42}$$

The space Z is closed in V, then we can apply the Lax-Miligram theorem on the problem (Q) under the hypothesis that the bilinear form a is coercive on $Z = KerB$. Consequently, the Lax-Miligram theorem under this hypothesis imposes the following conditions:

Continuity:

$$\begin{aligned} &\exists M > 0, \forall \mathbf{v}, \forall \mathbf{w} \in V \\ &|a(\mathbf{v}, \mathbf{w})| \leq M ||\mathbf{v}||_V ||\mathbf{w}||_V \end{aligned} \tag{2.43}$$

Coercivity or (ellipticity) on $Z = KerB$:

$$\exists \alpha > 0, \forall \mathbf{w} \in Z = KerB, a(\mathbf{w}, \mathbf{w}) \geq \alpha ||\mathbf{w}||_X^2 \tag{2.44}$$

If this condition is realized, problem $(P^{'})$ admits a unique solution $\mathbf{v} \in Z_f$. In addition, to have the uniqueness and existence of the solution of the initial problem (P) (existence and uniqueness of the pressure p), we have to add the following hypothesis:
the operator $B : V \longrightarrow M$ is surjective. Since $\mathbf{v}$ is unique, consequently if B is surjective, it exists a unique solution $p = B(l - A\mathbf{v})$. The surjectivity of the operator $B : V \longrightarrow M$ is equivalent to the following *inf-sup* condition satisfied by b and defined in equation(2.45).

$$\underset{q \in M}{inf} \, \underset{\mathbf{w} \in V}{sup} \frac{b(\mathbf{v}, q)}{||\mathbf{w}||_V \, ||q||_M} \geq C \tag{2.45}$$

Then, the Brezzi-Babũska theorem used to prove the existence and uniqueness of the solution of problem (P) is enunciated as:

Brezzi-Babũska theorem:

$$\begin{array}{l} i)\,\text{The bilinear form } a(.,.) \text{ is continuous and coercive on } Z = ker(B). \\ ii)\,\text{The } \textit{inf-sup} \text{ condition } \underset{q\in M}{inf}\ \underset{\mathbf{w}\in V}{sup} \frac{b(\mathbf{v},q)}{||\mathbf{w}||_V, ||q||_M} \geq C \text{ is satisfied on } V \times M, \\ \text{this condition is also equivalent to: the operator } B : V \longrightarrow M \text{ is surjective.} \end{array} \tag{2.46}$$

Existence and uniqueness of the solution with the Babũska theorem

In some cases, particulary to study the stabilized bilinear forms, it is preferable to use the following form of the problem (P):
Find $[\mathbf{v}, p] \in V \times Q$ such that:

$$B([\mathbf{v}, p], [\mathbf{w}, q]) = L([\mathbf{w}, q]) \,\forall\, [\mathbf{w}, q] \in V^0 \times Q^0$$

where B is a bilinear continuous form and L is a linear continuous form. In this case, (P) admits a unique solution if and only if it satisfies Babũska theorem (2.47).

Babũska theorem:

$$\begin{array}{l} i)\,\text{Suppose that } B \text{ is weakly coercive: for some constant } c > 0 \text{ and all } [\mathbf{v}, p] \in V \times Q : \\ \qquad \underset{|||[\mathbf{w},q]|||=1}{sup} |B([\mathbf{v}, p], [\mathbf{w}, q])| \geq c \times |||[\mathbf{v}, p]||| \\ ii) \qquad \text{For} [\mathbf{w}, q] \neq 0 \in V, \exists c_1 > 0 : \\ \qquad \underset{|||[\mathbf{v},p]|||=1}{sup} |B([\mathbf{v}, p], [\mathbf{w}, q])|| \geq c_1 |||[\mathbf{w}, q]|| \end{array} \tag{2.47}$$

These two conditions are also equivalent to:

$$\begin{array}{l} \exists C > 0 \,\text{for all}\, [\mathbf{v}, p] \in V \times Q, \exists [\mathbf{w}, q] \in V^0 \times Q^0 \text{such that } : \\ B([\mathbf{v}, p], [\mathbf{w}, q]) \geq C\, |||[\mathbf{v}, p]||_{V\times Q}\, |||[\mathbf{w}, q||_{V^0\times Q^0} \end{array} \tag{2.48}$$

To allow a better understanding of the application of these theorems, we will take the "Stokes" problem as example. We will apply the "Brezzi-Babũska" theorem on Stokes problem, for this reason, we will write it in its abstract form.

$$\begin{array}{rcl} a(\mathbf{v_s}, \mathbf{w_s}) + b(\mathbf{w_s}, p_s) & = & < \mathbf{f_s}, \mathbf{w_s} >_{\Omega_s} + < p_{ext,s}.\mathbf{n_s}, \mathbf{w_s} >_{\Omega_s} \\ b(\mathbf{v_s}, q_s) & = & 0 \end{array} \tag{2.49}$$

Taking into consideration the Riesz representation, explained before, we will have $A = -\Delta$, $B = -div$ and $B^{'} = \nabla$. Consequently, Z will be defined by:

$$Z = KerB \quad = \quad \{\mathbf{v_s} \in V_s,\, div\mathbf{v_s} = 0\} \tag{2.50}$$

For that, we will prove the existence and unicity of the solution of Stokes problem by using the Brezzi-Babũska theorem(2.46).

First, to prove the condition (i) of theorem (2.46), we will demonstrate the continuity of a, then its coercivity on $KerB$.

Continuity of $a(.,.)$:

$$\begin{aligned} |a(\mathbf{v_s}, \mathbf{w_s})| \quad &= \quad | < \nabla \mathbf{v_s}, \nabla \mathbf{w_s} > | \\ &\leq ||\nabla \mathbf{v_s}||_0 \, ||\nabla \mathbf{w_s}||_0 \, \text{(Cauchy-Shwarz)} \\ &\leq ||\mathbf{v_s}||_1 \, ||\mathbf{w_s}||_1 \end{aligned} \tag{2.51}$$

Coercivity of a(.,.)

$$a(\mathbf{v_s}, \mathbf{v_s}) = ||\nabla \mathbf{v_s}||_0^2$$

$$\begin{aligned} ||\mathbf{v_s}||_1{}^2 \quad &= \quad ||\mathbf{v_s}||_0{}^2 + ||\nabla \mathbf{v_s}||_0{}^2 \\ &\leq c'||\nabla \mathbf{v_s}||_0{}^2 + ||\nabla \mathbf{v_s}||_0{}^2 \text{(use of Poincaré inequality)} \\ &\simeq (c'+1)||\nabla \mathbf{v_s}||_0{}^2 \end{aligned} \tag{2.52}$$

Then, $||\nabla \mathbf{v_s}||_0 \geq C|\mathbf{v_s}||_1$, which means the coercivity of the bilinear form $a(.,.)$ over $V_s \times V_s$.

Consequently, the bilinear form of Stokes problem $a(.,.)$ satisfies the condition (i) of the theorem (2.46).

The second condition of theorem (2.46) comes from the following corollary:

Let Ω be an open and connected set with a Lipshitz boundary, then the operator div is surjective from $H_0^1(\Omega) \longrightarrow L_0^2(\Omega)$ [F.Brezzi & M.Fortin 1991]. By satisfying these two conditions of theorem (2.46) the existence and uniqueness of the solution of Stokes problem has been proved.

2.3.2 Stability of the Galerkin discretized mixed problem

The whole domain $\Omega_s \subset \mathrm{R^m}$ is discretized with one single mesh made up of triangles if $m = 2$ and of tetrahedrons if $m = 3$. Let us consider for all the methods proposed here:

- $V_{h,s}$ the finite element space of discretized velocity,

- $V^0_{h,s}$ the finite element space of discretized test function of velocity,
- $Q_{h,s}$ the finite element space of discretized pressure.

The discretized form of the abstract formulation consists in finding $(\mathbf{v_{h,s}}, p_{h,s}) \in V_{h,s} \times Q_{h,s}$ such that:

$$\begin{array}{rcl} a(\mathbf{v_{h,s}}, \mathbf{w_{h,s}}) + b(\mathbf{v_{h,s}}, p_{h,s}) & = & < \mathbf{f_s}, \mathbf{v_{h,s}} > \\ b(\mathbf{v_{h,s}}, q_{h,s}) & = & < h, q_{h,s} > \end{array} \tag{2.53}$$

and the discretized algebraic operators, $A_h : V_{h,s} \longrightarrow V'_{h,s}$, $B_h : V_{h,s} \longrightarrow Q'_{h,s}$ can be defined as:

$$< A_h \mathbf{v_{h,s}}, \mathbf{w_{h,s}} >= a_h(\mathbf{v_{h,s}}, \mathbf{w_{h,s}})$$

$$< B_h \mathbf{v_{h,s}}, q_{h,s} >= b_h(\mathbf{v_{h,s}}, q_{h,s})$$

If the problem is well defined and can be studied using the Lax-Miligram theorem on a space V_s, any of its finite element space $V_{h,s} \subset V_h$ can be also treated by the Lax-Miligram theorem. The discrete problem inherits the properties of the continuous problem and therefore the well-posedness. However in some cases, the well posedness of the mixed variational problem (2.49) does not imply in general that its discrete contrepart is also well posed. The reasons for this are:

- First, if one defines $Z_{h,s} = KerB_h = \{\mathbf{v_{h,s}} \in V_{h,s}, \forall q_{h,s} \in Q_{h,s}, b(\mathbf{v_{h,s}}, q_{h,s}) = 0\}$, then if $V_{h,s} \nsubseteq V_s$, and the continuous problem satisfies property (i) of theorem (2.46) on $KerB$, it does not imply that the discrete problem satisfies the analogous property on $KerB_h$.
- Second, the *inf-sup* condition on $V_s \times Q_s$:

$$\exists \beta > 0 \quad \inf_{q_s \in Q_s} \quad \sup_{\mathbf{v_s} \in V_s} \frac{b(\mathbf{v_s}, q_s)}{||\mathbf{v_s}||_1 ||q_s||_0} \geqslant \beta \tag{2.54}$$

  only implies

$$\exists \beta > 0 \quad \inf_{q_{h,s} \in Q_{h,s}} \quad \sup_{\mathbf{v_s} \in V_s} \frac{b(\mathbf{v_s}, q_{h,s})}{||\mathbf{v_s}||_1 ||q_{h,s}||_0} \geqslant \beta \tag{2.55}$$

  which is an *inf-sup* condition on $V_s \times Q_{h,s}$. The latter does not imply in general an *inf-sup* condition on $V_{h,s} \times Q_{h,s}$ even if $V_{h,s} \subset V_s$.

Therefore, it is necessary to prove that assumptions (i) and (ii) of theorem (2.46) are satisfied by the discrete problem on $V_{h,s} \times Q_{h,s}$ itself. In many practical cases, the *inf-sup* condition and the coercivity of the bilinear form $a(.,.)$ are not satisfied if spaces $V_{h,s}$ and $Q_{h,s}$ are not compatible. For example, as we will see in the next section, some finite element spaces

are compatible to satisfy the conditions of theorem (2.46). In opposite to this situation, in some cases, we have to find adequate norms on $V_{h,s}$ and $Q_{h,s}$ and a stabilized bilinear form which satisfies the "Babũska" theorem (theorem (2.47)). The condition of stability generated by the "Babũska" theorem leads to:

$$\inf_{[\mathbf{v_{h,s}},p_{h,s}]\in V_{h,s}\times Q_{h,s}} \sup_{[\mathbf{w_{h,s}},q_{h,s}]\in V^0_{h,s}\times Q_{h,s}} \frac{B_s([\mathbf{v_{h,s}},p_{h,s}],[\mathbf{w_{h,s}},q_{h,s}])}{|||[\mathbf{v_{h,s}},p_{h,s}]|||||[\mathbf{w_{h,s}},q_{h,s}]|||} \geq \beta$$

equivalent to the stability condition:

$$\begin{aligned} &\forall [\mathbf{v_{h,s}},p_{h,s}] \in V_{h,s}\times Q_{h,s}, \exists [\mathbf{w_{h,s}},q_{h,s}] \in V^0_{h,s}\times Q_{h,s} \text{ such that} \\ &B_s([\mathbf{v_{h,s}},p_{h,s}],[\mathbf{w_{h,s}},q_{h,s}]) \geq \beta |||[\mathbf{v_{h,s}},p_{h,s}]|_{V_{h,s}\times Q_{h,s}} |||[\mathbf{w_{h,s}},q_{h,s}]||_{V^0_{h,s}\times Q_{h,s}} \end{aligned} \tag{2.56}$$

In the next sections, we will detail the compatible stable elements for Stokes where theorem (2.46) is satisfied, then, we will detail some stabilized methods on uncompatible spaces. After, we will do the same with the mixed variational formulation of Darcy problem

2.4 Mixed stable and stabilized finite elements for Stokes problem

Section 2.3.2 has provided the theoretical results needed for analyzing the Galerkin discretization of the variational mixed problem, especially the Stokes problem. For the Stokes problem, as we mentioned before, the main difficulty is to find spaces $V_{h,s}$ and $Q_{h,s}$ that satisfy the *inf-sup* condition (2.46 i) applied to discretized problem:

$$\exists \beta_h > 0, \quad \inf_{q_{h,s}\in Q_{h,s}} \sup_{\mathbf{v_{h,s}}\in V_{h,s}} \frac{\int_{\Omega_s} q_{h,s} div \mathbf{v_{h,s}}}{||\mathbf{v_{h,s}}||_1 ||q_{h,s}||_0} \quad \geq \quad \beta_h \tag{2.57}$$

For example, the pairs P_r/P_r for $r \geq 1$, and P_1/P_0 are known to be unstable. This means that the spaces $V_{h,s}$ and $Q_{h,s}$ built on these finite elements do not satisfy the *inf-sup* condition (2.57). In the next sections, we will see some examples of stable pairs of finite elements for Stokes problem, then we will see some stabilized methods which modify unstable Stokes discretized equations to make them stable.

2.4.1 Stable mixed finite elements

These finite elements are defined in particular finite element spaces with specific orders of approximations for pressure and velocity. These elements satisfy the usual *inf-sup* condition ((2.46) i)) and converge for both pressure and velocity. Crouzeix-Raviart in [Crouzeix & Raviart 1973], MINI-elements in [Arnold *et al.* 1984], Taylor-Hood elements in [C.Taylor & P.Hood 1973] are mixed stable elements for the Stokes problem. In this section, we will detail Taylor-Hood elements and the MINI-element (P1+/P1).

2.4.1.1 Taylor Hood elements

The dimensional finite element spaces for velocity, pressure and test functions are:

$$\begin{aligned} V_{h,s} &= \{\, \mathbf{v_{h,s}} \in C^0(\Omega_s)^m, \mathbf{v_{h,s}}_{|K} \in R_l(K)\} \\ V^0_{h,s} &= \{\mathbf{w_{h,s}} \in C^0(\Omega_s)^m, \mathbf{w_{h,s}}_{|K} \in R_l(K), \mathbf{w_{h,s}}_{\Gamma_{s,D}} = 0\} \\ Q_{h,s} &= \{\, q_{h,s} \in C^0(\Omega_s),\, p_{h,s|K} \in R_{l-1}(K)\} \end{aligned} \tag{2.58}$$

Here, $V_{h,s} \subset V_s$, $V^0_{h,s} \subset V^0_s$ and $Q_{h,s} \subset Q_s$.
The Lagrangian finite element spaces $R_l(K)$ are defined by:

$$R_l(K) = \begin{cases} P_l(K) & \text{if K is a tetrahedron or triangles} \\ Q_l(K) & \text{if K is a quadrilateral or hexahedrons} \end{cases} \tag{2.59}$$

where P_l are polynomial of order l and Q_l are quadratics of order l. The Taylor Hood elements satisfy the *inf-sup* conditions (2.46 ii)), it means $\forall[\mathbf{w_{h,s}}, q_{h,s}] \in V^0_{h,s} \times Q_{h,s}$ the bilinear form $B_s([\mathbf{v_{h,s}}, p_{h,s}], [\mathbf{w_{h,s}}, q_{h,s}])$ is stable over $V_{h,s} \times Q_{h,s}$.

Taylor Hood approximations for the Stokes problem lead to the following error estimates:

$$\begin{aligned} ||p_s - p_{h,s}||_0 &\leq c\, h^{l+1}(|v_s|_{l+2} + |p_s|_{l+1}) \\ ||\mathbf{v_s} - \mathbf{v_{h,s}}||_1 &\leq c\, h^{l+1}(|v_s|_{l+2} + |p_s|_{l+2}) \end{aligned} \tag{2.60}$$

$||\ ||_0$ and $||\ ||_1$ are the general L^2 and H^1 norms. Those rates of convergence are optimal for pressure in L^2 norm and for velocity in H^1 norm.

The most popular and simple element form in the Taylor Hood families is the P2/P1 element. This element is related to families of high order elements and to the popular Taylor Hood element (Figure 2.2). It has 15 degrees of freedom in 2D (12 for velocity and 3 for pressure) and 34 degrees of freedom (30 for velocity and 4 for pressure). It is more expensive in space and CPU time than P1+/P1 elements which we detail in section 2.4.1.2. This element

satisfies the usual *inf-sup* condition (2.46 i)).

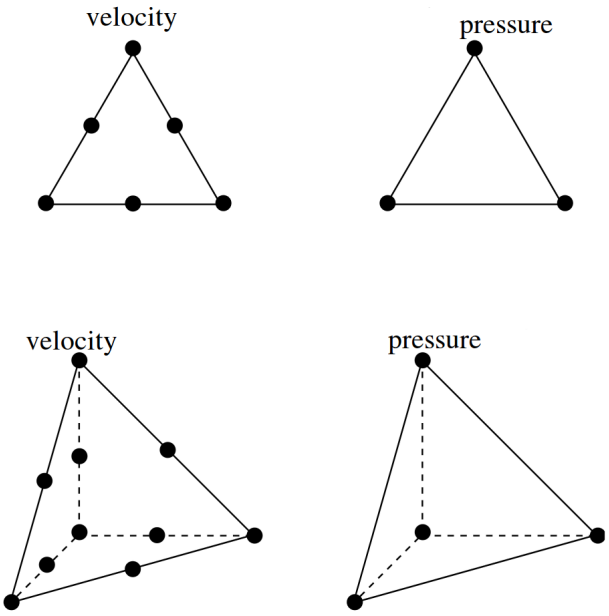

Figure 2.2: P2/P1 element

2.4.1.2 MINI-elements (P1+/P1 element)

Another popular stable element is the so-called P_1+/P_1 pair, also known as the MINI-element. This element is introduced in [Arnold *et al.* 1984]. It consists of adding to the P_1/P_1 element one degree of freedom for each component of the velocity on the barycenter of the triangles ($m = 2$) or of the tetrahedrons ($m = 3$). Let $b_{h,s}$ denotes a function which takes the value 1 at the barycenter of the element K and vanishes on its boundary ∂K and verifies $0 \leq b_{h,s} \leq 1$ such a function is known as a "bubble function". To write the discretized form of the Stokes problem solved with the MINI-element, we decompose the velocity into its linear part $\mathbf{v_{h,s}}$ and its bubble part $\mathbf{b_{h,s}}$:

$$\begin{array}{rcl} \mathbf{v^1_{h,s}} & = & \mathbf{v_{h,s}} + \mathbf{b_{h,s}} \\ \mathbf{v^1_{h,s}} \in V^1_{h,s} & = & V_{h,s} \oplus B_{h,s} \end{array} \tag{2.61}$$

$V_{h,s}$ is the space of the piecewise linear and continuous functions, $B_{h,s}$ is the space of bubble functions. $V_{h,s}$ and $B_{h,s}$ are defined by:

$$V_{h,s} = \{\mathbf{v_{h,s}} \,|\mathbf{v_{h,s}} \in C^0(\Omega_s)^m, \mathbf{v_{h,s}}_{|K} \in P_1(K)^m\} \tag{2.62}$$

$$B_{h,s} = \{\mathbf{b_{h,s}} \in C^0(\Omega_s)^m, \mathbf{b_{h,s}} = 0 \text{ on } \partial K, \mathbf{b_{h,s}}_{STi} \in P_1(STi)^m\} \quad (2.63)$$

where STi are the sub-elements of the element K ($i = 1, 2, 3$ if $m = 2$). This element satisfies the usual *inf-sup* condition (2.46 ii)), and the *inf-sup* constant β_h of this MINI-element is independant of h which ensures convergence rates. P1+/P1 has 9 degrees of freedom, in 2D (6 for velocity and 3 for pressure), and 16 degrees of freedom, in 3D (12 for velocity and 4 in pressure). Figure 2.3 shows the degrees of freedom for P1+/P1 element in 2D and 3D.

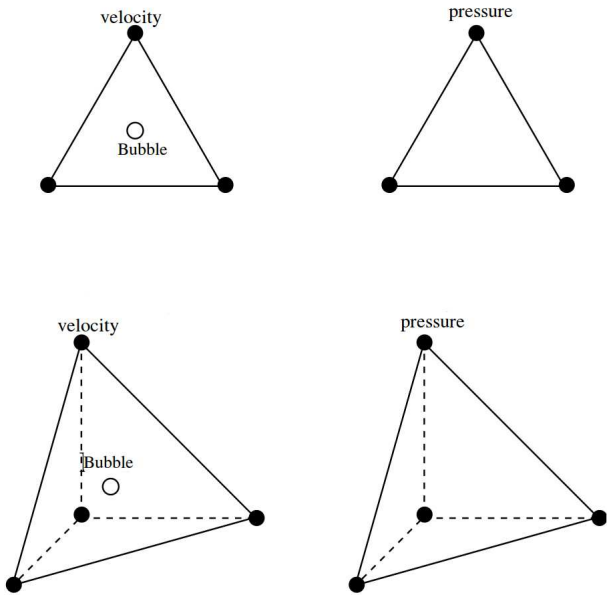

Figure 2.3: P1+/P1 element

Conclusions

After introducing the compatible elements for Stokes, where conditions of theorem (2.46) are satisfied on the discretized velocity and pressure spaces generated by these elements, we will describe next some stabilization methods used for the finite element spaces where the ellipticity is not satisfied on $KerB$, it does not satisfy the condition (i) of theorem (2.46). The use of stabilization methods generates a stable bilinear form which satisfies the conditions of Babũska theorem (2.47).

2.4.2 Residual and penalized methods

In these methods, the standard Galerkin formulation is modified by the addition of mesh-dependent terms which are residuals of the differential equations. By this technique, it is

possible to avoid the stability problem related to the classical mixed methods and hence the convergence can be established for a wide family of simple interpolations. This methodology was first used in connection with advective flows in the works of Brooks and Hughes [T.J.R.Hughes 1982], Hughes et al. [T.J.R.Hughes & A.N.Brooks 1979], [T.J.R.Hughes *et al.* 1989]. Developments of these formulations to mixed methods started in Hughes et al [Hughes *et al.* 1986], motivated by the stabilization procedure proposed by Brezzi and Pikaranta [F.Brezzi & J.Pitkaranta] to the Stokes problem, relying on linear elements for both velocity and pressure. Different from the formulation proposed by Brezzi and Pitkaranta, the work in Hughes et al. [Hughes *et al.* 1986] presented a consistent formulation which allowed the construction of a higher order approximation with optimal accuracy. Later numerous variants and extension have been proposed and analysed such as in Hughes and Franca [T.J.R.Hughes 1987], Franca et al [L.Franca & T.J.R.Hughes 1988], Brezzi and Douglas [F.Brezzi & J.Douglas 1988], Douglas and Wang [J.Douglas & J.wang 1989], Silvester and Kechkar [D.J.Silvester & N.Kechkar 1990a], and Franca et al [L.P.Franca *et al.*]. In the next sections, we will develop the first method developed in [Hughes *et al.* 1986] and the method developed in [J.Douglas & J.wang 1989].

2.4.2.1 Hughes-Balestra-Franca methods [Hughes *et al.* 1986]

Hughes, Balastra, and Franca [Hughes *et al.* 1986] proposed to modify the discretized form of Stokes equations. One proposes to consider a non conforming space of pressure ($Q_{h,s} \nsubseteq Q_s$) by taking the space of $p_{h,s}$ in $H^1(\Omega_s)$ rather than $L^2(\Omega_s)$ and to test the first equation (momentum balance) of the system defined in (2.33) against $\nabla q_{h,s}$, ($q_{h,s} \in Q_{h,s}$) over each triangle ($m = 2$) or tetrahedron ($m = 3$), then multiply the result by h_k^2 (h_k is the size of mesh) and add their sum to the weak formulation of the first equation of the system defined in (2.33).

Remark: This method is based on homogenous conditions for velocity, it means that $\mathbf{v_s} = 0$ on $\Gamma_{s,D}$, because of the coercivity of the bilinear form of Stokes which is demonstrated in a manner which requires the homogeneity on the solution $\mathbf{v_{h,s}} \in V_{h,s}^0 \subset V_s^0$ rather than $V_{h,s} \subset V_s$. To define a procedure over the space $V_{h,s}$ (for velocity), we have to introduce a method based on some ideas corresponding to those discussed by Nitshe for Dirichlet problems [J.Nitsche 1977].

Then we have to solve the discretized form of Stokes defined by:
Find $[\mathbf{v_{h,s}}, p_{h,s}] \in V_{h,s}^0 \times Q_{h,s}$ such as:

$$B_{s,stable}([\mathbf{v_{h,s}}, p_{h,s}], [\mathbf{w_{h,s}}, q_{h,s}]) = L_{s,stable}([\mathbf{w_{h,s}}, q_{h,s}]) \quad (2.64)$$
$$\forall [\mathbf{w_{h,s}}, q_{h,s}] \in V^0_{h,s} \times Q_{h,s}$$

where the bilinear form $B_{s,stable}$ and the linear form $L_{s,stable}$ are defined by:

$$\begin{aligned} B_{s,stable}([\mathbf{v_{h,s}}, p_{h,s}], [\mathbf{w_{h,s}}, q_{h,s}]) &= B_s([\mathbf{v_{h,s}}, p_{h,s}], [\mathbf{w_{h,s}}, q_{h,s}]) \\ &+ \underbrace{\beta \sum_K h_k^2 < \nabla p_{h,s}, \nabla q_{h,s} >_K - 2\mu\beta \sum_K h_k^2 < \Delta(\mathbf{v_{h,s}}), \nabla q_{h,s} >_K}_{residual} \end{aligned} \quad (2.65)$$

$$\begin{aligned} L_{s,stable}[\mathbf{w_{h,s}}, q_{h,s}] &= L_s([\mathbf{w_{h,s}}, q_{h,s}]) \\ &+ \beta \sum_K h_k^2 < \mathbf{f_s}, \nabla q_{h,s} >_K \end{aligned} \quad (2.66)$$

The constant β should be chosen so that the bilinear form $B_{s,stable}$ is coercive with respect to the norm:

$$||[\mathbf{v_{h,s}}, p_{h,s}]||_a = [\|\mathbf{v_{h,s}}\|_1^2 + \sum_K h_k^2 \|\nabla p_{h,s}\|_0^2]^{1/2}$$

One can propose that whenever $V_{h,s}$ and $Q_{h,s}$ consist of C^0 piecewise polynomial spaces of fixed degrees, if the Dirichlet boundary condition ($\mathbf{v_{s|\Gamma_{s,D}=0}}$) holds, we have the desired stability relatively to the norm $||\ ||_a$ for small values of β. In addition, this stability implies immediatly the existence and uniqueness of a solution $[\mathbf{v_{h,s}}, p_{h,s}]$. A convenience of this method is the choice of approximation spaces $V_{h,s}$ and $Q_{h,s}$ (defined in Equations (2.67)) without specifying particular fixed degrees. The finite element spaces can be defined as:

$$\begin{aligned} V_{h,s} &= \{\mathbf{v_{h,s}} \in C^0(\Omega_s) : \mathbf{v_{h,s}}_{|K} \in P_n(K)^m\} && n \geq 1 \\ V^0_{h,s} &= \{\mathbf{w_{h,s}} \in C^0(\Omega_s) : \mathbf{w_{h,s}}_{|K} \in P_n(K)^m, \mathbf{w_{h,s}}_{\Gamma_{s,D}} = 0\} && n \geq 1 \\ Q_{h,s} &= \{p_{h,s} \in C^0(\Omega_s) : p_{|K} \in P_l(K)\} && l \geq 0 \end{aligned} \quad (2.67)$$

In this case, $V_{h,s} \subset V_s$, $V^0_{h,s} \subset V^0_s$ but $Q_{h,s} \not\subseteq Q_s$ because $Q_{h,s}$ belongs to $H^1(\Omega_s)$.

2.4.2.2 Douglas and Wang methods [J.Douglas & J.wang 1989]

Due to the constraints imposed on the value of β and the necessary homogeneity of the velocity ($\mathbf{v_{s|\Gamma_{s,D}}} = 0$) in the previous method, Douglas and Wang proposed a modification of the method of [Hughes *et al.* 1986]. This method is called "an absolute stabilized finite element method for Stokes problem". The authors assume that the velocity on the boundary $\partial\Omega_s$ $\mathbf{v_{s|\Gamma_D}} = \mathbf{v^1}$ should only respect the compatibility condition $\int_{\partial\Omega_s} \mathbf{v^1}.\mathbf{n_s} ds = 0$. Douglas and Wang modify also the method proposed by [Hughes *et al.* 1986] to deal with non continuity of pressure interpolation by introducing a jump operator. We will not detail here the jump term in the discontinous case for this method.
The discretized spaces of velocity and pressure are defined by:

$$V_{h,s} = \{\mathbf{v_{h,s}} \in C^0(\Omega_s)^m : \mathbf{v_{h,s}}_{|K} \in P_n(K)^m\}$$

$$V^0_{h,s} = \{\mathbf{w_{h,s}} \in C^0(\Omega_s)^m : \mathbf{w_{h,s}}_{|K} \in P_n(K)^m, \mathbf{w_{h,s}}_{\Gamma_{s,D}} = 0\}$$

$$Q_{h,s} = \{p_{h,s} \in L^2(\Omega_s) \cap H^1(\Omega_s) : p_{h,s|K} \in P_l(K)\}$$

where l and n are the degrees of polynomials and l can be independant of n.
In this case, $V_{h,s} \subset V_s$, $V^0_{h,s} \subset V^0_h$ and $Q_{h,s} \subset L^2(\Omega_s)$. The mesh dependant norm $|||\ |||$ on $V_{h,s} \times Q_{h,s}$ is defined by:

$$|||(\mathbf{v_{h,s}}, p_{h,s})||| = ||\nabla \mathbf{v_{h,s}}||^2_0 + |||\nabla p_{h,s} - \mu\Delta \mathbf{v_{h,s}}|||^2_0 \tag{2.68}$$

where $|||\nabla p_{h,s} - \Delta \mathbf{v_{h,s}}|||^2_0 = \beta \sum_K h_k^2 \, ||\nabla p_{h,s} - \mu\Delta \mathbf{v_{h,s}}||^2_{0,K}$

Then we have to solve the discretized form of Stokes defined by:
Find $[\mathbf{v_{h,s}}, p_{h,s}] \in V_{h,s} \times Q_{h,s}$ such that:

$$B_{s,stable}([\mathbf{v_{h,s}}, p_{h,s}], [\mathbf{w_{h,s}}, q_{h,s}]) \quad = \quad L_{s,stable}([\mathbf{w_{h,s}}, q_{h,s}]) \tag{2.69}$$
$$\forall [\mathbf{w_{h,s}}, q_{h,s}] \in V^0_{h,s} \times Q_{h,s}$$

where the stabilized bilinear $B_{s,stable}$ and the linear $L_{s,stable}$ forms are defined by:

$$\begin{aligned} B_{s,stable}([\mathbf{v_{h,s}}, p_{h,s}], [\mathbf{w_{h,s}}, q_{h,s}]) &= B_s([\mathbf{v_{h,s}}, p_{h,s}], [\mathbf{w_{h,s}}, q_{h,s}]) \\ &\quad \underbrace{+\beta \sum_K h_k^2 < \nabla p_{h,s} - \mu \Delta \mathbf{v_{h,s}}, \nabla q_{h,s} - \mu \Delta \mathbf{w_{h,s}} >}_{residual} \end{aligned} \tag{2.70}$$

$$\begin{aligned} L_{s,stable}([\mathbf{w_{h,s}}, q_{h,s}]) &= L_s([\mathbf{w_{h,s}}, q_{h,s}]) \\ &\quad +\beta \sum_K h_k^2 < \mathbf{f_s}, \nabla q_{h,s} - \mu \Delta \mathbf{w_{h,s}} > \end{aligned} \tag{2.71}$$

One has been demonstrated that the coercivity of the bilinear form then the uniqueness and the existence of the solution do not depend on the value of β. One can choose $\beta = 1$ for the sake of simplicity [J.Douglas & J.wang 1989] which makes the essential difference between this method and the method proposed by [Hughes *et al.* 1986].

Different numerous variants and extensions of these two methods have been proposed and analysed [R.Duran & R.Notchetto 1989], [L.P.Franca & R.Stenberg 1991a], [D.J.Silvester & N.Kechkar 1990b] and [franca et al 1990].

2.4.3 Multiscale Methods

These methods are different from the penalized and residual methods because they use stabilization terms provided by the effect of the fine scales which are not captured by the finite element solution and not captured with the residual of differential equations as the residual methods introduced above. A theoretical formulation for multiscale methods can be found in the homogenization theory [Bramble & Xu 1989]. One multiscale method that has its roots in this theory and has got lot of recognition is the multiscale finite element method presented by Hou and Wu [T.Y.Hou & X.-H.Wu 1997].
In this method, the standard finite element basis functions are replaced by new basis functions containing fine scale structure. These new functions are calculated by solving local fine scale problems. Lately, Aarnes [J.E.Aarnes *et al.* 2005] have extended this method to the mixed problems. We have two essential types of Multiscale Methods: the Variational Multiscale Methods (VMS) and the Adaptive Variational Multiscale Methods. In the next sections, for Stokes and Darcy problems, we are interested in developing the Variational Multiscale Method widely used in stabilizing Stokes and Darcy problems.

The original idea of the subgrid scale methods is introduced in [Hughes 1988] and in [Hughes 1995]. **The Variational MultiScale method (VMS)** is based on the idea of splitting the finite element spaces into a coarse and a fine parts ($X = X_h + X'$). The coarse space X_h is a standard finite element space but the fine space X' is an infinite dimensional space. Hughes suggests that the fine scale solution x' could be solved by analytical approximation on each coarse element in terms of x_h. After this is done, x_h can be calculated directly in the coarse space X_h. In the literature, we can find two important Variational Multiscale Methods: Hughes Variational Method (HVM) developed in [Nakshatrala *et al.* 2006a], and used for stabilizing Stokes and Darcy; and another type of methods which introduces operators of projection onto the fine scale spaces. These methods are the Algebraic SubGrid Scale (ASGS) and Orthogonal SubGrid Scale (OSGS) methods developed in [S.Badia & R.Codina 2010]. We will develop the HVM method in the stabilization methods of Darcy problem, while we will develop both ASGS and OSGS methods in the next chapter. But we note that the essential difference between these two methods is that the "HVM" method consists in decomposing only the spaces of velocity onto coarse and fine spaces while both "ASGS" and "OSGS" methods consist in decomposing both spaces of velocity and pressure onto coarse and fine spaces.

2.4.4 Stabilized finite element methods based on multiscale enrichment of Stokes problem and Petrov Galerkin approximation

The justification of the "stabilized methods" becomes a subject of interest. In [Baiocchi *et al.* 1993], [Russo 1996] and [Barrenechea & Valentin 2002] the connection between stabilized finite element methods and Galerkin methods enriched with bubble functions has been used to propose new stabilized finite element methods used to solve the Stokes equations.
In this section, we choose to describe the method of **Araya, Barrenchea Valention method** developed in [Araya *et al.* 2006] which uses multiscale functions to enrich the standard polynomial spaces of velocity. On the other hand, the test function space is enriched with bubble functions and consequently, to use Petrov-Galerkin approximation.
This method is stable for $P1/P0$ elements and $P1/P1$ elements. We will be interested to detail continuous and linear elements in this section ($P1/P1$ elements).

The finite element spaces of velocity, pressure and test functions are defined by:

$$\begin{aligned} V_{h,s} &= \{\mathbf{v_{h,s}} \in C^0(\Omega_s)^m, \mathbf{v_{h,s}}_{|K} \in P_1(\Omega_s)\} \\ V^0_{h,s} &= \{\mathbf{w_{h,s}} \in C^0(\Omega_s)^m, \mathbf{w_{h,s}}_{|K} \in P_1(\Omega_s), \mathbf{w_{h,s}}_{\Gamma_{s,D}} = 0\} \\ Q_{h,s} &= \{P_{h,s} \in C^0(\Omega_s), p_{h,s|K} \in P_1(\Omega_s)\} \end{aligned} \tag{2.72}$$

In this method, $V_{h,s} \subset V_s$, $Q_{h,s} \subset Q_s$ and $V^0_{h,s} \subset V^0_s$.
Let $E_h \subset V^0_s$ be the finite dimensional space called "multiscale space". The Petrov-Galerkin method proposes to find $\mathbf{v_{h,s}} + \mathbf{v_{h,e}} \in V^0_{h,s} \oplus E_h$ and $p_{h,s} \in Q_{h,s}$ such that:

$$B_s([\mathbf{v_{h,s}} + \mathbf{v_{h,e}}, p_{h,s}], [\mathbf{w_{h,1}}, q_{h,s}]) = L_s([\mathbf{w_{h,1}}, q_{h,s}]) \tag{2.73}$$

$$\forall \mathbf{w_{h,1}} = \mathbf{w_{h,s}} + \mathbf{w_{h,b}} \in V^0_{h,s} \oplus H^{1,t}_{\Gamma_{s,D}}(\Omega_s)^m \text{ and } q_{h,s} \in Q_{h,s}$$

By replacing $\mathbf{w_{h,1}}$ by its expression $(\mathbf{w_{h,s}} + \mathbf{w_{h,b}})$ we get two systems:

$$B_s([\mathbf{v_{h,s}} + \mathbf{v_{h,e}}, p_{h,s}], [\mathbf{w_{h,s}}, q_{h,s}]) = L_s([\mathbf{w_{h,s}}, q_{h,s}]) \tag{2.74}$$
$$\forall [\mathbf{w_{h,s}}, q_{h,s}] \in V^0_{h,s} \times Q_{h,s}$$

$$B_s([\mathbf{v_{h,s}} + \mathbf{v_{h,e}}, p_{h,s}], [\mathbf{w_{h,b}}, q_{h,s}]) = L_s([\mathbf{w_{h,b}}, q_{h,s}]) \tag{2.75}$$
$$\forall [\mathbf{w_{h,b}}, q_{h,s}] \in H^{1,t}_{\Gamma_{s,D}}(\Omega_s)^m \times Q_{h,s}$$

Equation (2.75) is equivalent to:

$$< -\mu\Delta\mathbf{v_{h,e}}, \mathbf{w_{h,b}} >_K = < \mathbf{f_s} + \mu\Delta\mathbf{v_{h,s}} - \nabla p_{h,s}, \mathbf{w_{h,b}} >_K \tag{2.76}$$

One proposes to introduce approximation operators to solve Equation (2.76) (this is the idea of multiscale stabilization used in this method). This operator is defined by:

$$M_K : L^2(\Omega_s)^m \longrightarrow H^{1,t}_{\Gamma_{s,D}}(\Omega_s)^m$$

such that:

$$\mathbf{v_{h,e}} = \frac{1}{\mu} M_k(\mathbf{f_s} + \mu\Delta\mathbf{v_{h,s}} - \nabla p_{h,s}) \tag{2.77}$$

The algebraic operator $\frac{1}{\mu}M_k$ in Equation (2.77) can be approximated by $\tau_k = \frac{c_1 h_k^2}{\mu}$ [Araya *et al.* 2006]. By replacing the approached solution $\mathbf{v_{h,e}}$ by the expression in Equation (2.74),

the stabilized formulation of Stokes and Darcy problem becomes:
Find $[\mathbf{v_{h,s}}, p_{h,s}] \in V^0_{h,s} \times Q_{h,s}$ such that:

$$B_{s,stable}([\mathbf{v_{h,s}}, p_{h,s}], [\mathbf{w_{h,s}}, q_{h,s}]) = L_{s,stable}([\mathbf{w_{h,s}}, q_{h,s}]) \tag{2.78}$$
$$\forall [\mathbf{w_{h,s}}, q_{h,s}] \in V^0_{h,s} \times Q_{h,s}$$

The stabilized bilinear and linear forms $B_{s,stable}$ and $L_{s,stable}$ are defined by:

$$\begin{aligned} B_{s,stable}([\mathbf{v_{h,s}}, p_{h,s}], [\mathbf{w_{h,s}}, q_{h,s}]) &= B_s([\mathbf{v_{h,s}}, p_{h,s}], [\mathbf{w_{h,s}}, q_{h,s}] \\ &\quad + \tau_k \sum_K < -\mu \Delta \mathbf{v_{h,s}} + \nabla p_{h,s}, \mu \Delta \mathbf{w_{h,s}} + \nabla q_{h,s} > \end{aligned} \tag{2.79}$$

$$\begin{aligned} L_{s,stable}([\mathbf{w_{h,s}}, q_{h,s}]) &= L_s([\mathbf{w_{h,s}}, q_{h,s})] \\ &\quad + \tau_k \sum_K < \mathbf{f_s}, \mu \Delta \mathbf{w_{h,s}} + \nabla q_{h,s} > \end{aligned} \tag{2.80}$$

Remarks: If the normal components of velocity are not continous, we have to add a stabilized jump term to the bilinear form which is

$$\sum_K [[\mu \frac{\partial \mathbf{v_{h,s}}}{\partial \mathbf{n}}]][[\mu \frac{\partial \mathbf{w_{h,s}}}{\partial \mathbf{n}}]]$$

If we want to take the case of P1/P0 elements, we have to take into consideration the jump terms of pressure corresponding to the discontinuities of pressure over the interior edges.
[Araya *et al.* 2006] proves improvements to this multiscale formulation for piecewise linear elements for velocity and pressure (P1/P1 elements) and for piecewise linear/piecewise constant (P1/P0 elements). The constant c_1 in the stabilization term $\tau_k = \frac{c_1 h_k^2}{\mu}$ [Araya *et al.* 2006] has been suggested to be equal to $\frac{1}{8}$. This eliminates the numerical costs spent to select an adequate value for the numerical constant c_1. Then, the stabilization term τ_k depends essentially on the size of mesh h_k. This method arises from multiscale enrichment of the space of velocity coupled with Petrov Galerkin strategy. Petrov Galerkin strategy yields the possibility of statical condensation of bubbles at the element level and at the edges (in the case of discontinuities). Then the method takes the form of classical stabilized finite elements with jump terms and stabilization parameter known exactly.

2.5 Stabilized finite elements for discretization of Darcy's equations

Some numerical method for the Darcy's equations are based on a mixed two field velocity-pressure formulation. It is well known that the choice of the finite element spaces for the mixed formulation is subject to the *inf-sup* stability condition as we explained in section 2.3 for Stokes problem. The whole domain $\Omega_d \subset \mathrm{R}^m$ is discretized with a mesh made up of triangles if $m = 2$ and of tetrahedrons if $m = 3$. Let $V_{h,d}$, $V^0_{h,d}$ and $Q_{h,d}$ be the finite element spaces which contain the finite element solution of velocity $\mathbf{v_{h,d}}$, the test function of velocity $\mathbf{w_{h,d}}$ and the finite element solution of pressure $p_{h,d}$. As for the Stokes problems, the standard mixed finite element method for Darcy problem is based on finding a pair of finite element spaces $V_{h,d} \times Q_{h,d}$ which satisfies the condition i) and ii) of the Brezzi-Babũska theorem (2.46) such as:

$$\underset{q_{h,d} \in Q_{h,d}}{inf} \; \underset{\mathbf{w_{h,d}} \in V^0_{h,d}}{sup} \frac{< div \mathbf{w_{h,d}}, q_{h,d} >}{\|\mathbf{w_{h,d}}\|_{1,d} \, \|q_{h,d}\|_0} \geqslant \beta \tag{2.81}$$

$|| \; ||_{1,d}$ is a norm defined on the space of velocity $V_{h,d} \subset H(div, \Omega_d)$. The norm can be defined in different forms depending on the stabilized method that is used and β is a positive constant independant of the size of mesh h_k. In the sections below, we will present some methods used in literature to stabilize dual formulations of Darcy's equations.

Some elements are stable for the Darcy's problem, as Raviart-Thomas (RT) and Brezzi-Douglas-Marini (BDM) finite elements. Approches based on these elements show good accuracy for both velocity and pressure. This accuracy has its draw back complexity as we will see in the next section for RT elements. Stabilized finite element methods have been extended to the Darcy's equations. Some stabilization methods are based on the residual of the Darcy's law which is added to the classical Galerkin formulation to make the stable formulation for all combination of conforming continuous velocity-pressure approximations [A.Masud & Hughes 2002]. Another class of stabilized methods has been derived using Galerkin methods enriched with bubble functions [Araya *et al.* 2006], [G.R.Barrenechea *et al.* 2007]. Alternative stabilization techniques based on a least-square formulation have been proposed by [Hughes & L.Franca 1989], [Franca *et al.* 1989], [Bochev & Gunzburger 1998], [L.P.Franca & R.Stenberg 1991b] and [J.J.Droux & Hughes 1994]. In addition, some methods based on Variational MultiScale methods, consisting in finding the part of the solution that is missed in classical finite element approximation, is also used to stabilize the Darcy's equations [Codina & S.Badia 2010]. Recently, local projection methods that seem less sensitive to the choice of

parameters and have better local conservation properties were proposed. The pressure gradient stabilization method for Darcy's equations developed in [Nafa & Wathen 2008], [Nafa & Wathen 2009], [Nafa 2009] proved its stability by constructing an interpolant with additional orthogonality property with respect to the projection space.
In this section, we will developp the stable elements for Darcy like BDM and RT elements, a method based on residual stabilization idea, a method based on Variational MultiScale method (HVM: Hughes Variational MultiScale method) and a method based on Least-square principle.

2.5.1 Stable mixed elements

Some stable mixed elements introduced in Stokes (Taylor-Hood elements) are stable for Stokes and not stable for Darcy. The MINI-element is a stable mixed element for the primal formulation of Darcy and not for the dual formulation. Raviart-Thomas and Brezzi-Douglas-Marini introduce in [P.A.Raviart & J.M.Thomas 1977] new mixed stable elements for Darcy problem with a structure close to the Taylor-Hood space structure. These spaces, compatible for Darcy problem, allows the discretized problem to satisfy the conditions of the Brezzi-Babũska theorem (2.46). On the other hand, on some spaces where the discretized problem is not elliptic on $KerB$, we will use methods of stabilization which make the problem satisfying the conditions introduced in the Babũska theorem (2.47).

The Raviart-Thomas (RT) and Brezzi-Douglas-Marini (BDM) vector spaces [P.A.Raviart & J.M.Thomas 1977] are commonly used as approximation spaces of $H(div, \Omega_d)$. For $l \in N$, P_l denotes the set of polynomials of degree l, associated with the unknown vector $\mathbf{X} = (x_i)$ with $1 \leq i \leq m$. For the sake of simplicity, we will define the finite element of Raviart-Thomas of first order 1.

The Raviart-Thomas (RT) vector spaces of order 1 is defined by:

$$RT(K) \quad = \quad P_0(K)^2 + x\, P_0(K) \tag{2.82}$$

P_0 is the polynomial of order 0 which means that if $f(\mathbf{X}) \in RT(K)$ then, $f(\mathbf{X}) = \mathbf{a} + \lambda \mathbf{X}$ with $a \in \mathrm{R^m}$ and $\lambda \in \mathrm{R}$

The Brezzi-Douglas-Marini (BDM) spaces are defined by:

$$BDM_l(K) \quad = \quad P_0(K)^2 \tag{2.83}$$

To explain the finite element of Raviart-Thomas of order 1, we have also to introduce Σ,

the set of linear forms (l) defined on RT, such as:

$$l = \{l_i : f(\mathbf{X}) \longrightarrow \mathbf{f}(\mathbf{m_i}).\mathbf{n_i}\}$$

with $1 \leq i \leq s$ where s is the number of edges of the triangle or the tetrahedron K, m_i is the middle of the edges and $\mathbf{n_i}$ is the normal on each edge. The triplet $K, RT(K), l$ is called the finite element of order 1 of Raviart-Thomas.

The discretized spaces of velocity using (RT) or (BDM) vector spaces are defined by:

$$\begin{array}{rcl} V_{h,d} & = & \{\mathbf{v_{h,d}}_{|K} \in (RT(K) \text{ or } BDM_l(K))\} \\ V^0_{h,d} & = & \{\mathbf{w_{h,d}}_{|K} \in (RT_l(K) \text{ or } BDM_l(K)), \mathbf{w_{h,d}}_{\Gamma_{d,D}} = 0\} \end{array} \tag{2.84}$$

In this case, $V_{h,d} \subset V_d$ and $V^0_{h,d} \subset V^0_d$.

Commonly used stable elements for the velocity and pressure approximation of Darcy equations are the Raviart-Thomas pairs (RT_l for velocity and discontinous P_l for pressure) and the Brezzi-Marini-Pairs (BDM_{l+1} for velocity and discontinous P_l for pressure) [P.A.Raviart & J.M.Thomas 1977]. The simplest is also the use of $RT(K)$ elements of order one for velocity with P_0 elements for pressure.

This method seems to be sometimes complicated because the element unknowns are the normal fluxes on the faces, but all components are needed inside every element domain. This make the implementation complex especially in three dimensional problems.

2.5.2 Residual and penalized methods

The philosophy of stabilized residual techniques for Darcy problem is to strengthen the classical variational formulations, with stabilization additional terms which are residual of differential equations. Then the unstable Galerkin formulation becomes stable and convergent. The technique consists of perturbating the indefinite problem in such a way that the finite element approximation can violate the *inf-sup* condition in the functional continuous problem. One of the methods based on this technique is the method proposed by Masud and hughes that we will develop in the next paragraph.

In the method of **Masud and Hughes method [A.Masud & Hughes 2002]**, we search also a "stability norm". The natural "stability norm" is the norm which provides $L^2(\Omega_d)$ control for the velocity on its space ($\subset H(div, \Omega_d)$). In the continuous pressure case, the pressure is stable in $H^1(\Omega_d)$. Any combination of continous velocity and pressure converges in the stability norm. Therein, the stabilized problem in this case imposes that the pressure

belongs to $H^1(\Omega_d)$ (non-conforming discretized space for pressure). The stability norm, in this method, is then defined by:

$$|||[\mathbf{v_{h,d}}, p_{h,d}]|||_{stab} = \frac{1}{2}\,(\frac{\mu}{k}||\mathbf{v_{h,d}}||_0^2 + \frac{k}{\mu}||\nabla p_{h,d}||_0^2)^{\frac{1}{2}} \tag{2.85}$$

Then, the stabilized formulation of Darcy problem is:
Find the velocity $\mathbf{v_{h,d}}$ and the pressure $p_{h,d}$ in $V_{h,d} \times Q_{h,d}$ such that:

$$B_{d,stable}([\mathbf{v_{h,d}}, p_{h,d}], [\mathbf{w_{h,d}}, q_{h,d}]) = L_{d,stable}([\mathbf{w_{h,d}}, q_{h,d}]) \tag{2.86}$$

$$\forall [\mathbf{w_{h,d}}, q_{h,d}] \in V_{h,d}^0 \times Q_{h,d}$$

$$\begin{aligned} V_{h,d} &= \{\mathbf{v_{h,d}} \in C^0(\Omega_d)^m,\ \mathbf{v_{h,d}}_{|K} \in P_l(K)\} \\ V_{h,d}^0 &= \{\,\mathbf{v_{h,d}} \in C_0(\Omega_d)^m,\ \mathbf{v_{h,d}}_{|K} \in P_l(K), \mathbf{v_{h,d}}_{\Gamma_{d,D}} = 0\} \\ Q_{h,d} &= \{q_h \in H(\Omega_d), q_h \in C^0(\Omega_d), q_{h|K} \in P_n(K)\} \end{aligned} \tag{2.87}$$

In this case, the space $Q_{h,d} \nsubseteq Q_d$ because $Q_{h,d}$ belongs to $H^1(\Omega_d)$ but, $V_{h,d} \subset V_d$ and the stabilized bilinear and linear forms are defined by:

$$\begin{aligned} B_{d,stable}([\mathbf{v_{h,d}}, p_{h,d})], [\mathbf{w_{h,d}}, q_{h,d}]) &= B_d([\mathbf{v_{h,d}}, p_{h,d})], [\mathbf{w_{h,d}}, q_{h,d}]) \\ &\quad + \tfrac{1}{2} < -\tfrac{\mu}{k}\mathbf{w_{h,d}} + \nabla q_{h,d}, \tfrac{k}{\mu}(\tfrac{\mu}{k}\mathbf{v_{h,d}} + \nabla p_{h,d}) > \end{aligned} \tag{2.88}$$

$$\begin{aligned} L_{d,stable}([\mathbf{w_{h,d}}, q_{h,d}] &= L_d([\mathbf{w_{h,d}}, q_{h,d}]) \\ &\quad \underbrace{-\frac{1}{2} < -\frac{\mu}{k}\mathbf{w_{h,d}} + \nabla q_{h,d}, \frac{k}{\mu}\mathbf{f_d} >}_{residual} \end{aligned} \tag{2.89}$$

The most interesting feature of this formulation is that there are no mesh-dependant parameters in the stabilization terms.

2.5.3 Multiscale Methods

Some subgrid scale methods used to stabilize Darcy's equations are introduced in [S.Badia & R.Codina 2010] and in [Nakshatrala *et al.* 2006a]. In [Nakshatrala *et al.* 2006a], where the HVM method is introduced for Darcy problem, the "fine scale" of velocity is only taken into consideration while in [S.Badia & R.Codina 2010], where variational multiscale methods are

introduced, "fine scale" of pressure and velocity are taken into consideration. In this section we will detail "HVM" methods and in the next chapter we will detail "VMS" methods.

HVM formulation used in stabilization of Darcy's equations [Nakshatrala *et al.* 2006a] is a derivation from the previous formulation introduced in section 2.5.2, the interesting feature of the previous formulation is that there is no mesh dependant parameters. However, the robustness of the new formulation is preserving the advantage by performing numerical simulation on complex geometries [Nakshatrala *et al.* 2006a].
HVM formulation consists in decomposing the velocity field $\mathbf{v_d}$ into coarse scale and fine scale components:

$$\mathbf{v_d} = \mathbf{v_{h,d}} + \mathbf{v'_{h,d}}$$

where $\mathbf{v'_{h,d}}$ is the fine scale which cannot be captured by the finite element solution. We decompose also the test functions into coarse scale $\mathbf{w_{h,d}}$ and fine scale $\mathbf{w'_{h,d}}$. By taking into consideration that the fine scale components vanish along each element boundary, the Darcy's problem can be written as two subproblems:
The coarse scale problem:

$$B_d([\mathbf{v_{h,d}} + \mathbf{v'_{h,d}}, p_{h,d}], [\mathbf{w_{h,d}}, q_{h,d}]) = L_d([\mathbf{w_{h,d}}, q_{h,d}]) \tag{2.90}$$

and the fine scale problem:

$$B_d([\mathbf{v_{h,d}} + \mathbf{v'_{h,d}}, p_{h,d}], [\mathbf{w'_{h,d}}, q_{h,d}]) = L_d([\mathbf{w'_{h,d}}, q_{h,d}]) \tag{2.91}$$

The main idea of the HVM formulation is to solve the fine scale problem (2.91) to obtain the fine scale velocity $\mathbf{v'_{h,d}}$ in terms of the coarse scale $\mathbf{v_{h,d}}$ and $p_{h,d}$, then substitute the fine scale solution into the coarse scale problem (2.90).
The approximation form of the fine scale solution is:

$$\mathbf{v'_{h,d}} = -\mathbf{v_{h,d}} + \tfrac{k}{\mu}(\nabla p_{h,d} + \mathbf{f_d}) \text{ on } K \tag{2.92}$$

Then, the stabilized formulation of Darcy problem consists in finding $\mathbf{v_{h,d}} \in H(div, \Omega_d)$ and $p_d \in L^2(\Omega_d)$ such that:

$$B_{d,stable}([\mathbf{v_{h,d}}, p_{h,d}], [\mathbf{w_{h,d}}, q_{h,d}]) = L_{d,stable}([\mathbf{w_{h,d}}, q_{h,d}]) \tag{2.93}$$

where the stabilized bilinear and linear forms are defined by:

$$\begin{aligned} B_{d,stable}([\mathbf{v_{h,d}}, p_{h,d}], [\mathbf{w_{h,d}}, q_{h,d}]) &= B_d([\mathbf{v_{h,d}}, p_{h,d}], [\mathbf{w_{h,d}}, q_{h,d}]) \\ &\quad + \sum_K \tau < \frac{-\mu}{k}\mathbf{w_{h,d}} + \nabla q_{h,d}, \mathbf{v_{h,d}} + \frac{k}{\mu}\nabla p_{h,d} >_{\Omega_d} \end{aligned} \tag{2.94}$$

τ is a constant (taken in general equal to 1/2).

$$\begin{aligned} L_{d,stable}([\mathbf{w_{h,d}}, q_{h,d}]) &= L_d([\mathbf{w_{h,d}}, q_{h,d}]) \\ &\quad + \sum_K -\tau < \mathbf{f_d}, \frac{-\mu}{k}\mathbf{w_{h,d}} + \nabla q_{h,d} > \end{aligned} \tag{2.95}$$

2.5.4 Galerkin Least Squares methods

Least square methods are based on a completely different variational principle associated with unconstrained global minimization of a problem-dependant quadratic functional. Many types of methods based on this concept were developed in [Hughes & L.Franca 1989], [Franca *et al.* 1989], [Bochev & Gunzburger 1998], [L.P.Franca & R.Stenberg 1991b] and [J.J.Droux & Hughes 1994].
In this section we will detail the basic scheme of these methods introduced by [Hughes & L.Franca 1989], the L^2 least square method introduced by [Bochev & Gunzburger 1998] and GLS method in connection with the Galerkin gradient least square method developed in [Franca *et al.* 1989].

2.5.4.1 Least-square methods [Hughes & L.Franca 1989]

The basic scheme of these methods is introduced in [Hughes & L.Franca 1989]):
Find $[\mathbf{v_{h,d}}, p_{h,d}]$ such that:

$$B_d([\mathbf{v_{h,d}}, p_{h,d}], [\mathbf{w_{h,d}}, q_{h,d}]) = L_d([\mathbf{w_{h,d}}, q_{h,d}]) \tag{2.96}$$

derived from the classical formulation:

$$A[\mathbf{v_{h,d}}, p_{h,d}] = [\mathbf{f_d}, h_d]$$

A is a scalar advection-diffusion operator of this scheme such that:

$$A[\mathbf{v_{h,d}}, p_{h,d}] = [\tfrac{\mu}{k}\mathbf{v_{h,d}} + \nabla p_{h,d}, -div\mathbf{v_{h,d}}] \tag{2.97}$$

The basic scheme (idea) of Galerkin Least Square stabilization is to find $[\mathbf{v_{h,d}}, p_{h,d}]$ satisfying:

$$\begin{array}{rcl} B_d([\mathbf{v_{h,d}}, p_{h,d}], [\mathbf{w_{h,d}}, q_{h,d}]) & + & \tau < A[\mathbf{v_{h,d}}, p_{h,d}], A[\mathbf{w_{h,d}}, q_{h,d}] >= \\ L_d([\mathbf{w_{h,d}}, q_{h,d}]) & + & \tau < [\mathbf{f_d}, h_d], A[\mathbf{w_{h,d}}, q_{h,d}] > \end{array} \tag{2.98}$$

The operator A defined in Equation (2.97), is well posed in the space $V_{h,d} \times Q_{h,d}$ and the *a priori* estimate verifies:

$$||[\mathbf{v_{h,d}}, p_{h,d}]||_c \leq C||A([\mathbf{v_{h,d}}, p_{h,d}])||_d \tag{2.99}$$

$||\ ||_c$ is a norm defined on $V_{h,d} \times Q_{h,d}$ and $||\ ||_d$ is a norm defined on R^{m+1}.

In order to set up a "normal-functional", residual of Equation (2.98) must be measured in the norms indicated by the a priori estimate (Equation (2.99)). We associate a quadratic least-square functional of the form:

$$J([\mathbf{v_{h,d}}, p_{h,d}]) = \tfrac{1}{2}(||A([\mathbf{v_{h,d}}, p_{h,d}]) - [\mathbf{f_d}, h_d]||_d^2) \tag{2.100}$$

A minimizer of (Equation (2.100)) is given by:
Find $[\mathbf{v_{h,d}}, p_{h,d}] \in V_{h,d} \times Q_{h,d}$ such that:

$$J([\mathbf{v_{h,d}}, p_{h,d}]) \leq J([\mathbf{w_{h,d}}, q_{h,d}]) \tag{2.101}$$

$$\forall [\mathbf{w_{h,d}}, q_{h,d}] \in V_{h,d}^0 \times Q_{h,d}$$

Condition defined in (2.101) is equivalent to find $[\mathbf{v_{h,d}}, p_{h,d}]$ such that:

$$B_d([\mathbf{v_{h,d}}, p_{h,d}], [\mathbf{w_{h,d}}, q_{h,d}]) = [\mathbf{f_d}, h_d]([\mathbf{w_{h,d}}, q_{h,d}]) \tag{2.102}$$

Consequently, we have:

$$B_d([\mathbf{v_{h,d}}, p_{h,d}], [\mathbf{v_{h,d}}, p_{h,d}]) = A([\mathbf{v_{h,d}}, p_{h,d}])([\mathbf{v_{h,d}}, p_{h,d}]) \tag{2.103}$$

A consequence of the *a priori* estimate norm (2.99) is that the bilinear form B_d is coercive because:

$$B_d([\mathbf{v_{h,d}}, p_{h,d}], [\mathbf{v_{h,d}}, p_{h,d}]) \geq \frac{1}{C}||[\mathbf{v_{h,d}}, p_{h,d}], [\mathbf{v_{h,d}}, p_{h,d}]||_c$$

Then, the existence and uniqueness of minimizers lead to a stable solution of the problem which makes the bilinear form stable. Then, to apply the least square method principle on Darcy's equations (some methods of least square are also compatible for stabilized form of Stokes equations), we have to choose a functional setting and a finite-dimensional subspace which can be conforming ($V_{h,d} \times Q_{h,d} \subset V_d \times Q_d$) or non-conforming ($V_{h,d} \times Q_{h,d} \nsubseteq V_d \times Q_d$). Different methods based on the least square formulation have been developed [Franca *et al.* 1989] to stabilize Darcy's equations. In next sections, we will detail one of these methods.

2.5.4.2 GLS method [Franca *et al.* 1989]

Another Galerkin least-squares method is based on the concept of the Galerkin gradient least squares method introduced by Franca and Dutra in [Franca *et al.* 1989]. The spaces of pressure, velocity and test functions are defined in Equations (2.104).

$$\begin{aligned} V_{h,d} &= \{\mathbf{v_{h,d}} : \mathbf{v_{h,d}}_{|K} \in P_l(K)\} \\ V^0_{h,d} &= \{\mathbf{w_{h,d}} : \mathbf{w_{h,d}}_{|K} \in P_l(K), \mathbf{v_{h,d}}_{\Gamma_{s,D}} = 0\} \\ Q_{h,d} &= \{p_{h,d} : {p_{h,d}}_{|K} \in P_n(K)\} \end{aligned} \tag{2.104}$$

In this method, $Q_{h,d}$ is a conforming space ($Q_{h,d} \subset Q_d$).
The stabilized form of Darcy problem is obtained by summing up the standard Galerkin equations with the least squares. This least squares formulation writes

$$\frac{\mu}{K} < div\mathbf{v_{h,d}} + \mathbf{f_d}, div\mathbf{w_{h,d}} > \quad + \quad < \tfrac{k}{\mu} curl(\tfrac{\mu}{k}\mathbf{v_{h,d}}), curl(\tfrac{\mu}{k}\mathbf{w_{h,d}}) >^* \tag{2.105}$$

$< , >^*$ is used to denote the adjoint form of the L^2 scalar product. Then, the stabilized bilinear formulation of Darcy's equations consists in finding $[\mathbf{v_{h,d}}, p_{h,d}]$ such that:

$$B_{d,stable}([\mathbf{v_{h,d}}, p_{h,d}], [\mathbf{w_{h,d}}, q_{h,d}]) = L_{d,stable}([\mathbf{w_{h,d}}, q_{h,d}])$$

$$\forall [\mathbf{w_{h,d}}, q_{h,d}] \in V^0_{h,d} \times Q_{h,d}$$

$B_{d,stable}$ and $L_{d,stable}$ are defined by:

$$\begin{aligned} B_{d,stable}([\mathbf{v_{h,d}}, p_{h,d}], [\mathbf{w_{h,d}}, q_{h,d}]) &= B_d([[\mathbf{v_{h,d}}, p_{h,d}]) \\ &\quad + \tfrac{\mu}{k} < div\mathbf{v_{h,d}}, div\mathbf{w_{h,d}} > \\ &\quad + \tfrac{k}{\mu} < curl(\tfrac{\mu}{k}\mathbf{v_{h,d}}), curl(\tfrac{k}{\mu}\mathbf{w_{h,d}}) > \end{aligned} \tag{2.106}$$

$$\begin{aligned} L_{d,stable}([\mathbf{w_{h,d}}, q_{h,d}]) &= L_d([\mathbf{w_{h,d}}, q_{h,d}]) \\ &\quad -\tfrac{\mu}{k} < \mathbf{f_d}, div\mathbf{w_{h,d}} > \end{aligned} \tag{2.107}$$

2.6 Stabilized finite elements for Stokes-Darcy coupled problem

In Stokes domain, many types of stabilized finite elements were described in Section 2.4. In the porous medium, many types of stabilized finite elements were described in Section 2.5. But, the key issue in the stabilized Stokes-Darcy coupling is that we cannot couple any stable elements for Stokes with any stable elements for Darcy. The choices are different between "unified" and "decoupled" approaches. In this section, we will explain how to choose compatible stable finite elements for Stokes and Darcy in both approaches.

Decoupled strategies use different spaces for Stokes and Darcy. For this reason, coupling of different finite elements leads to stable formulations in coupling problems for decoupled strategy and not for unified strategies.
The main decoupled strategies used in the literature for coupling Stokes-Darcy are:

- Taylor-Hood for Stokes (Section 2.4.1.1) with C^0 Lagrangian for Darcy, this coupling is presented in [M.discacciati *et al.* 2007].
- Taylor-Hood for Stokes (Section 2.4.1.1) with Raviart-Thomas elements for Darcy, this coupling is presented in [W.J.Layton *et al.* 2003].
- MINI-element for Stokes and MINI-element for primal formulation of Darcy's equations, this coupling is developed in [Celle *et al.* 2008].

For a unified strategy, it is argued that finite element discretizations based on the same finite element spaces for both region will have some advantages with respect to the implementation. However, the difficulty is that the stable Stokes elements will not be stable in the Darcy region and that most of stable Darcy elements will not be stable with Stokes problem. For example, we cannot use MINI-elements for Stokes and MINI-elements for primal formulation of Darcy's equations within a unified approach, because the velocity in Stokes belongs to $H^1(\Omega_s)$ and the pressure belongs to $L^2(\Omega_s)$ while with the stable $P_1 + /P_1$ used for the primal formulation of Darcy's equations, the velocity belongs to $L^2(\Omega_d)$ and the pressure belongs to $H^1(\Omega_d)$ which is compatible for decoupled strategy and uncompatible for unified strategy. Then, the plan for choosing finite elements stable for Stokes, stable for Darcy and compatible with a unified coupling is:

- Start from a stable finite element space for Stokes (Taylor-Hood element, for example, introduced in Section 2.4.1.1, particularly in this case $p_{h,s} \in L^2(\Omega_s)$.
- Construct a compatible stabilization for Darcy problem, *i.e* take stabilization methods for Darcy where the pressure is stable in $L^2(\Omega_d)$ in $H^1(\Omega_d)$(for example Galerkin Least Squares stabilization (GLS) (Section 2.5.4.2))
- Prescribe interface conditions between Stokes' and Darcy's domains.

The goal in this example is to obtain a finite element method with the same structure of Taylor-Hood approximation in both domains with compatible spaces. Different standard "finite element couples" are used to couple "Stokes" and "Darcy" in a unified strategy:

- P1/P0 with pressure stabilization (jump terms) for Stokes and Darcy problems. This coupling is introduced in [E.Burmana & P.Hansbob 2007].
- Taylor-Hood element or MINI-element for Stokes (detailed in Sections 2.4.1.1 and 2.4.1.2 respectively) with BDM or RT elements in Darcy (Section 2.5.1). This coupling is developed in [W.J.Layton *et al.* 2003].
- Mixed finite element method designed for the entire Stokes-Darcy system [Arbogast & Brunson 2007]

2.7 Conclusions

We presented in this chapter residual and penalized stable methods for Stokes and Darcy, subgrid scale methods for Stokes and Darcy, stable mixed elements for Stokes and Darcy, pressure projection method and Galerkin-Least-Square method to stabilize Darcy's equations. Then, we presented the two main strategies to couple Stokes and Darcy, the "unified" strategy and the "decoupled" strategy and the way to choose"compatible finite elements" for each strategy.

We are interested in this manuscript in using the "unified approach". Hence, it is difficult, as shown in Section 2.6, to find a standard finite element couple which statisfies the Brezzi-Babũska condition for both Stokes and Darcy equations and which exhibits accuracy properties. The use of "MINI- element" (in Stokes) with "HVM" method in Darcy leads to some accuracy problems: oscillations around the interface and consistency errors [Pacquaut *et al.* 2012] especially for low permeabilities ($K < 10^{-9}\mathrm{m}^2$) while the preforms in composite materials have a permeability down to $10^{-15}\mathrm{m}^2$. P1/P0 used in [E.Burmana & P.Hansbob 2007] requires special interpolation orders and constant pressure which is not a general case. Taylor-Hood

elements with Raviart-Thomas elements used in [W.J.Layton *et al.* 2003] is expensive in space and CPU time and the resulting mixed interpolations are expensive and in some cases restricted to specific typologies of meshes. In order to overcome these difficulties, especially difficulties met with P1+/P1 coupled with HVM in severe regimes, we choose the use of Variational Multiscale Methods for both Stokes and Darcy's domains that we will developp in the next chapter.

Chapter 3

Variational MultiScale method to stabilize Stokes, Darcy and Stokes-Darcy coupled problem

Contents

3.1 Introduction

Stabilized methods based on the Variational MultiScale method (VMS) decomposition are in fact Subgrid scale methods introduced by [Hughes 1995]. The view point of these methods is that there are two sets of scales, one associated with the "fine scale" numerically unresolvable, one associated with the "large scale" numerically resolvable.

This kind of approach was introduced as a framework for incorporating missing fine scale effects into numerical problems governing coarse scale behavior ("large scale"). This chapter, will develop the theory of Variational MultiScale method for Stokes, Darcy and Stokes-Darcy coupling problem.

3.2 Variational MultiScale method "VMS" applied to Darcy problem

3.2.1 Stability of the continuous problem of Darcy

The definition of a norm over velocity and pressure spaces of Darcy's equations should hold for the continuous functional form of the continuous problem. This means that the continuous problem should verify the *inf-sup* condition (2.46 (ii)) relatively to this norm . We define the spaces of velocity and pressure $V_d \times Q_d$ and the space of test functions $V_d^0 \times Q_d$ by:

$$\begin{aligned} Q_d &= \{p_d, \int_{\Omega_d} p_d^2 < \infty\}, \ \|q\|_0 = (\int_{\Omega_s} q^2 d\Omega_d)^{1/2} \\ V_d &= \{\mathbf{v_d} \in L^2(\Omega_d)^m, div\, \mathbf{v_d} \in L^2(\Omega_d)\,, \mathbf{v_d}.\mathbf{n_d} = g \,\text{on}\, \Gamma_{d,D}\} \\ V_d^0 &= \{\mathbf{w_d} \in L^2(\Omega_d)^m, div\, \mathbf{v_d} \in L^2(\Omega_d), \mathbf{v_d}.\mathbf{n_d} = 0 \,\text{on}\, \Gamma_{d,D}\} \end{aligned} \tag{3.1}$$

The *inf-sup* condition (2.46 i) which is a condition of the stability of the bilinear form of the continuous Darcy problem is satisfied relatively to the regularity of the data:

- The term $\mathbf{f_d}$ should be well defined in V_d', the dual space of V.
- $h = -div\mathbf{v_d}$ should be well defined in $(L^2(\Omega_d))' = L^2(\Omega_d)$.

In order to introduce the new ideas of "VMS" method, we will define a new norm on the space $V \times Q$. For Darcy problem, we need to control $||\mathbf{v_d}||_0$ and $||div\mathbf{v_d}||_0$ to obtain stability in V_d. The L^2 norm is denoted by $||\ ||_0$ in all this chapter and defined in Equation (3.1).

A method to incorporate both norms in a single way is through the introduction of a characteristic length scale L_0 independant of the size of mesh h_K. Thus, the new norm on V_d is defined by:

$$||\mathbf{v_d}||_{L_d} = ||\mathbf{v_d}||_0 + L_0||div\mathbf{v_d}||_0 \tag{3.2}$$

The functional setting is well posed as a consequence of the *inf-sup* condition:

$$\exists\beta > 0, \quad \inf_{q_d \in L^2(\Omega_d)} \sup_{\mathbf{v_d} \in H^t_{\Gamma_{d,D}}(div,\Omega_d)} \frac{< q_d, div\,\mathbf{w_d} >}{||q_d||_0||\mathbf{w_d}||_{L_d}} \geq 0 \tag{3.3}$$

This condition is true because the divergence operator is surjective from $H(div, \Omega_d)$ to $L^2(\Omega_d)$, then $< q_d, div\mathbf{w_d} >$ is well defined (see the condition ii) of Theorem (2.46)).

Let now $|||\ |||_d$ be the norm on $V_d \times Q_d$ defined by:

$$|||[\mathbf{v_d}, p_d]|||_d = \frac{\mu}{k}||\mathbf{v_d}||_0^2 + \frac{\mu}{k}L_0^2||div\mathbf{v_d}||_0^2 + \frac{k}{\mu}\frac{1}{L_0}^2||p_d||_0^2 \tag{3.4}$$

The existence and unicity of the solution of the continuous problem is verified using the condition of Babũska theorem (2.48). By defining the bilinear form of Darcy problem in Equation (3.5), Babuska condition is enunciated in Equation (3.6).

$$\begin{aligned} B_d([\mathbf{v_d}, p_d], [\mathbf{w_d}, q_d]) = & \frac{\mu}{k} < \mathbf{v_d}, \mathbf{w_d} >_{\Omega_d} \\ & - < p_d, div\,\mathbf{w_d} >_{\Omega_d} \\ & + < q_d, div\,\mathbf{v_d} >_{\Omega_d} \\ & + < p_d,\ \mathbf{w_d}.\mathbf{n_d} >_{\Gamma_{d,N}} \end{aligned} \tag{3.5}$$

Then $\forall[\mathbf{v_d}, q_d] \in V_d \times Q_d, \exists[\mathbf{w_d}, q_d] \in V_d^0 \times Q_d$ and $C > 0$ such that [Codina & S.Badia 2010], [S.Badia & R.Codina 2008]:

$$B_d([\mathbf{v_d}, p_d], [\mathbf{w_d}, q_d]) \geqslant C|||[\mathbf{v_d}, p_d]|||_d|||[\mathbf{w_d}, q_d]|||_d \tag{3.6}$$

This condition (3.6) is obtained because the *inf-sup* condition (3.3) is verified and the data $(\mathbf{f_d}, h_d)$ is regular enough which lead to the continuity of the linear form L_d, [S.Badia & R.Codina 2008], [Codina & S.Badia 2010].

3.2.2 Stabilized finite element method based on "VMS" theory

The use of the Variational MultiScale method ("VMS") is introduced in [T.J.R.Hughes 1995] and in [Nakshatrala *et al.* 2006b]. The essential difference between the Variational Multiscale Methods developed in [S.Badia & R.Codina 2008] and the other methods is the introduction of

a characteristic length scale L_0 which appears in the stabilization terms. Four different choices of this length scale will lead to different numerical methods with interesting properties. Moreover, a subgrid projection appears when we stabilize our equations with "VMS" methods. The choice of this subgrid projection leads to two different types of "VMS" methods so called "Algebraic Subgrid Scale" method (ASGS) and Orthogonal Subgrid Scale method (OSGS). The ideas of such projection subgrid scale approach, especially the "Orthogonal Subgrid Scale", appear to stabilize transient incompressible flows in [Codina 2002]. Stabilization methods based on "VMS" can be stable for continuous and discontinuous approximations. In this chapter, we will detail continuous approximations which correspond to our approach.

3.2.3 VMS method for Darcy problem

As indicated previously, the technique used in "VMS" method is based on the decomposition of the unknowns into their finite element scale (or resolvable scale) and a finer scale (or unresolvable scale) which cannot be captured by the finite element solution. Here, the domain $\Omega_d \subset \mathrm{R}^m$ is discretized with one unstructed mesh made up of triangles if $m = 2$ and of tetrahedrons if $m = 3$. Let $V_{h,d}$ and $Q_{h,d}$ be the finite element spaces of the piecewise continuous functions, which contain the solution $\mathbf{v_{h,d}}$ and $p_{h,d}$. In order to have a unique decomposition, the spaces are such that $V_d \times Q_d = V_{h,d} \times Q_{h,d} \bigoplus V'_d \times Q'_d$. This decomposition is only true for the conforming approximations because $V_{h,d} \subset V_d$ and $Q_{h,d} \subset Q_d$ (conforming spaces). The velocity, pressure and test functions are decomposed as:

$$\begin{aligned}
\mathbf{v_d} &= \underbrace{\mathbf{v_{h,d}}}_{finite\,element\,scales} + \underbrace{\mathbf{v'_d}}_{fine\,scales} \\
\mathbf{w_d} &= \underbrace{\mathbf{w_{h,d}}}_{finite\,element\,scales} + \underbrace{\mathbf{w'_d}}_{fine\,scales} \\
p_d &= \underbrace{p_{h,d}}_{finite\,element\,scales} + \underbrace{p'_d}_{fine\,scales} \\
q_d &= \underbrace{q_{h,d}}_{finite\,element\,scales} + \underbrace{q'_d}_{fine\,scales}
\end{aligned} \tag{3.7}$$

Invoking the decomposition of pressure and velocity in Darcy for both solution and test functions as given in Equation (3.7), the system (3.8) is decomposed in two-scale systems.

$$B_d([\mathbf{v_d}, p_d], [\mathbf{w_d}, q_d]) \quad = \quad L_d([\mathbf{w_d}, q_d]) \tag{3.8}$$

$$\forall \mathbf{w_d} \in V_d^0,\ \forall q_d \in Q_d$$

where the bilinear form B_d is defined in Equation (3.5) and the linear form L_d is defined in Equation (3.9) by:

$$\begin{aligned} L_d([\mathbf{w_d}, q_d]) &= < \mathbf{f_d}, \mathbf{w_d} >_{\Omega_d} \\ &+ < h_d, q_d > \\ &+ < p_{ext,d}.\mathbf{n}, \mathbf{w_d} >_{\Gamma_{d,N}} \end{aligned} \tag{3.9}$$

The finite element problem writes:

$$\begin{aligned} B_d([\mathbf{v_{h,d}}, p_{h,d}], [\mathbf{w_{h,d}}, q_{h,d}]) &+ B_d([\mathbf{v'_d}, p'_d], [\mathbf{w_{h,d}}, q_{h,d}]) \\ &= L_d([[w_{h,d}, q_{h,d}]) \end{aligned}$$

The fine scale problem writes:

$$\begin{aligned} B_d([\mathbf{v_{h,d}}, p_{h,d}], [\mathbf{w'_d}, q'_d]) &+ B_d([\mathbf{v'_d}, p'_d], [\mathbf{w'_d}, q'_d]) \\ &= L_d(\mathbf{w'_d}, q'_d]) \end{aligned} \tag{3.10}$$

for all $[\mathbf{w_{h,d}}, q_{h,d}] \in V_{h,d}^0 \times Q_{h,d}$ and $[\mathbf{w'_d}, q'_d] \in V'_d \times Q'_d$.
We assume that the fine scale functions $[\mathbf{w'_d}, q'_d]$ vanish on the boundary of every mesh element. After integration by parts of some terms, and assuming that the subgrid component can be localized inside every finite element, one gets:

$$\begin{aligned} B_d([\mathbf{v_{h,d}}, p_{h,d}], [\mathbf{w_{h,d}}, q_{h,d}]) &+ \sum_K < \mathbf{v'_{h,d}}, \frac{\mu}{k}\mathbf{w_{h,d}} + \nabla q_{h,d} >_K \\ &+ \sum_K < p'_{h,d}, -div\mathbf{w_{h,d}} >_K \\ &+ \sum_K < v'_{h,d}, +\nabla q_{h,d} >_K \\ &= L_d([\mathbf{w_{h,d}}, q_{h,d}]) \end{aligned} \tag{3.11}$$

Remark: $< p'_{h,d}, \mathbf{w_{h,d}}.\mathbf{n_d} >_{\Gamma_{d,N}} = 0$ because $p'_{h,d}$ vanishes on the boundary of Ω_d.

The fine scale problem (3.10) writes:

$$\begin{aligned} < \tfrac{\mu}{k}\mathbf{v'_{h,d}} + \nabla p'_{h,d} &+ \tfrac{\mu}{k}\mathbf{v_{h,d}} + \nabla p_{h,d}, \mathbf{w_{h,d}} > &&= < \mathbf{f_d}, \mathbf{w_{h,d}} > \\ &< div\mathbf{v'_{h,d}} + div\mathbf{v_{h,d}}, q_{h,d} > &&= < h_d, q_{h,d} > \end{aligned} \tag{3.12}$$

which is equivalent to:

$$P'([\frac{\mu}{k}\mathbf{v'_d} + \nabla p'_d, div\mathbf{v'_d}]) = P'([\mathbf{f_d} - \frac{\mu}{k}\mathbf{v_{h,d}} - \nabla p_{h,d}, \mathbf{h_d} - div\mathbf{v_{h,d}}]) \tag{3.13}$$

where P' is the L^2 broken onto $V'_d \times Q'_d$. Equation (3.13) is the subgrid equation. Inside every element, the subgrid projection P' is approximated by an appropriate approximation $P'_h := [P'_{h,v}, P'_{h,p}]$ where $P'_{h,v}$ is the L^2 projection onto $V'_{h,d}$ and $P'_{h,p}$ is the L^2 projection onto $Q'_{h,d}$. Then Equation (3.13) becomes:

$$\begin{array}{lcl} P'_{h,v}(\frac{\mu}{k}\mathbf{v'_d} + \nabla p'_d) & = & P'_{h,v}(\mathbf{f_d} - \frac{\mu}{k}\mathbf{v_{h,d}} - \nabla p_{h,d}) \\ P'_{h,p}(div\mathbf{v'_d}) & = & P'_{h,p}(\mathbf{h_d} - div\mathbf{v_{h,d}}) \end{array} \tag{3.14}$$

The next step consists in replacing the operators $\frac{\mu}{k}\mathbf{v'_d} + \nabla p'_d$ and $div\mathbf{v'_d}$ by algebraics operators where the stabilization terms τ_u and τ_p are used such as [Codina & S.Badia 2010]:

$$\begin{array}{lcl} \frac{\mu}{k}\mathbf{v'_d} + \nabla p'_d & \simeq & \tau_u^{-1}\mathbf{v'_d} \\ div\mathbf{v'_d} & \simeq & \tau_p^{-1}p'_d \end{array} \tag{3.15}$$

In this case, we obtain:

$$\begin{array}{lcl} \mathbf{v'_d} & = & \tau_u P'_{h,v}(\mathbf{f_d} - \frac{\mu}{k}\mathbf{v_{h,d}} - \nabla p_{h,d}) \\ p'_d & = & \tau_p P'_{h,p}(h_d - div\mathbf{v_{h,d}}) \end{array} \tag{3.16}$$

Using these expressions for the subscales in the finite element problem (3.11), we get the stabilized forms $B_{d,stable}$ and $L_{d,stable}$. Stabilized Darcy problem finally writes:
Find $[\mathbf{v_{h,d}}, p_{h,d}] \in V_{h,d} \times Q_{h,d}$ such as:

$$B_{d,stable}([\mathbf{v_{h,d}}, p_{h,d}][\mathbf{w_{h,d}}, q_{h,d}]) = L_{d,stable}([\mathbf{w_{h,d}}, q_{h,d}]) \tag{3.17}$$

$$\forall [\mathbf{w_{h,d}}, q_{h,d}] \in V^0_{h,d} \times Q_{h,d}$$

$$\begin{array}{lcl} B_{d,stable}([\mathbf{v_{h,d}}, p_{h,d}], [\mathbf{w_{h,d}}, q_{h,d}]) & = & B_d([\mathbf{v_{h,d}}, p_{h,d}], [\mathbf{w_{h,d}}, q_{h,d}]) \\ & & +\tau_u \sum_K < P'_{h,v}(\underbrace{\frac{\mu}{\mathrm{k}}\mathbf{v_{h,d}} + \nabla p_{h,d}}_{residual}), -\frac{\mu}{\mathrm{k}}\mathbf{w_{h,d}} + \nabla q_{h,d} >_K \\ & & +\tau_p \sum_K < P'_{h,p}(div\mathbf{v_{h,d}}), div\mathbf{w_{h,d}} >_K \end{array} \tag{3.18}$$

$$\begin{aligned} L_{d,stable}([\mathbf{w_{h,d}}, q_{h,d}]) &= L_d([\mathbf{w_{h,d}}, q_{h,d}]) \\ &+\tau_p \sum_K < P'_{h,p}(h_d), \nabla.\mathbf{w_{h,d}} >_K \\ &+\tau_u \sum_K < P'_{h,v}(\mathbf{f_d}), -\frac{\mu}{\mathrm{k}}\mathbf{w_{h,d}} + \nabla q_{h,d} >_K \end{aligned} \tag{3.19}$$

where $B_d([\mathbf{v_{h,d}}, p_{h,d}], [\mathbf{w_{h,d}}, q_{h,d}])$ and $L_d([\mathbf{w_{h,d}}, q_{h,d}])$ are defined in (3.5) and (3.9).

3.2.4 Choice of the subgrid projection

We have at least, two choices of the subgrid projection P'_h when acting on the FE residual. The simplest choice is to consider P'_h the identity operator, then the method is so called "ASGS" (Algebraic SubgridScale) method. Invoking this, the bilinear form (3.18) and the linear form (3.19) become:

$$\begin{aligned} B_{d,stable}([\mathbf{v_{h,d}}, p_{h,d}], [\mathbf{w_{h,d}}, q_{h,d}]) &= B_d([\mathbf{v_{h,d}}, p_{h,d}], [\mathbf{w_{h,d}}, q_{h,d}]) \\ &+\tau_p \sum_K < div\mathbf{v_{h,d}}, div\mathbf{w_{h,d}} >_K \\ &+\tau_u \sum_K < \frac{\mu}{\mathrm{k}}\mathbf{v_{h,d}} + \nabla p_{h,d}, -\frac{\mu}{\mathrm{k}}\mathbf{w_{h,d}} + \nabla q_{h,d} >_K \end{aligned} \tag{3.20}$$

$$\begin{aligned} L_{d,stable}([\mathbf{w_{h,d}}, q_{h,d}]) &= L_d([\mathbf{w_{h,d}}, q_{h,d}]) \\ &+\tau_p \sum_K < h_d, div\, \mathbf{w_{h,d}} >_K \\ &+\tau_u \sum_K < \mathbf{f_d}, -\frac{\mu}{\mathrm{k}}\mathbf{w_{h,d}} + \nabla q_{h,d} >_K \end{aligned}$$

Another choice of the subgrid projector is the orthogonal subgrid projector. Let P_X be the L^2 projection defined by:

$$P_X \quad : \quad L^2(\Omega_d) \to X \tag{3.21}$$

where X is a Hilbert space. $\forall g \in L^2(\Omega_d), g_{|K} \in L^2(K)$, $P_X(g_{|K})$ is the solution of:

$$(P_X(g), u) = \sum_K < g, u >_K \quad \forall u \in X \tag{3.22}$$

Introducing

$$P_X^{\perp} \quad = \quad g - P_X(g) \ \in L^2(\Omega_d) \tag{3.23}$$

the orthogonal projection $[P'_{h,v}, P'_{h,p}]$ is then defined by:

$$[P'_{h,v}, P'_{h,p}] \quad := \quad [{P^{\perp}}_{V_h}, {P^{\perp}}_{Q_h}] \tag{3.24}$$

This method is called "OSGS" (Orthogonal SubGrid Scale). The bilinear form defined in (3.18) and the linear form defined in (3.19) become:

$$\begin{aligned} B_{d,stable}([\mathbf{v_{h,d}}, p_{h,d}], [\mathbf{w_{h,d}}, q_{h,d}]) \quad = \quad & B_d([\mathbf{v_{h,d}}, p_{h,d}], [\mathbf{w_{h,d}}, q_{h,d}]) \\ & +\tau_p \sum_K < {P^{\perp}}_{Q_h}(div\mathbf{v_{h,d}}), div\mathbf{w_{h,d}} > \\ & +\tau_u \sum_K < {P^{\perp}}_{V_h}(\nabla p_{h,d}), +\nabla q_{h,d} > \end{aligned} \tag{3.25}$$

$$L_{d,stable}([\mathbf{w_{h,d}}, q_{h,d}]) \quad = \quad L_d([\mathbf{w_{h,d}}, q_{h,d}]) \tag{3.26}$$

Codina in [S.Badia & R.Codina 2010] mentioned that this formulation of OSGS method introduces a consistency error that does not spoil the accuracy of the discrete solution and explains that the introduction of $P^{\perp}_{Q_h}(g)$ and $P^{\perp}_{V_h}(\mathbf{f})$ makes the OSGS formulation of Darcy problem more consistent when $L_d([\mathbf{w_{h,d}}, q_{h,d}]$ (3.19) becomes:

$$\begin{aligned} L_{d,stable}([\mathbf{w_{h,d}}, q_{h,d}]) \quad = \quad & L_d([\mathbf{w_{h,d}}, q_{h,d}]) \\ & +\tau_p \sum_K < P^{\perp}_{Q_h}(h_d), div\mathbf{v_{h,d}} >_K \\ & +\tau_u \sum_K < P^{\perp}_{V_h}(\mathbf{f_d}), \nabla q_{h,d} >_K \end{aligned} \tag{3.27}$$

We consider that $\frac{\mu}{k}\mathbf{v_{h,d}} \in V_{h,d}$. For this we have ${P^{\perp}}_{V_h}(\frac{\mu}{k}\mathbf{v_{h,d}}) = 0$.
This formulation introduces less stabilization terms than the ASGS method, but it imposes two additional resolutions of equations to get $P^{\perp}_{Q_h}(div\mathbf{v_{h,d}})$ and $P^{\perp}_{V_h}(\nabla p_{h,d})$ with the non consistent version of OSGS. With the consistent version, we have also to determine $P^{\perp}_{V_h}(\mathbf{f})$ and $P^{\perp}_{Q_h}(g)$.

3.2.5 Choice of the length scale

The stabilization terms τ_u and τ_p are defined using a heuristic Fourier transformation. The details of the computation of these stabilization parameters are given in [Codina &

S.Badia 2010].

The stabilization parameters are:

$$\begin{aligned} \tau_u &= \frac{h^2}{l_u^2}\frac{k}{\mu} \\ \tau_p &= \frac{\mu}{k} l_p^2 \end{aligned} \tag{3.28}$$

where l_u and l_p are parameters that have the dimensions of lengths. Different choices of l_u and l_p lead to different methods [Codina & S.Badia 2010]:

$$\begin{array}{lcll} \text{Method A} & : & l_u = c_u \times h & \text{and} \quad l_p = c_p \times h \\ \text{Method B} & : & l_u = c_u \times L_0^{\frac{1}{2}} \times h^{\frac{1}{2}} & \text{and} \quad l_p = c_p \times L_0^{\frac{1}{2}} \times h^{\frac{1}{2}} \\ \text{Method C} & : & l_u = c_u \times L_0 & \text{and} \quad l_p = c_p \times L_0 \\ \text{Method D} & : & l_u = c_u \times h & \text{and} \quad l_p = c_p \times L_0 \end{array} \tag{3.29}$$

c_u and c_p are algorithmic dimensionless constants.

Discussion of the choice of l_u and l_p

The accuracy, optimality and stability of the method depend on the choices of l_u and l_p (for continuous and discontinuous approximations) and on the order of interpolations of pressure and velocity.

Let $V_{h,d}$ and $V_{h,d}^0$ be the finite element spaces of velocity and the test functions of velocity respectively and $Q_{h,d}$ the finite element space of pressure.

$$\begin{aligned} V_h &= \{\mathbf{v_{h,d}} \in C^0(\Omega_d)^m : \mathbf{v_{h,d}}_{|K} \in P_n(K)^m\} \\ V_{0,h} &= \{\mathbf{w_{h,d}} \in C^0(\Omega_d)^m : \mathbf{w_{h,d}}_{|K} \in P_n(K)^m, \mathbf{v_{h,d}}_{\Gamma_{d,D}} = 0\} \\ Q_h &= \{q_{h,d} \in C^0(\Omega_d) : p_{h,d_{|K}} \in P_l(K)\} \end{aligned} \tag{3.30}$$

Three cases will be discussed:

- $n < l$: it is unusual to find this situation in porous media flow applications because the velocity field can not be approximated by piecewise constant velocities, this is the method for the Poisson problem of Darcy ($\Delta p = 0$).
- $n = l$: we have the same interpolation orders for both velocity and pressure, this method requires less CPU time than elements where interpolation orders are different. In the case of continuous approximations of velocity and pressure with equal orders of interpolations, method B is the most accurate and optimal.
- $n > l$: this method is optimal if $n = l + 1$ for any interpolation pairs (such as $P2/P1$ elements). Method C is the most accurate in this case.

We conclude that "VMS" methods conduct to different and essential methods stable for Darcy problem: method C optimal for different orders of velocity-pressure and method B optimal for the same orders of velocity-pressure.

In our case, we will use continuous and linear elements for Darcy problem (P1/P1) elements then we test method B which must be the most accurate in this case.

3.2.6 Stability of the ASGS method for Darcy problems

Following Codina [S.Badia & R.Codina 2008], [Codina & S.Badia 2010], we choose the subgrid projection operator equal to identity (ASGS method) and as we mentioned in the previous subsection, we will use P1/P1 elements and the following parameters of stabilization corresponding to method B.

$$\begin{aligned} \tau_u &= \frac{h^2}{c_u L_0 h}\,\frac{k}{\mu} \\ \tau_p &= \frac{\mu}{k}\, c_p L_0 h \end{aligned} \tag{3.31}$$

The finite element spaces of velocity, pressure and test functions are:

$$\begin{aligned} V_{h,d} &= \{\mathbf{v_{h,d}} \in C^0(K)^m : \mathbf{v_{h,d}}_{|K} \in P_1(K)^m\} \\ V^0_{h,d} &= \{\mathbf{w_{h,d}} \in C^0(K)^m : \mathbf{w_{h,d}}_{|K} \in P_1(K)^m, \mathbf{w_{h,d}}_{\Gamma_{d,D}} = 0\} \\ Q_{h,d} &= \{p_{h,d} \in C^0(K) : {p_{h,d}}_{|K} \in P_1(K)\} \end{aligned} \tag{3.32}$$

Stability of the bilinear stabilized form of Darcy

The ASGS method applied to Darcy problem is stable if and only if the bilinear form $B_{d,stable}([\mathbf{v_{h,d}}, p_{h,d}], [\mathbf{w_{h,d}}, q_{h,d}])$ defined in Equation (3.20) is stable over $V_{h,d} \times Q_{h,d}$. The mesh dependant-norm defined on $V_h \times Q_h$ is $|||\ |||_{h,d}$ defined by:

$$|||[\mathbf{v_{h,d}}, p_{h,d}]|||^2_{h,d} = |||[\mathbf{v_{h,d}}, p_{h,d}]|||^2_h + \frac{k}{\mu}\frac{1}{L_0^2}||p_{h,d}||^2_0 \tag{3.33}$$

with

$$|||[\mathbf{v_{h,d}}, p_{h,d}]|||^2_h = \frac{\mu}{k}||\mathbf{v_{h,d}}||^2_{0,K} + \tau_p \sum_K ||div\mathbf{v_{h,d}}||^2_{0,K} + \tau_u \sum_K ||\nabla p_{h,d}||^2_K \tag{3.34}$$

By introducing this mesh-dependant norm, we have to control $\sum_K ||div\mathbf{v_{h,d}}||_{0,K}$ and $\sum_K ||\nabla p_{h,d}||_{0,K}$. This control is obtained if at the element level, we have:

– $\nabla Q_{h,d} \subset V_{h,d}$

- $divV_{h,d} \subset Q_{h,d}$
- The second item $divV_{h,d} \subset Q_{h,d}$ in our case is satisfied naturally since the divergence operator is surjective from $H_{\Gamma_{d,D}}(div, \Omega_d)$ to $L^2(\Omega_d)$ then $div\mathbf{v_{h,d}} \in L^2(K)$ for all K.
- Also, in our case, by using P1/P1 elements $\nabla Q_{h,d} \subset V_{h,d}$ because $\nabla p_{h,d}$ has constant components due to the linearity of $p_{h,d}$. Then $\nabla p_{h,d} \in L^2(K)^m \forall K$ a triangle ($m = 2$) or tetrahedrons ($m = 3$) and $div(\nabla p_{h,d}) = 0 \in L^2(K)$, which means that $\nabla Q_h \subset V_h$.

Then, we have by choosing these elements, the control on $||\mathbf{v_{h,d}}||_{0,K}$ and $||\nabla p_{h,d}||_{0,K}$ $\forall K$. These conditions also do not affect the conforming conditions which implies that $V_h \subset V$ and $Q_h \subset Q$, necessary in the theory of "VMS" methods.

Proof of the stability for the stabilized bilinear form and conditions on numerical constants

The stability of the bilinear form means that, [Codina & S.Badia 2010], [S.Badia & R.Codina 2008]:

$$\begin{array}{l} \forall [\mathbf{w_{h,d}}, q_{h,d}] \in V^0_{h,d} \times Q_{h,d} \exists C > 0 \text{ and } [\mathbf{v_{h,d}}, p_{h,d}] \in V_{h,d} \times Q_{h,d} \text{ such that :} \\ B_{d,stable}([\mathbf{v_{h,d}}, p_{h,d}], [\mathbf{w_{h,d}}, q_{h,d}]) \geq C|||[\mathbf{v_{h,d}}, p_{h,d}]|||_{h,d}|||[\mathbf{w_{h,d}}, q_{h,d}]|||_{h,d} \end{array} \tag{3.35}$$

We take $[\mathbf{w_{h,d}}, q_{h,d}] = [\mathbf{v_{h,d}}, p_{h,d}]$ then

$$\begin{array}{rcl} B_{d,stable}([\mathbf{v_{h,d}}, p_{h,d}], [\mathbf{v_{h,d}}, p_{h,d}]) & = & \frac{\mu}{k}||\mathbf{v}_{h,d}||^2 \\ & & + < p_{h,d}, \mathbf{v_{h,d}}.\mathbf{n_d} >_{\Gamma_{d,N}} \\ & & +\tau_p \sum_K ||div\mathbf{v_{h,d}}||^2_{0,K} \\ & & +\tau_u \sum_K ||\nabla p_{h,d}||^2_{0,K} \\ & & -\tau_u \sum_K ||\frac{\mu}{k}\mathbf{v_{h,d}}||^2_{0,K} \end{array} \tag{3.36}$$

In the general case, also in [Codina & S.Badia 2010], one considers that the imposed pressure on $\Gamma_{d,N}$, $p_{h,d_{|\Gamma_{d,N}}} = 0$, then the term $< p_{h,d}, \mathbf{v_{h,d}}.\mathbf{n_d} >_{\Gamma_{d,N}}$ in Equation (3.36) is zero, in this case:

$$\begin{array}{rcl} B_{d,stable}([\mathbf{v_{h,d}}, p_{h,d}], [\mathbf{v_{h,d}}, p_{h,d}]) & = & ||\mathbf{v_{h,d}}||^2_0(1 - \tau_u\frac{\mu}{k}) \\ & & +\tau_p \sum_K ||div\mathbf{v_{h,d}}||^2_{0,K} \\ & & +\tau_u \sum_K ||\nabla p_{h,d}||^2_{0,K} \end{array} \tag{3.37}$$

Then $B_{d,stable}([\mathbf{v_{h,d}}, p_{h,d}], [\mathbf{v_{h,d}}, p_{h,d}]) \geq C|||[\mathbf{v_{h,d}}, p_{h,d}]|||_h$ if and only if $1 - \tau_u\frac{\mu}{k} > 0$ Since,

$\tau_u = \frac{h^2}{c_u^2 L_0 h}$ in the method B, then

$$\frac{h}{c_u^2 L_0} < 1$$

.

Because $|||[\mathbf{v_{h,d}}, p_{h,d}]|||_h$ and $|||[\mathbf{v_{h,d}}, p_{h,d}]|||_{h,d}$ are equivalent norms then the bilinear form $B_{d,stable}[.,.]$ is coercive over $V_{h,d} \times Q_{h,d}$ with respect to the mesh-dependant norm $|||.|||_{h,d}$.

3.3 Variational MultiScale method "VMS" applied to Stokes problem

It was shown by Codina that the ASGS stabilization was convergent [S.Badia & R.Codina 2008], [Codina & S.Badia 2010]. Here we propose to detail this state to the slightly Stokes problem and to show its convergence.

3.3.1 Stability of the continuous Stokes problem

The spaces of velocity and pressure in Stokes problem and the regularity of the source terms $\mathbf{f_s}$ and h_s are important to maintain the continuity of the general functional setting of the problem.

Let $V_s = H^1_{\Gamma_{s,D}}(\Omega_s)^m$ be the space of velocity and $Q_s = L^2(\Omega_s)$ the space of pressure. The data is such that $\mathbf{f_s} \in (V_s)' = H^{-1}_{\Gamma_{s,D}}(\Omega_s)^m$ the dual space of $H^1_{\Gamma_{s,D}}(\Omega_s)^m$, and $h_s = div\mathbf{v_s} \in (Q_s)' = L^2(\Omega_s)$.

To control the velocity in $H^1_{\Gamma_{s,D}}(\Omega_s)^m$, we have to control $||\nabla \mathbf{v_s}||_0$ and $||\mathbf{v}||_0$. Due to the inequality of Poincare defined in Equation (3.38), the semi-norm $||\nabla \mathbf{v_s}||_0$ is sufficient to control the norm of velocity $\mathbf{v_s}$ in all the space $H^1_{\Gamma_{s,D}}(\Omega_s)^m$.

$$\forall \mathbf{v_s} \in H^1_{\Gamma_{s,D}}(\Omega_s)^m, \exists C > 0 \qquad ||\mathbf{v_s}||_0 \leq C||\nabla \mathbf{v_s}||_0 \tag{3.38}$$

Then, a stability estimate in the semi-norm $||\nabla \mathbf{v_s}||_0$ is sufficient. The introduction of length scale is unnecessary contrary to Darcy's equations. The norm defined in the space of velocity is then $\mu||\nabla \mathbf{v_s}||_0$ and the norm defined in the space of pressure is $(\frac{1}{\mu}||q_s||_0^2 - ||\nabla q_s||^2_{H^{-1}})$. The norm on the dual space $H^{-1}_{\Gamma_{s,D}}(\Omega_s)^m$ is defined by Equation (3.39):

$$||\nabla q_s||_{H^{-1}} \quad = \quad \underset{\mathbf{w_s} \in V_s}{sup} \frac{< \nabla q_s, \mathbf{w_s} >}{||\mathbf{w_s}||_{H^1}} \tag{3.39}$$

and the norm on the space V_s, denoted by $||\mathbf{v_s}||_{H^1}$ is:

$$||\mathbf{v_s}||_{H^1} = \mu||\nabla \mathbf{v_s}||_0 \tag{3.40}$$

The norm on the whole domain $V_s \times Q_s$ is defined by:

$$|||[\mathbf{v_s}, p_s]|||_s^2 = \mu||\nabla \mathbf{v_s}||_0^2 + \frac{1}{\mu}||q_s||_0^2 + ||\nabla q_s||_{H^{-1}}^2 \tag{3.41}$$

The functional setting of Stokes problem is well posed as a consequence of the *inf-sup* condition:

$$\underset{q_s \in Q_s}{inf} \underset{\mathbf{w_s} \in V_s}{sup} \frac{< q_s, div \mathbf{w_s} >}{||q_s||_0 ||\nabla \mathbf{w_s}||_0} > \beta \tag{3.42}$$

This condition is well-posed because the divergence operator is well defined from $H^1_{\Gamma_{s,D}}(\Omega_s)^m$ to $L^2(\Omega_s)$ (Theorem (2.46) ii)),[F.Brezzi & M.Fortin 1991]. This *inf-sup* condition (3.42) and the regularity of the data $(\mathbf{f_s}, h_s)$ lead to the stability of the bilinear form B_s proved in Equation (3.43) which means the existence and unicity of the solution of the continuous problem of Stokes due to the Babũska theorem (2.47).

$$\begin{aligned} &\forall [\mathbf{v_s}, p_s] \in V_s \times Q_s, \exists [\mathbf{w_s}, q_s] \in V_s^0 \times Q_s \,\text{and}\, C > 0 \\ &B_s([\mathbf{v_s}, p_s], [\mathbf{w_s}, q_s]) \geq C|||[\mathbf{v_s}, p_s]|||_s |||[\mathbf{w_s}, q_s]|||_s \end{aligned} \tag{3.43}$$

3.3.2 VMS method for Stokes problem

Let $V_{h,s}$ and $Q_{h,s}$ be the finite element spaces of the discretized velocity and pressure, which contain the solutions $\mathbf{v_{h,s}}$ and $p_{h,s}$. Similarly to the Darcy problem, the "VMS" technique consists in splitting the continuous solution $[\mathbf{v_s}, p_s]$ of the continuous problem, into the finite element solution $[\mathbf{v_{h,s}}, p_{h,s}]$ and the subgrid scale residual $[\mathbf{v'_s}, p'_s]$. This decomposition is applied for velocity, pressure and test functions as we did in Equation (3.7) for Darcy problem. We invoke the decomposition of pressure and velocity in the bilinear and linear equations of the continuous problem (3.44) and (3.45) for both solution and test functions as in Equation (3.7).

$$\begin{aligned} B_s([\mathbf{v_s}, p_s], [\mathbf{w_s}, q_s]) = \; & 2\mu < \dot{\boldsymbol{\varepsilon}}(\mathbf{v_s}) : \dot{\boldsymbol{\varepsilon}}(\mathbf{w_s}) >_{\Omega_s} \\ & - < p_s, div \mathbf{w_s} >_{\Omega_s} \\ & + < div \mathbf{v_s}, q_s >_{\Omega_s} \end{aligned} \tag{3.44}$$

$$L_s([\mathbf{w_s}, q_s]) = < \mathbf{f_s}, \mathbf{w_s} >_{\Omega_s} + < h_s, q_s >_{\Omega_s} - < p_{ext,s}.\mathbf{n_s}, \mathbf{w_s} >_{\Gamma_{s,N}} \tag{3.45}$$

The finite element problem writes:

$$\begin{aligned} B_s([\mathbf{v_{h,s}}, p_{h,s}], [\mathbf{w_{h,s}}, q_{h,s}]) &+ B_s([\mathbf{v'_s}, p'_s], [\mathbf{w_{h,s}}, q_{h,s}]) \\ &= L_s([\mathbf{w_{h,s}}, q_{h,s}]) \end{aligned} \tag{3.46}$$

and the fine scale problem writes:

$$\begin{aligned} B_s([\mathbf{v_{h,s}}, p_{h,s}], [\mathbf{w'_s}, q'_s]) &+ B_s([\mathbf{v'_s}, p'_s], [\mathbf{w'_s}, q'_s]) \\ &= L_s([\mathbf{w'_s}, q'_s]) \end{aligned} \tag{3.47}$$

for all $[\mathbf{w_{h,s}}, q_{h,s}] \in V^0_{h,s} \times Q_{h,s}$ and $[\mathbf{w'_s}, q'_s] \in V'_s \times Q'_s$.

The Variational MultiScale method for Stokes problem is stable for any interpolation orders of the velocity and pressure. Here, we choose the continuous and linear elements (P1/P1 elements) according to the Darcy problem. Then, the finite element spaces $V_{h,s}$, $V^0_{h,s}$ and $Q_{h,s}$ can be written as:

$$\begin{aligned} V_{h,s} &= \{\mathbf{v_{h,s}} \in C^0(K)^m : \mathbf{v_{h,s}}_{|K} \in P_1(K)\} \\ V_{0,h} &= \{\mathbf{w_{h,s}} \in C^0(K)^m : \mathbf{w_{h,s}}_{|K} \in P_1(K), \mathbf{w_{h,s}}_{\Gamma_{s,D}} = 0\} \\ Q_h &= \{: q_{h,s} \in C^0(K), q_{h,s|K} \in P_1(K)\} \end{aligned} \tag{3.48}$$

We assume that the fine scale functions vanish on the boundary of every mesh element. After integration by parts of some terms, problem (3.46) writes as:

$$\begin{aligned} B_s([\mathbf{v_{h,s}}, p_{h,s}], [\mathbf{w_{h,s}}, q_{h,s}]) &+ < \mathbf{v'_s}, 2\mu(\Delta \mathbf{w_{h,s}} - grad(div(\mathbf{w_{h,s}})) > \\ + < div\mathbf{v'_s}, q_{h,s} > &+ < \nabla p'_s, \mathbf{w_{h,s}} > \\ &= L_s([\mathbf{w_{h,s}}, q_{h,s}]) \end{aligned} \tag{3.49}$$

Since velocity is linear and continuous ($P1$ element), $\Delta \mathbf{w_{h,s}} - grad(div(\mathbf{w_{h,s}})) = 0$. Problem (3.47), can then be written as:

$$< \nabla p'_s, \mathbf{w'_s} > + < div\mathbf{v'_s}, q'_s > = < \mathbf{f_s} - \nabla p_{h,s}, \mathbf{w'_s} > + < h_s - div\mathbf{v_{h,s}}, q'_s > \tag{3.50}$$

for all $[\mathbf{w'_s}, q'_s] \in V'_s \times Q'_s$.

We consider P$'$ the L^2 projection operator onto $V'_s \times Q'_s$. The subgrid projection P$'$ is

approximated by $P'_h := [P'_{h,v}, P'_{h,q}]$ where $P'_{h,v}$ is the L^2 projection onto V'_s and P'_q is the L^2 projection onto Q'_s. Then problem (3.50) becomes:

$$\begin{aligned} P'_{h,v}(\nabla p'_s) &= P'_{h,v}(\mathbf{f_s} - \nabla p_{h,s}) \\ P'_{h,q}(div\mathbf{v}'_\mathbf{s}) &= P'_{h,q}(h_s - div\mathbf{v_{h,s}}) \end{aligned} \tag{3.51}$$

The next step consists in replacing the operators $\nabla p'_s$ and $div\mathbf{v}'_\mathbf{s}$ by Fourier operators where we use the stabilization terms τ_v and τ_q [S.Badia & R.Codina 2008] :

$$\begin{aligned} \nabla p'_s &\approx \tau_v^{-1}\mathbf{v}'_\mathbf{s} \\ div\mathbf{v}'_\mathbf{s} &\approx \tau_q^{-1}p'_s \end{aligned} \tag{3.52}$$

In this case, we obtain :

$$\begin{aligned} \mathbf{v}'_\mathbf{s} &= \tau_v P'_{h,u}(\mathbf{f_s} - \nabla p_{h,s}) \\ p'_s &= \tau_q P'_{h,p}(h_s - div\mathbf{v_{h,s}}) \end{aligned} \tag{3.53}$$

Using these expressions for the subscales in the finite element problem (3.49), we get the stabilized forms of B_s and L_s:

$$\begin{aligned} B_{s,stable}([\mathbf{v_{h,s}}, p_{h,s}], [\mathbf{w_{h,s}}, q_{h,s}]) &= B_s([\mathbf{v_{h,s}}, p_{h,s}], [\mathbf{w_{h,s}}, q_{h,s}]) \\ &\quad + \tau_q \sum_K < P'_{h,p}(div\mathbf{v_{h,s}}), div\mathbf{w_{h,s}} >_K \\ &\quad + \tau_v \sum_K < P'_{h,u}(\nabla p_{h,s}), -\nabla q_{h,s} >_K \\ L_{s,stable}([\mathbf{w_h}, q_h]) = L_s([\mathbf{w_h}, q_h]) & \\ &\quad + \tau_q \sum_K < P'_{h,p}(h_s), div\mathbf{w_{h,s}} >_K \\ &\quad + \tau_v \sum_K < P'_{h,p}(\mathbf{f_s}), \nabla q_{h,s} >_K \end{aligned}$$

As explained, in Section 3.2.4, we have two possibilities for the L^2 projection operator onto $V'_s \times Q'_s$, the identity operator (ASGS method) and the orthogonal operator(OSGS method). In order to apply the same method in Stokes and Darcy's domain, we choose the Algebraic SubgridScale method ($P^{'} = \mathbf{I}$).

Then, the Stokes problem stabilized with ASGS method becomes:

Find $[\mathbf{v_{h,s}}, p_{h,s}] \in V_{h,s} \times Q_{h,s}$ such as:

$$B_{s,stable}([\mathbf{v_{h,s}}, p_{h,s}], [\mathbf{w_{h,s}}, q_{h,s}]) = L_{s,stable}([\mathbf{w_{h,s}}, q_{h,s}]) \tag{3.54}$$

$$\forall [\mathbf{w_{h,s}}, q_{h,s}] \in V^0_{h,s} \times Q_{h,s}$$

where the stabilized bilinear ($B_{s,stable}$) and linear ($L_{s,stable}$) are defined in Equations (3.55) and (3.56).

$$\begin{aligned} B_{s,stable}([\mathbf{v_{h,s}}, q_{h,s}], [\mathbf{w_{h,s}}, q_{h,s}]) &= B_s([\mathbf{v_{h,s}}, p_{h,s}], [\mathbf{w_{h,s}}, q_{h,s}]) \\ &\quad +\tau_q \sum_K < \nabla.\mathbf{v_{h,s}}, \nabla.\mathbf{w_{h,s}} >_K \\ &\quad +\tau_v \sum_K < \nabla p_{h,s}, +\nabla q_{h,s} >_K \end{aligned} \tag{3.55}$$

$$\begin{aligned} L_{s,stable}([\mathbf{w_{h,s}}, q_{h,s}]) &= L_s([\mathbf{w_{h,s}}, q_{h,s}]) \\ &\quad +\tau_q \sum_K < h_s, \nabla.\mathbf{w_{h,s}} >_K \\ &\quad +\tau_v \sum_K < \mathbf{f_s}, +\nabla q_{h,s} >_K \end{aligned} \tag{3.56}$$

3.3.3 Stability of the ASGS method for Stokes problem

The stability of the discretized problem of Stokes stabilized with ASGS method is proved relatively to a mesh dependant-norm on the space $V_{h,s} \times Q_{h,s}$. Let us define the mesh dependant norm on $V_{h,s} \times Q_{h,s}$:

$$||| [\mathbf{v_{h,s}}, p_{h,s}] |||^2_{h,s} = ||| [\mathbf{v_{h,s}}, p_{h,s}] |||^2_h + \tfrac{1}{\mu} ||p_{h,s}||^2_0 \tag{3.57}$$

where $||| [\mathbf{v_{h,s}}, p_{h,s}] |||_h$ is defined by:

$$||| [\mathbf{v_{h,s}}, p_{h,s}] |||^2_h = \mu ||\nabla \mathbf{v_{h,s}}||^2_0 + \tau_v \sum_K ||\nabla p_{h,s}||^2_{0,K} \tag{3.58}$$

In this mesh dependant norm, $||\nabla \mathbf{v_{h,s}}||_0$ is well controlled due to the definition of the operator div from $H^1_{\Gamma_{d,D}}(\Omega_s)^m$ to $L^2(\Omega_s)^m$, $||p_{h,s}||_0$ is well defined because the pressure $p_{h,s}$ is in $L^2(\Omega_s)$. To control $||\nabla p_{h,s}||_K$ which is the L^2 norm defined locally on the triangles or tetrahedrons K of the domain, the order of approximation of velocity and pressure must verify at the element level "$\nabla Q_{h,s} \subset V_{h,s}$". In our case, the use of linear continous elements (P1/P1 elements), verifies this condition because $\nabla p_{h,s}$ is formed by constant components which mean that $\nabla p_{h,s} \in L^2(K)$

for every triangle or tetrahedrons K. Then, $||\nabla p_{h,s}||_{0,K}$ is well defined.
The parameters of stabilization τ_v and τ_q are obtained by heuristic Fourier transformation, the details of computation are in [S.Badia & R.Codina 2008]:

$$\begin{aligned} \tau_v &= \frac{1}{c_1 \mu} h_K^2 \\ \tau_q &= c_1 \mu \end{aligned} \tag{3.59}$$

with c_1 is an algorithmic constant and h_K is the size of mesh.
Remark:
We note that the term of stabilization τ_q does not appear in the mesh-dependant norm in Stokes because the control over $||div\mathbf{v_{h,s}}||_K$ is not required as for the Darcy problem. We can deduce that the pressure subscale can be neglected in Stokes because the $H^1(\Omega_s)$ stability comes from Galerkin terms and only the pressure $p_{h,s}$ requires an *inf-sup* condition. For the Darcy problem, this pressure cannot be neglected, the term of stabilization τ_q (which is the result of the introduction of fine scales (p'_s) for pressure) appears in the mesh dependant-norm $||||[\mathbf{v_{h,d}}, q_{h,d}]||||_{h,d}$ and allows to control $||div\mathbf{v_{h,d}}||_0$ since the Galerkin terms do not control the velocity in $H(div, \Omega_d)$.

Proof of the stability of the bilinear form of Stokes stabilized with ASGS method
The bilinear form of Stokes stabilized with ASGS method is stable if and only if
$B_{s,stable}([\mathbf{v_{h,s}}, p_{h,s}], [\mathbf{w_{h,s}}, q_{h,s}])$ is stable on $V_{h,s} \times Q_{h,s}$ $\forall [\mathbf{w_{h,s}}, q_{h,s}] \in V^0_{h,s} \times Q_{h,s}$.

Then, we have to prove that:

$$\begin{aligned} &\forall [\mathbf{v_{h,s}}, p_{h,s}] \in V_{h,s} \times Q_{h,s}, \exists [\mathbf{w_{h,s}}, q_{h,s}] \in V^0_{h,s} \times Q_{h,s} \,\text{and}\, \exists C > 0 \,\text{such as} \\ &B_{s,stable}([\mathbf{v_{h,s}}, p_{h,s}], [\mathbf{w_{h,s}}, q_{h,s}]) \geq C ||||[\mathbf{v_{h,s}}, p_{h,s}]||||_{h,s} ||||[\mathbf{w_{h,s}}, q_{h,s}]||||_{h,s} \end{aligned} \tag{3.60}$$

Let us take $[\mathbf{w_{h,s}}, q_{h,s}] = [\mathbf{v_{h,s}}, p_{h,s}]$, then

$$\begin{aligned} B_{s,stable}([\mathbf{v_{h,s}}, p_{h,s}], [\mathbf{v_{h,s}}, p_{h,s}]) &= 2\mu ||\dot{\boldsymbol{\varepsilon}}(\mathbf{v_{h,s}})||_0^2 \\ &\quad + \tau_q \sum_K ||div\mathbf{v_{h,s}}||_{0,K}^2 + \tau_v \sum_K ||\nabla p_{h,s}||_{0,K}^2 \end{aligned} \tag{3.61}$$

Consequently,

$$\begin{aligned} B_{s,stable}([\mathbf{v_{h,s}}, p_{h,s}], [\mathbf{v_{h,s}}, p_{h,s}]) &\geq \mu ||\nabla \mathbf{v_{h,s}}||_0^2 + \tau_v \sum_K ||\nabla p_{h,s}||_{0,K}^2 \\ &= |||[\mathbf{v_{h,s}}, p_{h,s}]|||_h^2 \end{aligned} \tag{3.62}$$

Either, $|||[\mathbf{v_{h,s}}, p_{h,s}]|||_h$ and $|||[\mathbf{v_{h,s}}, p_{h,s}]|||_{h,s}$ are equivalent, then

$$\begin{aligned} &\exists C > 0 \,\text{such that}\, \forall [\mathbf{v_{h,s}}, p_{h,s}] \in V_{h,s} \times Q_{h,s} \\ &B_{s,stable}([\mathbf{v_{h,s}}, p_{h,s}], [\mathbf{v_{h,s}}, p_{h,s}]) \geq C|||[\mathbf{v_{h,s}}, p_{h,s}]|||^2_{h,s} \end{aligned} \tag{3.63}$$

without any condition on the algorithmic constant c_1.

3.4 "VMS" methods applied to Stokes-Darcy coupled problem

As it was introduced in Stokes and Darcy problems in Chapter 2, the Galerkin approximation requires the use of velocity-pressure interpolations able to satisfy the conditions (*i* and *ii*) of theorem (2.46). Different interpolations detailed in Chapter 2 satisfy this condition, but the key issue is to find interpolations that satisfy the *inf-sup* condition for both problems at the same time. The important concept with VMS methods is that we are able to deal with both problems at the same time with the same technique and with the possibility to use any velocity-pressure pair. In our approach, we choose the continuous and linear elements (P1/P1) for Stokes-Darcy coupling problem. The most important feature is that the finite element spaces are conforming $V_h \times Q_h \subset V \times Q$ and that the finite element spaces in Stokes and Darcy are the same because we use monolithic approach. Also, the possibility of using the same orders of interpolation for each problem offered by stabilized formulations clearly simplifies the enforcement of the transmission conditions.

Remark: Let us note, that even if in the discussion of "VMS" methods applied to Stokes problem, we claimed that the fine subscales of pressure decomposition can be eliminated, we take them into consideration to have the same technique applied to "Stokes" and "Darcy" at the same time.

3.4.1 Generalized study of the continuous coupled problem

It was explained for Stokes and Darcy separately that the functional setting of the problem will be determined by an *inf-sup* condition and the regularity of the data. The *inf-sup* condition of the continuous problem (2.46 ii) is translated into stability of the bilinear form of the continuous problem, which implies the existence and uniqueness of the velocity and pressure.

Let us redefine the general bilinear form of Stokes-Darcy coupled problem that was detailed in Chapter 2.

$$\begin{aligned} B_c([\mathbf{v},q],[\mathbf{w},q]) &= <2\mu\dot{\boldsymbol{\varepsilon}}(\mathbf{v}):\dot{\boldsymbol{\varepsilon}}(\mathbf{w})H_s> + <\frac{\mu}{k}\mathbf{v},\mathbf{w}\,H_d> \\ &\quad - <p\,,div\,\mathbf{w}> + <q,\,div\mathbf{v}> + <\frac{\alpha\mu}{\sqrt{k}}\mathbf{v}\,,\mathbf{w}>_\Gamma \end{aligned} \tag{3.64}$$

$$\begin{aligned} L_c([\mathbf{v},p],[\mathbf{w},q]) &= <\mathbf{f},\mathbf{w}> + <h,q> \\ &\quad + <\mathbf{t_s},\mathbf{w}>_{\Gamma_{s,N}} + <p_{ext},\mathbf{w}>_{\Gamma_{d,N}} \end{aligned} \tag{3.65}$$

The spaces of velocity, pressure and test functions are defined by:

$$V_c = V_s \times V_d$$

$$V_c^0 = V_s^0 \times V_d^0$$

$$Q_c = Q_s \times Q_d$$

The term $\mathbf{f} = \mathbf{f_s}$ should be in $V_s' = H^{-1}_{\Gamma_{s,D}}(\Omega_s)^m$ and $h = h_s$ should be in $Q_s' = L^2(\Omega_s)$. The term $\mathbf{f} = \mathbf{f_d}$ should be in V_d' and $h = h_d$ should be in $Q_d' = L^2(\Omega_d)$.

The norm associated with the spaces $V_c \times Q_c$ for the coupled problem is:

$$\begin{aligned} |||[v,p]|||_c^2 &= \mu||H_s\nabla\mathbf{v}||_0^2 + \tfrac{\mu}{k}\sum_K ||H_d div\mathbf{v}||_{0,K}^2 \\ &\quad + \tfrac{1}{\mu}||H_s q||_0^2 + \sum_K \frac{k}{\mu L_0^2}||H_d q||_{0,K}^2 \\ &\quad + ||\nabla q||_{L'} \end{aligned} \tag{3.66}$$

H_i is the Heaviside function equal to 1 in the domain i ($i = s$ or $i = d$) and vanishing elsewhere.

- If $H_s = 1$, $\mathbf{v} = \mathbf{v}_{|\Omega_s} = \mathbf{v_s}$ and $p = p_{|\Omega_s} = p_s$.
- If $H_d = 1$, $\mathbf{v} = \mathbf{v}_{|\Omega_d} = \mathbf{v_d}$ and $p = p_{|\Omega_d} = p_d$.
- The term $\mu||H_s\nabla\mathbf{v}||_0^2$ is well defined because velocity in Stokes is in $H^1_{\Gamma_{s,D}}$
- The term $\frac{1}{\mu}||H_s p||_0^2$ is well defined because pressure is in $L^2(\Omega_s)$.
- The terms $\frac{\mu}{k}||H_d div\mathbf{v}||_0^2$ is well defined because of the surjectivity of the divergence operator from $H_{\Gamma_{d,D}}(div,\Omega_d)$ to $L^2(\Omega_d)$, which means that $divv \in L^2(\Omega_d)$, then $||divv||_0^2$ is well defined.
- The term $\frac{k}{\mu L_0^2}||H_d p||_0^2$ is well defined because the pressure is in $L^2(\Omega_d)$.

– The norm $||\nabla q_i||_{L'}$ is defined by:

$$||\nabla q_i||_{L'} = \sup_{\mathbf{v_i}\in L} \frac{|<\nabla q_i, \mathbf{v_i}>|}{||\mathbf{v_i}||_L} \tag{3.67}$$

where L is $H^1_{\Gamma_{s,D}}(\Omega_s)^m$ or $H^1_{\Gamma_{d,D}}(div, \Omega_d)$, and L' denotes the dual space of L, i is s in Stokes and d in Darcy. This norm is the finest norm in which one can prove the stability of Stokes-Darcy coupled problem. Badia and Codina in [S.Badia & R.Codina 2008] demonstrate the stability of the bilinear form $B_c([\mathbf{v}, q], [\mathbf{w}, q])$ on the space $V_c \times Q_c$ relatively to the norm $||| \; |||_c$ defined in Equation (3.66). Then:

$$\begin{aligned} &\forall [\mathbf{v}, p] \in V_c \times Q_c, \exists [\mathbf{w}, q] \in V_c^0 \times Q_c \,\text{and}\, C > 0 \,\text{such that} \\ &B_c([\mathbf{v}, q], [\mathbf{w}, q]) \geq C |||[\mathbf{v}, p]|||_c |||[\mathbf{w}, q]|||_c \end{aligned} \tag{3.68}$$

3.4.2 Stokes-Darcy problem stabilized with ASGS method

The formulation of Stokes-Darcy coupled problem is obtained by summing up the formulations of Darcy stabilized with ASGS method (3.20) and (3.21) and the formulations of Stokes stabilized with ASGS method (3.55) and (3.56). For Stokes and Darcy flow coupled through their interface, the stabilized problem with ASGS can be written as follows:
Find $[\mathbf{v_h}, p_h] \in V_{h,c} \times Q_{h,c}$ such as:

$$B_{c,stable}([\mathbf{v_h}, p_h][\mathbf{w_h}, q_h]) = L_{c,stable}([\mathbf{w_h}, q_h]) \tag{3.69}$$

$$\forall [\mathbf{w_h}, q_h] \in V_{h,c}^0 \times Q_{h,c}$$

$$\begin{aligned} B_{c,stable}([\mathbf{v_h}, p_h], [\mathbf{w_h}, q_h]) = \; & B_c([\mathbf{v_h}, p_h], [\mathbf{w_h}, q_h]) \\ & + \tau_{p,c} \sum_K < div\mathbf{v_h}, div\mathbf{w_h} >_K \\ & + \tau_u \sum_K < H_d(\frac{\mu}{\mathrm{k}}\mathbf{v_h} + \nabla p_h), -\frac{\mu}{\mathrm{k}}\mathbf{w_h} + \nabla q_h >_K \\ & + \tau_v \sum_K < H_s \nabla p_h, +\nabla q_h >_K \end{aligned} \tag{3.70}$$

$$\begin{aligned} L_{c,stable}([\mathbf{w_h}, q_h]) = \; & L_c([\mathbf{w_h}, q_h]) \\ & + \tau_{p,c} \sum_K < h_c, \nabla . \mathbf{w_h} >_K \\ & + \tau_{u,c} \sum_K < \mathbf{f_c}, -\frac{\mu}{\mathrm{k}} \nabla q_h >_K \\ & + \tau_u \sum_K < H_d \mathbf{f_d}, -\frac{\mu}{k} \mathbf{w_h} > \end{aligned} \tag{3.71}$$

$\tau_{p,c}$, $\tau_{u,c}$, τ_u and τ_v are the stabilization parameters obtained by Fourier transformation, that we compute as [S.Badia & R.Codina 2008]

$$\begin{aligned}
\tau_{p,c} &= c_p \frac{\mu}{\mathrm{k}} l_p^2 + c_1 \mu \\
\tau_{u,c} &= (c_1 \mu + c_u \frac{\mu}{\mathrm{k}} l_u^2)^{-1} h_K^2 \qquad (3.72) \\
\tau_u &= \frac{h_K^2}{c_u \times l_u^2} \frac{k}{\mu} \qquad (3.73) \\
\tau_v &= \frac{1}{c_1 \mu} h_K^2 \qquad (3.74) \\
& \qquad (3.75)
\end{aligned}$$

In our case, we use method B (Equation (eq3:darcy-methods)), which means that $l_u = l_p = \sqrt{L_0\, h}$

3.4.3 Stability of the bilinear form of the Stokes-Darcy coupled problem

To prove the stability of the bilinear form of the Stokes-Darcy coupled problem on the finite element spaces $V_{h,c} \times Q_{hc}$, we have to define a mesh dependant-norm:

$$\begin{aligned}
|||[\mathbf{v_h}, p_h]|||_{h,c} &= \mu ||H_s \nabla \mathbf{v_h}||_0^2 + \frac{\mu}{k} ||H_d \mathbf{v_h}||_0^2 + \frac{\mu}{k} \tau_p \sum_K ||H_d div \mathbf{v_h}||_0^2 \\
&+ \frac{1}{\mu} ||H_s p_h||_0^2 + \frac{k}{\mu L_0} ||H_d p_h||_0^2 \qquad (3.76) \\
&+ \tau_v \sum_K ||H_s \nabla p_h||_K^2 + \tau_u \sum_K ||H_d \nabla p_h||_K^2
\end{aligned}$$

where τ_p, τ_v and τ_u are the stabilization parameters in Stokes and Darcy respectively.

As explained for Darcy and Stokes separately, all these norms are well controlled in the specific spaces of velocity and pressure. In our cases we choose P1/P1 elements for Stokes and Darcy, then ∇p_h is a constant vector $\in L^2(K)$

The stability of the bilinear form $B_{c,stable}([\mathbf{v_h}, p_h], [\mathbf{w_h}, q_h])$ leads to:

$$\begin{aligned}
&\exists C > 0, \exists [\mathbf{w_h}, q_h] \in V_{h,c}^0 \times Q_{h,c}, \forall [\mathbf{v_h}, q_h] \in V_{h,c} \times Q_{h,c} \\
&B_{c,stable}([\mathbf{v_h}, p_h], [\mathbf{w_h}, q_h]) \geq C |||[\mathbf{v_h}, p_h]|||_{h,c} |||[\mathbf{w_h}, q_h]|||_{h,c}
\end{aligned} \qquad (3.77)$$

$$\begin{aligned} B_{c,stable}([\mathbf{v_h}, p_h], [\mathbf{v_h}, p_h]) &= 2\mu||H_s\dot{\boldsymbol{\varepsilon}}(\mathbf{v_s})||^2 + \sum_K \frac{\mu}{k}||H_d\mathbf{v_h}||^2_{0,K}(1-\tau_u\frac{\mu}{k}) \\ &\quad + \sum_K ||\nabla p_h||^2_{0,K}(H_s\tau_v + H_d\tau_u) \\ &\quad + \sum_K \tau_{p,c}||div\mathbf{v_h}||^2_{0,K} + \frac{\alpha\mu}{\sqrt{k}}||\mathbf{v_h}.\tau||^2 \\ &\geq C||[\mathbf{v_h}, \mathbf{p_h}]||^2_h \end{aligned} \tag{3.78}$$

if and only if $1-\tau_u\frac{\mu}{k} \geq 0$, *i.e*, if and only if $\frac{h}{c_u^2 \times L_0} < 1$ (because we use also method B for Darcy's problem in Stokes-Darcy coupling problem).

Either, $||[\mathbf{v_h}, \mathbf{p_h}]||_h$ and $||[\mathbf{v_h}, \mathbf{p_h}]||_{h,c}$ are equivalent, then $B_{c,stable}([\mathbf{v_h}, p_h], [\mathbf{w_h}, q_h])$ is coercive if and only if $\frac{h}{c_u^2 \times L_0} < 1$. We conclude, that also for the Stokes-Darcy coupled problem, the more efficient conditions are the conditions reported above on the algorithmic constants of the stabilization parameters of Darcy's equations.

3.5 Interface capturing

The interface Γ separating both Stokes and Darcy domains is not described by a set of boundary elements. This interface passes throughout the mesh elements, consequently a function ϕ has to be introduced to depict this interface. ϕ is chosen as the signed function to Γ defined by:

$$\phi(\mathbf{x}, t=0) = \begin{cases} \min\limits_{p\in\Gamma} \|\mathbf{x}-p\| & \text{if} \quad \mathbf{x} \in \Omega_s \\ -\min\limits_{p\in\Gamma} \|\mathbf{x}-p\| & \text{if} \quad \mathbf{x} \in \Omega_d \end{cases} \tag{3.79}$$

Consequently, Γ is the zero isosurface of ϕ: $\Gamma = \{\phi = 0\}$. Considering the discrete problem, ϕ is approximated by a piecewise linear function ϕ_h. As the interface does not correspond to some boundaries of elements, we have two ways to compute the surface integral involved in (3.64): either the surface integral is turned into a volume integral by introducing a Dirac delta function, or it is computed exactly by rebuilding a piecewise linear interface. In what follows we will introduce these two different methods to compute the surface integral over the interface.

3.5.1 Turning a surface integral into a volume integral

The transformation of surface integrals into volume integrals in presented in [Cottet & E.Maitre 2006]. First, a function L is defined by:

$$L(\frac{\phi}{\epsilon}) = \begin{cases} \frac{1}{2}(1 + cos(\pi\frac{\phi}{\epsilon})) & \text{if} \quad -\epsilon < \phi < \epsilon \\ 0 & \text{if} \quad |\phi| > \epsilon \end{cases} \tag{3.80}$$

where ϵ corresponds to the width of the interface. The Dirac delta function is approximated by the expression introduced in [Cottet & E.Maitre 2006]:

$$\delta_{\{\phi=0\}} \simeq \frac{1}{\epsilon} L(\frac{\phi}{\epsilon}) ||\nabla\phi|| \tag{3.81}$$

Consequently, by using the expression of (3.81), the surface integral can be approximated by a volume integral:

$$\int_\Gamma f(x)ds \simeq \int_\Omega \frac{1}{\epsilon} L(\frac{\phi}{\epsilon}) \, ||\nabla\phi|| f(x)dv$$

In our case, the function f is given by the BJS condition: $f(x) = \frac{\alpha\mu}{\sqrt{k}}(\mathbf{v_h}.\tau)(\mathbf{w_h}.\tau)$.

3.5.2 Exact computation of the surface integral

This technique consists in retrieving the segments ($m = 2$), triangles or quadrilaterals ($m = 3$) from the intersection of the interface with mesh elements. The surface integral can then be exactly computed on this set of segments or plans.

2D case

The mesh is made up by a set of triangles. The first step is to select the triangles which intersect the isovalue function $\Gamma = \{\phi = 0\}$. For this, on every triangle K of the mesh, we consider the function ϕ at the nodes x_0, x_1, and x_2 of a triangle. If ϕ has the same sign at these nodes (Equation (3.82)), the triangle doest not intersect the interface.

$$\begin{aligned} \phi(x_0)\phi(x_1) &> 0 \\ \phi(x_0)\phi(x_2) &> 0 \end{aligned} \tag{3.82}$$

If the sign of ϕ at the nodes is different, we note j_0 the node of different sign and the two others j_1 and j_2. The intersection with the triangle K is the segment $[a, b]$ (see figure 3.1), where the points a and b are defined by:

$$\begin{aligned} a &= \theta_1 j_0 + (1-\theta_1) j_1 \\ b &= \theta_2 j_0 + (1-\theta_2) j_2 \end{aligned} \tag{3.83}$$

where θ_1 and θ_2 are defined by:

$$\begin{aligned} \theta_1 &= \frac{\phi(j_1)}{\phi(j_1) - \phi(j_0)} \\ \theta_2 &= \frac{\phi(j_2)}{\phi(j_2) - \phi(j_0)} \end{aligned} \tag{3.84}$$

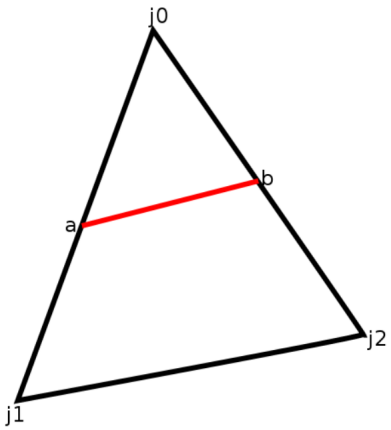

Figure 3.1: The segment of intersection of the triangle with the Stokes-Darcy interface Γ defined as the isovalue zero of a level set function

Remark: Some particular cases have to be considered:

- If ϕ vanishes at a node of the triangle K and keeps the same sign on the other nodes, the triangle does not intersect the interface Γ.
- If ϕ vanishes on two nodes of the triangle K then these nodes represent the segment of intersection.
- If ϕ vanishes on three nodes of the triangle K, we have to exclude this triangle from the mesh, because it is a degenerated case.

3D case

The mesh is made up by a set of tetrahedrons. The first step is to select the tetrahedrons which intersect the isovalue zero of ϕ. For this, on a tetrahedron K of the mesh, we consider the function ϕ on the nodes x_0, x_1, x_2 and x_3. If ϕ has the same sign at these nodes (Equation (3.85)), the tetrahedron does not intersect the zero level set.

$$\begin{aligned} \phi(x_0)\phi(x_1) &> 0 \\ \phi(x_0)\phi(x_2) &> 0 \\ \phi(x_0)\phi(x_3) &> 0 \end{aligned} \tag{3.85}$$

If ϕ changes its sign at the nodes, two cases have to be considered:

Case 1

If the function ϕ has the same sign on three nodes and a different sign on the fourth, we note j_0 the node of different sign. In this case, the intersection is a triangle noted "abc" (See figure 3.2) where:

$$\begin{aligned} a &= \theta_1 j_0 + (1-\theta_1) j_1 \\ b &= \theta_2 j_0 + (1-\theta_2) j_2 \\ c &= \theta_3 j_0 + (1-\theta_3) j_3 \end{aligned} \tag{3.86}$$

where θ_1, θ_2 and θ_3 are defined by:

$$\begin{aligned} \theta_1 &= \frac{\phi(j_1)}{\phi(j_1)-\phi(j_0)} \\ \theta_2 &= \frac{\phi(j_2)}{\phi(j_2)-\phi(j_0)} \\ \theta_3 &= \frac{\phi(j_3)}{\phi(j_3)-\phi(j_0)} \end{aligned} \tag{3.87}$$

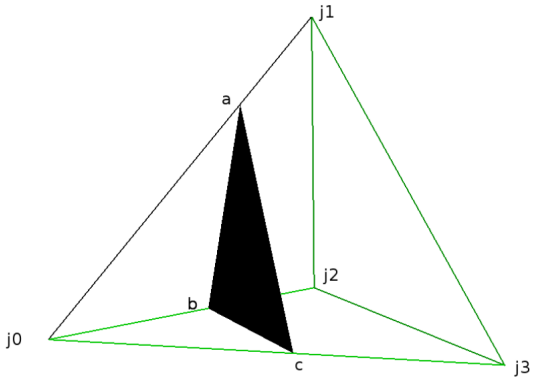

Figure 3.2: The triangle of intersection of the tetrahedron with the zero level set function Γ

We have some particular cases:

– If ϕ vanishes on a node or on two nodes and keeps the same sign on the other node or

the two other nodes, the tetrahedron does not intersect the level set.

– If ϕ vanishes on three nodes of the tetrahedrons, then the triangle formed by these three nodes is the triangle of intersection.
– If ϕ vanishes on four nodes of the tetrahedrons, then the tetrahedron is excluded from the computation, we are in a degenerated case.

Case 2

If the level set function ϕ has a negative sign on two nodes q_0 and q_1 and a positif sign on the other two nodes q_2 and q_3, the intersection is a quadrilateral (see Figure 3.3).

$$\begin{aligned} a &= \theta_1 q_0 + (1-\theta_1) q_2 \\ b &= \theta_2 q_1 + (1-\theta_2) q_2 \\ c &= \theta_3 q_0 + (1-\theta_3) q_3 \\ d &= \theta_4 q_1 + (1-\theta_4) q_3 \end{aligned} \tag{3.88}$$

where θ_1, θ_2, θ_3 and θ_4 are defined by:

$$\begin{aligned} \theta_1 &= \frac{\phi(q_2)}{\phi(q_2) - \phi(q_0)} \\ \theta_2 &= \frac{\phi(q_2)}{\phi(q_2) - \phi(q_1)} \\ \theta_3 &= \frac{\phi(q_3)}{\phi(q_3) - \phi(q_0)} \\ \theta_4 &= \frac{\phi(q_3)}{\phi(q_3) - \phi(q_1)} \end{aligned} \tag{3.89}$$

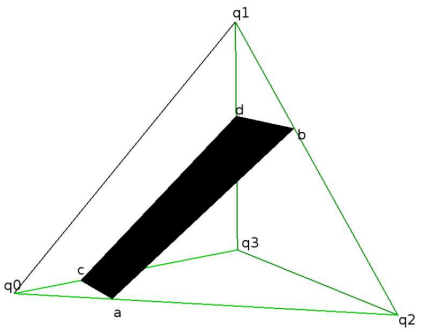

Figure 3.3: The quadrilateral of intersection of the tetrahedron with the zero level set function Γ

In the next chapter, we will see that rebuilding the interface gives more accurate results.

3.6 Conclusions

In this chapter, we have motivated the set of VariationalMultiScale methods for the numerical approximation of Stokes, Darcy and Stokes-Darcy coupling problems. We used piecewise continuous linear elements ($P1/P1$ elements) and the optimal method prescribed for the case of equal interpolation orders. We proved the stability of the bilinear forms of Stokes, Darcy and Stokes-Darcy coupled problems taking into consideration some conditions on the algorithmic constants in the parameters of stabilization. Finally, we presented the ways of computing the surface integral which appears in Stokes-Darcy coupling problem due to the presence of "BJS" condition.

Chapter 4

Validation of ASGS method for Stokes-Darcy coupled problem in severe regimes

Contents

4.1 Introduction

As mentioned before, coupling Stokes-Darcy using a "monolithic approach" may be quite challenging because of the difficulty to find some elements which are stable at the same time for both Stokes and Darcy. For this, we motivated the use of "VMS" methods. In this chapter, we will test ASGS method for Stokes, Darcy and Stokes-Darcy coupled problem. To evaluate the "ASGS" method we carried out two types of tests. First, we assess the convergence of this method along with the code robustness and performance using manufactured solutions. Second, we realise some tests where the analytical solution is known. In addition, our method is tested in severe regimes (permeability down to 10^{-15} m^2 and complex geometries). Some cases are compared with another "monolithic" coupling [Pacquaut *et al.* 2012], [Pacquaut 2009] to show the relevance of the ASGS method with respect to the VMS method. Moreover, we compare our "monolithic" approach in some cases to a decoupled approach [Celle *et al.* 2008] which is used to simulate industrial cases. In this chapter, we will validate Stokes problem with Poiseuille flow, then we will test its convergence using manufactured solutions. Furthermore, we will valid Darcy problem with a radial flow and test its convergence. Finally, we will test the convergence of Stokes-Darcy coupled problem with manufactured solutions, and will validate this coupled problem using different tests in 2D and 3D in severe regimes (perpendicular flow, parallel flow, inclined flow and complex flows). We will validate also the different methods of Stokes-Darcy interface capturing.

Remark: All the numerical simulations are implemented in Zebulon code based on C++ langage [1]

4.2 Validation of the Stokes problem

The numerical constant c_1 in the stabilization terms τ_v and τ_q (Equation (3.59)) is taken equal to 1 in all the tests [S.Badia & R.Codina 2008].

4.2.1 Poiseuille flow

In order to validate the Stokes problem stabilized with an "ASGS" method, we carried out a Poiseuille flow test. The incompressible fluid flows through rectangular geometry of length

1. This code is developed at École Nationale Supérieure des Mines de Paris, ONERA, Northwest Numerics and Modeling society (USA) and École Nationale Supérieure des Mines de Saint-Etienne.

L and of height H in Figure 4.1. We apply a parabolic velocity on the entry of the domain, defined as

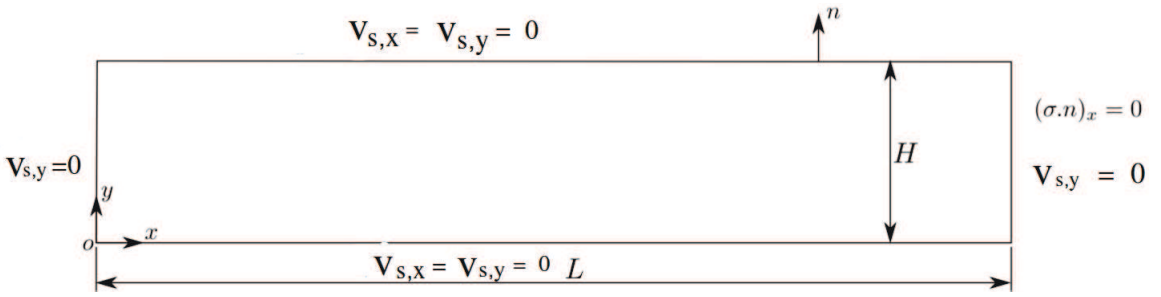

Figure 4.1: Domain of study of Poiseuille test used in Stokes problem

$$\mathbf{v_s} = \begin{cases} \mathbf{v_{s,x}} &= \frac{6Q}{H^3}(yH - y^2) \\ \mathbf{v_{s,y}} &= 0 \end{cases} \tag{4.1}$$

Other boundary conditions are such that in Figure 4.1, on the output of the domain at $x = L$, the first component of the normal stress is zero and the second component of the velocity is $\mathbf{v_{s,y}} = 0$. Other boundaries represent sticking conditions. The analytical solution of the velocity is given by the parabolic velocity imposed at the entry of the domain, defined in Equation (4.1). The analytical solution of pressure is:

$$p_s = (\frac{-12Q\mu}{H^3})\, x + p_0 \tag{4.2}$$

where p_0 is a constant. This problem is solved for $H = 1$, $L = 5$, $\mu = 1$ and $Q = 1$.
Figure 4.2 and 4.3 show the isovalues for velocity and pressure respectively. A comparison between analytical and numerical solutions of Stokes velocity in Figure 4.4 shows an excellent correlation of the results. The same conclusion can be drawn in Figure 4.5 for the pressure. This proves the stability of numerical solutions obtained for Stokes flow stabilized with an ASGS method.

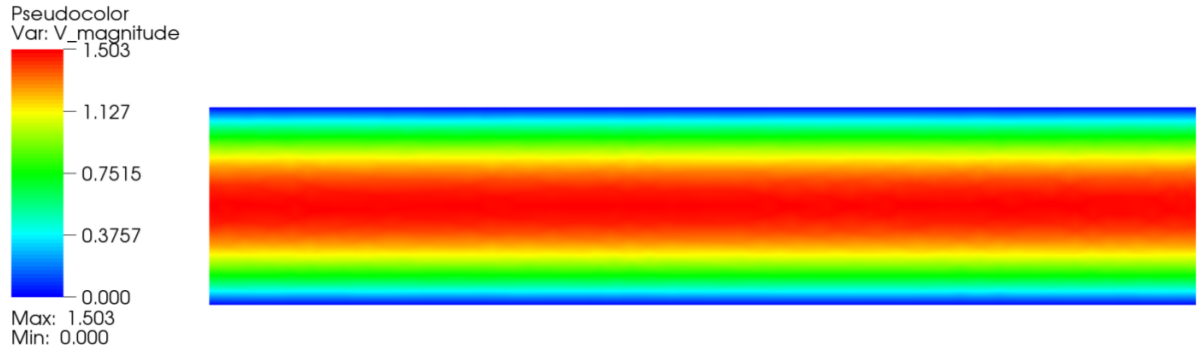

Figure 4.2: Isovalues of velocity for Poiseuille test (Figure 4.1)

Figure 4.3: Isovalues of pressure for Poiseuille test, (Figure 4.1)

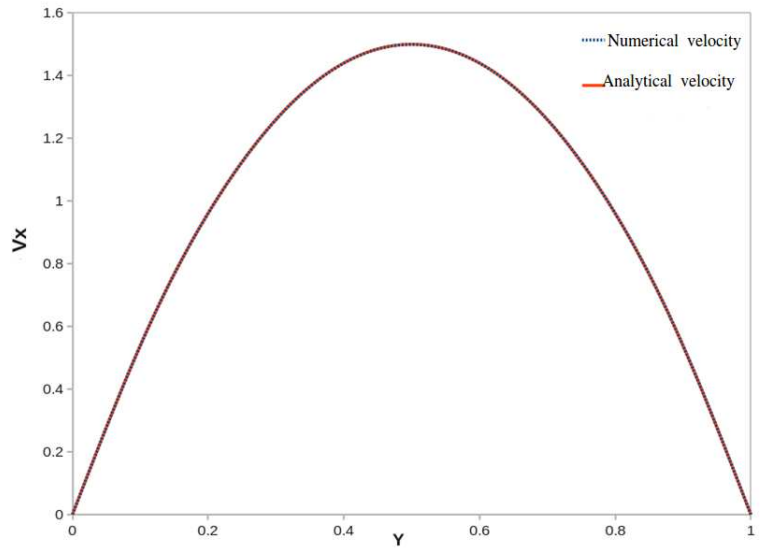

Figure 4.4: Comparison between numerical and analytical solutions of velocity for Poiseuille test, (Figure 4.1)

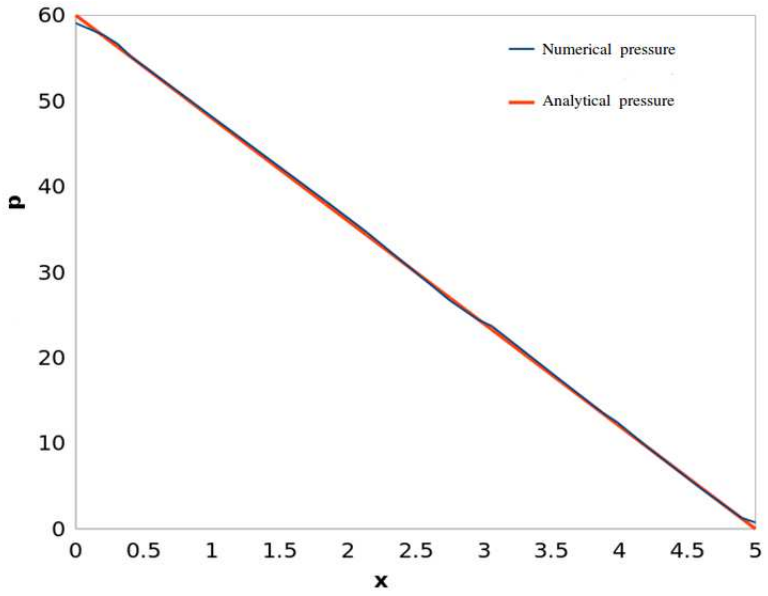

Figure 4.5: Comparison between numerical and analytical solutions of pressure for Poiseuille test, (Figure 4.1)

4.2.2 Study of the rate of convergence

To verify the implementation and to investigate the convergence of the "ASGS" method used to stabilize the Stokes problem, the method of manufactured solution [Chamberland *et al.* 2010], [Salari & Knupp 2000] is used. It consists in building an analytical solution that is fed into the system of equations under consideration and permits to compute the corresponding right-hand side terms. These terms are subsequently implemented into the numerical code to obtain the numerical solution of the discrete problem. Finally the difference between the general analytical solution and the numerical one is computed and permits to assess the capability of the method to solve the PDE set of equations.

Let us recall that we have to solve the following system for Stokes

$$\begin{aligned} -div\,(2\mu\dot{\varepsilon}(\mathbf{v_s})) + \nabla p_s &= \mathbf{f_s}\,\text{on}\,\Omega_{s,D} \\ div\,\mathbf{v_s} &= h_s\ \text{on}\ \Omega_{s,D} \\ \mathbf{v_s} &= \mathbf{0}\ \text{on}\ \Gamma_{s,D} \end{aligned} \tag{4.3}$$

Let us consider the following velocity and pressure fields [Donea & Huerta 2003]:

$$\begin{aligned} \mathbf{v_{s,x}} &= x^2(1-x)^2(2y-6y^2+4y^3) \\ \mathbf{v_{s,y}} &= -y^2(1-y)^2(2x-6x^2+4x^3) \\ p_s &= x(1-x) \end{aligned} \tag{4.4}$$

From which one deduces the term f_s for the corresponding Stokes problem in Equation (4.3).

$$\begin{aligned} f_{s,x} &= (12-24y)x^4 + (-24+48y)x^3 \\ &+ (-48y+72y^2-48y^3+12)x^2 \\ &+ (-2+24y-72y^2+48y^3)x + 1 - 4y + 12y^2 - 8y^3 \\ \\ f_{s,y} &= (8-48y+48y^2)x^3 + (-12+72y-72y^2)x^2 \\ &+ (4-24y+48y^2-48y^3+24y^4)x - 12y^2 + 24y^3 - 12y^4 \\ \\ \text{and}\, h_s &= 0 \end{aligned} \tag{4.5}$$

This problem is solved numerically on a square $[0,1]\times[0,1]$. The studied area is divided into squares, each square is itself divided into two triangles. In this way, a regular mesh is obtained. Several meshes are used: 10×10, 20×20, 40×40 and 80×80. A Dirichlet condition of zero velocity is imposed on the overall boundary of the domain Ω_s. For every mesh and every

numerical solution $\mathbf{v_{h,s}}$ and $p_{h,s}$, the errors are calculated using the following norms.

– L^2 Norm:

$$\|u\|_{0,\Omega_s} = \Big(\int_{\Omega_s} u^2 d\Omega_s\Big)^{1/2} \tag{4.6}$$

– H^1 Norm :

$$\|u\|_{1,\Omega_s} = \Big(\|u\|^2_{0,\Omega_s} + \sum_{j=1}^{m} \Big\|\frac{\partial u}{\partial x_j}\Big\|^2_{0,\Omega_s}\Big)^{1/2} \tag{4.7}$$

For the Stokes equations, the use of linear and continuous elements implies rates of convergence which verify [A.Ern 2005]:

$$\|\boldsymbol{v} - \boldsymbol{v_h}\|_{1,\Omega_s} + \|p - p_h\|_{0,\Omega_s} \leqslant C\, h(\|\boldsymbol{v}\|_{2,\Omega_s} + \|p\|_{1,\Omega_s}) \tag{4.8}$$

where C is a constant and $\|.\|_{2,\Omega_s}$ is the H^2 norm:

$$\|u\|_{2,\Omega_s} = \Big(\|u\|^2_{0,\Omega_s} + \sum_{j=1}^{m} \Big\|\frac{\partial u}{\partial x_j}\Big\|^2_{0,\Omega_s} + \sum_{i,j=1}^{m} \Big\|\frac{\partial^2 u}{\partial x_i x_j}\Big\|^2_{0,\Omega_s}\Big)^{1/2} \tag{4.9}$$

Table 4.1 shows the error on velocity in L^2 and H^1 norms and the error on pressure in L^2 norm.

mesh	h	$\|\|\mathbf{v_s} - \mathbf{v_{h,s}}\|\|_{L^2}$	$\|\|\mathbf{v_s} - \mathbf{v_{h,s}}\|\|_{H^1}$	$\|\|p_s - p_{h,s}\|\|_{L^2}$
10×10	0.1	0.00087005	0.015	0.0018497
20×20	0.05	0.000231	0.0079	0.000486
40×40	0.025	$5.975\,10^{-5}$	0.00398	0.00016041
80×80	0.0125	$1.46\,10^{-5}$	0.00199	$4.8\,10^{-5}$

Table 4.1: Errors of velocity and pressure for the Stokes problem

Figure 4.6 (a) shows that pressure converges with a rate [1.64 : 1.92] in L^2 norm. Figure 4.6 (b) shows that velocity converges with a rate [1.93 : 2.04] in norm L^2 (theoretical order is equal to 2) and with a rate [0.93 : 1.74] in norm H^1 (theoretical order is equal to 1). These results correspond to the theoretical convergence rates determined by Equation (4.8). Figures 4.7 (a) and 4.7 (b) show the isovalues of pressure and velocity.

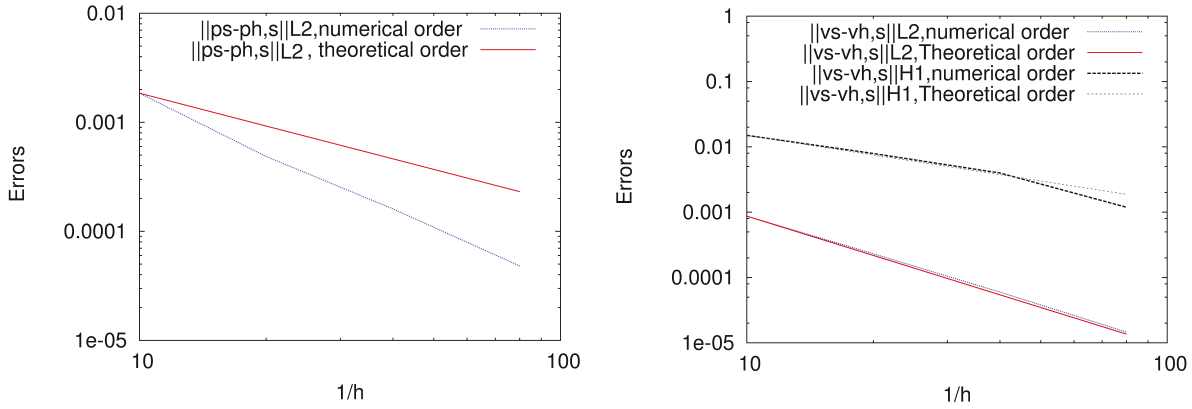

a) b)

Figure 4.6: Convergence of the error for pressure (a) and velocity (b) for the Stokes problem, with $\mu = 1Pa.s$, $h = 0.0125m$

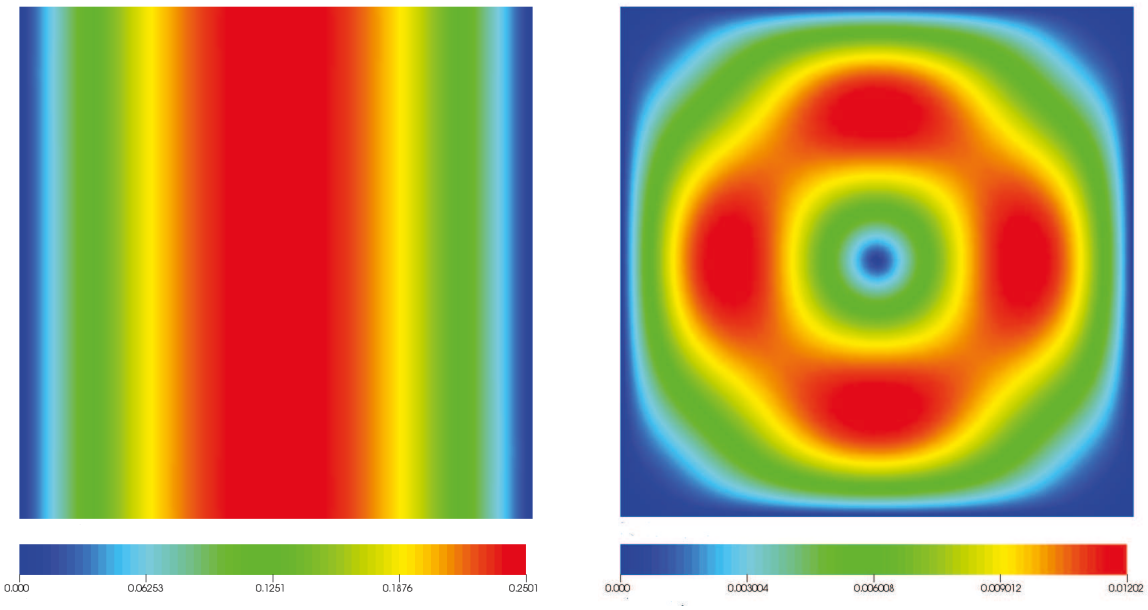

a) b)

Figure 4.7: Isovalues of the pressure (a) and velocity (b) fields for the Stokes problem, with $\mu = 1Pa.s$, $h = 0.0125m$

4.3 Validation of the Darcy problem

The numerical constants in the stabilization terms τ_u and τ_p (Equation (3.28)) in Darcy problem are taken $c_u = 2$, $c_p = 2$ and $L_0 = \sqrt[m]{meas(\Omega_d)}$ where $meas(\Omega_d)$ is the surface of Ω_d in 2D and the volume of Ω_d in 3D [S.Badia & R.Codina 2008].

4.3.1 Radial flow

To validate the implementation of the ASGS method for the Darcy's flow, we test a radial flow. The geometry of the domain is given in Figure 4.8. The analytical solutions of the radial velocity and of pressure are given in Equation (4.10).

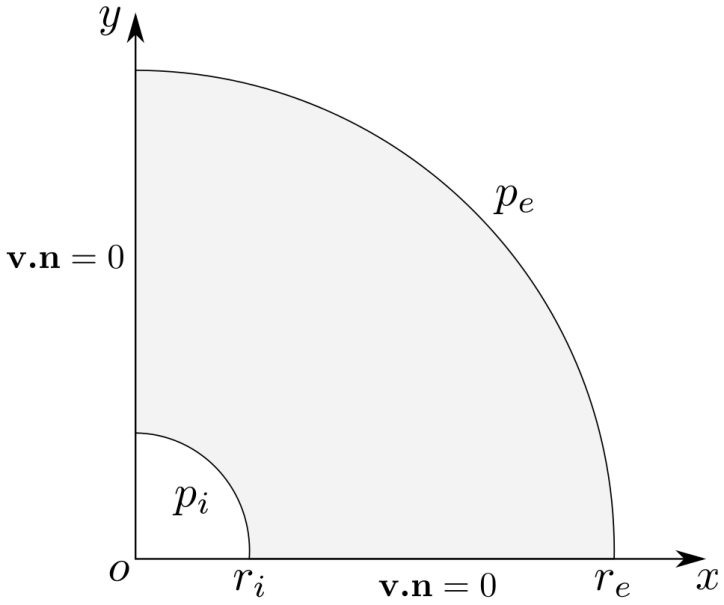

Figure 4.8: Domain of study and boundary conditions for the radial flow

$$\begin{cases} v_r &= \dfrac{-k}{\mu}\dfrac{1}{r}\dfrac{p_e - p_i}{ln(\frac{r_e}{r_i})} \\ p_r &= p_i + (p_e - p_i)\dfrac{ln(\frac{r}{r_i})}{ln(\frac{r_e}{r_i})} \end{cases} \tag{4.10}$$

where r_i and r_e are respectively the inner and outer radius of the disc, while p_e and p_i are the internal and external pressure applied to the disc. The physical parameters of this simulation are: $k = 10^{-10}\mathrm{m}^2$, $\mu = 1Pa.s$ $r_e = 1m$ $r_i = 0.1m$ $p_e = 10^5 Pa$ and $p_i = 0Pa$. Figure 4.9 and 4.10 show the isovalues of velocity and pressure. Figure 4.11 shows a comparison between ana-

lytical and numerical solutions of pressure. The result shows an excellent correlation between analytical and numerical solutions which illustrates the stability of "ASGS" method applied to Darcy's equations.

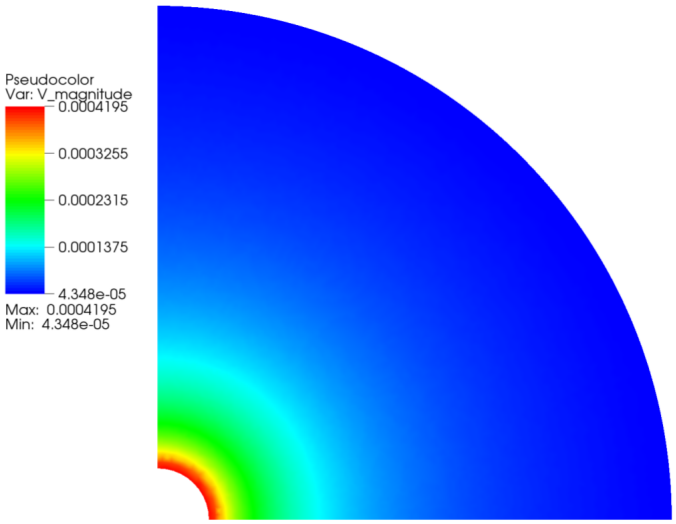

Figure 4.9: Isovalues of velocity for radial flow, (Figure 4.8)

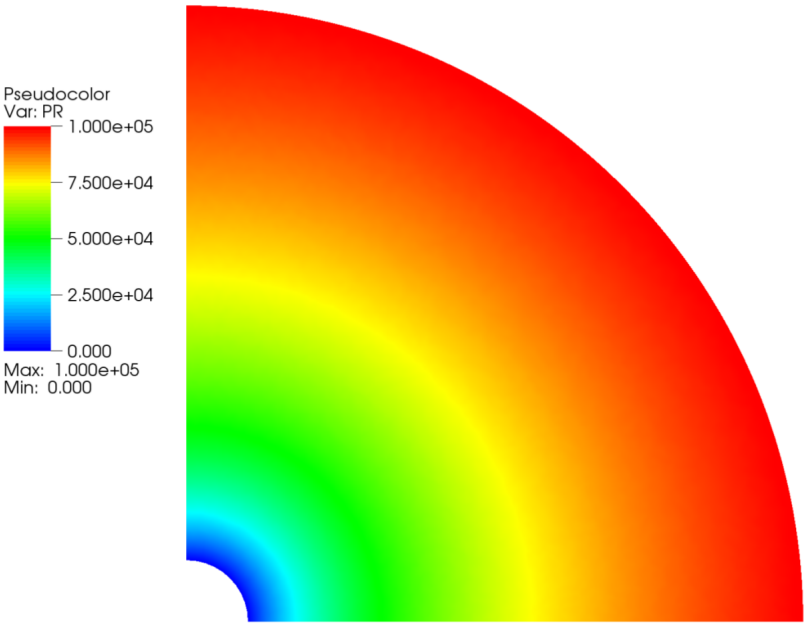

Figure 4.10: Isovalues of pressure for Darcy flow, (Figure 4.8)

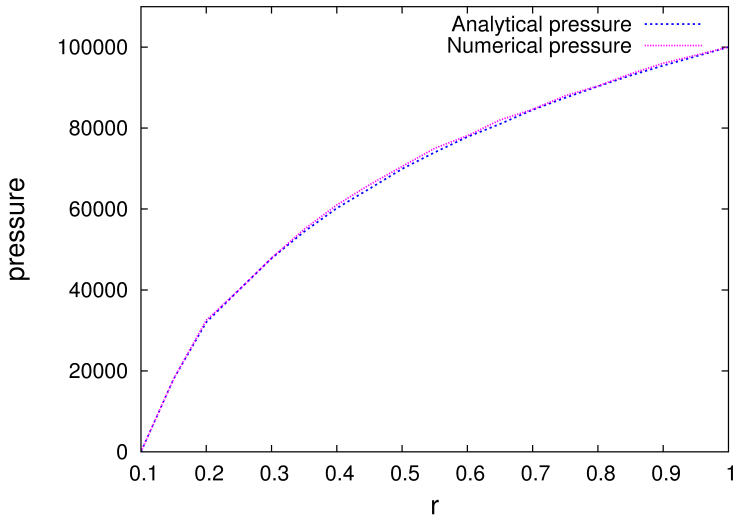

Figure 4.11: Comparison between analytical solution and numerical solution of pressure for the radial flow, (Figure 4.8)

4.3.2 Study of the rate of convergence

An analysis similar to the convergence rate analysis proposed for Stokes is carried out for both pressure and velocity in the porous medium Ω_d. Contrary to the previous case where $h_s = 0$, here the chosen velocity for the manufactured solution is not divergence-free and $h_d \neq 0$. In this case, a compatibility condition has to be satisfied [Masud & Hughes 2002]:

$$\int_{\Omega_d} div\, \mathbf{v_d}\, d\Omega_d = \int_{\Omega_d} h_d\, d\Omega_d = \int_{\partial\Omega_d} \mathbf{v_d}.\mathbf{n_d}\, d\Omega_d = \int_{\partial\Omega_d} g_d\, d\Omega_d \tag{4.11}$$

with

$$h_d = div(\mathbf{v_d}) \text{ in } \Omega_d$$

$$g_d = \mathbf{v_d}.\mathbf{n_d} \text{ on } \partial\Omega_d$$

In this case, the permeability is $k = 1\text{m}^2$ and the viscosity is $\mu = 1Pa.s$. The analytical pressure is [Masud & Hughes 2002], [Codina & S.Badia 2010]:

$$p_d = \sin(2\pi x)\sin(2\pi y) \tag{4.12}$$

while the velocity field is computed using the Darcy's law $\mathbf{v_d} = \frac{k}{\mu}\nabla p_d = \nabla p_d$, and the right

hand side term h_d is computed from the divergence of $\mathbf{v_d}$.

$$v_{x,d} = -2\pi cos(2\pi x) sin(2\pi y)$$

$$v_{y,d} = -2\pi sin(2\pi x) cos(2\pi y)$$

$$h_d = div\mathbf{v_d} = 8\pi^2 \sin(2\pi x) \sin(2\pi y)$$

Dirichlet condition on pressure is prescribed on the overall boundary of the domain Ω_d. For the Darcy's resolution, using linear approximation per elements, the rate of the convergence has to satisfy [A.Ern 2005]:

$$\begin{aligned} &\|\mathbf{v_d} - \mathbf{v_{h,d}}\|_{0,\Omega_d} + \|div(\mathbf{v_d} - \mathbf{v_{h,d}})\|_{0,\Omega_d} + \|(p_d - p_{h,d})\|_{0,\Omega_d} \\ &\qquad \leqslant C\, h(\|\mathbf{v_d}\|_{1,\Omega_d} + \|div\mathbf{v_d}\|_{0,\Omega_d} + \|p_d\|_{1,\Omega_d}) \end{aligned} \tag{4.13}$$

where C is a constant. Table 4.2 shows the pressure errors in both L^2 and H^1 norms and the velocity error in L^2 norm.

mesh	h	$\|\|\mathbf{v_d} - \mathbf{v_{h,d}}\|\|_{L^2}$	$\|\|p_d - p_{h,d}\|\|_{L^2}$	$\|\|p_d - p_{h,d}\|\|_{H^1}$
10×10	0.1	0.27	0.035	1.3
20×20	0.05	0.055	0.0041	0.7
40×40	0.025	0.015	0.0015	0.33
80×80	0.0125	0.0037	0.00045	0.164

Table 4.2: Errors of velocity and pressure in Darcy's domain

Figure 4.12 (a) shows a superconvergence of the pressure [1.85 : 2.9] (theoretical order is 2) in L^2 norm. The pressure converges with the rate [0.93 : 1.05] in H^1 norm (theoretical order is 1). Figure 4.12 (b) shows also a superconvergence of the velocity [2 : 2.59] in norm L^2 (theoretical order is 2). This result corresponds to the theoretical convergence rates determined by Equation (4.13), in [S.Badia & R.Codina 2008], [Codina & S.Badia 2010]. Figure 4.13 (a) and 4.13 (b) show the isovalues of pressure and velocity.

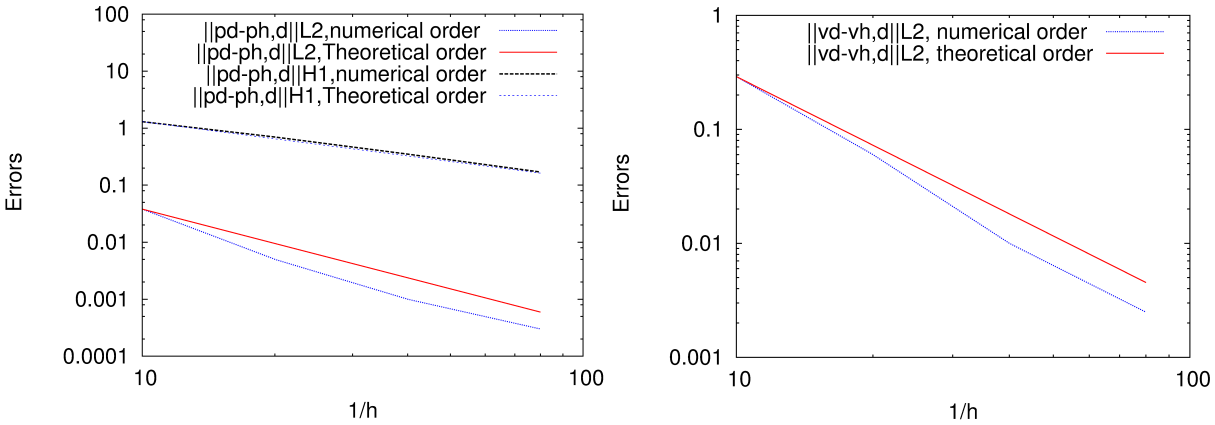

a) b)

Figure 4.12: Convergence of the error for (a) the pressure and (b) the velocity for Darcy problem, with $\mu = 1Pa.s$, $k = 1\text{m}^2$

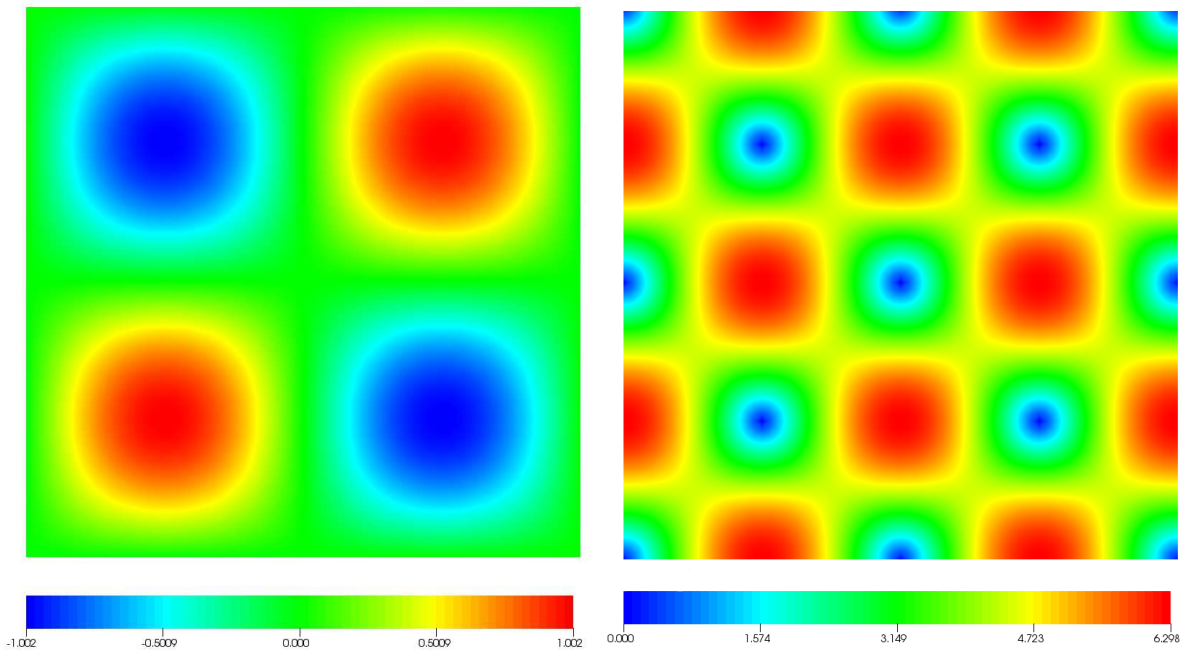

a) b)

Figure 4.13: Isovalues of pressure and velocity for Darcy problem, with $\mu = 1Pa.s$, $k = 1\text{m}^2$, $h = 0.0125m$.

4.4 Validation of Stokes-Darcy coupled problem

The constants in the stabilization parameters are taken as for Stokes and Darcy problems, $c_1 = 1$, $c_u = 2$,$c_p = 2$ and $L_0 = \sqrt[m]{meas(\Omega_d)}$.

4.4.1 Study of the rate of convergence

The coupled problem is solved on a square $[0,1] \times [0,1]$. Interface Γ corresponds to the line $x = 0.5$ (See Figure 4.14). The purely fluid domain Ω_s is located on the left side of the interface ($x < 0.5$) and the porous medium on the right side ($x > 0.5$). We have chosen the following velocity and pressure fields (Equation(4.15)) and (Equation(4.14)).

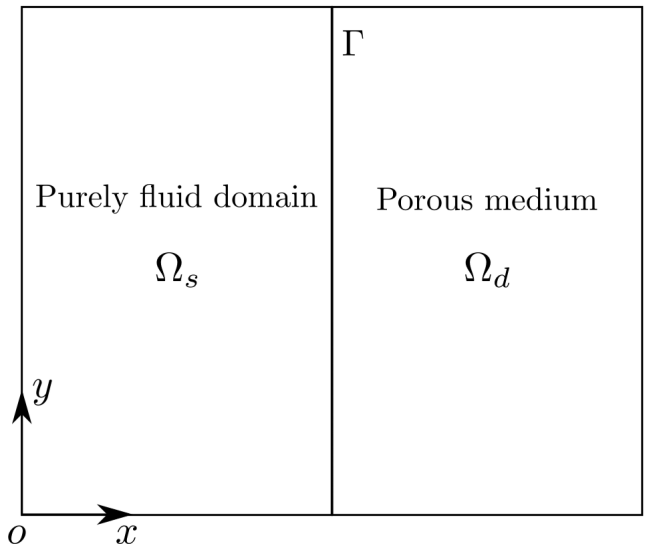

Figure 4.14: Domain of study for the manufactured solutions for Stokes-Darcy coupled problem.

$$\begin{aligned} p_d &= -y^4 exp(x) \\ v_{x,d} &= y^4 exp(x) \\ v_{y,d} &= -\frac{1}{5} y^3 exp(x) \end{aligned} \tag{4.14}$$

$$\begin{aligned} p_s &= -y^4 exp(x) \\ v_{x,s} &= y^4 exp(x) \\ v_{y,s} &= -\frac{1}{5} y^5 exp(x) \end{aligned} \tag{4.15}$$

Dirichlet conditions are prescribed on the boundary of the domain with respect to the analytical fields (Equations (4.14), (4.15)) chosen for the manufactured solutions. Additional terms are added to the interface conditions in Equations (4.16) and (4.17), as follows

$$p_s - 2\mu \mathbf{n}.\dot{\boldsymbol{\varepsilon}}(\mathbf{v_s}).\mathbf{n} = p_d + \mu_1 \quad \text{on} \quad \Gamma \tag{4.16}$$

$$\mathbf{v_s}.\boldsymbol{\tau_u} = \frac{-\sqrt{k}}{\alpha} 2\mathbf{n}.\dot{\boldsymbol{\varepsilon}}(\mathbf{v_s}).\boldsymbol{\tau_u} + \mu_2 \quad \text{on} \quad \Gamma \tag{4.17}$$

where μ_1 and μ_2 are given by

$$\mu_1 = -2y^4 e^x \tag{4.18}$$

$$\mu_2 = -\frac{2}{5} y^5 exp(x) + 4\, y^3 exp(x) \tag{4.19}$$

The physical parameters are $\mu = 1Pa.s$, $\alpha = 1$ and $k = 1\text{m}^2$.

An analysis of the convergence is carried out for both pressure and velocity in the subdomains Ω_s and Ω_d. We compare our results with the results from a previous monolithic approach developed in [Pacquaut *et al.* 2012] which uses a linear approximation for both velocity and pressure fields stabilized with $P1 + /P1$ in Stokes domain and with HVM method in Darcy's domain. The errors obtained in Stokes domain are presented in Table 4.3 for both ASGS and P1+/P1-HVM methods.

The rate of convergence for the velocity is $[1.17 : 3.2]$ in norm L^2 for the ASGS method, a superconvergence is noticed when h_K decreases from 0.05 to 0.025 due to the optimal choice of the constant c_1 while the rate of convergence decreases when the mesh size h_k decreases from 0.025 to 0.0125. For P1+/P1-HVM method, the rate of convergence for velocity is 1.73. The rate of convergence for the pressure in norm L^2 for ASGS method is $[1.14 : 2.4]$ (theoretical order is 1) while the rate of convergence for P1+/P1-HVM is $[0.98 : 1.1]$.

	ASGS		HVM/P1+P1	
h	$\|v - v_h\|_{L^2,Stokes}$	$\|p - p_h\|_{L^2,Stokes}$	$\|v - v_h\|_{L^2,Stokes}$	$\|p - p_h\|_{L^2,Stokes}$
0.1	0.8	0.8	0.04	0.17
0.05	0.178	0.2917	0.01	0.08
0.025	0.018	0.053	0.0026	0.044
0.0125	0.008	0.024	0.00073	0.022

Table 4.3: Errors for velocity and pressure in norm L^2 for both ASGS and P1+/P1-HVM methods in Stokes domain

	ASGS		HVM/P1+P1	
h	$\|v - v_h\|_{L^2,Darcy}$	$\|p - p_h\|_{L^2,Darcy}$	$\|v - v_h\|_{L^2,Darcy}$	$\|p - p_h\|_{L^2,Darcy}$
0.1	0.75	0.092	0.08	0.32
0.05	0.27	0.046	0.04	0.21
0.025	0.034	0.0044	0.021	0.15
0.0125	0.017	0.002	0.0106	0.107144

Table 4.4: Errors for velocity and pressure in L^2 norm for both ASGS and P1+/P1-HVM methods in Darcy's domain

Also, an analysis of the convergence is carried out and shown in Table 4.4 for both pressure and velocity in the Darcy's subdomain. The convergence orders of the P1+/P1-HVM method are low: the rate of convergence for the velocity in norm L^2 is of order $[0.5 : 0.6]$ (theoretical order is 2) and the rate of convergence for the pressure in norm L^2 is of order 1 (theoretical order is 2). The presence of the interface deteriorates the order of convergence. However, for ASGS method, the rate of convergence is $[1.1 : 2.98]$ for velocity in norm L^2 (theoretical order is 2). ASGS method solves therefore the deterioration of the convergence for the velocity, even if the rate of convergence decreases when we pass to a small size of mesh.

The rate of convergence for pressure in L^2 norm is $[1.14 : 3.3]$, the superconvergence of the method is noticed when we pass from $h = 0.05$ to $h = 0.025$. Figure 4.15 (a) shows the isovalues of pressure for Stokes-Darcy coupling problem stabilized with ASGS method, Figure 4.15 (b) shows the isovalues of pressure obtained with P1+/P1-HVM method. The oscillations present especially around the interface with P1+/P1-HVM method disappear completely with ASGS method. The same comparison for the velocity is shown in Figures 4.16 (a) for ASGS method and 4.16 (b) for P1+/P1-HVM method.

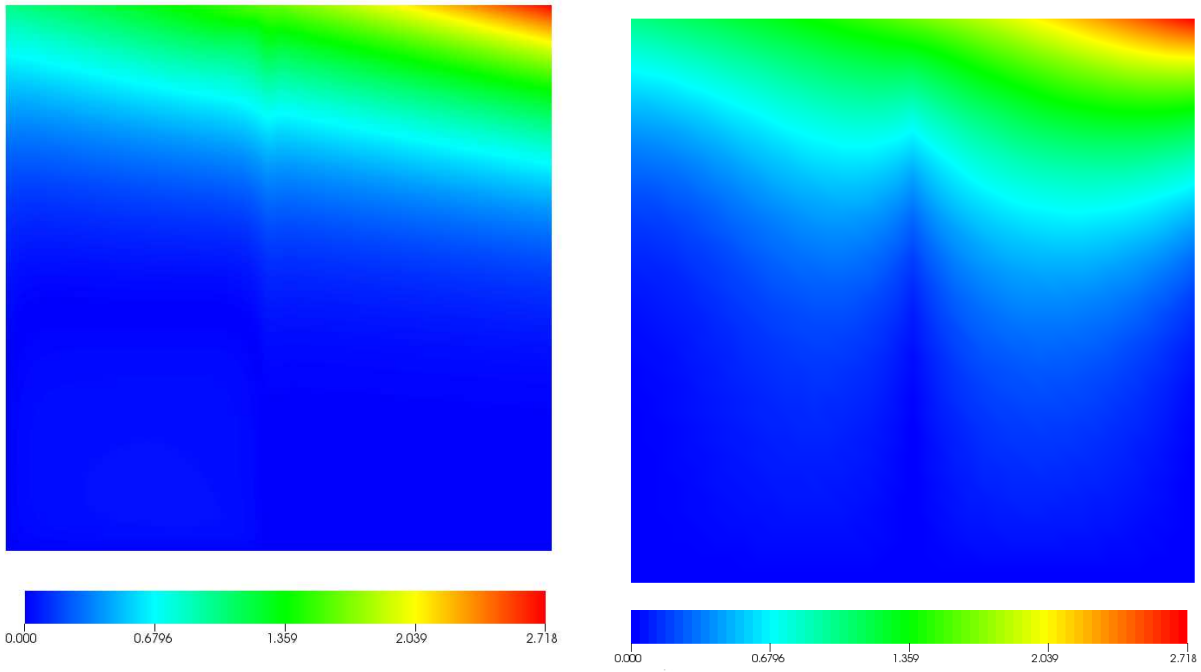

a) b)

Figure 4.15: Isovalues of pressure obtained with ASGS method (a) and with P1+/P1-HVM method (b) for $\mu = 1Pa.s$, $k = 1\text{m}^2$ and $\alpha = 1$

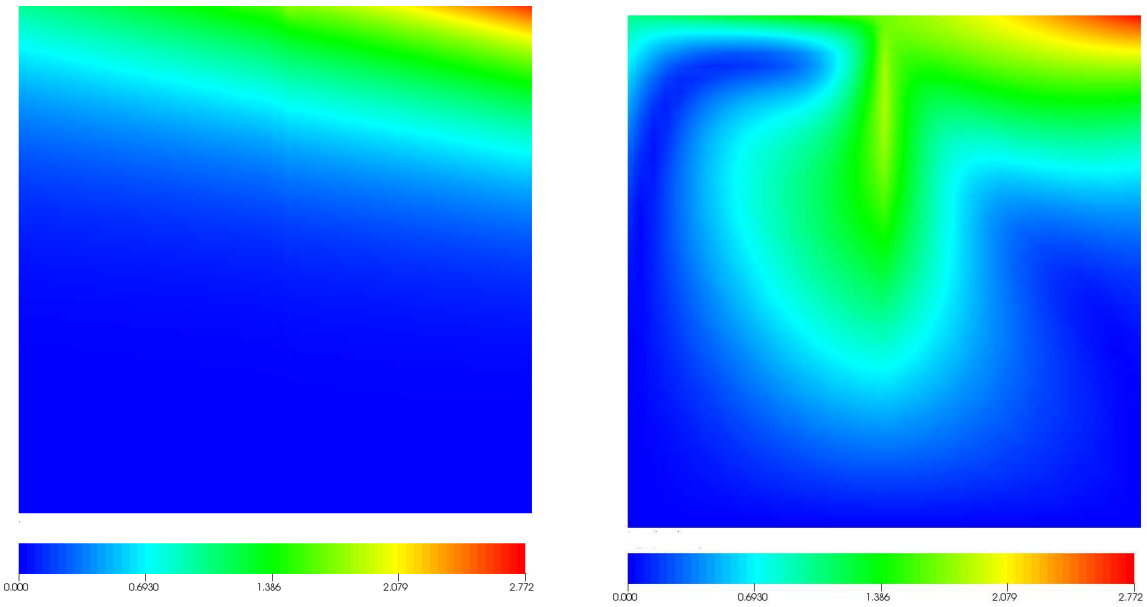

a) b)

Figure 4.16: Isovalues of velocity obtained with ASGS method (a) and with P1+/P1-HVM method (b) for $\mu = 1Pa.s$, $k = 1\text{m}^2$ and $\alpha = 1$

This comparison between ASGS method and P1+/P1-HVM shows the relevance of VMS methods for coupling Stokes-Darcy problem. Figure 4.17 (a) and Figure 4.17 (b) show in logarithmic scale the convergence of the errors for pressure and velocity in Stokes for the Stokes-Darcy coupled problem stabilized with ASGS method. Figure 4.18 (a) and Figure 4.18 (b) show in logarithmic scale the convergence of the errors for pressure and velocity in Darcy for the Stokes-Darcy coupled problem stabilized with ASGS method.

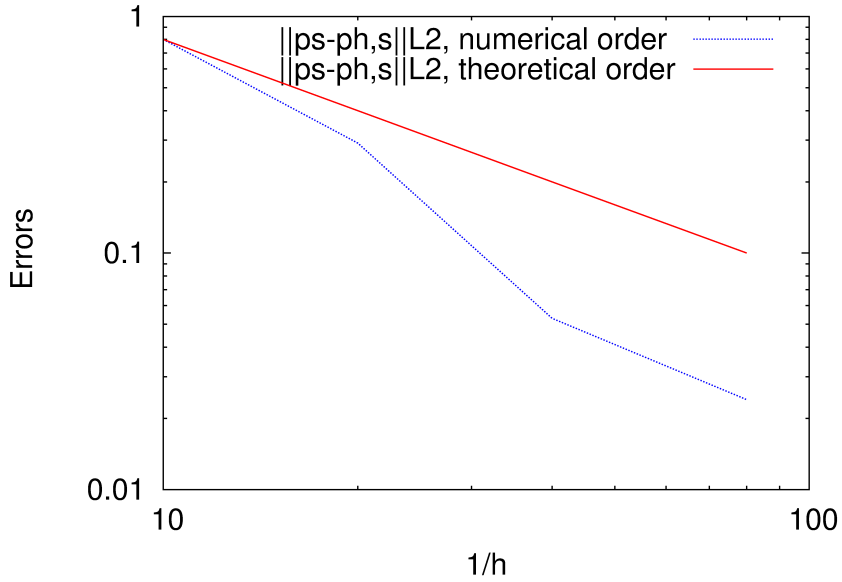

(a) pressure

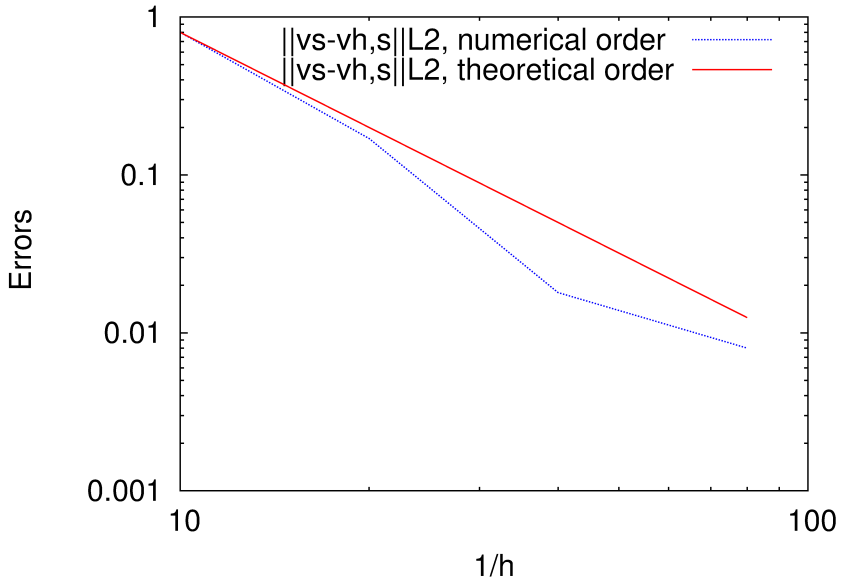

(b) velocity

Figure 4.17: Convergence of the error for the pressure and velocity in Stokes domain for Stokes-Darcy coupled problem with $\mu = 1Pa.s$,$k = 1\mathrm{m}^2$,$\alpha = 1$.

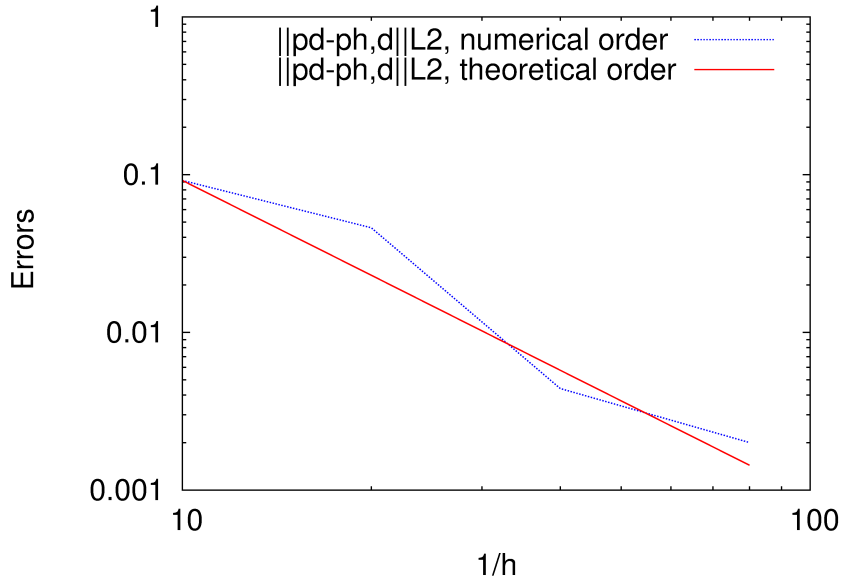

(a) pressure

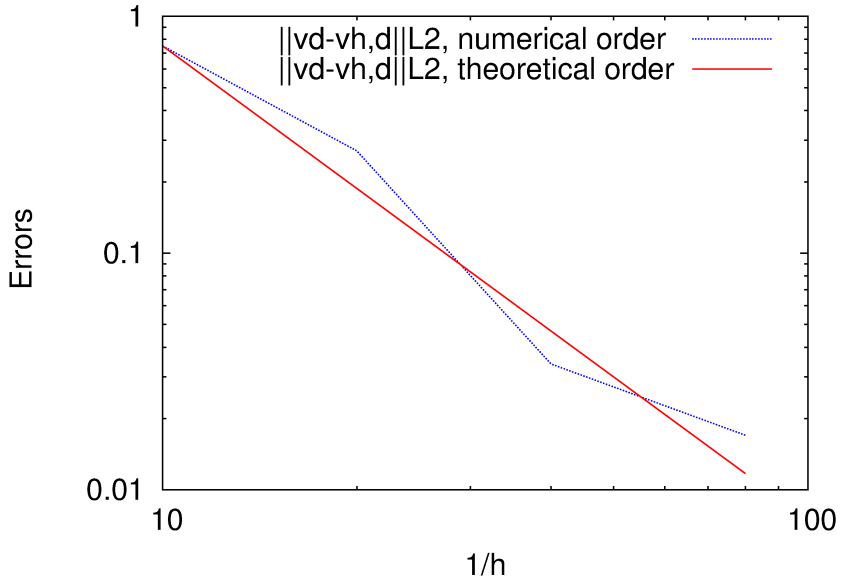

(b) velocity

Figure 4.18: Convergence of the error for the pressure and velocity in Darcy domain for Stokes-Darcy coupled problem with $\mu = 1Pa.s$,$k = 1\mathrm{m}^2$,$\alpha = 1$

4.4.2 Perpendicular flow

2D simulation

To validate the enforcement of the normal velocity continuity on the Stokes-Darcy interface, we study the case of a flow perpendicular to the interface of normal y in the global frame, which is a quite severe test. Normal velocity in Stokes depends solely on the Darcy normal velocity since no other boundary condition will set this velocity. Let us consider a domain $\Omega = [0,5] \times [0,2]\text{m}^2$ composed of two subdomains: a purely fluid domain $\Omega_s = [0,5] \times [1,2]\text{m}^2$ and a porous medium $\Omega_d = [0,5] \times [0,1]\text{m}^2$. A pressure p_{ext} of $1\,bar$ is applied on the top and a zero pressure is imposed on the bottom of the domain (Figure 4.19). Additional boundary conditions are zero normal velocity on the left and right hand sides of the geometry.

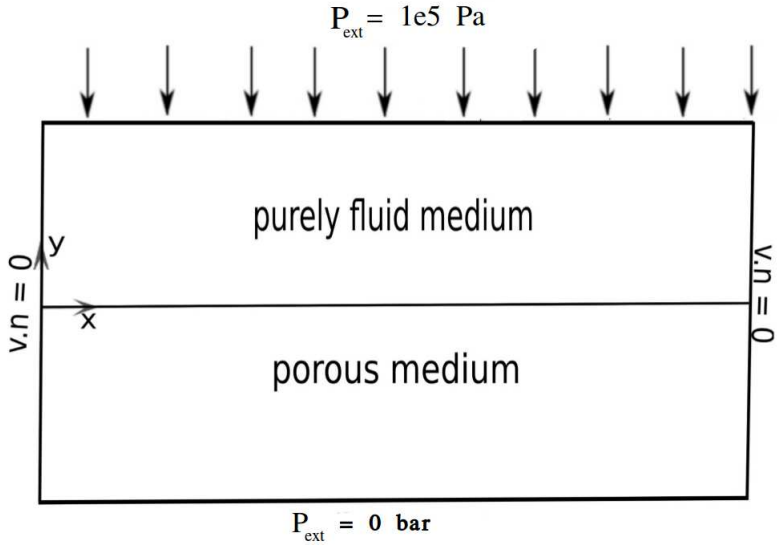

Figure 4.19: Computational domain of perpendicular flow and associated boundary conditions

The theoretical velocity is $\mathbf{v_d} = -\frac{k}{\mu}\nabla p$, then for $k = 10^{-11}\text{m}^2$, $\mu = 1$ Pa.s and $p_{ext} = 10^5$ Pa, $\mathbf{v_{d,y}} = -10^{-6}$ m/s. The normal velocity in Stokes should be equal to the normal velocity in Darcy due to the continuity of normal velocity applied on the Stokes-Darcy interface. Figure 4.20 shows spurious oscillations around the interface ($y = 1m$) when using the P1+/P1-HVM method, while a quasi absence of oscillations is noticed with the ASGS method for this low value of permeability $k = 10^{-11}\text{m}^2$. To assess the accuracy of the ASGS method for very low permeability, we did the same comparison with $k = 10^{-14}\text{m}^2$. Figure 4.21 shows larger oscillations of velocity around the interface for P1+/P1-HVM method and absence of

oscillations around the interface with the ASGS method. Moreover, a consistency error appears when using the P1+/P1-HVM method, since the normal velocity in Stokes is not equal to the one in Darcy. The ASGS method does not exhibit such a behaviour and ensures the continuity of the normal velocity, even when the ratio k/μ is small.

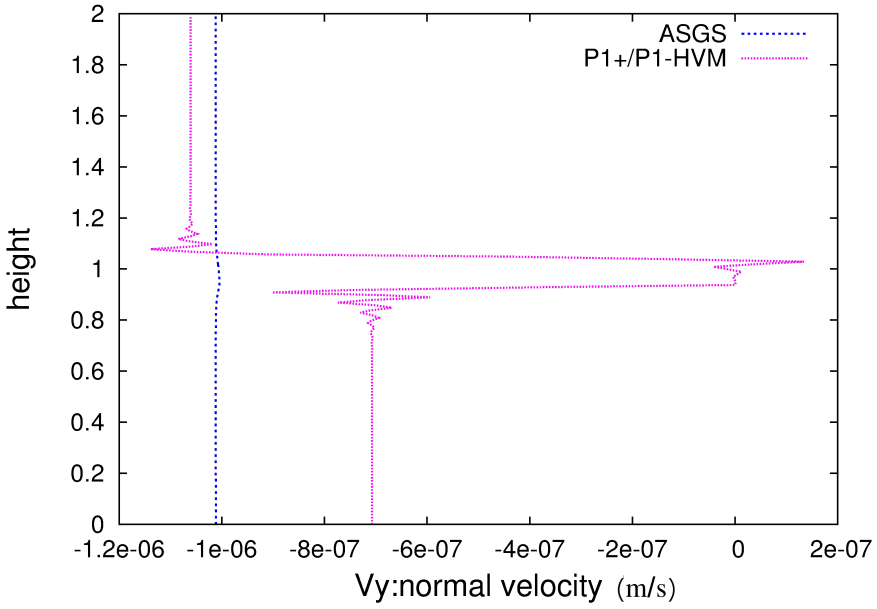

Figure 4.20: Comparison of velocity in perpendicular flow test between ASGS method and P1+/P1-HVM method, with $k = 10^{-11}\text{m}^2$, $\mu = 1Pa.s$, $p = 10^5 Pa$ and $\alpha = 1$

These results are obtained with structured meshes. With unstructured meshes, some oscillations may appear around the Stokes-Darcy interface, even with ASGS method. However their intensity is low and their effect is limited to a few nodes contrary to the P1+/P1-HVM method. Furthermore, those oscillations do not affect the consistency and the convergence of the method. The monolithic approach stabilized with "ASGS" method is also compared with the decoupled approach developed by [Celle *et al.* 2008]. Results show clearly that the ASGS method stabilization is as robust as the one used in industrial framework such as the decoupled approach developed in École des Mines de Saint-Étienne and by ESI group, to simulate resin infusion processes [Celle *et al.* 2008], [L.Abouorm *et al.*], [A.Dereims 2013]. Indeed ,Figure 4.22 presents the normal velocities obtained with both monolithic and decoupled approaches in the domain Ω, normalized by the normal velocity of the Darcy medium, $\mu = 1Pa.s$, $\alpha = 1$. As

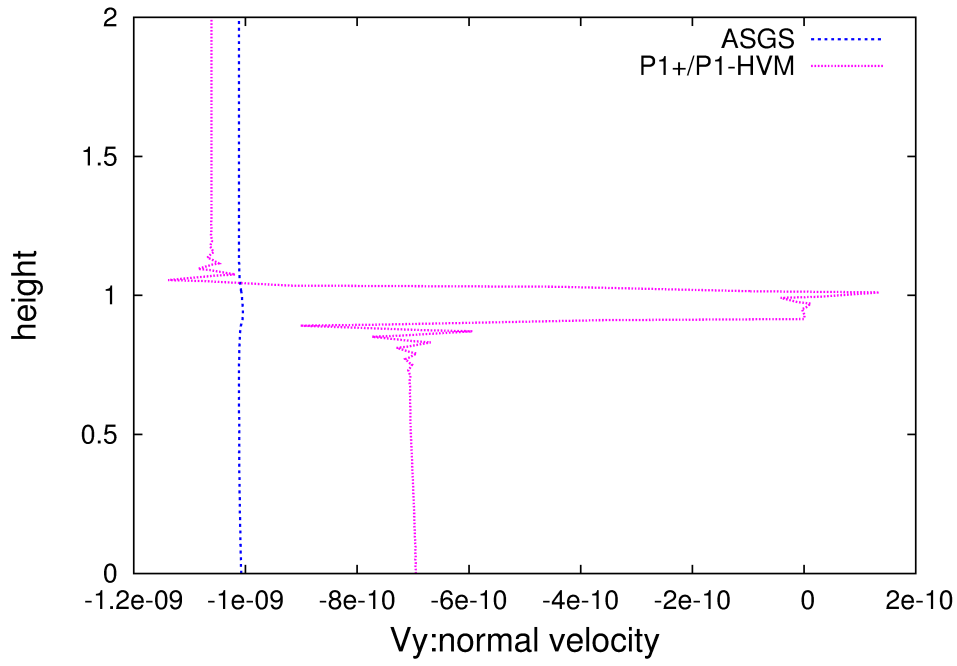

Figure 4.21: Comparison of velocity in perpendicular flow test between ASGS method and P1+/P1-HVM method, with $k = 10^{-14}\mathrm{m}^2$, $\mu = 1Pa.s$, $p = 10^5 Pa$ and $\alpha = 1$

it can be seen, in both approaches the continuity of the normal velocity is verified. The slight difference Δ between values of normal velocity computed with both decoupled and monolithic approaches is equal to $0.001 \times 10^{-6} m/s$ if $k = 10^{-11}\mathrm{m}^2$ and 0.01×10^{-9} if $k = 10^{-14}\mathrm{m}^2$.

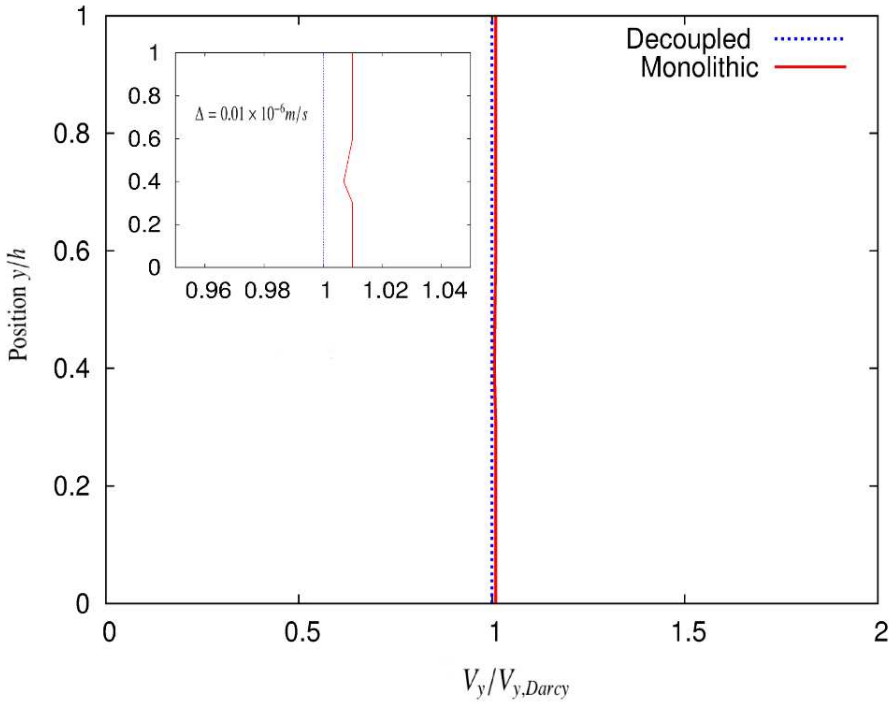

(a) $K = 10^{-11}\mathrm{m}^2$

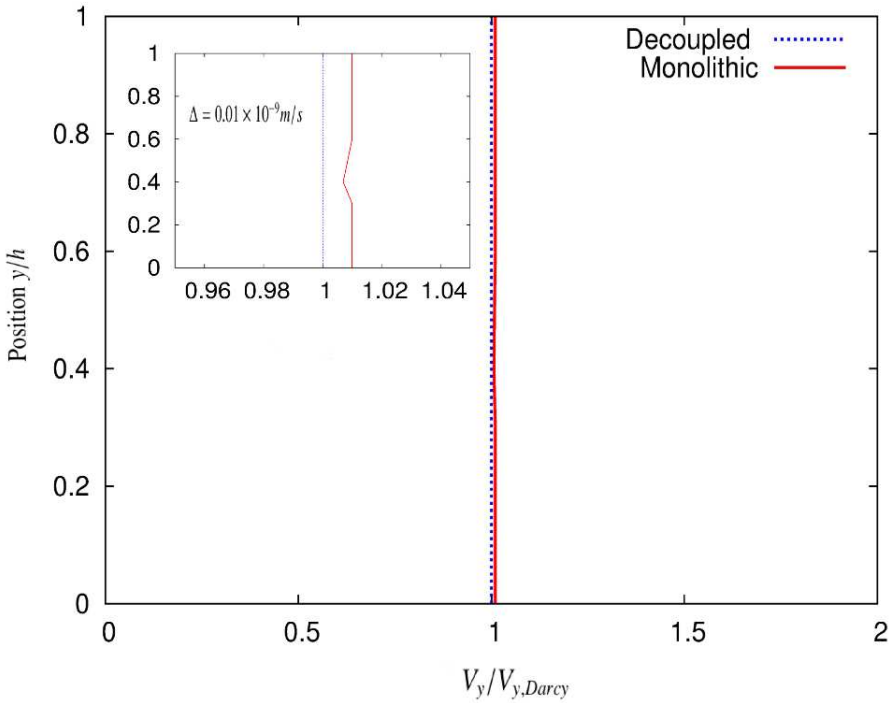

(b) $K = 10^{-14}\mathrm{m}^2$

Figure 4.22: Normalized normal velocity v_y for viscosity $\mu = 1Pa.s$ with different permeabilities and $\alpha = 1$

Convergence of the solution, as well as relative errors, have been considered for the case of the perpendicular flow. We compare the numerical results obtained with ASGS and P1+/P1-HVM methods respectively, with analytical ones given previously for $k = 10^{-14}$ m^2. The error is computed as $\|v_{error}\| = \frac{\|v-v_h\|_{L^2}}{\|v\|_{L^2}}$. Several regular meshes are used (100 ×10, 100 × 25, 100 × 50 and 100 × 100). The large drop in the relative error between ASGS and P1+/P1-HVM methods shown in Table 4.5, demonstrates the good behavior of the ASGS approach contrary to P1+/P1-HVM approach [Pacquaut *et al.* 2012].

Results for pressure field are presented in Figure 4.23. The pressure distribution does not depend on the permeability (but only on the enforced normal stress), and coincides with theoretical results.

	ASGS		HVM/P1+P1 [Pacquaut *et al.* 2012]	
h, $[m]$	$\|v_{y,error}\|_{stokes}$, [%]	$\|v_{y,error}\|_{darcy}$, [%]	$\|v_{y,error}\|_{stokes}$, [%]	$\|v_{y,error}\|_{darcy}$, [%]
0.15	0.77 %	1.13 %	12.41 %	9.37 %
0.077	0.38 %	0.242 %	10.41 %	9.37 %
0.041	0.14 %	0.069 %	6.32 %	5.94 %

Table 4.5: Relative errors for normal velocities in Stokes and Darcy regions, ASGS method and P1+/P1-HVM, $k = 10^{-14}$ m^2, perpendicular flow.

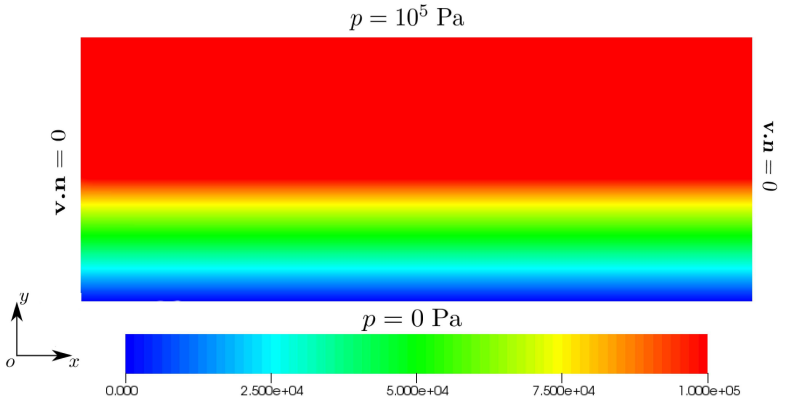

Figure 4.23: Isovalues of pressure for perpendicular flow with $k = 10^{-14}$m^2, $p = 1\,bar$, $\mu = 1Pa.s$ and $\alpha = 1$

3D extension

For the case of perpendicular flow, 3D simulations are carried out. Geometry and boundary conditions are the same as in 2D case, extruded along the **z** axis. We use structured mesh in this case. Results for pressure are presented in Figure 4.24 and for velocity in Figure 4.25, for $p_{ext} = 10^5 Pa$, $k = 10^{-14}\text{m}^2$ and $\mu = 1 Pa.s$. These results are in accordance with the results obtained for the 2D case. Normal velocity is continuous, and the oscillations disappear around the interface contrary to P1+/P1-HVM where oscillations are still more important in 3D cases. For unstructured meshes, some oscillations may appear around the Stokes-Darcy interface. However, their intensity is weak and their effect is limited to a few nodes. Furthermore, they do not affect the consistency and the convergence of the method.

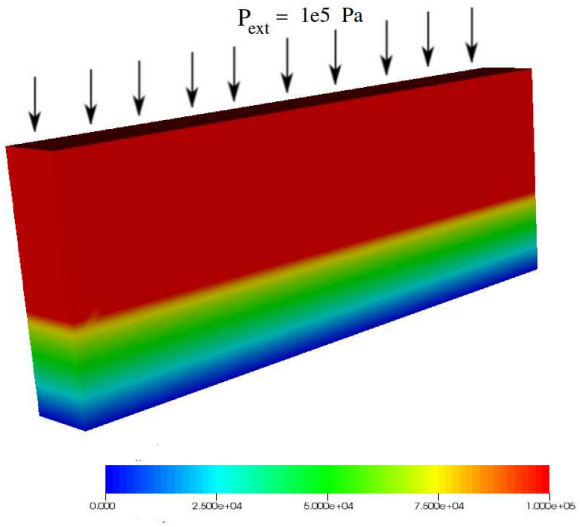

Figure 4.24: Isovalues of pressure for perpendicular flow in 3D with $k = 10^{-14}\text{m}^2$, $p = 1\,bar$, $\mu = 1 Pa.s$ and $\alpha = 1$

4.4.3 Parallel flow

The case of a flow parallel to the Stokes / Darcy interface is now investigated in order to validate the enforcement of the BJS condition (see [Gartling *et al.* 1996]). Hence, we consider a domain Ω composed of two sub-domains: a purely fluid domain $\Omega_s = [0;5] \times [0;1]\text{m}^2$ and porous medium $\Omega_d = [0;5] \times [-2;0]$ m^2 .The boundary conditions on $\partial\Omega$ for velocity and pressure are shown in Figure 4.26. The physical parameters for this simulation are $\mu = 1 Pa.s$,

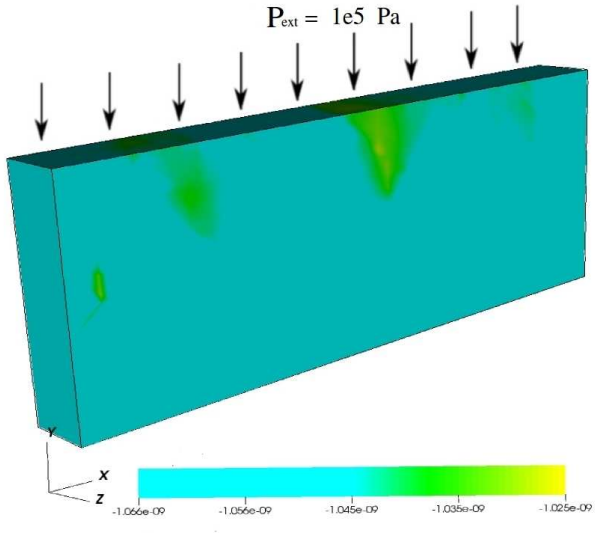

Figure 4.25: Isovalues of velocity for perpendicular flow in 3D with $k = 10^{-14}\text{m}^2$, $p = 1\,bar$, $\mu = 1Pa.s$ and $\alpha = 1$

$\alpha = 1$ (slip coefficient), $p_{ext} = 10^5$ Pa and $k = 10^{-14}$ m^2. In the Stokes domain, the normal velocity v_y is equal to zero, while the tangential velocity v_x, solution of the Stokes equations and verifying both the BJS condition on the interface Γ and the condition $v_x = 0$ on the upper side (*i.e.* for $y = H_s$), can be analytically calculated [Pacquaut *et al.* 2012]:

$$\begin{aligned} v_x &= -\frac{k}{2\mu}\Big(\frac{\lambda^2 + 2\alpha\lambda}{1+\alpha\lambda}\Big)\frac{dp}{dx}\Big(1 + \frac{\alpha}{\sqrt{k}}y\Big) \\ &\quad + \frac{1}{2\mu}\Big(y^2 + 2\alpha y\sqrt{k}\Big)\frac{dp}{dx} \\ v_y &= 0 \\ \lambda &= \frac{H_s}{\sqrt{k}} \end{aligned} \tag{4.20}$$

where H_s is the thickness of the Stokes domain.

Since pressure is linear, its derivative is consequently equal to $\frac{(p_1 - p_0)}{L}$, p_1 is the pressure applied on the right side, equal to $10^5 Pa$, and p_0 is the pressure applied on the left hand side, equal to $0Pa$, and L is the width of Ω. This leads to a pressure equal to $p(x) = \frac{(p_1 - p_0)}{L}x + p_0$, the Darcy's velocity is then equal to

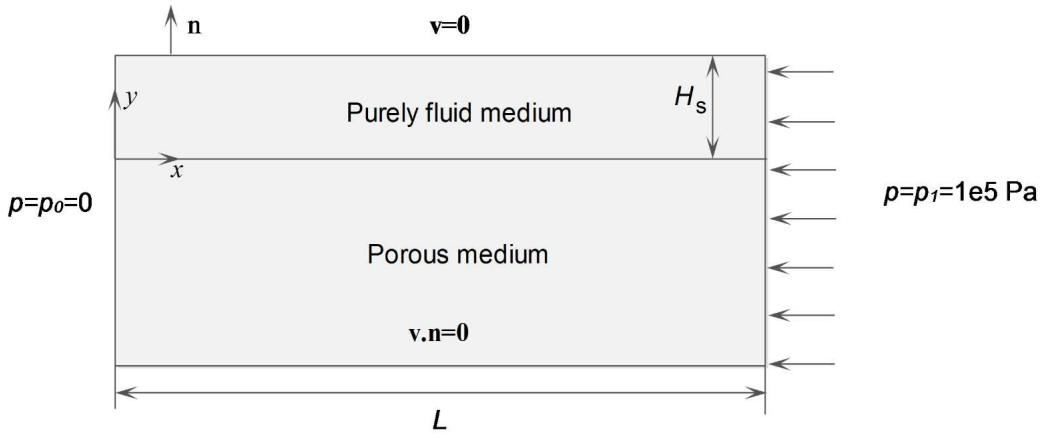

Figure 4.26: Computational domain for parallel flow and boundary conditions

$$\begin{aligned} v_x &= -\frac{k}{\mu}\nabla p = -\frac{k}{\mu}\frac{p_1 - p_0}{L} \\ v_y &= 0 \end{aligned} \tag{4.21}$$

Figures 4.27 and 4.28 show the distribution of velocity and pressure. Note that the values of this velocity, depending only on the imposed pressure gradient, are not in a real physical range but are relevant in this validation case. Different tests with different permeabilities (down to $10^{-14}\mathrm{m}^2$) are realized. Figure 4.29 compares the Stokes tangential velocity obtained by simulation with the analytical solution (4.20). One can verify a good correlation between the analytical and the numerical solutions, which shows that the BJS condition is correctly computed. The largest difference Δ between the analytical and numerical solution is equal to $85m/s$ ($\frac{\Delta}{\mathbf{v}_{max}} = 0.03(3\%)$), it is due to the mixture on the interface for elements belonging both to the Stokes and Darcy domains. A reduction of the mesh size around the interface may reduce this difference. However, that does not affect the validity of our comparison, and could be removed just by changing the physical units. Figure 4.30 compares the analytical solution for pressure with the simulation results for both ASGS and P1+/P1-HVM methods. It appears clearly that the simulation with ASGS method provides the expected linear pressure, while with the P1+/P1-HVM method some perturbations appear on either side of the computational domain.

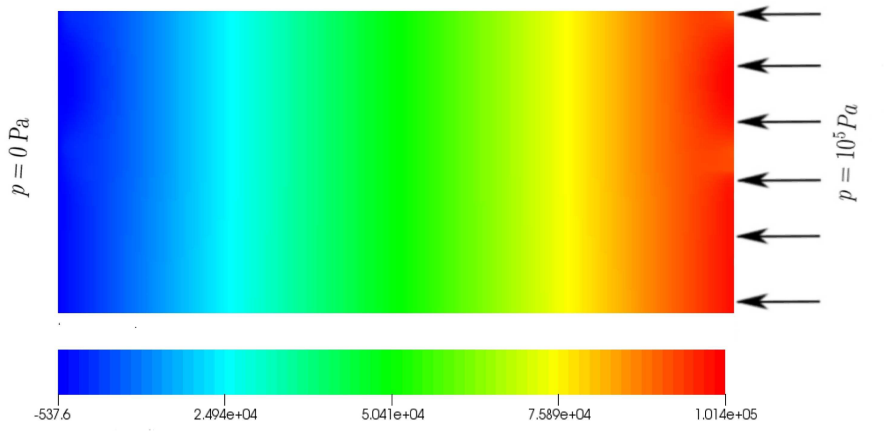

Figure 4.27: Isovalues of pressure (Pa) for parallel flow with $k = 10^{-14}\mathrm{m}^2$, $\mu = 1$, $\alpha = 1$ and $p = 10^5 Pa$

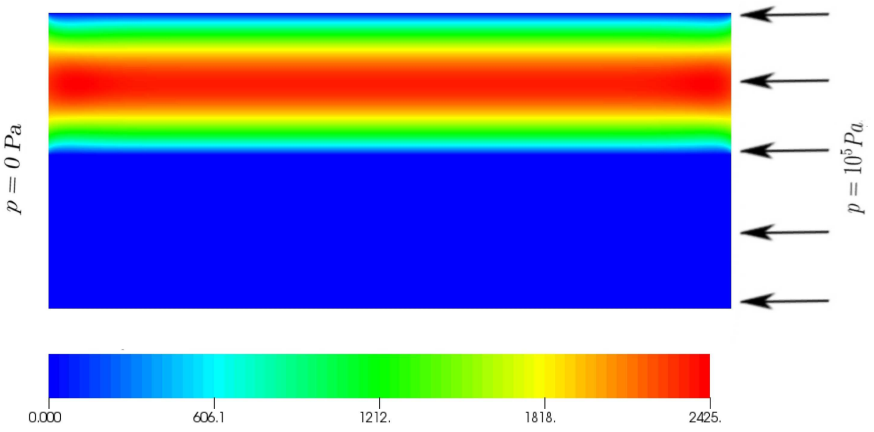

Figure 4.28: Isovalues of velocity (magnitude-velocity m/s) for parallel flow with $k = 10^{-14}\mathrm{m}^2$, $\mu = 1$, $\alpha = 1$ and $p = 10^5 Pa$

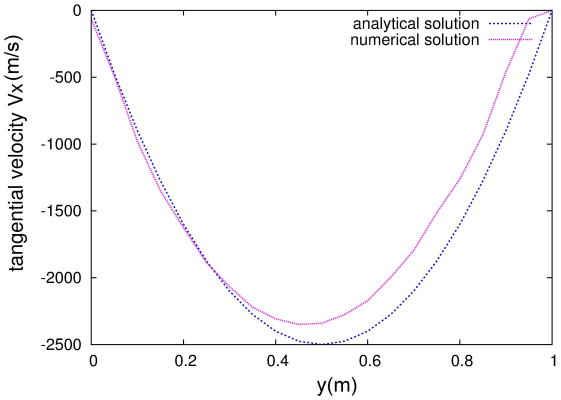

Figure 4.29: Comparison between analytical solution and numerical solution of Stokes velocity for $k = 10^{-14}\mathrm{m}^2$, $\mu = 1$, $\alpha = 1$ and $p = 10^5 Pa$, 2D parallel flow.

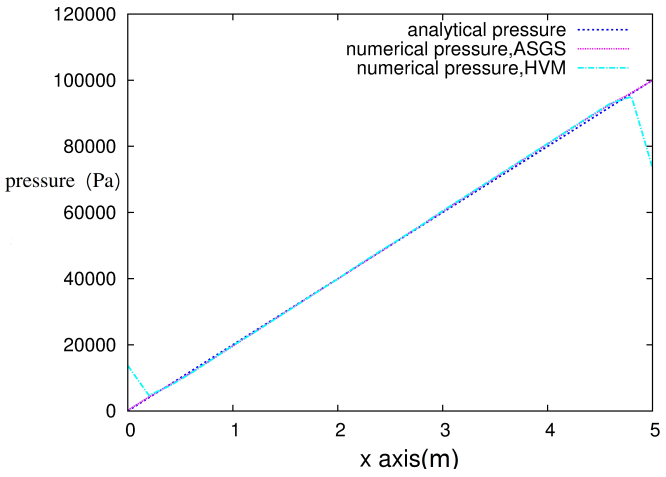

Figure 4.30: Comparison between analytical pressure, numerical pressure obtained with ASGS method and numerical pressure obtained with P1+/P1-HVM method for parallel flow with $k = 10^{-14}\mathrm{m}^2$, $\mu = 1$, $\alpha = 1$ and $p = 10^5 Pa$.

3D extension

For the case of parallel flow, 3D simulations are conducted. Geometry and boundary conditions are the same as in 2D case, extruded along the **z** axis. We use a structured mesh in this case. Results for pressure are presented in Figure 4.31 and velocity in Figure 4.32 for $p_{ext} = 10^5 Pa$, $k = 10^{-14}\text{m}^2$, $\mu = 1 Pa.s$ and $\alpha = 1$. These results are in accordance with the results obtained for the 2D case. With ASGS method, the pressure does not show any problem on the boundary contrary to P1+/P1-HVM method, for which the pressure shows, as in 2D cases, some problems on the boundary.

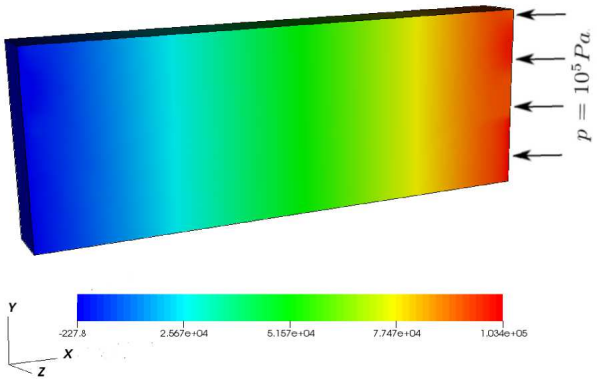

Figure 4.31: Isovalues of pressure for parallel flow with $k = 10^{-14}\text{m}^2$, $\mu = 1$, $\alpha = 1$ and $p = 10^5 Pa$.

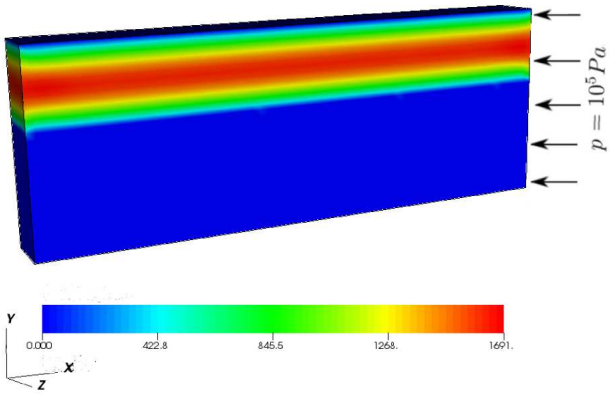

Figure 4.32: Isovalues of velocity for parallel flow with $k = 10^{-14}\text{m}^2$, $\mu = 1$, $\alpha = 1$ and $p = 10^5 Pa$.

4.4.4 Interface capturing

As explained in Chapter 3, Section 3.5, we have two methods to compute the surface integral which appears due to the presence of BJS condition on the interface $(\frac{\alpha\,\mu}{\sqrt{k}}\int_{\Gamma}(\mathbf{v}.\tau).(\mathbf{w}.\tau))$. In this section, we will show the results of the flow parallel to the interface in 3D case, with the following physical parameters: $\mu = 1Pa.s$, $k = 10^{-14}\mathrm{m}^2$, $p = 10^5 Pa$ and $\alpha = 1$ in a domain $\Omega_s = [0;5]\times[1;2]\times[0;0.3]$ and $\Omega_d = [0,5]\times[0,1]\times[0;0.3]$ In this case, we compute successfully the surface integral by exact integration and by turning it into a volume integral. Figure 4.33 shows a zoom on the mesh used in this test, the interface which cuts the elements and ensures that tests are conducted on coarse meshes. Figure 4.34 shows a comprarison between the analytical solution of the velocity, the numerical solution obtained by turning the surface integral into a volume integral and the numerical solution obtained by exact integration of the surface integral on the interface. Figure 4.34 shows that we have more accurate results when we compute exactly the integral on the interface. Let us note that the difference between analytical solution and numerical solution is due to the elements on the interface which belong to Stokes and Darcy's domains at the same time.

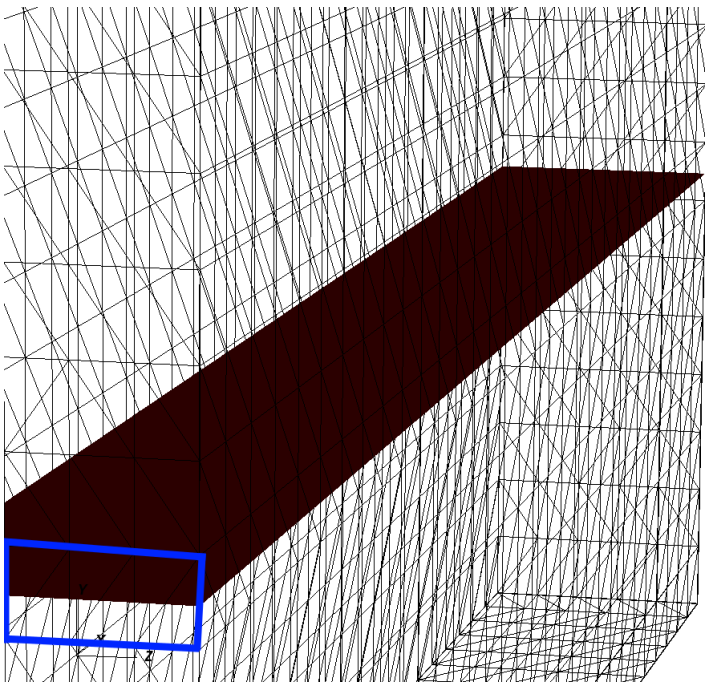

Figure 4.33: Part of the computational domain of the interface-capturing test and zoom on the interface which cuts the elements

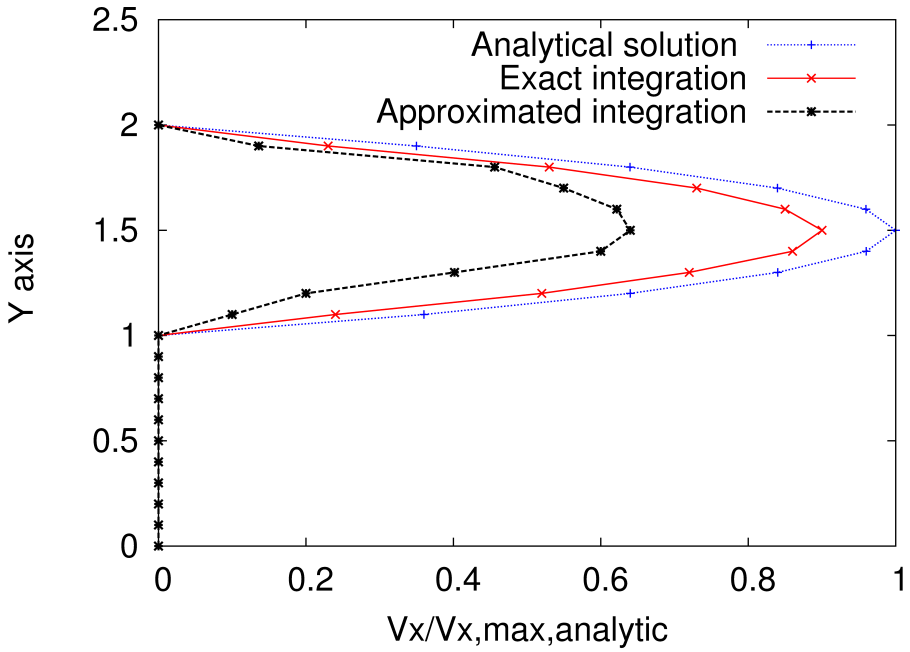

Figure 4.34: Comparison of numerical solutions for monolithic approaches for a parallel flow, with analytical solution. Velocity is normalized by the maximum analytical velocity ($\mathbf{v_{x,max,analytical}}$). Interface reconstruction and Dirac approximation for the surface integral are presented, $k = 10^{-14}\text{m}^2$, $p_{ext} = 1Bar$, $\mu = 1Pa.s$ and $\alpha = 1$

4.4.5 Inclined interface

The case of an inclined Stokes / Darcy interface is now considered in order to evaluate the proposed monolithic approach when the interface is not parallel to some mesh element edges. This test allows again to verify the influence of the BJS condition on the tangential velocity. The mesh of the domain which is the unit square is described in Figure 4.35 (a) with the Stokes domain size H_s which varies from 0.8 (for $x = 0$) to 0.2 (for $x = L = 1$). Prescribed boundary conditions in velocity and pressure are shown in Figure 4.35 (b). We set: $\mu = 1$ Pa.s, $k = 10^{-11}$ m^2, $\alpha = 1$ and $p_{ext} = 10^5$ Pa. Figure 4.36 shows the pressure field obtained with the presented monolithic approach. In Figures 4.37(a) and 4.37(b), we compare the distribution of velocity obtained with both ASGS method and the P1+/P1-HVM method. It is clear that also in this case of inclined interface, the ASGS method shows an improved robustness compared with P1+/P1-HVM method, especially in ensuring the continuity of normal velocity and reducing the oscillations around the interface.

To demonstrate the validity of "ASGS" method in this case, we compare the test of inclined

interface between monolithic approach and decoupled approach for a very low permeability $10^{-15}\mathrm{m}^2$, with $\alpha = 1$, $\mu = 1Pa.s$ and $p_{ext} = 10^5 Pa$. Pressure p in the middle of the domain ($x = 0.5$) is plotted against position across the thickness in Figure 4.38(a) and the velocity $\mathbf{v}$ in the middle of the domain ($x = 0.5$) is plotted in Figure 4.38(b) for both approaches. As we can see, there are no oscillations and the normal velocity is continue through the interface. A good correlation can be noticed for both studied methods with a maximum difference on the y velocity component $\Delta = 0.19m/s$ (Figure 4.38(b)).

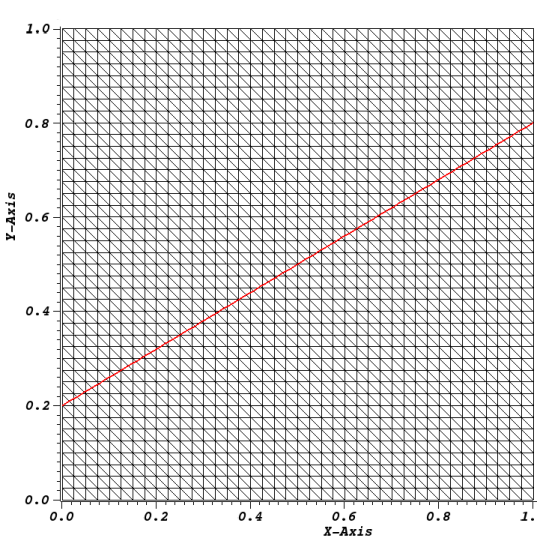

a)

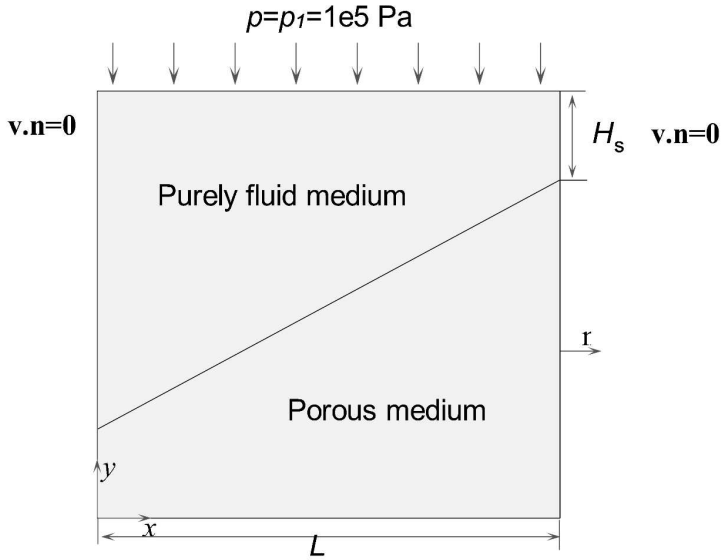

b)

Figure 4.35: (a) The mesh of the inclined domain with the interface (in red) which cuts the elements, (b) Computational domain with inclined interface and boundary conditions

Figure 4.36: Isovalues of pressure (Pa) for ASGS method for $k = 10^{-11}\mathrm{m}^2$

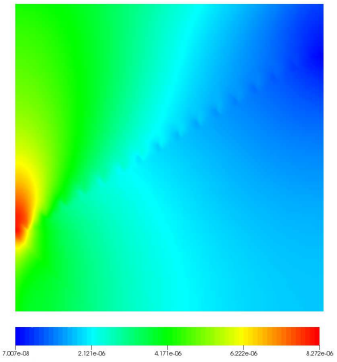

(a) ASGS

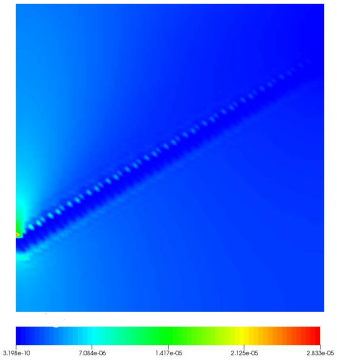

(b) P1+/P1-HVM

Figure 4.37: 2D simulation for the 2D flow with inclined interface, ($k = 10^{-11}\mathrm{m}^2, \alpha = 1, \mu = 1Pa.s, P_{ext} = 1bar$), magnitude-velocity ($m/s$)

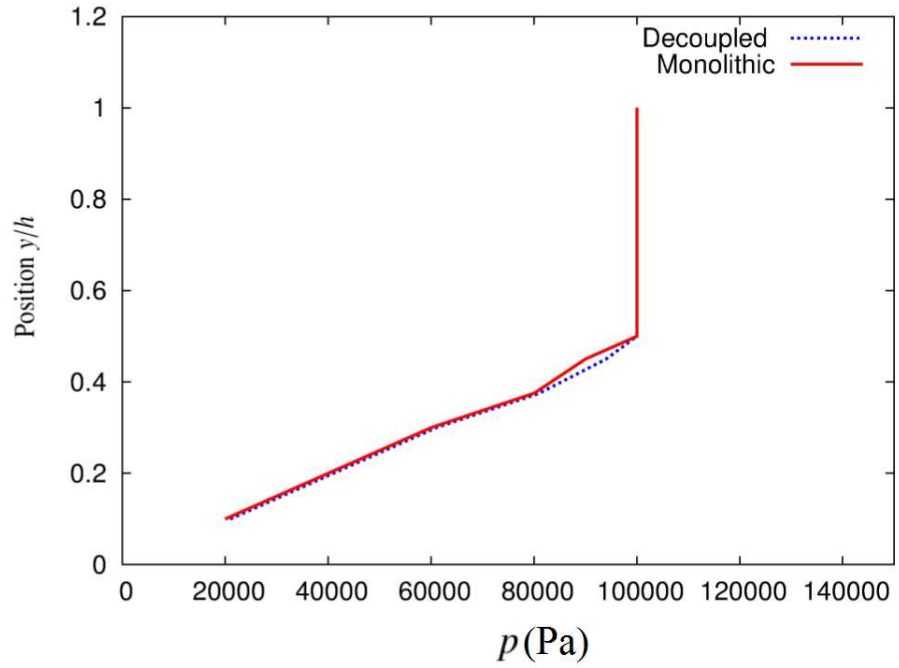

(a) Pressure

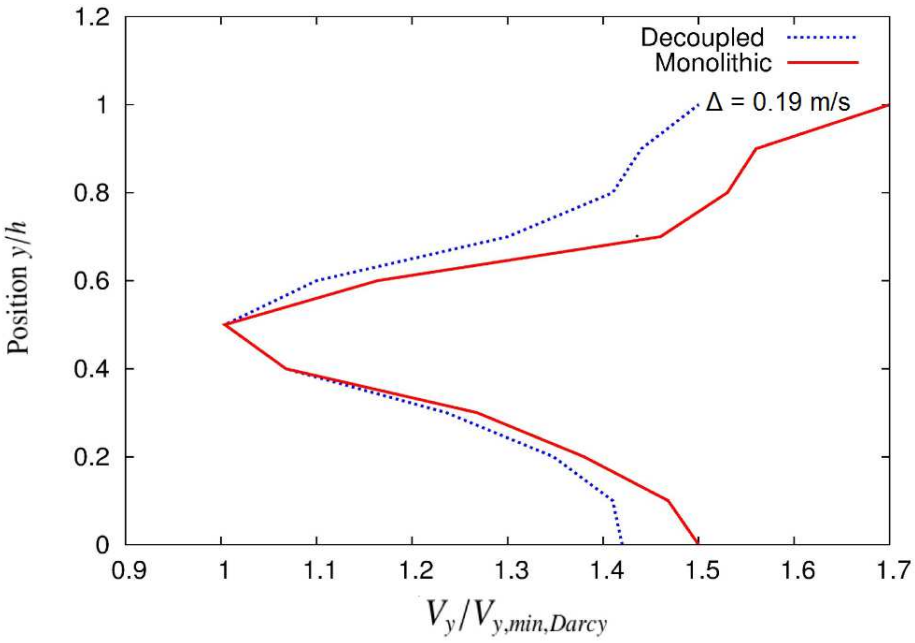

(b) Velocity

Figure 4.38: Profil of pressure and velocity in the middle of the domain, $x = 0.5m$, $k = 10^{-11}\mathrm{m}^2$, $p = 1bar$, $\mu = 1Pa.s$ and $\alpha = 1$

4.5 Complex geometries

The Stokes-Darcy coupled problem is used here to simulate stationary regimes in complex composite pieces elaborated through infusion processes [Celle *et al.* 2008], [Wang *et al.* 2010]. Previously, the mathematical models for this simulation were derived, and the monolithic approach where analytical solution is available, i.e tests with simple geometry, was validated. But in infusion processes, pieces with complex geometries have to be considered. In this section coupled problems for 2D and 3D pieces with complex geometries are investigated.

4.5.1 Curved interface, 2D simulation

A case deriving from the parallel flow is first considered, with a 2D curved interface (Figure 4.39) with $k = 10^{-14}$ m^2, $\mu = 1$ Pa.s, $\alpha = 1$ and for a Stokes region thickness of $\frac{1}{10}$ of the total thickness.

Initialization of the distance function (level set function)

The technical difficulty in the case of curved interface is that the interface which separates Stokes and Darcy domains does not have a simple geometrical shape. To initialize the level set function, we have to compute the smallest distance from every node to the segments that constitute the interface.

Let us consider M_j the nodes of the domain and $[A_i, B_i]$ the set of the segments that define the zero level set. Furthermore, we consider M'_j the orthogonal projection from M_j on (A_i, B_i). Two cases are possible, if M'_j belongs to the segment $[A_j, B_j]$, the distance is $\overline{M_j M'_j}$. Else if M'_j is outside the segment, the distance is the minimum between $\overline{M_j A_i}$ and $\overline{M_j B_i}$ (see Figure 4.40). After computing the distance from a node M_j to any segment $[A_i, B_i]$ which constitutes the interface, we take the minimum of all these distances and initialize our distance function (level set function). Figure 4.41 shows the isovalues of this level set function.

Numerical results

Results for pressure field are presented in Figure 4.42, while the velocity field is shown in Figure 4.43. The results obtained for pressure and velocity are in correlation with those obtained for the parallel and perpendicular flow cases. Note that the normal to this interface involved in the BJS coupling condition is simply calculated through the gradient of the distance function describing the interface: $\mathbf{n} = \nabla\phi / \|\nabla\phi\|$. Despite this curved interface, velocity and pressure fields computed with the monolithic approach do not exhibit any spurious oscillations.

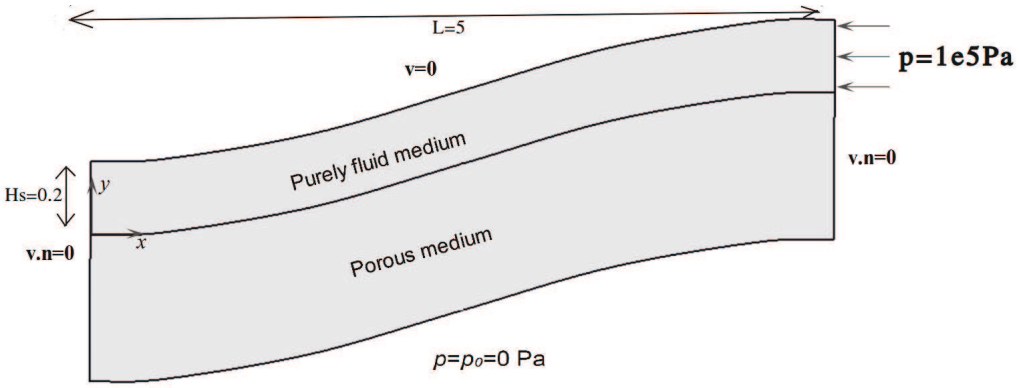

Figure 4.39: Computational domain with curved interface

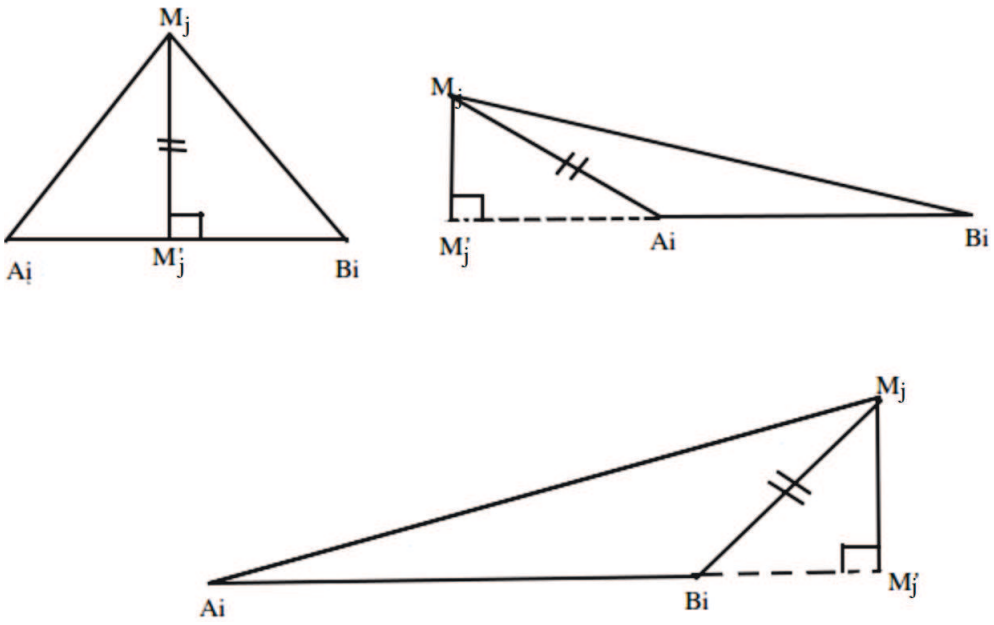

Figure 4.40: Computation of the smallest distance between a node M_j and the segments of the zero level set

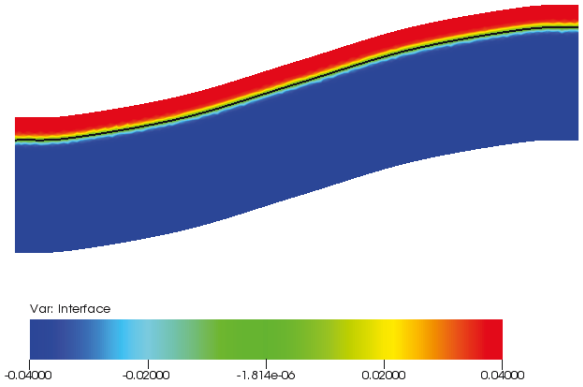

Figure 4.41: Isovalues of the level-set function between Stokes and Darcy, the black curve represents the isovalue zero of the level-set function (Stokes-Darcy interface).

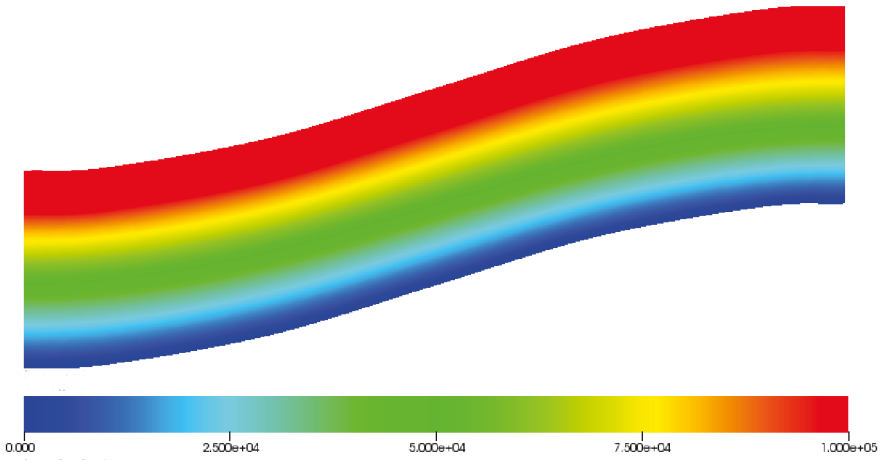

Figure 4.42: Isovalues of pressure, 2D flow with curved interface

4.5.2 3D simulation

4.5.2.1 Flow in a 3D regular geometry with an injection inlet

The computational domain has dimensions of $56mm \times 292mm \times 20mm$ with an injection channel (Figure 4.44). The boundary conditions prescribed for this simulation are a normal stress on the inflow part of the domain, and a null pressure over the bottom surface of Darcy's region. Boundary conditions of zero velocity and zero normal velocity are imposed on Stokes and Darcy domains respectively, except the bottom surface which acts like a vent.

Results for velocity field are presented in Figure 4.44 and results for pressure are presented

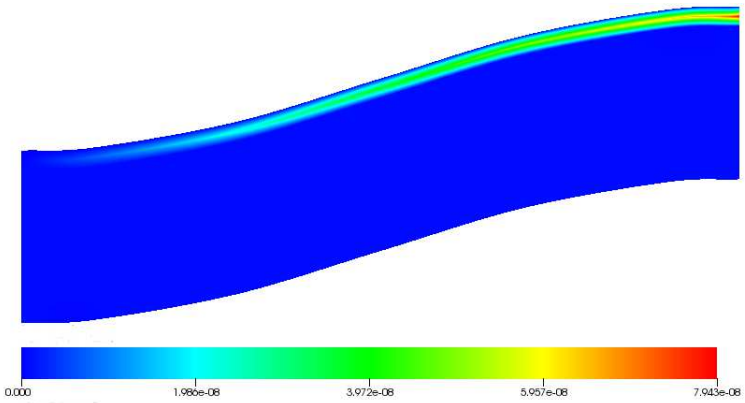

Figure 4.43: Isovalues of velocity, 2D flow with curved interface (m/s)

in Figure 4.45. Physical parameters in these simulations are $k = 10^{-14}\mathrm{m}^2$, $p = 10^5 Pa$ and $\mu = 1Pa.s$.

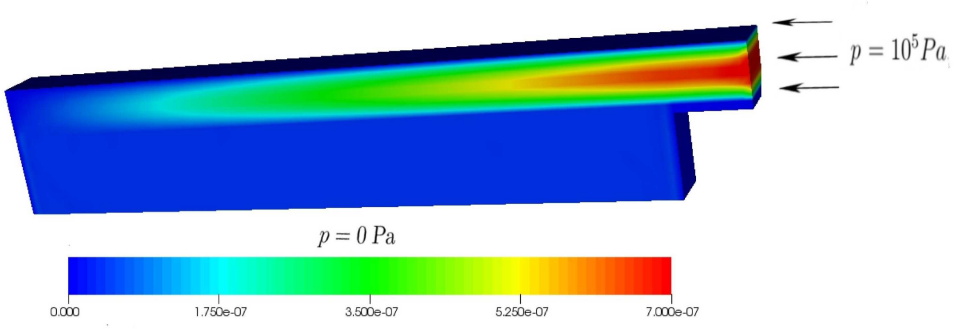

Figure 4.44: Isovalues of pressure (Pa), 3D flow on a regular piece with injection channel

4.5.2.2 3D simulation with curved interface

For the 3D flow in a piece with complex geometry (Figure 4.46), a simulation is considered for $k = 10^{-9}\mathrm{m}^2 \mu = 1Pa.s$ and $\alpha = 1$. Geometry, mesh and boundary conditions are presented in Figure 4.48 (a). Geometry consists in two layers, a layer of thickness 2 mm, that corresponds to the Stokes region, and layer of thickness $10mm$ that corresponds to Darcy region. For the boundary conditions, pressure is prescribed on the right hand side in Stokes region, and vent is present on the bottom of Darcy region. Also conditions of zero velocity for Stokes region and zero normal velocities for Darcy region are prescribed for all the other boundaries of the piece

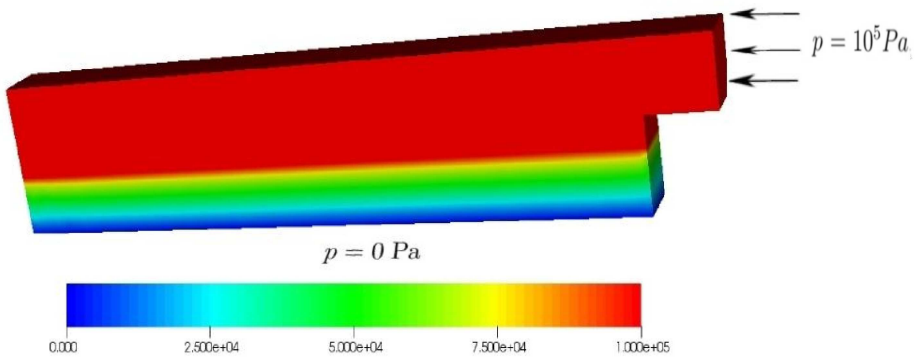

Figure 4.45: Isovalues of velocity (m/s), 3D flow on a regular piece with injection channel

except the bottom surface. Note that the normal velocity is enforced on the curved boundary by using a nodal penalty technique [Bruchon *et al.* 2009]. Similar to the 2D case, the difficulty in this case is that the interface which separates Stokes and Darcy domains does not have a simple geometrical shape. To overcome this problem, we define it by a set of points A_i and we compute the minimal distance between each node of the mesh and the points A_i. Figure 4.46 shows in red the isovalue zero of the level set function (Γ) and Figure 4.47 shows the isovalues of this level set function.

The stationary case, presented in Figures 4.48 (a) and 4.48 (b), illustrates the capability to represent realistic geometries. Presented results for pressure field, as well as results for velocity field are in accordance with expected results.

One of the advantages of the method in this case, is that the geometry can be meshed "independently" of the interface position. However, from a practical point of view, we have choosen here to define the interface from nodes coordinates.

One will have noticed that velocity ranges in the cases presented can vary. This can be due to the effect of the regime (transverse flow, or parallel flow, or mixed), but more certainly due to the ratio of the Stokes thickness with respect to the Darcy thickness. This will be further investigated in chapter 6.

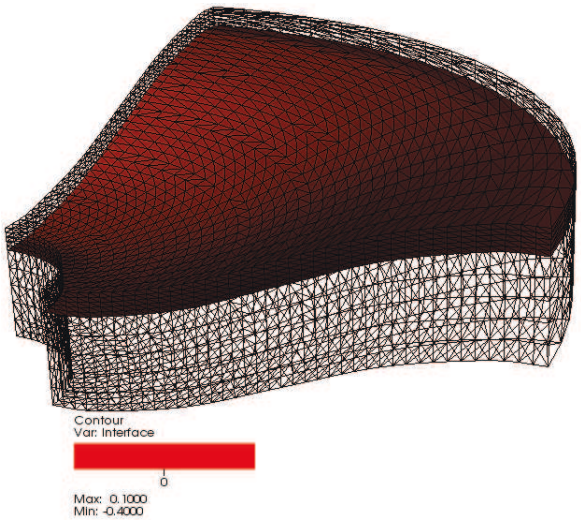

Figure 4.46: The isovalue zero of the level-set function between Stokes and Darcy

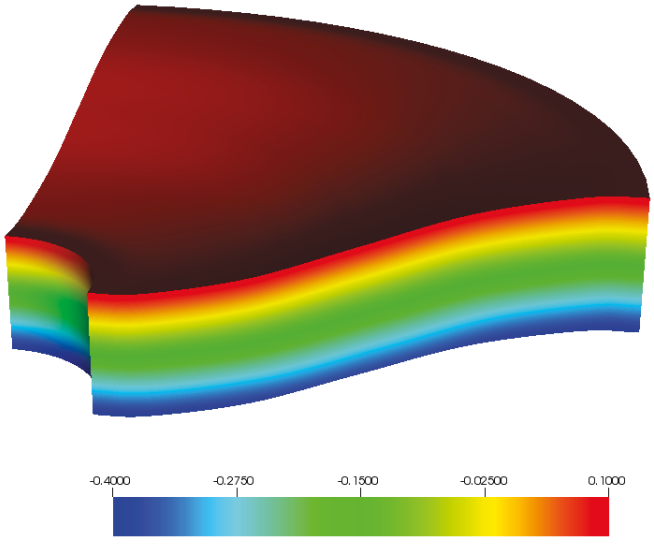

Figure 4.47: Isovalues of the level-set function between Stokes and Darcy.

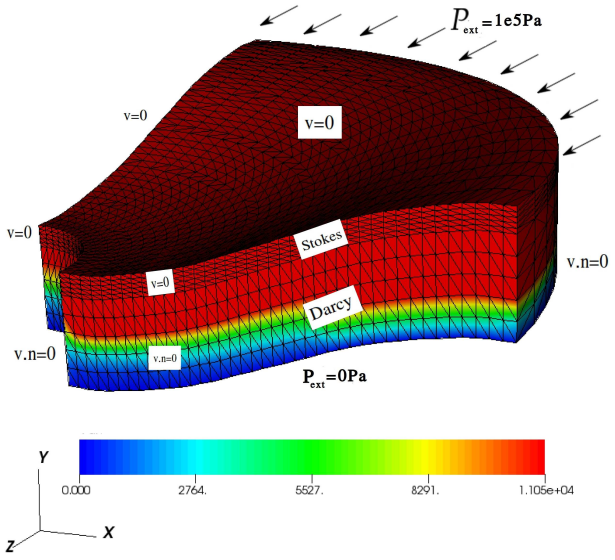

(a) Pressure (Pa)

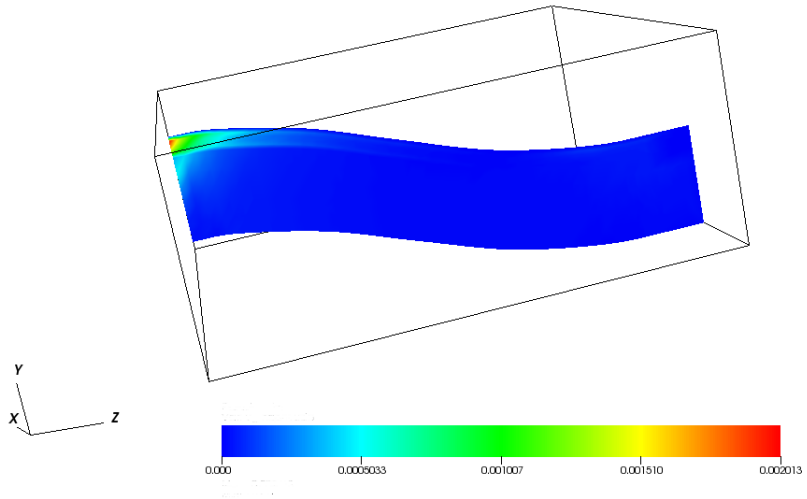

(b) Cutting plane of the velocity, magnitude velocity (m/s)

Figure 4.48: 3D simulation for the flow in 3D complex piece with curved interface, $(k = 10^{-9}\mathrm{m}^2, \alpha = 1, \mu = 1Pa.s, P_{ext} = 1bar)$

4.6 Conclusions

Manufactured solutions were conducted to study the convergence of the ASGS method for Stokes, Darcy and Stokes-Darcy coupled problem. The given rates of convergence are optimal and correspond to the theoretical orders of convergence. In addition, numerical simulations of a flow perpendicular to the interface, a flow parallel to the interface, and an inclined interface flow were presented to verify both the continuity of normal velocity and the BJS condition enforcement. These tests were conducted for permeability down to $10^{-15}\mathrm{m}^2$, different values of fluid viscosity and thickness of the fluid distribution medium. Also it was shown that the methods can be used for more complex geometries, which is essential in the sense of industrial applications.

Results obtained with "ASGS" method were compared with the results obtained with "P1+/P1-HVM" method and showed how ASGS method manages all the problems generated with $P1+/P1-HVM$ [Pacquaut *et al.* 2012] method. Furthermore, the monolithic approach were compared with the decoupled approach in a recent submitted article [2]. The results are comparable in an industrial context, but meshes are simpler in the monolithic approach because only one single mesh is considered contrary to the decoupled approach where one has to define two meshes and the interface for each case. Also the monolithic approach is more efficient in term of computation time. Finally, it was shown that the method could be used for more complex geometries and with a wide range of permeability, which is essential in the industrial applications.

2. Stokes/Darcy coupling in severe regimes: monolithic approach versus decoupled approach. L.Abouorm, R.Troian, S.Drapier, J.Bruchon, N.Moulin

Chapter 5

Interface capturing and large deformation of preforms

Contents

5.1 Introduction

To reach the essential goal of this work, the "simulation of resin infusion processes", we have to develop a numerical method able to follow the evolution of the fluid front during its infusion into the fluid distribution medium and preforms. In the first part of this chapter we will describe the movement of "interfaces", where "interface" is the current word used to design the boundary between two different physical domains. In our simulations, the fluid modelling problem deals with two interfaces, one between air and resin and one between Stokes and Darcy. This second interface moves also because preforms undergo large deformations. Consequently, these deformations have to be taken into consideration in the modelling of processes. The second part of this chapter is devoted to take into consideration the deformation of preforms. For this reason, we will describe in this chapter the Lagrangian updated formulation used to deal with these deformations. In the third part, we will focus on the behavior of wet and dry preforms during their deformations taking into consideration that preforms have a non linear elastic behavior and that fluid will modify the wet preforms response also.

5.2 Interface capturing

5.2.1 Monitoring of interfaces

In this section, we will detail the most popular numerical methods used in literature to describe moving interfaces. There exist two main descriptions: the Lagrangian description and the Eulerian description.

5.2.1.1 Lagrangian description

In Lagrangian description of fluid flow, individual fluid particles are marked, and their positions, velocities $\cdots$ are described as a function of time. Interface tracking methods based on Lagrangian description are called "front tracking" methods. They can be divided into three categories with increasing flexibility and computational complexity. These are surface tracking methods, volume tracking methods and Lagrangian methods.

Surface tracking methods

Surface tracking methods are specified by an ordered set of marker points located on the interface [B.J.Daly & W.E.Pracht 1968]. Each marker point is moved by the velocity of the physical problem. Between these points, surface is approximated by an interpolant, usually

a piecewise polynomial. The marker points may be represented by the distance from some reference surface: some straight segments, defined by a height function (Figure 5.1 a)) or by a parametric interpolant (Figure 5.1 b)). This method permits to determine the position of the interface with high precision in simple cases. In addition, the interface location and orientation are known at each time step. But, this method presents many disadvantages:

- this method fails when interface geometry becomes complex.
- the interface position is stored and dynamically updated, in addition, one has to make regular operations to redistribute markers to ensure their a good distribution of the markers on the interface.
- these operations become more and more complicated in 3D cases.

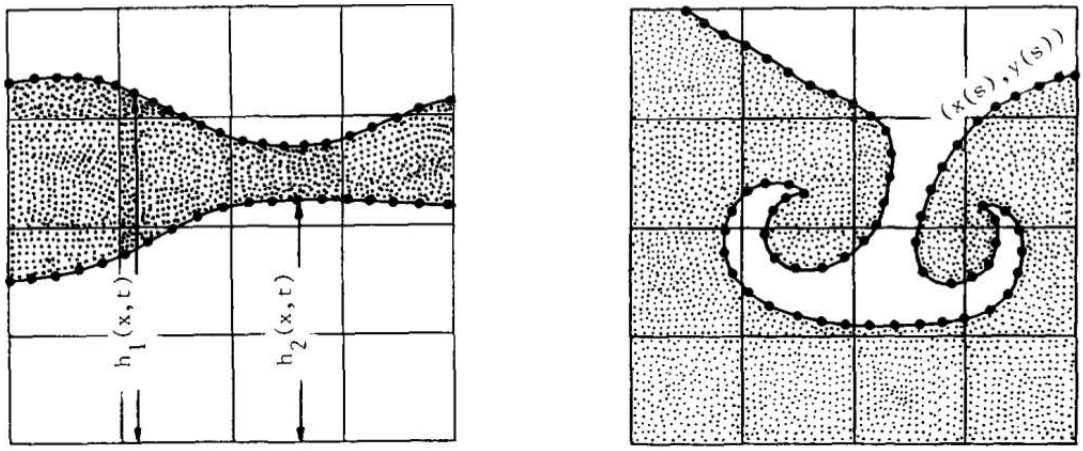

a) b)

Figure 5.1: (a) definition of height function and (b) parametric interpolant [Hyman 1984]

Volume tracking method

The volume tracking method has been developed by Harlow and Welch [F.H.Harlow & J.E.Welch 1965] in 1965. An example of the use of this method is Marker and Cell (MAC). It consists in distributing the markers in the fluid to be followed. These markers move through a fixed grid, their motion is given by the differential Equation (5.1)

$$\frac{dx_n}{dt} = \mathbf{v_n}(x_n, t) \tag{5.1}$$

where x_n is the position vector of the marker n at the time t and $\mathbf{v_n}$ is the velocity at this point. This differential equation is solved using an Euler explicit scheme for example:

$$x_n^{t+\Delta t} = x_n^t + \Delta t \mathbf{v_n}(x_n, t) \tag{5.2}$$

where Δt is the time step. This method presents many disadvantages:

- we cannot resolve details of the interface smaller than the mesh size.
- it is expensive in computer time and memory.

Lagrangian method

In the Lagrangian method, the grid follows the fluid motion. This method permits to represent explicitly the interface as a set of segments (2D) or a set of faces (3D). However, a remeshing operation is necessary to improve the quality of elements since they can be strongly deformed during the movement of the interface. This operation can be time and memory consuming and causes sometimes a loss of informations during the transfer of fields from a mesh to another. Hence, this method is difficult to use in complex flows involving large distortions of the interface.

5.2.1.2 Eulerian description

As we have seen that in the methods based on a Lagrangian description, the grid is adaptive, the points on interface are convected by transport equation and a new interface is found by fitting a curve through the advected points. On the contrary, with an Eulerian description, as we will detail in the following section, the grid is fixed and we have to introduce a new field to describe two different domains on either side of the interface (Level-set function or volume fraction). In these two cases, the field is convected by a transport equation(5.3):

$$\frac{\partial \phi}{\partial t} + \mathbf{v}.\nabla\phi = 0 \tag{5.3}$$

where $\mathbf{v}$ is the velocity computed from the physical problem. There exist two types of such methods, "Volume Of Fluid" methods where the function ϕ which separates the two domains is discontinuous, and the "Level-set" method in which the function ϕ is continuous.

Volume of fluid method (VOF)

The method was introduced by Hirt and Nichols in 1981 [C.W.Hirt & B.D.Nichols 1981]. The philosophy of this method consists on an implicit representation of the interface. A fraction (C), or color function is defined to indicate the local fraction of the mesh that is filled with a particular phase, *i.e* the fraction of the mesh-cell that is filled. Basically, when the element (cell) is empty, with no fluid inside, the value of C is zero, when the element (cell) is fully filled, $C = 1$, and when the interface cuts the element (cell), then $0 < C < 1$. The geometry of the interface can be reconstructed from the values of the color function C, and there are several schemes to perform this interface reconstruction:

SLIC (Simple Line Interface Calculation) [W.Noh & P.Woodward 1976]:
The SLIC algorithm rebuilds the front by defining simple lines (in 2D) or planes (3D) inside the cells. These straight lines are parallel to one of the coordinate directions and their direction and position are deduced from the values of the volume fraction of liquid in the cells in a certain nighbourhood of the considered element. Figure 5.2 shows a schematic representation of the original geometry and Figure 5.3 (a) shows the reconstruction obtained by using the SLIC method for x direction and Figure 5.3(b) shows the reconstruction for y direction.

Hirt-Nichols [C.W.Hirt & B.D.Nichols 1981]: Like the SLIC method, the interface is reconstructed using straight lines in 2D (planes in 3D) parallel to the coordinate directions. The difference is that the interface is computed by considering nine-cell neighbourhood. Figure 5.2 represents the original geometry and Figure 5.4 (a) shows the reconstruction obtained by using the Hirt-Nichols method.

Young method [D.L.Youngs 1982]: This method uses a more accurate interface reconstruction algorithm than SLIC and Hirt-Nichols method. An orientation β of a line segment in $2D$ (or plane in $3D$) cuts the element (cell) in such a way that the fractional fluid volume (the value of the color function) does not change. Figure 5.2 shows a schematic representation of the original geometry and figure 5.4 (b) shows the reconstruction obtained by using the Young's method.

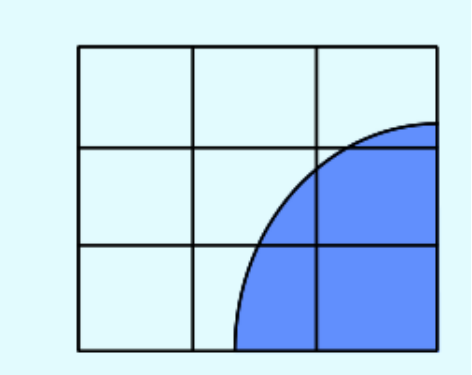

Figure 5.2: Actual geometry [M.Rudman 1997]

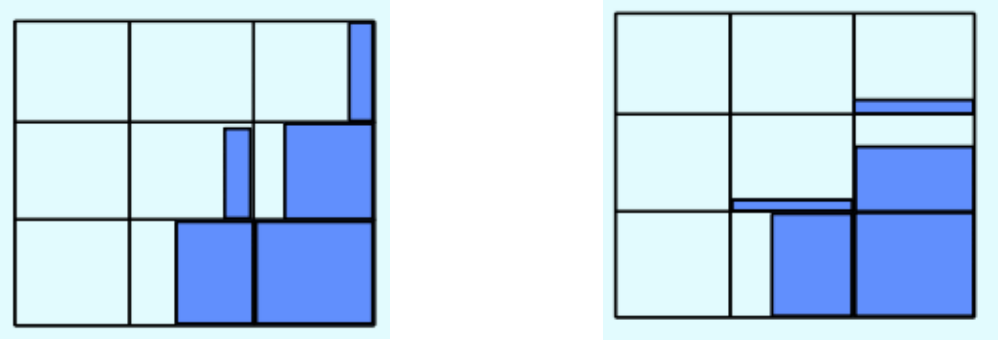

a) b)

Figure 5.3: (a) SLIC (x) and (b) SLIC (y)

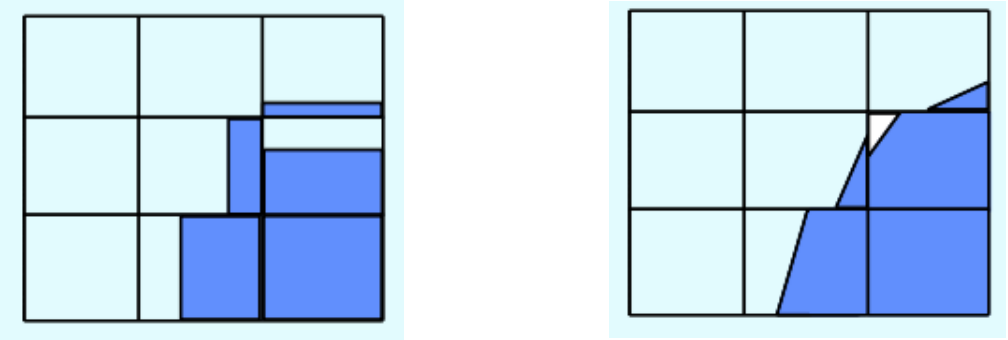

a) b)

Figure 5.4: (a) Hirt-Nichols and (b) Young-VOF

Level set method

The level set method was introduced by Osher and Sethian [S.Osher & J.A.Sethian 1988],

[J.A.Sethian 1999]. It has become popular in many disciplines such as image processing, computational geometry, optimization and computational fluid dynamics. The level set method represents a closed curve Γ using a higher dimensional function ϕ, called the level set function, and such as

$$\Gamma(t) = \{(\mathbf{x}) \,|\, \phi(\mathbf{x}, t) = 0\}$$

ϕ is assumed to take positive values inside the region delimited by Γ and negative values outside. The advantage of the level set method lies in its performance to describe complex curves and complex surfaces on the fixed mesh without requiring a parametrization of these objects. Indeed, contrary to VOF methods, the interface is explicitly defined through the level set function. Moreover, with level set function, it is quite easy to follow the shapes that change of topology in $2D$ and $3D$ cases (coalescence or separation of interfaces). Furthermore, it is easy to compute geometrical quantities such as the curvature or the normal vectors associated with the interfaces. The level set function is convected by the velocity of the physical problem which can depend on position, time and geometry of the interface [S.Osher & R.P.Fedkiw 2001]. The disadvantage of the level set method is related to the volume conservation which cannot be ensured by transporting ϕ while VOF methods ensure a volume conservation. For that, a special care has to be paid to conserve the volume (Section 5.2.2.3).

5.2.1.3 Choice of the method

The fluid mechanics and the large distortions of interfaces in liquid resin infusion processes prevent us to use methods based on a Lagrangian description of the fluid front. Therefore, we will choose a method based on an Eulerian description. VOF approaches do not allow to have a precise description of the interface. Moreover, it is difficult to have a good estimation of the curvature and of the normal. Eventually, with this method, we choose a level set method which will offer a good management of the topological changes, and access to the geometrical properties. In the next section, we will detail the level set method, used to simulate the moving flow fronts in resin infusion processes.

5.2.2 Interface capturing with level set method

Let $\Omega \subseteq \mathrm{R}^m$ be the bounded domain such that $\Omega = \Omega_f \cup \Omega_a$ and $\Gamma_{fa} = \Omega_f \cap \Omega_a$ where a denotes the air and f denotes the fluid domain. To define the interface Γ_{fa} which separates Ω_a and Ω_f, we define a level-set function ϕ which is a smooth function given by Equation (5.4).

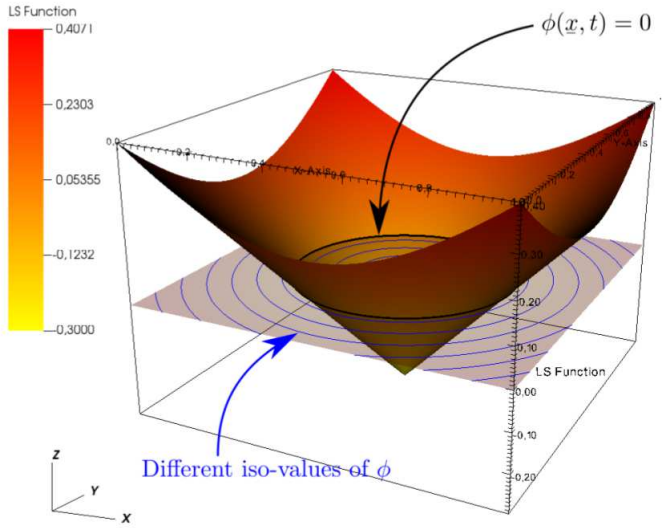

Figure 5.5: Level set function

$$\phi(\mathbf{x},t) = \begin{cases} \underset{p\in\Gamma}{min}||\mathbf{x}-p||, & \text{if} \quad \mathbf{x} \in \Omega_f \\ -\underset{p\in\Gamma}{min}||\mathbf{x}-p||, & \text{if} \quad x \in \Omega_a \end{cases} \tag{5.4}$$

where $\underset{p\in\Gamma}{min}||\mathbf{x}-p||$ is the Euclidean distance from any point x to the interface Γ_{fa}. The level set function is smooth, continuous and its gradient is unitary $||\nabla\phi|| = 1$.

Figure 5.5 shows the level set function corresponding to a circle of radius $R = 0.3$ centered in $x = 0.5$ and $y = 0.5$. The z axis represents the values of ϕ. Figure 5.6 represents the discretized linear function ϕ_h which is the distance between every node and the isosurface Γ_{fa}.

5.2.2.1 Transport equation

The interface evolution is governed by the transport Equation (5.5). Particular boundary conditions must be taken into consideration, we have to impose an initial condition at time $t = 0$, $(\phi(x, t = 0) = \phi_0(x))$ and a boundary condition on the inflow boundary $\partial\Omega^{-1}$ $(\phi(x,t) = g(x,t))$. The inflow boundary is defined by $\partial\Omega^- = \{x \in \partial\Omega \,|\, \mathbf{v}.\mathbf{n} < 0\}$. Then, we have to solve the following problem:

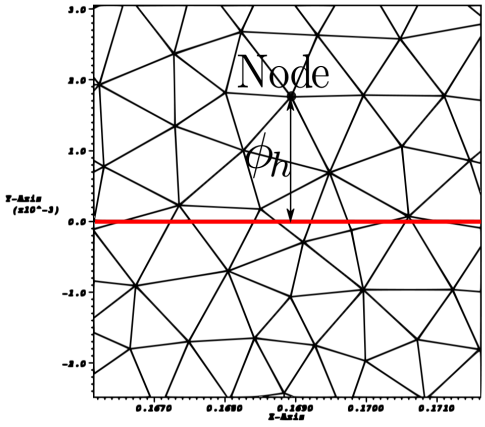

Figure 5.6: Discretized level set function ϕ_h

$$\begin{cases} \dfrac{\partial \phi}{\partial t} + \mathbf{v}.\nabla\phi &= 0 & \forall (x,t) \in \Omega \times [0,T] \\ \phi(x, t=0) &= \phi_0(x) & \forall\, x \in \Omega \\ \phi(x,t) &= g(x,t) & \forall\, x \in \partial\Omega^-, \forall\, t \in [0,T] \end{cases} \tag{5.5}$$

Some difficulties are related to the use of the level set method. First, we have to compute the values of ϕ_0, this may not be easy, especially for complex geometries. Second, we have to define precisely the function $g(x,t)$ on the inflow boundary $\partial\Omega^-$. To simplify the choice of this function, we propose to take $g(x,t) = \phi(x, t - \Delta t)$.

5.2.2.2 Geometrical properties of level set function

The level set function allows us to compute geometrical informations of the interface, the normal and curvature. Normal $\mathbf{n}$ can be computed as $\mathbf{n} = \frac{\nabla\phi}{||\nabla\phi||}$, $||\nabla\phi|| = 1$ if $\nabla\phi$ is close to the interface and the curvature is computed as $\kappa = div\mathbf{n}$.

5.2.2.3 Reinitialization step

The resolution of Equation (5.5) does not ensure that $||\nabla\phi|| = 1$. When we convect the level set function ϕ with velocity $\mathbf{v}$, function $\phi(t + \Delta t)$ can present steep gradients close to the interface, leading to numerical problems (degeneration of the interface). To avoid this, we

perform a reinitialization process to keep $||\nabla\phi|| = 1$. It consists on iteratively correcting the level set function ϕ in order to recover $||\nabla\phi|| = 1$ [T.Coupez 2006], [O.Basset 2006].
The reinitialization of ϕ consists in finding a new function φ with the same zero level set (which does not move) but with $||\nabla\varphi|| = 1$, by solving a Hamilton-Jacobi equation. We use this new function $\varphi(x,t)$ until the next round of reinitialization. A virtual time τ is introduced:

$$\begin{array}{rcl} \dfrac{\partial\varphi}{\partial\tau} + sign(\phi)(||\nabla\varphi|| - 1) & = & 0 \\ \varphi(\mathbf{x}, \tau = 0) & = & \phi(\mathbf{x}, t) \end{array} \tag{5.6}$$

where $sign(\phi)$ is a signed function defined by:

$$sign(\phi) = \begin{cases} 1 & \text{if} \quad \phi > 0 \\ -1 & \text{if} \quad \phi < 0 \\ 0 & \text{if} \quad \phi = 0 \end{cases} \tag{5.7}$$

If $\phi = 0$, the sign function $sign(\phi)$ is zero, and consequently Equation (5.6) is reduced to $\frac{\partial\varphi}{\partial\tau} = 0$ on the interface Γ. Position of the interface (isovalue zero) is then preserved during the reinitialization step. The sign function is discontinuous, for this reason, a smooth sign function is defined as $sign(\phi) = \frac{\phi}{\sqrt{\phi^2 + h_K^2}}$ [M.Sussman *et al.* 1994] where h_K is the size of the element K. For practical purpose, Equation (5.6) can be written as an advection equation:

$$\begin{array}{rcl} \dfrac{\partial\varphi}{\partial\tau} + \mathbf{v_r}\nabla\varphi & = & sign(\phi) \\ \varphi(\mathbf{x}, 0) & = & \phi(\mathbf{x}, t) \end{array} \tag{5.8}$$

where $\mathbf{v_r}$ is the unit velocity normal to the interface, defined by $\mathbf{v_r} = sign(\phi)\frac{\nabla\varphi}{||\nabla\varphi||}$, because $||\nabla\varphi||^2 = \nabla\varphi \cdot \nabla\varphi$.
The weak formulation defined in Equation (5.8) is also stabilized using the SUPG method.

To summarize the level set method resolution, we present the reinitialized level set algorithm (Algorithm (1)).

In this algorithm, ϵ is the convergence criteria and τ^* is the time which corresponds to the steady state where $\frac{\partial\varphi}{\partial\tau} = 0$, and then $||\nabla\varphi|| = 1$. The reinitialization Equation should be solved until the steady state is reached $||\nabla\varphi|| = 1$. But, in practical cases, One will usually generate a maximum of 5 iterations of reinitialization which is sufficient to ensure the metric properties of the function φ around the interface.

Algorithm 1 Reinitialized level set algorithm

$t \leftarrow 0$
$\phi_0(\mathbf{x}, t=0) \leftarrow$ definition of the geometry of isovalue zero at $t=0$
while $t < T$ **do**
  $\mathbf{v} \leftarrow$ From the physical problem (Stokes-Darcy coupled problem)
  $\phi(\mathbf{x}, t+\Delta t) \leftarrow$ From Equation (5.3)
  while $(|||\nabla\varphi - 1|||) < \epsilon$ **do**
    $\varphi(\mathbf{x}, \tau=0) = \phi(\mathbf{x}, t+\Delta t)$
    $\varphi(\mathbf{x}, \tau) \leftarrow$ From Equation (5.6)
    $\tau \leftarrow \tau + \Delta\tau$
  end while
  $\phi(\mathbf{x}, t+\Delta t) \leftarrow \varphi(\mathbf{x}, \tau^*)$
  $t \leftarrow t + \Delta t$
end while

5.2.3 Numerical scheme to transport the level set function

In this section we will present the weak formulation of the transport equation, the spatial and temporal discretizations of the weak formulation and the reinitialization algorithm used to keep the property of distance functions ($||\nabla\phi = 1||$). Then, we will show with a simple test the importance of the choice of the time discretization scheme.

Weak formulation of the transport equation

The functionnal spaces used to establish the weak formulation of the transport equation are:

$$\begin{aligned} V^g &= \{q \in H^1(\Omega) \,|\, q = g \text{ on } \partial\Omega^-\} \\ V^0 &= \{q \in H^1(\Omega) \,|\, q = 0 \text{ on } \partial\Omega^-\} \end{aligned} \tag{5.9}$$

$H^1(\Omega)$ is the Sobolev space included in $L^2(\Omega)$ and $L^2(\Omega)$ is the space of square integrable functions.

$$\begin{aligned} L^2(\Omega) &= \{q, \int_\Omega q^2 \, d\Omega < \infty\} \\ H^1(\Omega) &= \{q \in L^2(\Omega) \,|\, \nabla q \in L^2(\Omega)^m\} \end{aligned} \tag{5.10}$$

To obtain the weak formulation of the transport equation, we have to multiply Equation (5.5) by a test function ϕ^*, this yields: Find $\phi \in V^g$ such that:

$$\int_\Omega \frac{\partial\phi}{\partial t} \phi^* \, dv \quad + \quad \int_\Omega \mathbf{v}.\nabla\phi \, \phi^* = 0, \ \forall\phi^* \in V^0 \tag{5.11}$$

Discretization of the weak formulation of transport equations

To solve numerically this problem, a finite element approximation has to be taken into consideration. This discretization involves the approximation of the level set function by ϕ_h and the discretization of the computational domain Ω.
We have also to construct V_h^g and V_h^0 the discretized spaces of V^g and V^0. The computation domain Ω is discretized using non necessarily structured mesh $\mathcal{T}_h(\Omega_h)$. The elements of $\mathcal{T}_h(\Omega_h)$ are triangles in 2D and tetrahedrons in 3D such that:

$$\Omega_h = \bigcup_{K \in \mathcal{T}_h(\Omega_h)} K$$

Then, the weak space-discretized formulation is:
Find $\phi_h \in V_h^g$ such that:

$$\int_{\Omega_h} \frac{\partial \phi}{\partial t} \phi_h^* dv + \int_{\Omega_h} \mathbf{v}.\nabla \phi_h \phi_h^* dv \quad = \quad 0, \forall \phi_h^* \in V_h^0 \tag{5.12}$$

Time discretization

The time discretization consists in decomposing the time interval $[0, T]$ into N intervals:

$$[0, T] = \bigcup_N [t_n, t_{n+1}]$$

and to discretize the time derivative operator using a specific numerical scheme. In this section, we will introduce the θ method which lead to three numerical schemes: explicit Euler scheme, implicit Euler scheme and Cranck Nicholson scheme.
If we use an explicit scheme, a criterion on the time step must be added to ensure the stability of the scheme. With this type of equation, we obtain the stability by using a CFL condition ("Courant-Friedrichs-Lewy"):

$$\frac{h_k}{\Delta t} > |\mathbf{v}| \iff \Delta t < \frac{h}{max|\mathbf{v}|}$$

This condition prevents the interface to progress of more than an element during a time step Δt.
This condition can also be written as:

$$\Delta t = cfl \frac{h}{max|\mathbf{v}|}$$

where cfl is a number between 0 and 1, the so called "number of Courant-Friedrichs-Lewy".

Next, we present the standard general θ method currently used.
The θ method applied to the time discretization leads to:

$$\frac{\phi(t_{n+1}) - \phi(t_n)}{\Delta t} \quad + \quad (\theta \mathbf{v} \cdot \nabla \phi(t_{n+1}) + (1-\theta)\mathbf{v} \cdot \nabla \phi(t_n)) \quad = \quad 0 \tag{5.13}$$

– If we choose $\theta = 1$, we obtain the implicit Euler scheme:

$$\frac{\phi(t_{n+1}) - \phi(t_n)}{\Delta t} \quad + \quad \mathbf{v} \cdot \nabla \phi(t_{n+1}) \quad = \quad 0 \tag{5.14}$$

– If we choose $\theta = 0$, we obtain the explicit Euler scheme:

$$\frac{\phi(t_{n+1}) - \phi(t_n)}{\Delta t} \quad + \quad \mathbf{v} \cdot \nabla \phi(t_n) \quad = \quad 0 \tag{5.15}$$

– If we choose $\theta = \frac{1}{2}$, we obtain the Cranck Nicholson scheme:

$$\frac{\phi(t_{n+1}) - \phi(t_n)}{\Delta t} + \frac{1}{2}\mathbf{v} \cdot \nabla \phi(t_{n+1}) + \frac{1}{2}\mathbf{v} \cdot \nabla \phi(t_n) = 0 \tag{5.16}$$

The Euler explicit scheme is widely used for its simplicity of implementation and its low cost in computation time. However, for complex simulations requiring high precision, the explicit Euler scheme is often insufficient and requires small Δt for stability. Euler implicit scheme and Cranck Nicholson scheme require solving a linear system and consequently require more computational effort in each step, but they are more accurate, stable for complex simulations and can be used for large time step. In our manuscript, we choose the Cranck Nicholson and the Eulers implicit schemes ($\theta = \frac{1}{2}$ and $\theta = 1$) to discretize the transport equation. These two schemes will be compared in Section 5.2.4. After introducing the time discretization in the weak formulation of the convection equation (Equation (5.12)), we get:

$$\begin{aligned} \int_{\Omega_h} \phi_h(t_{n+1})\phi_h^* d\Omega + \theta \Delta t \int_{\Omega_h} \mathbf{v} \cdot \nabla \phi_h(t_{n+1})\phi_h^* d\Omega \\ = \int_{\Omega_h} \phi_h(t_n)\phi_h^* d\Omega - (1-\theta)\Delta t \int_{\Omega_h} \mathbf{v} \cdot \nabla \phi_h(t_n)\phi_h^* \end{aligned} \tag{5.17}$$

with $\theta = \frac{1}{2}$ or $\theta = 1$. The order of convergence of the implicit Euler scheme is in $\mathcal{O}(\Delta t)$ and the order of convergence of the Cranck Nicholson scheme is in $\mathcal{O}(\Delta t^2)$.

SUPG stabilization

It is known that Galerkin methods work well for elliptical differential equations. However, when it is applied to other classes of differential equations, it is often found to yield "unstable" solutions, *i.e*, solutions that exhibit spurious oscillations. One of the first studies to successfully

apply a new finite element theory based on discretization for second order problems with significant first derivates, was the use of the "Petrov-Galerkin" methods introduced by Christie et al in 1976 in [I.Christie *et al.* 1976]. Since then, the Petrov-Galerkin methods have generally come to be known as "stabilized" formulations because they prevent the spatial oscillations and yield to stable solutions where the classical Galerkin method would behave badly. One of the most popular methods is the "Streamline Upwind Petrov Galerkin" method. The principle of the SUPG method is to add a diffusion term along the direction of the convection velocity $\mathbf{v}$. It consists in choosing the weighting functions of the weak form to be solved in a functional space different from the one of the shape functions. Here we choose to take the weighting function as [T.J.R.Hughes & A.N.Brooks 1979]:

$$\tilde{\phi}^{*}_{h|K} = \{\phi^{*}_{h|K} + \tau_k \mathbf{v} \cdot \nabla \phi^{*}_{h|K}\}$$

on each element $K \in \mathcal{T}_h$ where τ_k is given by [Ville *et al.* 2011]:

$$\tau_k = \frac{1}{2}\frac{h_k}{||\mathbf{v_K}||}$$

with h_k the mesh size and $\mathbf{v_K}$ the average velocity on the element K. Then, the weak discretized formulation of the transport equation stabilized with SUPG method can be written as:

$$\begin{aligned}
&\underbrace{\sum_K \int_K \phi_h(t_{n+1})\phi^{*}_h dv + \sum_K \theta\Delta_t \int_K \mathbf{v}\cdot\nabla\phi_h(t_{n+1})\phi^{*}_h}_{1} \\
&\underbrace{+\sum_K \int_K \tau_k \phi_h(t_{n+1})\mathbf{v}\cdot\nabla\phi^{*}_h dv}_{2} + \underbrace{\sum_K \theta\Delta t \int_K \tau_k(\mathbf{v}.\nabla\phi_h(t_{n+1}))(\mathbf{v}.\nabla\phi^{*}_h)dv}_{3} \\
&\underbrace{= \sum_K \int_K \phi_h(t_n)\phi^{*}_h dv - \sum_K (1-\theta)\Delta t \int_K \mathbf{v}\cdot\nabla\phi_h(t_n)\phi^{*}_h}_{1} \\
&\underbrace{+\sum_K \int_{\Omega_h} \tau_k \phi_h(t_n)\mathbf{v}\cdot\nabla\phi^{*}_h dv}_{2} \underbrace{- \sum_K (1-\theta)\Delta t \int_K \tau_k(\mathbf{v}.\nabla\phi_h(t_n))(\mathbf{v}.\nabla\phi^{*}_h)dv}_{3}
\end{aligned} \tag{5.18}$$

Three terms appear in the weak discretized formulation. Term 1 corresponds to the standard discretized Galerkin form. Term 2 is a stabilization term which creates diffusion and term 3 ensures the consistency of the method.

Filtered level set function

The convection of the level set function is realized over the whole computational domain Ω which can be the cause of additional computational costs and numerical unstabilities [L.Ville *et al.* 2011]. However, the information contained in the level set function values are useful only in a narrow-band around the zero isosurface. It allow us to compute the normal and the curvature of the interface and to know the distance from every point to the interface. For this reason, it is not necessary to convect the level set over all the domain Ω. Then, we can cut the level set function at a defined thickness E using for example a hyperbolic tangent filter, which means that we have to modify the definition of the initial level set function. Then

$$\phi_0(\mathbf{x}) = E tanh\left(\frac{d(\mathbf{x})}{E}\right) \tag{5.19}$$

with $|d(\mathbf{x})| = \underset{p\in\Gamma}{min}||\mathbf{x}-\mathbf{p}||$, the signed distance from a point $\mathbf{x}$ to the interface and E is a numerical parameter related to the width of the interface. Using this function defined in Equation (5.19), the gradient of $\phi(\mathbf{x},t)$ becomes:

$$\nabla\phi = \left(1 - \left(tanh\left(\frac{d}{E}\right)\right)^2\right)\nabla d(\mathbf{x})$$

because $\dfrac{d\,tanh(x)}{dx} = 1 - tan^2h\,(\mathbf{x})\,, \forall\, x \in \mathcal{R}$. The usual reinitialization algorithm imposes $||\nabla\phi|| = 1$, while in this case $||\nabla\phi|| = |1-(tanh(\frac{d}{E}))^2|$ since d is a distance function ($||\nabla d|| = 1$). By setting $tanh(\frac{d}{E}) = \frac{\phi}{E}$, we have $||\nabla\phi|| = |1 - (\frac{\phi}{E})^2|$. To satisfy this property, for a given level set function $\phi(\mathbf{x}, t_n)$ at time t_n, the reinitialization equation given in (5.6) is transformed into the following expression:

$$\begin{aligned} \frac{\partial\varphi}{\partial\tau} + sign(\phi)(||\nabla\varphi|| - |1 - (\frac{\varphi}{E})^2|) &= 0\,\forall\,\mathbf{x}\in\Omega,\,\tau > 0 \\ \varphi(\mathbf{x}, \tau = 0) &= \phi(\mathbf{x}, t_n) \end{aligned} \tag{5.20}$$

As we explain in Algorithm (1), we solve Equation (5.20) iteratively until reaching the steady state. Equation (5.20) can be seen as a transport equation with an advection velocity equal to $sign(\phi)\frac{\nabla\varphi}{||\nabla\varphi||}$ and an additional term $sign(\phi)|1 - (\frac{\varphi}{E})^2|$. It is important to highlight that Equation (5.20) is non linear since the advection velocity and the additional term depend on φ. But it is linearized by computing the velocity $sign(\phi)\frac{\nabla\varphi}{||\nabla\varphi||}$ from the previous time step. In our work, for simplicity and robustness we choose to separate the advection and the reinitialization steps while in the reference [L.Ville *et al.* 2011], authors propose to combine both advection and reinitialization steps into one single advection-reinitialization equation.

5.2.4 Numerical tests

A Comparison between Cranck Nicholson and implicit Euler schemes is conducted in this test.

The level set method has been implemented in Zebulon [1] Implementation of this method, reinitialization algorithm and comparison between the Euler implicit scheme and the Cranck Nicholson schemes were validated on test cases.

One test is presented here, we validate the convection of the level set with a velocity field given in Equation(5.21).

We consider a circle initially centered at O$(0.25, 0.5)$ with a radius R of $0.15m$.. The zero level set function is defined by $\phi_0 = \sqrt{(X - X_O)^2 + (Y - Y_O)^2} - R$ (see Figure 5.7).

$$\begin{aligned} v_x &= -2\pi(Y - Y_O) \\ v_y &= 2\pi(X - X_O) \end{aligned} \tag{5.21}$$

A series of tests were conducted for different time steps for both implicit Euler scheme and Cranck Nicholson scheme. Values of mass loss relatively to the size of mesh and the time step, are shown in Table 5.1. In addition, we present in this table the CPU time of each test. We present the different positions of the circle at different time for Cranck-Nicholson scheme in Figure 5.7. Figure 5.8 and 5.9 compare the deformation of the circle with different time steps and meshes between Cranck-Nicholson and Euler implicit schemes. First, we deduce that in both schemes, the accuracy of the method depends on the mesh size. Moreover, refining the domain involves a smaller time step for a better result and a reduction of loss of mass. Second, we find that Cranck-Nicholson scheme is much better than implicit Euler scheme because it allows a better mass conservation.

Remark: Let us note that the matrix assembly time is higher in Cranck-Nicholson scheme than in Euler implicit scheme.

1. This code is developed at École Nationale Supérieure des Mines de Paris, ONERA, Northwest Numerics and Modeling society (USA) and École Nationale Supérieure des Mines de Saint-Etienne.

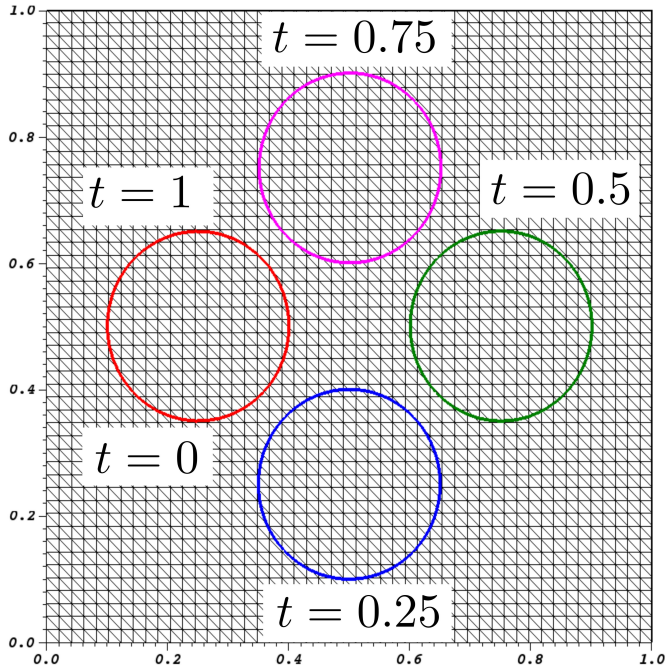

Figure 5.7: A complete turn of a circle using Cranck-Nicholson scheme

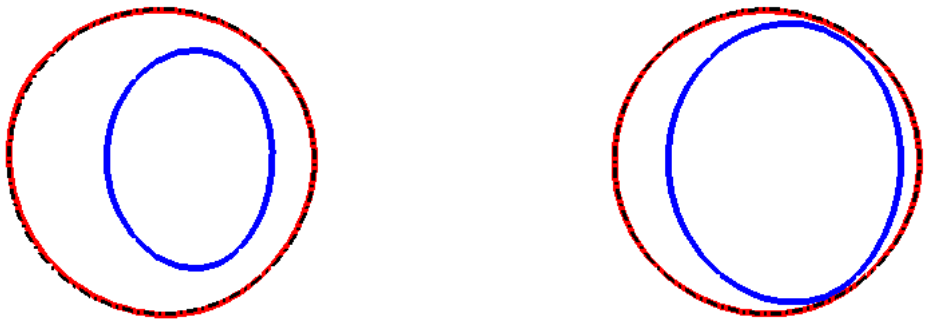

a) b)

Figure 5.8: Deformation of the circle: black line represents the initial position of the zero level set function, the red line represents the zero isovalue of the level set after one complete rotation using Cranck-Nicholson scheme and blue line represents the isovalue of the level set function after one complete rotation using implicit Euler scheme, (a) mesh: 50×50, $\Delta t = 0.01s$, (b) mesh:50×50, $\Delta t = 0.005s$

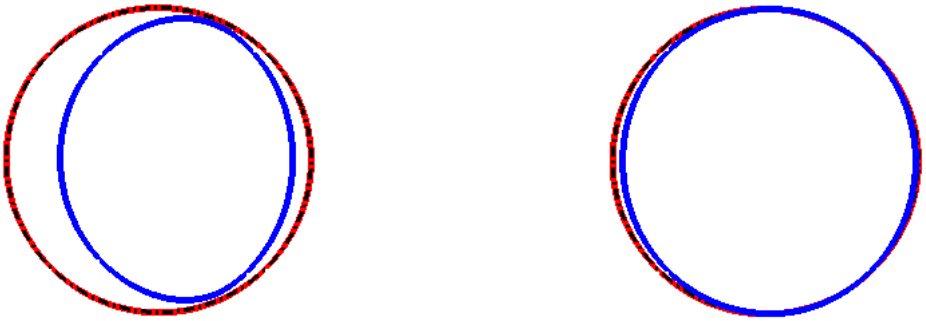

a) b)

Figure 5.9: Deformation of the circle: black line represents the initial position of the zero level set function, the red line represents the zero isovalue of the level set after one complete rotation using Cranck-Nicholson scheme and blue line represents the isovalue of the level set function after one complete rotation using implicit Euler scheme, (a) mesh: 100×100, $\Delta t = 0.005s$, (b) mesh: 200×200, $\Delta t = 0.0008s$.

Mesh grid	Time step (s)	CPU time (s) Cranck-Nicholson	mass loss (%)	CPU time (s) Euler implicit	mass loss (%)
50×50	0.01	20	13.11	13.1	61.2
50×50	0.005	77	1.52	25.6	30.2
50×50	0.0025	152	0.8	50.9	14.3
100×100	0.005	301	9.84	128.8	30.3
100×100	0.0025	698	2.39	258.1	14.6
100×100	0.001	1510	1.55	644.2	5.6
200×200	0.001	5850	0.8	3928.8	5.6
200×200	0.0008	7947	0.48	4701.8	4.46
200×200	0.0005	12150	0.41	7576.2	2.77

Table 5.1: CPU times and conservation of the mass of fluid for different size of mesh and time step in the simulation of the rotation of the circle, the conservation is the difference between the final $t = 1$ and the initial surface of the circle.

Conclusions

In our numerical model, we have two interfaces. First, the fluid-air interface Γ_{fa} which undergoes large deformations, is convected by a transport equation. This equation is discretized and stabilized with SUPG method. And another interface Γ, which separates Stokes and Darcy domains, described by a level set function and moved with the mechanical velocity due to the deformation of preforms. Since we use a Lagrangian updated formulation, this interface is transported with the mesh motion.

5.3 Large deformations of preforms

The preforms are deformable under the mechanical pressure applied on by the vacuum bag and the pressure of resin into pores. Eulerian and Lagrangian descriptions can be used to deal with the deformation of preforms. But, the adequate is the Lagrangian description because preforms are considered as a solid medium. There are many Lagrangian formulations to treat the finite strains and finite displacements, updated Lagrangian formulation, Total Lagrangian formulation. Before introducing the Lagrangian formulation that we use in this work, it is necessary to introduce some concepts and definitions taken into consideration to present this method. In continuum mechanics, the configuration is the geometry of a body at time t. A material body is a compact number of material elements $\mathbf{x}$ called the material particles or material points. A material point corresponds to a representative elementary volume, small enough relatively to the studied domain which allows to assimilate the average velocity of particles to their "real" velocity. Then, the representation of the relative movements of these material points will be used to characterize the deformation and the displacements of the medium. The reference configuration, corresponds to the geometry at time $t = 0$, without any influence of constraints (Ω^0). Under the influence of external loads, the body moves and changes its configuration. The configuration of the body at the current time t is called the present configuration (Ω^t).

Lagrangian and Eulerian description

In continuum mechanics, there are two different approaches to describe the state and the movement of a medium. The "Lagrangian" description and the "Eulerian" description. When the reference configuration is chosen to be the initial configuration at $t = 0$, the referential description is often called "the Lagrangian description", and the motion is described by the function $X(\mathbf{a}, t)$ giving the position of a point "$\mathbf{a}$" labelled at time t. The Eulerian description is based on the velocity field, the independant variable is the present position $\mathbf{x}$ occupied by

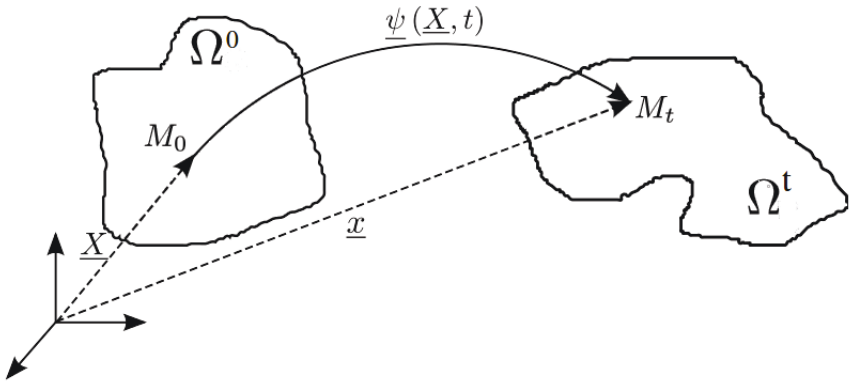

Figure 5.10: Lagrangian description of the movement of the domain Ω

the particles at the present time and the flow is described by the velocity at point $\mathbf{x}$ in the current configuration ($\mathbf{v}(\mathbf{x},t)$). "Eulerian" description is usually employed in fluid mechanics while Lagrangian description is usually used in solid mechanics.
In our work, we will adopt the **updated Lagrangian formulation** based on a Lagrangian description. A Lagrangain description formally consists in representing the movement of a medium using an application ψ defined from the reference configuration denoted Ω^0 to the material configuration denoted Ω^t which associates to every material point M_0 in the reference configuration of coordinate $\mathbf{X}$, a point M_t of coordinate $\mathbf{x}$ in its material configuration (Figure 5.10). The application ψ is defined by:

$$\begin{array}{rccl} \psi: & \Omega_0 & \longrightarrow & \Omega_t \\ & \mathbf{X} & \longrightarrow & \psi(\mathbf{X},t)=\mathbf{x};\ \forall\, t>0 \end{array} \tag{5.22}$$

This definition allows us to deduce the displacement vector $\mathbf{u}$ of the material point and its velocity.

$$\begin{array}{rcccl} \mathbf{u}(\mathbf{X},\mathbf{t}) & = & \mathbf{x}-\mathbf{X} & = & \psi(\mathbf{X},t)-\mathbf{X} \\ \mathbf{v}(\mathbf{X},\mathbf{t}) & = & \dfrac{\partial \mathbf{u}(\mathbf{X},t)}{\partial t} & = & \dfrac{\partial \psi(\mathbf{X},t)}{\partial t} \end{array} \tag{5.23}$$

According to the implicit function theorem, the mathematical condition that guaranties that two material points will not be superposed after transformation and do not intersect during the transformation is that the Jacobian determinant J of the Lagrangian gradient of ψ should be strictly positive.
Let us note $\mathbf{F}=\nabla_{\mathbf{X}}\psi$, $\mathbf{F}_{ij}=\psi=\frac{\partial \mathbf{x}_i}{\partial \mathbf{X_j}}$, $J(\mathbf{X},t)=det(\nabla_{\mathbf{X}}\psi)>0$.

These functions allow the definition of transport relations between two configurations related with the application ψ, the proofs of these formulations are detailed for instance [J.Bonet & D.R.Wood 1997], [J.Coirier 2001].

Transport of length scale

Let dX be a length element in its initial configuration. After deformation, this element is transformed into an element of length dx with

$$d\mathbf{x} = \mathbf{F}.d\mathbf{X} \tag{5.24}$$

Transport of surface element

A surface element dS oriented $\mathbf{N}dS$ in its initial configuration is transformed into a surface element ds oriented $\mathbf{n}ds$ after its deformation with:

$$\mathbf{n}ds = J\mathbf{F}^{-T}.\mathbf{N}dS \tag{5.25}$$

Transport of volume element

An element of volume dV in its initial configuration is transformed to an element of volume dv after its deformation with:

$$dv = JdV \tag{5.26}$$

Measures of deformations

The basic properties of the local behavior of deformation emerge from the possibility of decomposing a deformation into rotation ($\mathbf{R}$) and stretch tensors ($\mathbf{U}$ or $\mathbf{V}$). This decomposition is called "polar decomposition of the deformation gradient", and is summarized in the following theorem:

A non singular tensor $\mathbf{F}$ ($\det \mathbf{F} \neq 0$) permits the polar decomposition in two ways:

$$\mathbf{F} = \mathbf{R}.\mathbf{U} = \mathbf{V}.\mathbf{R}$$

where the tensors $\mathbf{R}$, $\mathbf{U}$ and $\mathbf{V}$ have the following properties:

- $\mathbf{U}$ and $\mathbf{V}$ are symmetric and positive defined.
- The tensor $\mathbf{R}$ is orthogonal $\mathbf{R}.\mathbf{R}^T = \mathbf{I}$, *i.e* $\mathbf{R}$ is a rotation tensor.
- $\mathbf{U}$, $\mathbf{V}$ and $\mathbf{R}$ are uniquely determined.

Table 5.2 presents different deformations. $\mathbf{E_0}$, $\mathbf{E_1}$ are the tensor of deformations of Hencky and Biot, $\mathbf{E_2}$ is the Green-Lagrange tensor. Deformation measurements defined on reference

configuration are so-called "Lagrangian" and deformation measurements defined on the current configuration are so-called "Eulerian".

Lagrangian configuration	Eulerian configuration
$\boldsymbol{E}_\alpha = \frac{1}{\alpha}[\boldsymbol{U}^\alpha - \boldsymbol{I}] \quad \alpha \neq 0$	$\boldsymbol{e}_\alpha = \frac{1}{\alpha}[\boldsymbol{I} - \boldsymbol{V}^\alpha] \quad \alpha \neq 0$
$\boldsymbol{E}_0 = \ln \boldsymbol{U} = \frac{1}{2} \ln \boldsymbol{C}$ $\boldsymbol{E}_1 = \boldsymbol{U} - \boldsymbol{I}$ $\boldsymbol{E}_2 = \frac{1}{2}[\boldsymbol{U}^2 - \boldsymbol{I}] = \frac{1}{2}[\boldsymbol{C} - \boldsymbol{I}]$	$\boldsymbol{e}_0 = \ln \boldsymbol{V} = \frac{1}{2} \ln \boldsymbol{B}$ $\boldsymbol{e}_1 = \boldsymbol{I} - \boldsymbol{V}$ $\boldsymbol{e}_{-2} = \frac{1}{2}[\boldsymbol{I} - \boldsymbol{V}^{-2}] = \frac{1}{2}[\boldsymbol{I} - \boldsymbol{B}^{-1}]$

Table 5.2: Measures of deformations

C and **B** are respectively the right and left Cauchy-Green tensors defined by:

$$\mathbf{C} = \mathbf{F}^T.\mathbf{F} = \mathbf{U}^2$$

$$\mathbf{B} = \mathbf{F}.\mathbf{F}^T = \mathbf{V}^2$$

Measures of stress

To define the different types of stress measurements, we use the following definitions:
Let us note, in the reference configuration (Ω_0), $\mathbf{N} = \mathbf{n_0}$ the outward normal to a surface element dS and the force acting on this surface is df_0. Now we will introduce three types of stress:

Cauchy stress:

The Cauchy stress, denoted there, measures the force acting on an element of area ds in the deformed configuration. This tensor is symmetric and defined via: $d\mathbf{f} = \mathbf{t}.ds$. $\mathbf{t} = \boldsymbol{\sigma}.\mathbf{n}$ is the traction and $\mathbf{n}$ is the normal of the surface where this traction acts.

Piola-Kirchhoff stress I:

The first Piola-Kirchhoff stress tensor denoted by $\mathbf{P}$, expresses the force df on the current configuration via:

$$df = \mathbf{P}.\mathbf{N}dS$$

This tensor is unsymmetric and relates the force applied on the deformed configuration to an oriented surface vector in the reference configuration (via $\mathbf{N}dS$).

Piola-Kirchhoff stress II :

The second Piola-Kirchhoff stress, denoted by $\mathbf{S}$ expresses the force df_0 on the reference configuration

$$df_0 = \mathbf{S}.\mathbf{N}\, d\mathbf{S}$$

.

$\mathbf{S}$ is symmetric which means $\mathbf{S} = \mathbf{S}^T$. This property is essential, and the Piola-Kirchhoff stress II tensor is widely used much more then Piola-Kirchhoff stress I.
There exist different useful relationships between stress tensors:

- **Relation between Piola-Kirchhoff I (P) and Piola-Kirchhoff II (S)**:

$$\mathbf{P} = \mathbf{F}.\mathbf{S} = J.\boldsymbol{\sigma}.\mathbf{F}^{-T}$$

- **Relation between Cauchy tensor $\boldsymbol{\sigma}$ and Piola-Kirchhoff tensor S**:

$$\sigma = \frac{1}{J}\mathbf{F}.\mathbf{S}.\mathbf{F}^T$$

5.3.1 Updated Lagrangian formulation

After introducing all the necessary concepts of solid mechanics, we will describe the implementation of the Lagrangian formulation of solid mechanics problem. When we neglect the inertia effects, the momentum conservation equation is defined by:

$$div\boldsymbol{\sigma} + \mathbf{f_v} = 0 \text{ in } \Omega^t \tag{5.27}$$

where $\mathbf{f_v}$ is the volume force vector and $\boldsymbol{\sigma}$ is the Cauchy stress tensor. Some boundary conditions would be added to this equation to complete the problem. The boundary $\partial\Omega^t$ is decomposed into two different parts: $\partial\Omega^t_D$ and $\partial\Omega^t_N$ where Dirichlet and Neumann conditions are imposed respectively. Non zero displacement is enforced on $\partial\Omega^t_D$ and a stress vector is imposed on $\partial\Omega^t_N$.

We will establish the weak formulation of Equation (5.27) on the deformed domain Ω^t, obtained by multiplying Equation (5.27) by vectorial test functions: $\mathbf{w} : \Omega^t \longrightarrow \mathrm{R^m}$. Then by integrating by parts on Ω^t, this formulation can be written as

$$\int_{\Omega^t} \boldsymbol{\sigma} : \nabla_{\mathbf{x}}\mathbf{w}dv \quad = \quad \int_{\partial\Omega^t_N} \mathbf{t}.\mathbf{w}ds \quad + \quad \int_{\Omega^t} \mathbf{f_v}\mathbf{w}dv \tag{5.28}$$

where $\mathbf{w}$ is a virtual vectorial velocity field kinematically admissible, i.e, $\mathbf{w} = 0$ on $\partial\Omega^t_D$ and

$\mathbf{t} = \boldsymbol{\sigma}.\mathbf{n}$ is the stress vector imposed as a Neumann condition. First, the computation is performed on the deformable geometry which is unknown. We will write this formulation on the initial configuration. Then, using $\mathbf{A} : \mathbf{B} = tr(\mathbf{A}.\mathbf{B}^T)$ and the transport equations from a configuration to another developed in this section, the left hand side of Equation (5.28), the inertial virtual power, becomes:

$$\begin{aligned} \int_{\Omega^t} \boldsymbol{\sigma} : \nabla_X \mathbf{w} dv &= \int_{\Omega^0} \boldsymbol{\sigma} : (\nabla_X \mathbf{w}.\mathbf{F}^{-1}) J dV \\ &= \int_{\Omega^0} tr[J.\boldsymbol{\sigma}.\mathbf{F}^{-T} \boldsymbol{\nabla}_X^T \mathbf{w}] dV \\ &= \int_{\Omega^0} \mathbf{P} : \boldsymbol{\nabla}_X \mathbf{w} dV \end{aligned} \tag{5.29}$$

with $\mathbf{P}$ is the first Piola-Kirchhoff tensor.

The right hand side tensor of Equation (5.28) is expressed using the transport equation of the surface element and the relation between Cauchy-stress tensor and the first Piola-Kirchhoff stress tensor $\mathbf{P}$:

$$\begin{aligned} \int_{\partial\Omega^t} (\boldsymbol{\sigma}.\mathbf{n}).\mathbf{w} ds \quad + \quad \int_{\Omega^t} \mathbf{f_v}.\mathbf{w} dv \quad &= \quad \int_{\partial\Omega^0} \boldsymbol{\sigma}(\mathbf{F}^{-T}.\mathbf{N}\frac{J}{J_s}).\mathbf{w} J_s dS \quad + \quad \int_{\Omega^0} \mathbf{f_v}.\mathbf{w} J dV \\ &= \quad \int_{\partial\Omega^0} (\mathbf{P}.\mathbf{N}).\mathbf{w} dS \quad + \quad \textstyle\int_{\Omega^0} \mathbf{f_v}.\mathbf{w} J dV \end{aligned} \tag{5.30}$$

with $\mathbf{P}.\mathbf{N} = \mathbf{t_0}$ on $\partial\Omega_N^0$ and $\mathbf{f_{v_0}} = J\mathbf{f_v}$, Equations (5.29) and (5.30) provide:

$$\int_{\Omega^0} \mathbf{P} : \nabla_X \mathbf{w} dV = \int_{\partial\Omega_N^0} \mathbf{t_0}.\mathbf{w} dS + \int_{\Omega^0} \mathbf{f_{v_0}}.\mathbf{w} dV$$

We can use the Piola-Kirchhoff second tensor $\mathbf{S}$ using the relation between $\mathbf{P}$ and $\mathbf{S}$ ($\mathbf{P} = \mathbf{F}.\mathbf{S}$), then, the formulation is finally written as:

$$\int_{\Omega_0} (\mathbf{F}.\mathbf{S}) \nabla_{\mathbf{X}} \mathbf{w} dV = \int_{\partial\Omega_N^0} \mathbf{t_0}.\mathbf{w} dS + \int_{\Omega^0} \mathbf{f_{v_0}}.\mathbf{w} dV \tag{5.31}$$

Using the relation, $(\mathbf{A}.\mathbf{B}) : \mathbf{C} = \mathbf{B} : (\mathbf{A}^T\mathbf{C})$, Equation (5.31) can be written as:

$$\int_{\Omega^0} \mathbf{S}(\mathbf{u}) : (\mathbf{F}^t.\nabla_{\mathbf{X}} \mathbf{w}) dV = \int_{\partial\Omega_N^0} \mathbf{t_0}.\mathbf{w} dS + \int_{\Omega^0} \mathbf{f_{v_0}}.\mathbf{w} dV \tag{5.32}$$

Because the computations are performed on the initial configuration, the formulation is called " Total Lagrangian", used in solid mechanics. However, because our problem is coupled

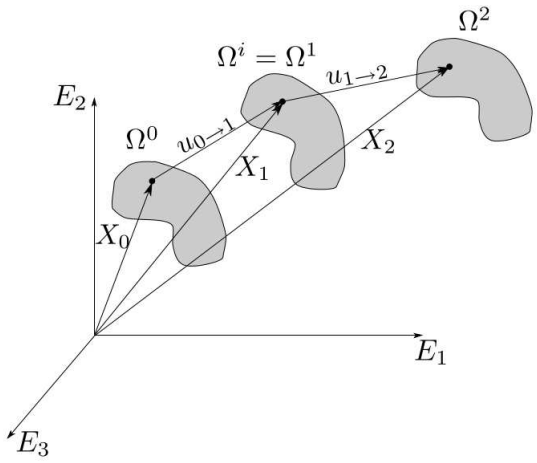

Figure 5.11: Intermediate configuration Ω^i

with fluid mechanics, we will use the "Updated Lagrangian" formulation which performs computation on the last known geometry before the final deformed geometry. For that, we have to introduce an intermediate geometry denoted Ω^i which will correspond to an intermediate computational domain in a non linear resolution scheme in Figure 5.11. For reasons of simplification, we consider three configurations initial geometry Ω^0, intermediate geometry $\Omega^i = \Omega^1$ and the final geometry $\Omega^t = \Omega^2$.

$\mathbf{X^i} = (X_1^i, X_2^i, X_3^i)$ is the position vector on the intermediate configuration and $\mathbf{u}_{i\longrightarrow j}$ is the displacement vector between the different configurations. The gradient transformation tensor $\mathbf{F_{i\longrightarrow j}}$ is written as $\mathbf{F_{i\longrightarrow j}} = \frac{\partial(\mathbf{X}^j)_m}{\partial(\mathbf{X}^i)_n}$, m is the m^{th} component of $\mathbf{X^j}$. Then, for passing from Ω^0 to Ω^2, we proceed as following:

$$\int_{\Omega^0} \mathbf{S(U)} : (F^T_{0\longrightarrow 2}.\boldsymbol{\nabla}_{X_0}\mathbf{w})dV_0 = \int_{\partial\Omega^0_N} \mathbf{t_0}.\mathbf{w}dS_0 + \int_{\Omega^0} \mathbf{f_{v_0}}.\mathbf{w}dV_0 \tag{5.33}$$

As we started before, one wants to write the formulation on the intermediate configuration because the large deformations do not allow to switch directly from the initial configuration (Ω^0) to the deformable configuration (Ω^2). Then, Equation (5.33) on the intermediate configuration becomes:

$$\int_{\Omega^1} \mathbf{S(u)} : (\mathbf{F^T}_{0\longrightarrow 1}.\mathbf{F^T}_{1\longrightarrow 2}\nabla_{X_1}\mathbf{w}\mathbf{F}_{0\longrightarrow 1})J^{-1}_{0\longrightarrow 1}dV_1 = \int_{\Gamma^1_N} (J)^{-1}_{0\longrightarrow 1}\mathbf{t_0}.\mathbf{w}dS_1 + \int_{\Omega_1} J^{-1}_{0\longrightarrow 1}\mathbf{f_{v_0}}.\mathbf{w}dV_1 \tag{5.34}$$

By writing, $\widetilde{\mathbf{S}} = J_{0\longrightarrow 1}^{-1}\mathbf{F}_{0\longrightarrow 1}\,\mathbf{S}\,\mathbf{F}_{0\longrightarrow 1}^{T}$, $\mathbf{t_1} = (J)_{0\longrightarrow 1}^{-1}\mathbf{t_0}$ and $\mathbf{f_{v_1}} = J_{0\longrightarrow 1}^{-1}\mathbf{f_{v_0}}$, the Updated formulation can be written as:

$$\int_{\Omega^1} \widetilde{\mathbf{S}} : (\mathbf{F}_{1\longrightarrow 2}^{T}\boldsymbol{\nabla}_{X_1}\mathbf{w})dV_1 = \int_{\partial\Omega_N^1} \mathbf{t_1}.\mathbf{w}dS_1 + \int_{\Omega^1} \mathbf{f_{v_1}}.\mathbf{w}dV_1 \tag{5.35}$$

In Equation (5.35), the unknown is the displacement $\mathbf{u}_{1\longrightarrow 2}$

To solve the non linear mechanical problem, we use a Newton-Raphson algorithm based on a first order Newton linearisation of the equation to be solved. Let us note $\mathbf{R}(\mathbf{u},\mathbf{w})$ the residual of the Lagrangian updated formulation.

$$\mathbf{R}(\mathbf{u},\mathbf{w}) = \int_{\Omega^1} \widetilde{\mathbf{S}}(\mathbf{u}) : (\mathbf{F}_{1\longrightarrow 2}^{T}.\boldsymbol{\nabla}_{X_1}\mathbf{w})dV_1 - \int_{\partial\Omega_N^1} \mathbf{t_1}.\mathbf{w}dS_1 - \int_{\Omega^1} \mathbf{f_{v_1}}.\mathbf{w}dV_1 \tag{5.36}$$

Starting from $\mathbf{u_0}$, we have to make a correction $\boldsymbol{\delta}_u$ which makes the residual vanishing such that:

$$\mathbf{R}(\mathbf{u_0}+\boldsymbol{\delta}_u,\mathbf{w}) \simeq \mathbf{R}(\mathbf{u_0},\mathbf{w}) + \frac{\partial \mathbf{R}(\mathbf{u_0},\mathbf{w})}{\partial \mathbf{u}}.\boldsymbol{\delta}_u = 0$$

The correction is obtained by solving the following equation:

$$\frac{\partial \mathbf{R}(\mathbf{u_0},\mathbf{w})}{\partial \mathbf{u}}.\boldsymbol{\delta}_u = -\mathbf{R}(\mathbf{u_0},\mathbf{w}) \tag{5.37}$$

where $\frac{\partial \mathbf{R}(\mathbf{u_0},\mathbf{w})}{\partial \mathbf{u}}$ is the tangent stiffness matrix. The first correction is not perfect numerically, for that we have to proceed iteratively until the convergence is reached $|R(\mathbf{u}^n,\mathbf{w})| < \epsilon$.

5.3.2 Evolution of the porosity and permeability

If the porous medium undergoes deformations, its porosity changes, consequently the permeability changes which affects the flow. This is one of the main features of this unique approach which permits to consider so well real infusion cases [Wang *et al.* 2010].

5.3.2.1 Computation of porosity

Evolution of the porosity is determined using the mass conservation equation. Let us consider that the preforms are formed by fibers and pores, the fibers are incompressible but the preforms are compressible. The mass conservation can be solved by a Lagrangian approach based on the Jacobian transformation, or by a finite element resolution.

Mass conservation

The mass conservation is enunciated as: the mass of the material domain Ω is constant during the time

$$\frac{D}{Dt}(m_s(\Omega)) = 0$$

We take an elementary material domain $\varpi \subset \Omega$,then

$$\frac{D}{Dt}\left(\int_{\varpi} \rho_s(\mathbf{x}, t)dv\right) = 0$$

.

Where $\rho_s(\mathbf{x}, t)$ is the density of preforms (solid part) at the point $\mathbf{x}$ and at the instant t.

$$\frac{D}{Dt}(\int_{\varpi} \rho_s dv) = \int_{\varpi} (\frac{D\rho_s}{Dt}dv + \rho_s \frac{D(dv)}{Dt}) = 0 \tag{5.38}$$

The derivate of the density (ρ_s) with respect to time, is given by the material derivate density [J.Coirier 2001].

$$\frac{D\rho_s}{Dt} = \frac{\partial \rho_s}{\partial t} + \mathbf{v_s}.\boldsymbol{\nabla}_{\mathbf{x}}\rho_s \tag{5.39}$$

and the derivate of the elementary volume is given by:

$$\frac{D(dv)}{Dt} = div_{\mathbf{x}}\mathbf{v_s}dv \tag{5.40}$$

Equations (5.39) and (5.40) are valid for all ϖ, therefore, it is valid on Ω. Then, Equation (5.38) becomes:

$$\frac{\partial \rho_s}{\partial t} + \mathbf{v_s}.\boldsymbol{\nabla}_{\mathbf{x}}\rho_s + \rho_s div_{\mathbf{x}}\mathbf{v_s} = 0 \tag{5.41}$$

Because of the use of the Updated Lagrangian method, the mesh changes. For this reason, we have to take into consideration the velocity $\mathbf{v_m}$ of the mesh. Consequently, Equation (5.41) can be written as function of a relative velocity $\mathbf{v_s} - \mathbf{v_m}$.

$$\frac{\partial \rho_s}{\partial t} + (\mathbf{v_s} - \mathbf{v_m})\boldsymbol{\nabla}_{\mathbf{x}}\rho_s + \rho_s div_{\mathbf{x}}\mathbf{v_s} = 0 \tag{5.42}$$

In our case, based on the Updated approach at each iteration, the velocity of the mesh is equal to the velocity of the preforms ($\mathbf{v_m} = \mathbf{v_s}$). Consequently, we obtain

$$\frac{\partial \rho_s}{\partial t} + \rho_s div_x\mathbf{v_s} = 0 \tag{5.43}$$

The density of preforms is $\rho_s = \frac{m_{fibre}+m_{pores}}{V_{total}}$. The mass of pores is equal to zero, then, $\rho_s = \frac{m_{fibre}}{V_{total}} = \frac{m_{fibre}}{V_{fibre}}\frac{V_{fibre}}{V_{total}} = \rho_f \frac{V_{fibre}}{V_{total}} = \rho_f(1-\psi)$ where ψ is the porosity. ρ_f is the density of fibers which is constant during time which means that $\frac{\partial \rho_f}{\partial t} = 0$. Hence, the mass conservation of porosity writes:

$$\frac{\partial \psi}{\partial t} - (1-\psi) div_{\mathbf{x}} \mathbf{v_s} = 0 \tag{5.44}$$

Resolution using finite element

Equation (5.44) can be solved using a finite element method. Then, the weak variational formulation is:

$$\int_\Omega \frac{\partial \psi}{\partial t} \psi^* dv = \int_\Omega [(1-\psi) div_{\mathbf{x}} \mathbf{v_s}] \psi^* dv \tag{5.45}$$

To solve Equation (5.45), we use an implicit Euler scheme for the discretization in time. Then, we have: $[0,T] = \cup_{n=1}^{N} [t_{n-1}, t_n]$ with $\Delta t = t_n - t_{n-1}$

Therefore, the discretized formulation of Equation (5.45) can be written as:

$$\int_\Omega \frac{(\psi(t_n) - \psi(t_{n-1}))}{\Delta t} \psi_h^* dv - \int_\Omega [(1-\psi(t_n)) div_x \mathbf{v_s}] \psi_h^* dv = 0 \tag{5.46}$$

An alternate approach to compute the evolution of porosity uses the Jacobian of transformation.

Resolution using the Jacobian of transformation

A Lagrangian version based on the Jacobian transformation can be used to describe the mass conservation of the system [P.Celle 2006]. We write the relation between two instants t and $t + \Delta t$ such as:

$$J(\mathbf{X}, t+\Delta t)\rho_s(\mathbf{X}, t) = J(\mathbf{X}, t)\rho_s(\mathbf{X}, t) \tag{5.47}$$

Using the relation between density and porosity expressed in Equation (5.48):

$$\rho_s(\mathbf{X}, t) = (1-\psi)\rho_f(\mathbf{X}, t) \tag{5.48}$$

we obtain the evolution of porosity in function of the Jacobian such that:

$$J(\mathbf{X}, t+\Delta t)(1-\psi(\mathbf{X}, t+\Delta t)) = J(\mathbf{X}, t)(1-\psi(\mathbf{X}, t)) \tag{5.49}$$

We prefer to use Equation (5.44) because its implementation in Zebulon is simpler. For

that we use the finite element resolution.

Validation of the resolution of the porosity evolution using a compaction test

To validate the resolution of porosity evolution, we compact a preform of width $L = 0.385\,m$ and of height $H = 0.056\,m$. A displacement of $0.01m$ is imposed on the top of the domain along y axis. Figure 5.12 shows the boundary conditions imposed in this test. The initial porosity is equal to 60%. First, we solve the momentum conservation equation to compute the displacement field $\mathbf{u}$ which is used in the mass balance equation to compute the velocity $\mathbf{v_s} = \frac{\mathbf{u}}{\Delta t}$ then to compute the porosity ψ.

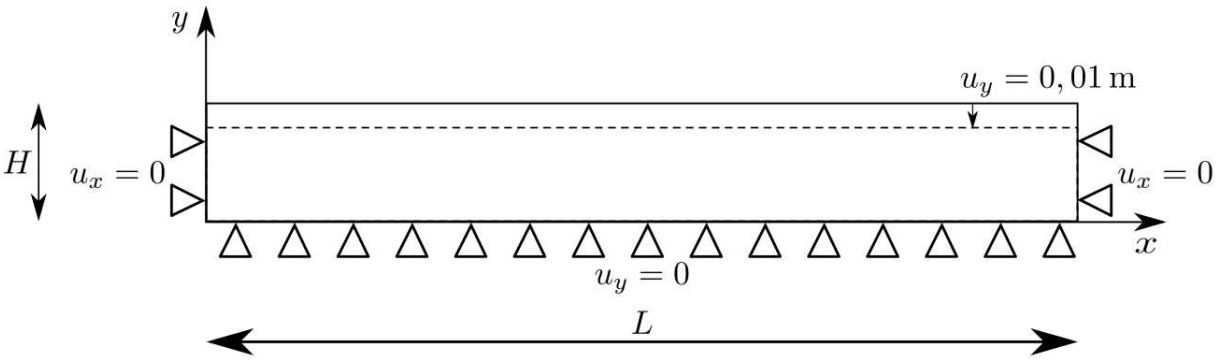

Figure 5.12: Compaction test

The analytical solution of the porosity at the time t is determined from the porosity at the initial time. Taking into consideration that the mass of fibers is constant during the time $m_f^t = m_f^0$, we get $V_f^t \rho_f^t = V_f^0 \rho_f^0$ where V_f^t and V_f^0 are the fiber volume fractions at the time t and the initial time respectively, ρ_f^t and ρ_f^0 are the density at the time t and the initial time respectively. But, the fiber volume fraction equal to $V_{total}^t(1-\psi^t)$ is constant during the time, consequently we have:

$$V_f = V_{total}^t(1-\psi^t) = V_{total}^0(1-\psi^0)$$

we obtain a relation to compute the porosity at the time t in function of the initial time:

$$\psi^t = 1 - \frac{V_{total}^0}{V_{total}^t}(1-\psi^0)$$

where V_{total}^0 and V_{total}^t are the volume of preforms at the initial time and the instant t. Table 5.3 compares the numerical and analytical solutions obtained with this test. An excellent correlation between numerical and analytical results ensures the robustness of the method used

to compute the evolution of the porosity. Figure 5.13 show the isovalue of the displacement u_y.

Results	Analytical results	Numerical results
Initial thickness	$0.056m$	$0.056m$
Final thickness	$0.046m$	$0.046m$
Initial porosity ψ_0	60%	60%
Final porosity ψ_t	51.3%	51.3%
Volume fiber fraction V_f	48.7%	48.7%

Table 5.3: Comparison between analytical and numerical results

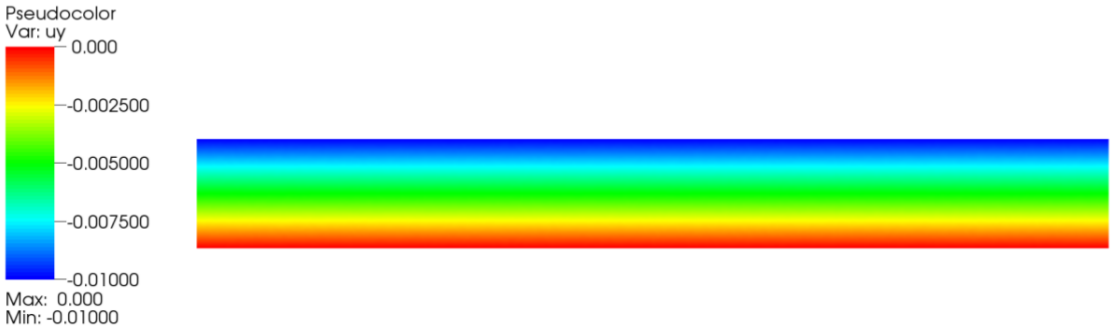

Figure 5.13: Isovalue of the displacement u_y

5.3.2.2 Computation of permeability

The permeability is an essential parameter which characterizes the preforms. The variation of the porosity leads to a variation of permeability. For this reason, we have to pay attention to the particular methods used to determine preform permeability as function of porosity. Two approaches can be found in the literature: the first one is based on physical empirical models, while the second one is based on experimental measurements. In this work, we choose the Carman-Kozeny law which is the most popular empirical law found in literature [J.Park & M.K.Kang 2003],[Dullien 1979]. This law, established for soils initially, expresses the permeability k as a function of the volume fraction of solid phases, here the fibers as:

$$k = \frac{d_f^2}{16h_c}\frac{(1-V_f)^3}{V_f^2}$$

where d_f is the fibers diameter, h_c is the Kozeny constant and V_f is the volume fraction of fibers. The Kozeny constant is taken equal to 10 in our cases.

5.3.3 Constitutive law of fibrous preforms

Preforms are constituted by fibers, their mechanical behavior is then anisotropic. We use the continuum mechanics at macroscopic scale, therefore preforms are seen as homogeneous media with an anisotropic response. We choose a planar isotropic behavior to model the behavior of preforms. We assume that in the plane, the behavior of preforms is isotropic, elastic and may be non linear while in transversal direction, the non linear behavior of preforms is related to the volume fraction of fibers and is independant on the plane response. In literature, we have different methods to establish the relation between the stress and the volume fraction of fibers. These relations are empirical or based on experimental results, but are isotropic in essence. We cite as examples, power laws, Gutowski's law ...

– **Power law** [S.Toll & Manson 1994]

$$\boldsymbol{\sigma} = a(V_f)^b$$

where a and b are constants determined experimentally and V_f is the volume fraction of fibers.

– **Gutowski's law** [T.G.Gutowski 1987]

$$\boldsymbol{\sigma} = A_s \frac{\sqrt{\frac{V_f}{V_0}} - 1}{(\sqrt{\frac{V_a}{V_f}} - 1)^4}$$

where V_a is the maximum volume fraction of fibers, V_f is the volume fraction of fibers during the compaction, V_0 is the initial volume fraction of fibers (before compaction) and A_s is a constant.

However, we did not use these relations established for appropriate needs because we prefer a relationship between the stress and the deformations of preforms which is more exhaustive for a mechanical approach. Some constitutive laws establish explicitly the relation between the transverse stress $\boldsymbol{\sigma}$ in function of the deformation ε with:

$$\boldsymbol{\sigma}(\varepsilon) = \mathbf{f}(\varepsilon)$$

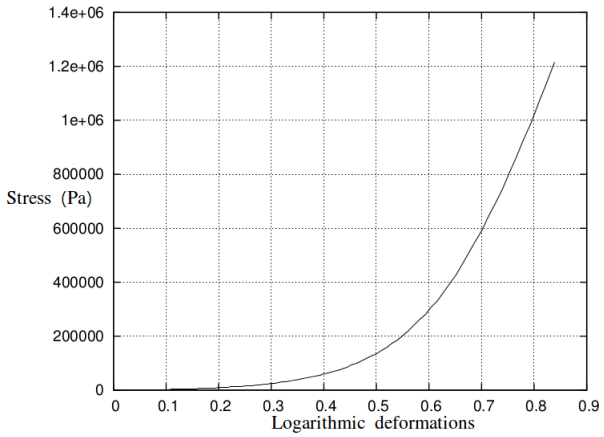

Figure 5.14: Constitutive law of NC2 preforms in compaction [Celle *et al.* 2008]

where $\mathbf{f}$ is the constitutive law.
In this work, we will use an experimental stress-strain relation based on the experimental work of P. Celle [Celle *et al.* 2008] at École Nationale Supérieure des Mines de Saint-Étienne on NC2 preforms which shows some evidence of the non linear elastic behavior in transverse direction. This approach establishes, using experiment, the relation between stress and the deformation of preforms for a given volume fraction of fibers. We will describe how to take the constitutive law of NC2 preforms into consideration in our work.

Experimental curve of NC2 preforms

P.Celle [Celle *et al.* 2008] realized a transverse compaction on 100 layers of NC2 preforms ($[0, 90]_{100}$) of basis weight per unit area $200g/m^2$. The initial thickness of NC2 preforms is $0.056m$ and the dimensions are $0.585 \times 0.385\, m^2$. The stress-strain curve is presented in Figure 5.14. The first part of this curve shows large deformations because of the space which disappears between the plies and the arrangement of the filaments relative to each other. The second part of the curve corresponds to the phase of compaction of preforms: very low deformations induce large stress. We need a 3D law which characterizes the behavior of preforms in their plane.

The relation between the stress tensor $\boldsymbol{\sigma(\varepsilon)}$ and the tensor of deformations ε is given by the relation:

$$\boldsymbol{\sigma} = \mathbf{C} : \varepsilon(\mathbf{u}) \tag{5.50}$$

where $\mathbf{C}(\varepsilon)$ is the 4^{th} order elasticity tensor that contains 81 coefficients in the most general case, which become 9 when the material is orthotropic and 5 for planar isotropic behaviors.

$$\begin{pmatrix}\sigma_{11}\\ \sigma_{22}\\ \sigma_{33}\\ \sigma_{12}\\ \sigma_{23}\\ \sigma_{13}\end{pmatrix} = \begin{bmatrix} \frac{(1-\nu_{tp}\nu_{pt})E_p}{\delta} & \frac{\nu_{tp}+\nu_{tp}\nu_p E_p}{\delta} & \frac{\nu_p+\nu_{tp}\nu_{pt}E_p}{\delta} & 0 & 0 & 0 \\ \frac{\nu_{pt}+\nu_p\nu_{pt}E_t}{\delta} & \frac{(1-\nu_p\nu_p)E_t}{\delta} & \frac{\nu_{pt}+\nu_{tp}\nu_p E_t}{\delta} & 0 & 0 & 0 \\ \frac{\nu_p+\nu_{tp}\nu_{pt}E_p}{\delta} & \frac{\nu_{tp}+\nu_p\nu_{tp}E_p}{\delta} & \frac{(1-\nu_{pt}\nu_{pt})E_p}{\delta} & 0 & 0 & 0 \\ 0 & 0 & 0 & G_t & 0 & 0 \\ 0 & 0 & 0 & 0 & G_p & 0 \\ 0 & 0 & 0 & 0 & 0 & G_t \end{bmatrix} \begin{pmatrix}\varepsilon_{11}\\ \varepsilon_{22}\\ \varepsilon_{33}\\ 2\varepsilon_{12}\\ 2\varepsilon_{23}\\ 2\varepsilon_{13}\end{pmatrix}$$

with:

$$\delta = (1 - 2\nu_{tp}\nu_p^2 - \nu_p^2 - \nu_{tp}\nu_p - \nu_{pt}\nu_p)$$

where E_p is the stiffness modulus in the plane of preforms, E_t is the stiffness transverse modulus, ν_p is the longitudinal Poisson's ratio, $\nu_{tp} = \nu_{pt}\frac{E_t}{E_p}$ is the transverse Poisson coefficient, $G_p = \frac{E_p}{2(1+\nu_p)}$ is the longitudinal shear modulus and G_t is the transverse shear modulus. Stiffness and suppleness tensors are symmetrical positive defined due to the structure of the elastic energy. Consequently, Poisson ratios have to satisfy:

$$\frac{\nu_{tp}}{E_t} = \frac{\nu_{pt}}{E_p}, \;\; G_p = \frac{E_p}{2(1+\nu_p)}$$

Response of the preforms relatively to the transverse direction

As explained before, the behavior in the transverse direction is the behavior of NC2 preforms which is elastic and non linear. The term $C_{22} = \frac{(1-\nu_p\nu_p)E_t}{\delta}$ is then given by the experimental stress-strain relation by computing the derivative of the relation between stress and strain plotted in Figure 5.14 ($C_{22}^t = \frac{\partial\sigma_{22}}{\partial\epsilon_{22}}$), this relation is interpolated using Lagrange polynomials. This interpolation allows to take into consideration the non linear behavior which is predominant in resin infusion process.

Response of the fluid distribution media

The fluid distribution medium is incompressible with respect to the preform deformability. For this reason, an isotropic linear elastic law introduced in Equation (5.51) is used.

$$\begin{pmatrix}\sigma_{11}\\ \sigma_{22}\\ \sigma_{33}\\ \sigma_{12}\\ \sigma_{23}\\ \sigma_{13}\end{pmatrix} = \frac{E}{(1+\nu)(1-2\nu)}\begin{bmatrix}1-\nu & \nu & \nu & 0 & 0 & 0\\ \nu & 1-\nu & \nu & 0 & 0 & 0\\ \nu & \nu & 1-\nu & 0 & 0 & 0\\ 0 & 0 & 0 & \frac{1-2\nu}{2} & 0 & 0\\ 0 & 0 & 0 & 0 & \frac{1-2\nu}{2} & 0\\ 0 & 0 & 0 & 0 & 0 & \frac{1-2\nu}{2}\end{bmatrix}\begin{pmatrix}\varepsilon_{11}\\ \varepsilon_{22}\\ \varepsilon_{33}\\ 2\varepsilon_{12}\\ 2\varepsilon_{23}\\ 2\varepsilon_{13}\end{pmatrix} \tag{5.51}$$

where E is the Young's modulus taken equal to $200\,kPa$ to provide the stiffness of the fluid distribution medium which is incompressible, and ν is the Poisson's ratio taken equal to 0.4.

Remark: We use the Zebfront langage to include directly the relation $\boldsymbol{\sigma} = \mathbf{C} : \varepsilon(\mathbf{u})$ in Zebulon.

Wet preforms response: coupling solid mechanics with fluid mechanics

Due to the pressure of the resin impregnated into preforms, the behavior of wet preforms is different from the behavior of dry preforms. In this work, we use the most popular model to represent the effect of the resin pressure on the fibrous preforms behavior. This model is the "Terzaghi's" model [K.Terzaghi *et al.* 1967], [E.A.Kempner & H.T.Hahn 1998] which generalizes a Voight's approach of the diphasic medium and writes

$$\boldsymbol{\sigma}(\varepsilon) = \boldsymbol{\sigma_{eff}}(\varepsilon) - p_d\, s\, \mathbf{I}H$$

where $\boldsymbol{\sigma}$ is the stress into preforms, $\boldsymbol{\sigma_{eff}}$ is the effective stress computed in the absence of the resin, s is the saturation taken equal to 1, here p_d is the pressure of resin and $\mathbf{I}$ is the second order identity tensor. Due to the use of the same mesh for wet and dry preforms ("monolithic" approach), we introduce H the Heaviside function equal to 1 in the wet preforms and vanishing elsewhere.

Validation of Terzaghi model

Terzaghi model was validated by Pacquaut [Pacquaut 2009]. This test is illustrated in Figure 5.15. The preform of width $2L$ with $L = 4.10^{-2}\,m$ and of height $H = 2.10^{-2}\,m$ is compacted with a pressure equal to $10^4 Pa$ applied on the top of the domain. A hydrostatic pressure corresponding to the pressure of the resin inside the pores is also applied inside the preform. This pressure is supposed to be linear and is expressed as:

$$p = a\,y + b$$

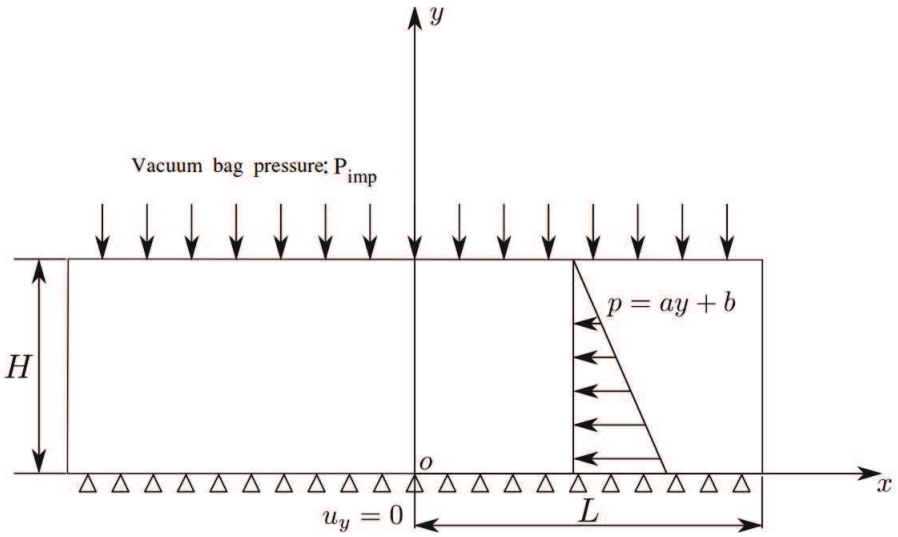

Figure 5.15: Compaction of a preform with free board

where p is the hydrostatic pressure of resin, a and b are coefficients equal to $-5.\,10^{-6}$ and 10^5 respectively. For this test, we choose a linear-elastic law for dry preforms. This simplification allows to obtain an analytical solution of the displacement u_y. This analytical solution is obtained using Airy functions and expressed in Equation (5.52)

$$u_y = \frac{1+\nu}{E}[(1-2\nu)(\frac{a}{2}y+b)y + (\nu-1)G_y] \tag{5.52}$$

with $G = aH + b + P_{imp}$. E is the Young's modulus equal to $266\,kPa$ in this case and ν is Poisson coefficient equal here to 0.3. The deformations are taken planar ($\varepsilon_{xz} = \varepsilon_{yz} = \varepsilon_{zz} = 0$). In addition, one uses updated small deformations because Airy functions are only employed in small deformations. Figure 5.16 shows a comparison between analytical and numerical solutions of the nodes positions for $x = 0$ (symmetric plane). A good correlation between analytical and numerical results is shown in Figure 5.16.

5.4 Conclusions

In this chapter, we presented the main methods used for describing the moving flow front of an interface. We detailed the method that we use in our simulations which is the "level set method". We convect the resin fluid front represented by level set function using the velocity of the coupled problem and we reinitialize it to conserve the property of signed distance.

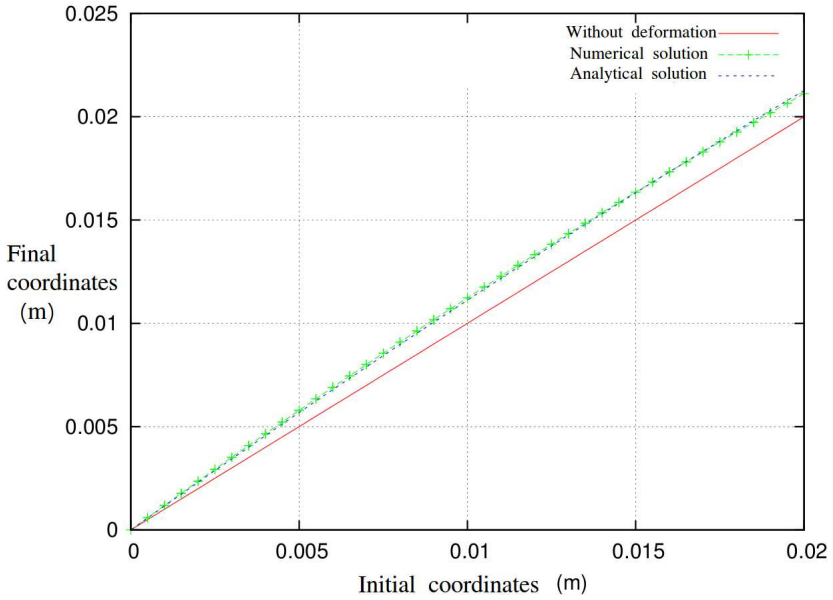

Figure 5.16: Comparison between analytical and numerical results of the node position in the compaction test with free boards

In addition, we have shown its ability to conserve the mass of fluid especially if we used the Cranck-Nicholson scheme. In the second part of this chapter, we presented the deformation of preforms which is an essential phenomenon in LRI processes. For that, we detailed a Lagrangian updated formulation to compute the deformations of preforms, then we used the mass conservation equation to compute the evolution of the porosity during the process and we expressed the permeability as a function of this porosity using Carman-Kozeny formulation. Then, we distinguished between the behavior of wet and dry preforms. The behavior of dry preforms is elastic and non linear, while the behavior of the wet preforms was taken into consideration with the Terzaghi model including the non linear response of the preforms.

The moving flow front of fluid and the deformation of preforms are coupled with Stokes-Darcy problem to represent a complete model used in the simulation of LRI processes. In the next chapter, Stokes-Darcy coupled problem, resin fluid front, solid mechanics problem (deformation of preforms, Terzaghi model, Carman-Kozeny) are coupled and solved with the numerical methods that I have presented so far.

Chapter 6

Numerical simulations of resin infusion processes

Contents

6.1 Introduction

In this chapter, we will present the numerical simulations of LRI processes, taking into consideration the resin flow and the deformation of preforms in severe regimes, with parameters corresponding to the physical reality (permeabilities down to $10^{-15}\mathrm{m}^2$, low thickness of distribution medium relatively to the thickness of porous medium, complex geometries). Some of these simulations will be compared with the experimental results obtained at École Nationale des Mines de Saint Étienne by P. Wang [P.Wang 2010]. Also, we will show the robustness of our model which is valid for large time steps and coarse meshes, leading to low CPU time.

6.2 Coupling algorithms

To explain the coupling between the resin flow, from a purely fluid domain into the porous domain, the evolution of the fluid front, and the deformation of preforms, we will present two algorithms named **"injection"** and **"infusion"** algorithms. The injection algorithm takes into consideration the coupling between the level set problem and the flow of the resin into the preforms. It is used to simulate the injection of the liquid resin into the preforms. Besides, the infusion algorithm is based on coupling the level set problem with the flow of the resin and the deformation of the prefoms. It is used to simulate the resin flow into preforms undergoing large deformations. In the next sections we will present the injection and infusion algorithms to explain the strategy used in coupling the different problems developed in the previous chapters.

6.2.1 Injection algorithm

Injection algorithm proposes a coupling between the resin flow problem and the level set problem. It corresponds to the simulation of the injection of resin into some preforms. At each time step, we solve two problems: Stokes-Darcy coupled problem (Equation (6.1)) and (Equation(6.2)) and level set problem (Equation (6.3)). First, by solving the Stokes-Darcy coupled problem, we get the velocity of the resin that we use in the level set problem to convect the level set function. This algorithm is shown in Figure 6.1.

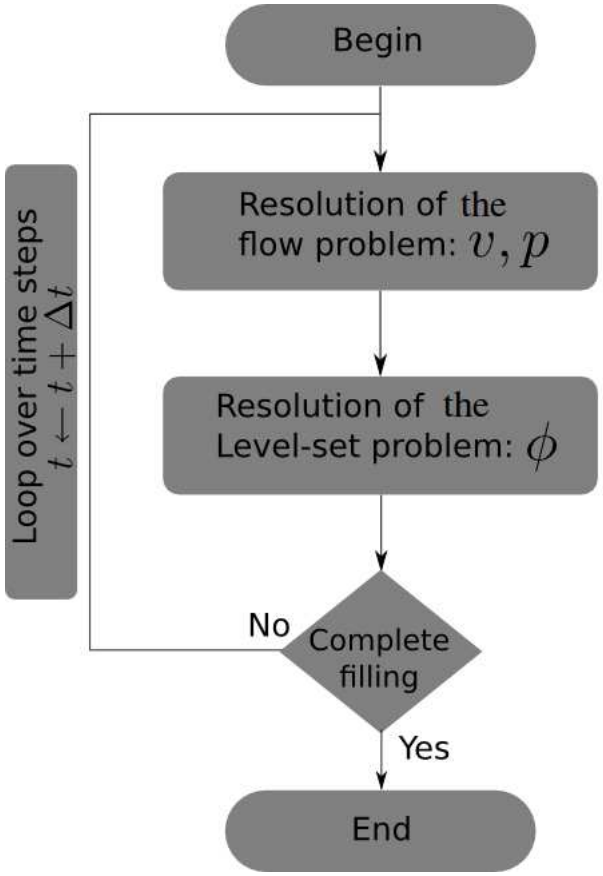

Figure 6.1: Injection algorithm

We have to solve the two following problems:

Stokes-Darcy coupled problem

The resolution of Stokes equations is used to model the flow of resin into the purely fluid domain:

$$\begin{array}{rcrcl} -div(2\mu\dot{\varepsilon}(\mathbf{v_s})) + \nabla p_s & = & 0 & \text{in} & \Omega_s \\ div\,\mathbf{v_s} & = & 0 & \text{in} & \Omega_s \end{array} \tag{6.1}$$

The resolution of Darcy's equations is used to model the flow of resin into the porous medium:

$$\begin{array}{rcrcl} \frac{\mu}{k}\mathbf{v_d} + \nabla p_d & = & 0 & \text{in} & \Omega_d \\ div(\mathbf{v_d}) & = & 0 & \text{in} & \Omega_d \end{array} \tag{6.2}$$

Furthermore we have the conditions on the Stokes-Darcy interface described in Chapter 2 as well as the boundary conditions.

Resolution of the level set problem

The level set problem is convected using the following transport equation:

$$\frac{\partial \phi}{\partial t} + \mathbf{v}.\boldsymbol{\nabla}\phi = 0 \tag{6.3}$$

where $\mathbf{v}$ is the velocity given, at each time step, from the Stokes-Darcy coupled problem.

6.2.2 Infusion algorithm

Compared to injection algorithms, infusion algorithm involves an additionnal problem to be solved (a solid mechanics problem). Indeed, we solve the problem of compaction of preforms obtained by applying a mechanical pressure on the distribution medium and the preforms. This pressure is due to the presence of a vacuum inside the vacuum bag surrounding the stacking. The problems that we have to solve are coupled, for example, through the geometry (resin fluid front, preform geometry). In this algorithm, as in injection algorithms, we propose an algorithm weakly coupled which means that for each time step, each problem is solved subsequently for a once. After this computation, the mesh is updated and a new geometry is obtained. After this step, at each time step, we have to solve four problems:

– The displacement field computed from Equation (6.4) allows us to compute a new porosity using Equation (6.6), then obtaining new permeability using, for instance, the Carman-

Kozeny relation ship (Equation(6.7)).

- The second step consists in solving the resin flow problem Equation(6.1) and Equation (6.2), the velocity and pressure field are obtained in the whole domain.
- The third step consists in solving the transport equation of the level set function (Equation(6.3)) using the velocity obtained by solving the resin flow problem and the mesh velocity ($\mathbf{v_m} = \frac{\Delta \mathbf{u}}{\Delta t}$) is taken into consideration.
- The fourth step consists in solving the deformation of preforms; taking into consideration the inflation of preforms due to the pressure of resin impregnated into preforms through the Terzaghi's model (6.9).
- At the end of each time step, the geometry is updated. The computation is performed until the total filling of preforms is reached.

The infusion algorithm is presented in Figure 6.2. We will recall briefly the additional problems related to the deformation of preforms that we use in infusion processes.

Compaction of preforms:

This problem is solved using an Updated Lagrangian formulation. The Updated Lagrangian formulation uses the Terzaghi's model to describe the response of the wet preforms, the dry preforms have an elastic non linear response.

$$div\boldsymbol{\sigma} = 0 \tag{6.4}$$

$$\boldsymbol{\sigma}(\mathbf{u}) = \boldsymbol{\sigma_{ef}}(\mathbf{u}) \tag{6.5}$$

where $\boldsymbol{\sigma}$ is the cauchy stress given by an orthotropic non linear elastic law with the NC2 preforms behavior in transverse direction.

Computation of porosity and permeability

The porosity is the solution of the transport equation:

$$-\frac{\partial \psi}{\partial t} + (1-\psi) div \mathbf{v_s} = 0 \tag{6.6}$$

where $\mathbf{v_s}$ is the velocity of the preforms, equal to the velocity of the mesh in our case. Using the obtained value of porosity, we compute the new value of the isotropic permeability obtained with the Carman-Kozeny relation (6.7):

$$K = \frac{d_f^2}{16\, h_K} \frac{\psi^3}{(1-\psi)^2} \tag{6.7}$$

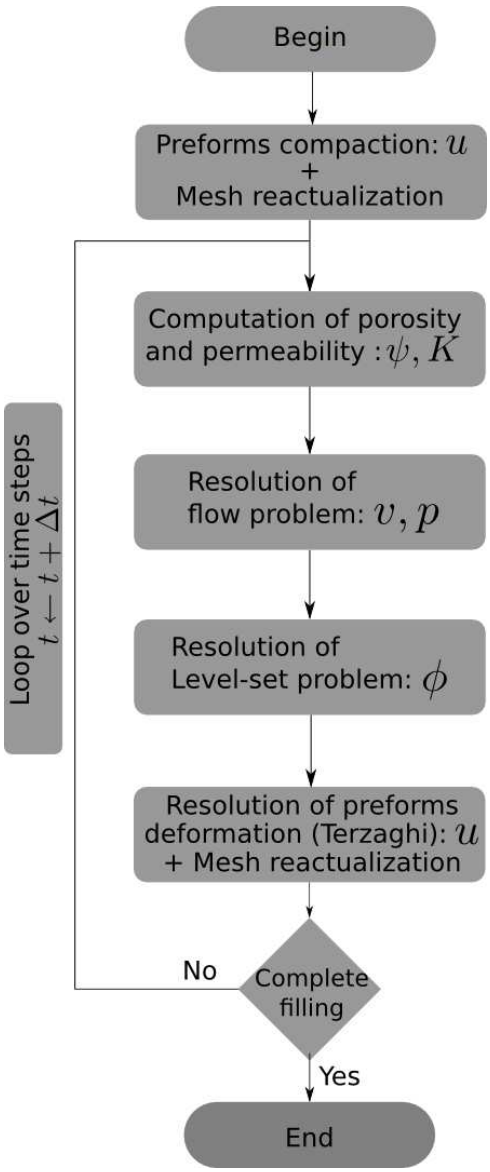

Figure 6.2: Infusion algorithm

where d_f is the diameter of the fibers and h_K is the Kozeny constant.

Deformation of preforms problem

An Updated Lagrangian formulation is used to compute the deformations of preforms. The behavior of preforms is orthotropic non linear elastic given by NC2 preforms behavior in transverse direction. The effect of resin in wet preforms in given by Terzaghi's model. This problem is solved by Equation (6.8).

$$div\boldsymbol{\sigma} = 0 \tag{6.8}$$

with

$$\boldsymbol{\sigma}(\mathbf{u}) = \boldsymbol{\sigma_{eff}}(\mathbf{u}) - p_d \mathbf{I}\, H_f \tag{6.9}$$

where p_d is the pressure of the resin (after its infusion) in porous medium and H_f is equal to 1 if the resin is present into preforms.

6.3 Simulation of the transient flow

Let us note that in all the simulations of the transient flow, the constants c_1, c_u and c_p in the stabilization terms are taken as $c_1 = 1$, $c_u = 2$ and $c_p = 2$. The term L_0 is also taken equal to $L_0 = \sqrt[m]{meas(\Omega_d)}$ (m is the dimension) and $meas(\Omega_d)$ is the surface of Ω in 2D cases and the volume of Ω in 3D cases. Moreover, the thickness E in the filtered level set function is $E = 20\, h_K$ where h_K is the size of mesh. In this section, we will present different numerical simulations of LRI processes based on the injection algorithm. These simulations are conducted with real physical parameters of composite materials. Different hypotheses are validated in these tests: Stokes-Darcy problem coupled with the level set, filling of a distribution medium of very low thickness relatively to the thickness of preforms, the robustness of the model for very low permeabilities ($10^{-14}\mathrm{m}^2$), for complex geometries (in 2D and 3D cases), for coarse meshes, and different ranges of time step ($[0.1s, 100s]$).

6.3.1 Injection of a plate with filled distribution medium

In this simulation, we suppose that the distribution medium is already filled with the resin. The aim is to simulate the impregnation of the resin through a preform of low permeability using Stokes-Darcy problem coupled with the level set problem.

6.3.1.1 Definition of the problem: geometry and boundary conditions

The first case corresponds to the simulation of the resin infusion into preforms of thickness $20\,mm$ and of width $385\,mm$. The thickness of the fluid distribution medium is $\frac{1}{10}$ of the porous media thickness ($2mm$). In Figure 6.3, one can verify that commonly used distribution media are of the order of a few mm, and consist in a polyester grid, supposed not to be deformable under the mechanical state prevailing in infusion processes.

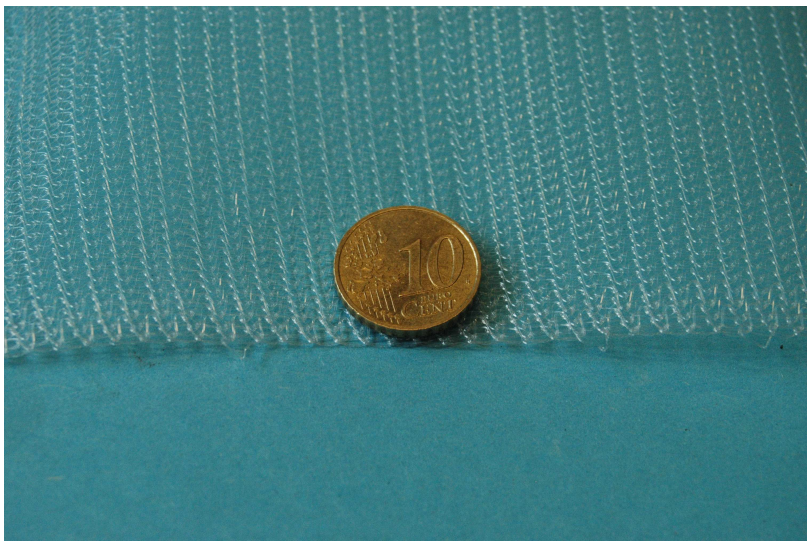

Figure 6.3: A distribution medium consisting in a polyester grid

Geometry and boundary conditions are shown in Figure 6.4. A pressure of $10^5 Pa$ is applied on the top of the domain and a zero pressure is imposed on the bottom. On the other sides of the domain, a zero normal velocity is prescribed.

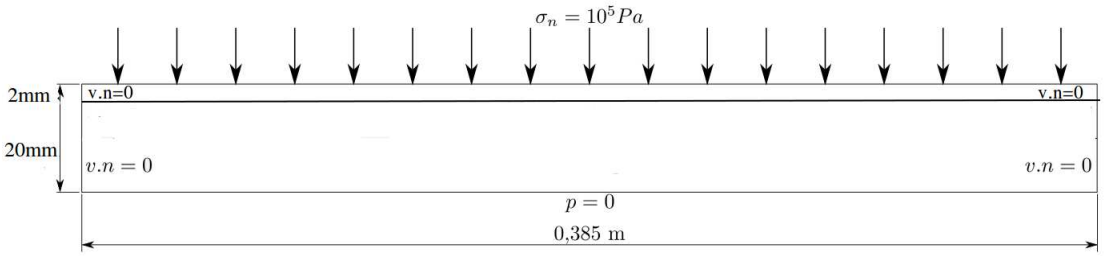

Figure 6.4: Geometry and boundary conditions of a plate with filled distribution medium

The mesh is realized with gmsh and made up of 2500 nodes. For this simulation, we choose a coarse mesh (Figure 6.5) and different time steps ($\Delta t \in [1s, 100s]$) which are relatively high regarding the velocities expected. For this simulation, we have two level set functions: the

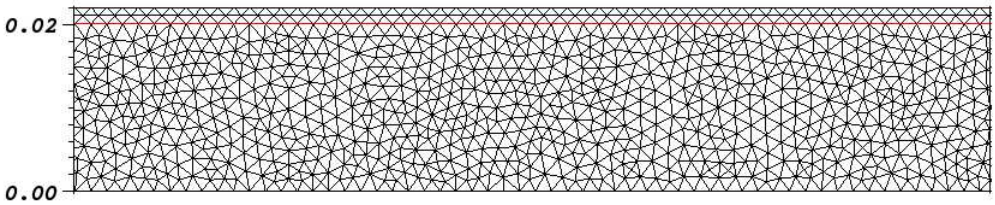

Figure 6.5: mesh made up by triangles and Stokes-Darcy interface in red (2500 nodes and 5000 elements).

level set function used to separate Stokes and Darcy domains and the level set function used to follow the resin flow front. Because the distribution medium is filled by resin, these two level set functions coincide at the begining of the simulation. Taking into consideration that we use a monolithic approach, the porous medium not impregnated with resin is filled with air assumed to behave as an incompressible Newtonian fluid with very low viscosity μ_a compared with the viscosity of the resin μ_f: $\mu_a << \mu_f$. To realize the transition between the properties of the air and the properties of the fluid, we use a mixing law on the interface. For that, we consider a particular thickness of the fluid-air interface ($\epsilon = 0.5\, h_K$, where h_K is the size of mesh) and we use the Heaviside function $H(\phi_f)$ equal to one in Stokes domain ($\phi_f > 0$), equal to zero in Darcy's domain ($\phi_f < 0$) and equal to $\frac{1}{2}(1 + \frac{\phi_f}{\epsilon})$ if $-\epsilon < \phi_f < \epsilon$. This mixing law is given by Equation (6.10).

$$\begin{array}{rcccl} \mu & = & H(\phi_f)\mu_f & + & (1 - H(\phi_f))\mu_a \\ \rho & = & H(\phi_f)\mu_f & + & (1 - H(\phi_f))\rho_a \end{array} \tag{6.10}$$

This simulation is conducted for different values of permeability $[10^{-9}, 10^{-11}]\mathrm{m}^2$. The other parameters of this simulation are presented in Table 6.1.

Injection pressure	Resin viscosity	air viscosity	preform thickness
$10^5 Pa$	$0.03 Pa.s$	$10^{-4} Pa.s$	0.02m

Table 6.1: Physical parameters of the numerical simulation

6.3.1.2 Results of the simulation

Figure 6.6 shows the flow of the resin into preforms for $k = 10^{-14}\mathrm{m}^2$ and $\Delta t = 100s$. Air is represented in blue and resin is represented in red. The distribution medium is filled with resin at the begining of the simulation and the unidirectional flow is verified.

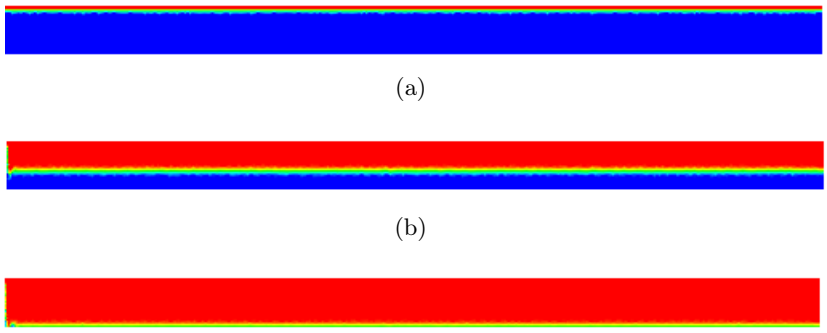

(a)

(b)

(c)

Figure 6.6: Results of a plate simulation with filled distribution medium. Air is shown in blue and resin is shown in red, $k = 10^{-14}m^2$, $\Delta t = 100s$.

One of the essential goals of the simulations of LRI processes is to predict the total time required to fill the preforms. Many parameters influence the filling time, the injection pressure, permeability of the porous medium, viscosity of the resin $\cdots$

In the presented case, the flow is unidirectional. For this reason, by using Darcy's law in porous media, an analytical solution is obtained to determine the position of the resin front as function of time. This relation writes

$$y(t)^2 = \frac{2k\Delta p}{\mu}\, t \tag{6.11}$$

where $y(t)$ is the position of the fluid front, k is the permeability of the preform, Δp is the difference of pressure between the top and the bottom of the domain, μ is the resin viscosity and t is time.

Computation of the position of the resin front

Figure 6.7 shows a comparison between the analytical and numerical position of the resin front as function of time for $\Delta t = 100s$ and $\Delta t = 1s$. This comparison is conducted for $k = 10^{-14}\mathrm{m}^2$.

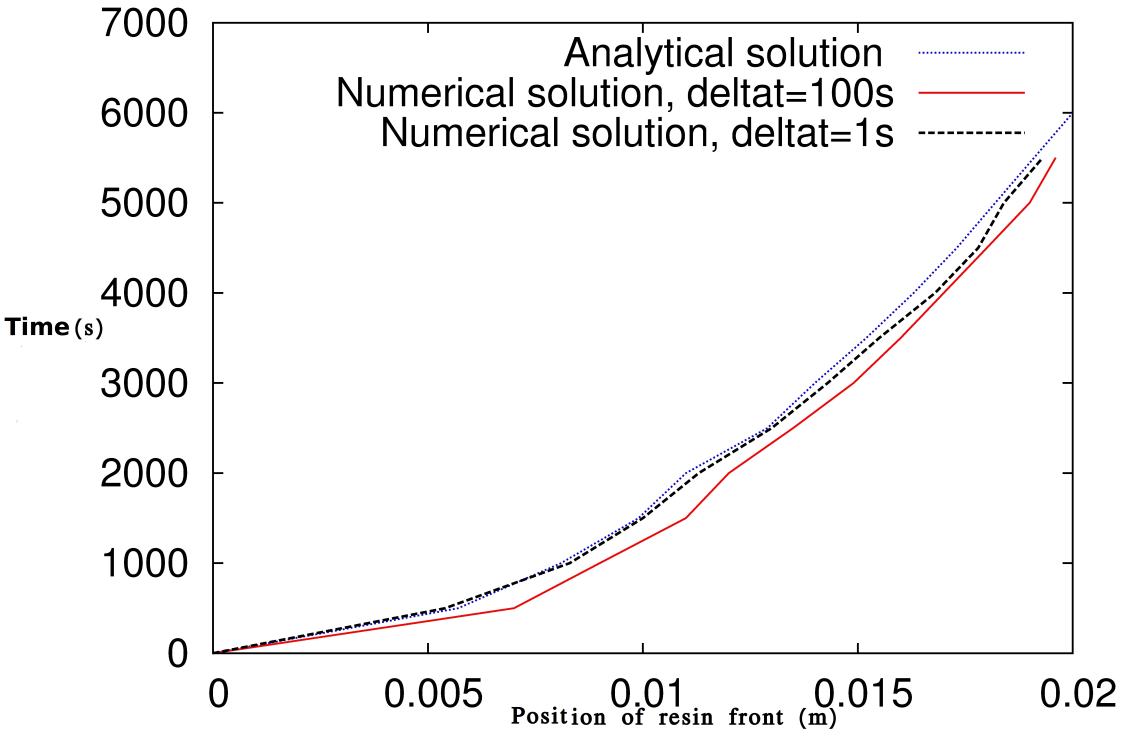

Figure 6.7: Position of the resin front in function of time

We deduce a good correlation between numerical and analytical results especially for $\Delta t = 1s$.

To focus on the importance of the time step on this simulation, we show in Table 6.2, the relative errors between the analytical and numerical values of the total filling time of the preforms relatively to the time step. Let us note that the relative error is computed as $\frac{|t_a - t_n|}{t_a} \times 100$ where t_a and t_n are respectively the analytical and numerical times for the complete filling of the preform. In this case, for a permeability $k = 10^{-14}\mathrm{m}^2$, a resin viscosity $\mu = 0.03Pa.s$, a differential of pressure $\Delta p = 10^5 Pa$, and a thickness of preform equal to $0.02m$, the anaytical time of filling the preform is $6000s$.

It is good to notice that even if the time step is high ($\Delta t = 100s$ for example), the relative error is a very good compromise regarding interesting CPU time that we have, more than 100 times lower than for $\Delta t = 1s$.

Δt	numerical filling time	relative error [%]	CPU time
$1s$	$5990s$	0.16%	$10200s$
$10s$	$5970s$	0.5%	$1020s$
$30s$	$5930s$	1.16%	$340s$
$50s$	$5900s$	1.66%	$200s$
$100s$	$5800s$	3.33%	$100s$

Table 6.2: Values of the relative errors of the filling time, and values of the CPU time of the simulation with respect to the time step

Influence of the permeability on the filling time

To study the influence of the permeability on the filling time, we did many simulations with different values of permeability $[10^{-11}, 10^{-14}]\mathrm{m}^2$. Figure 6.8 shows the change in the filling time as function of the permeability (the time step considered is $\Delta t = 1s$). Figure 6.8 shows that the filling time is proportional to $1/k$ which is in accordance with Equation (6.11).

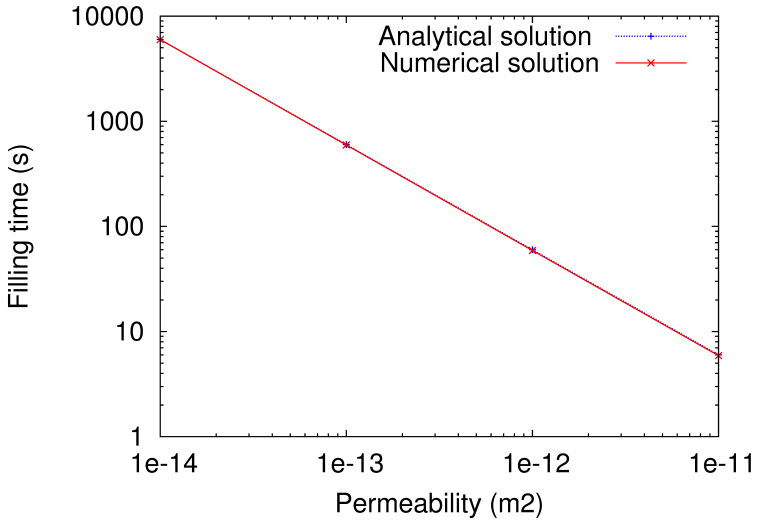

Figure 6.8: The filling time as a function of permeability in log-log scale with a slope equal to 1

This first case shows the robustness of our model in many points:

– The results are valid for all the permeabilities, included very low permeability ($k = 10^{-14}\mathrm{m}^2$)

– The model is robust for all the time steps and for large mesh sizes (coarse meshes)
– The CPU times are relatively low due to the low number of elements and the high time step

6.3.2 Injection of a plate with filling of the distribution medium

The aim of this simulation is to simulate the filling of the distribution medium for different thicknesses and the impregnation of the resin into the preforms. In this case, we can not compare the numerical results with an analytical solution, because the flow is not unidirectional, which means that there is no simple analytical solution to this simulation.

6.3.2.1 Definition of the problem: geometry and boundary conditions

The domain of computation is a rectangle $0.033\text{m} \times 0.292\text{m}$ with an injection inlet. Geometry and boundary conditions are presented in Figure 6.9. A normal stress of $1bar$ is imposed on the injection inlet and zero pressure is imposed on the bottom of the domain. On the other sides of the domain, a zero normal velocity is imposed.

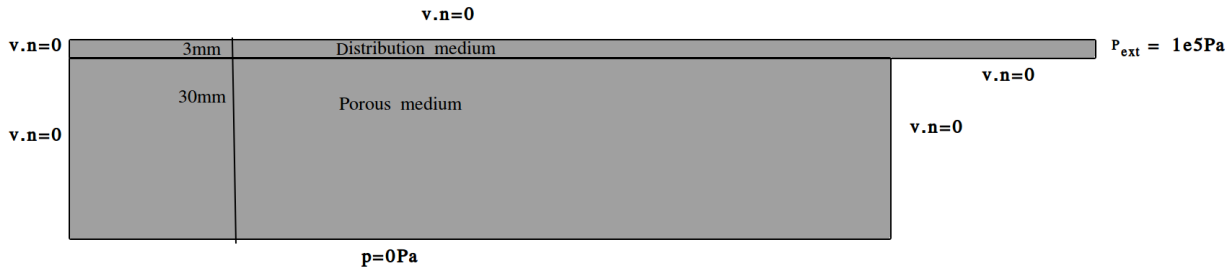

Figure 6.9: Geometry and boundary conditions

This simulation is carried out for different values of permeability $k \in [10^{-9}\text{m}^2, 10^{-14}\text{m}^2]$ and the other physical parameters are presented in Table 6.3.

Injection pressure	Resin viscosity	thickness of preform
$10^5 Pa$	$0.03 Pa.s$	0.03m

Table 6.3: Physical parameters of the numerical simulation

The mesh is realized with gmsh [Geuzaine & Remacle 2009] and is made up by 2300 nodes which is relatively high (Figure 6.10).

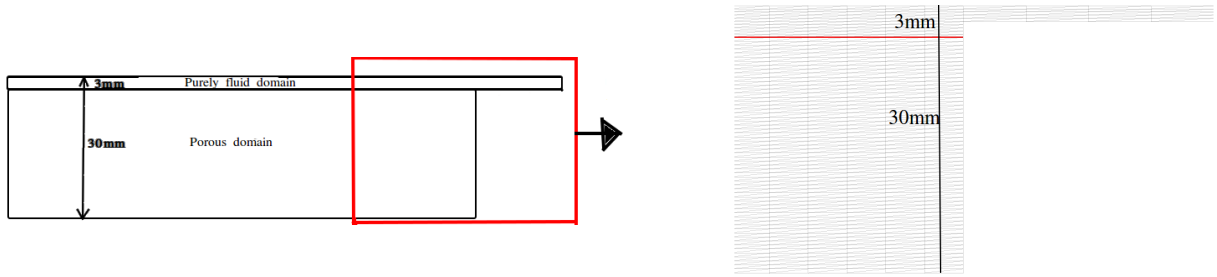

Figure 6.10: Zoom on the fluid medium and the porous medium mesh and Stokes-Darcy interface in red

6.3.2.2 Results of the simulation

Figure 6.11(a) and 6.11(b) show the results of pressure and velocity for this simulation. The pressure and velocity do not show oscillations for this low permeability ($10^{-14}\mathrm{m}^2$) and this low thickness of distribution medium.

Figure 6.12 shows the flow of the resin for a permeability $k = 10^{-14}\mathrm{m}^2$. Red color represents the resin and blue color represents the air. The total time of filling of the distribution media is of order $150s$ and the time for filling the preforms is $13870s$. The CPU time of this simulation is 30 minutes. First when filling the distribution medium the time step is $\Delta t = 1s$, then the time step is changed to $\Delta t = 10s$.

We deduce that the distribution medium is totally filled first, and then the impregnation of resin into preforms starts. This is due to the low permeability ($10^{-14}\mathrm{m}^2$) of the preforms. In the next paragraph, we will validate this hypothesis with two different permeabilities.

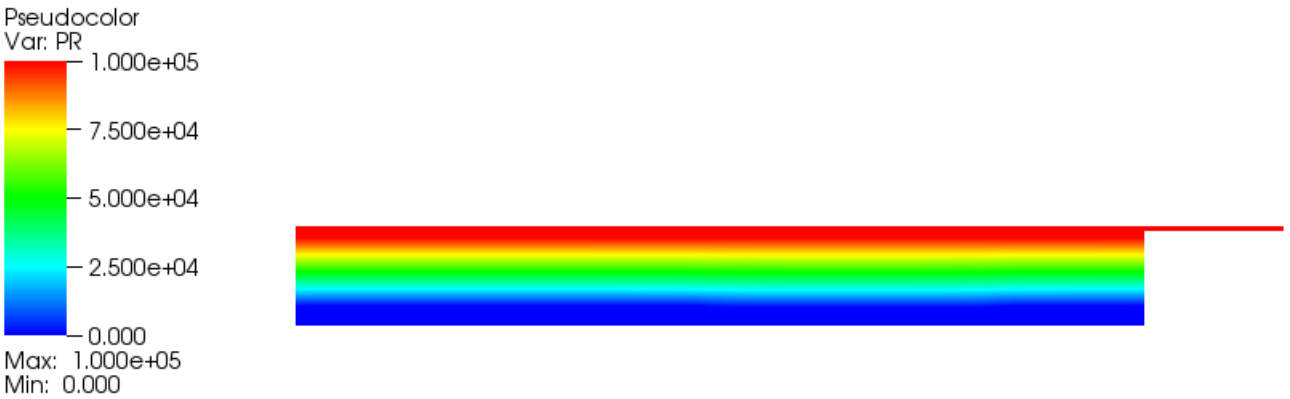

(a)

(b)

Figure 6.11: (a) Pressure distribution, (b) velocity distribution for a permeability $k = 10^{-14}\mathrm{m}^2$

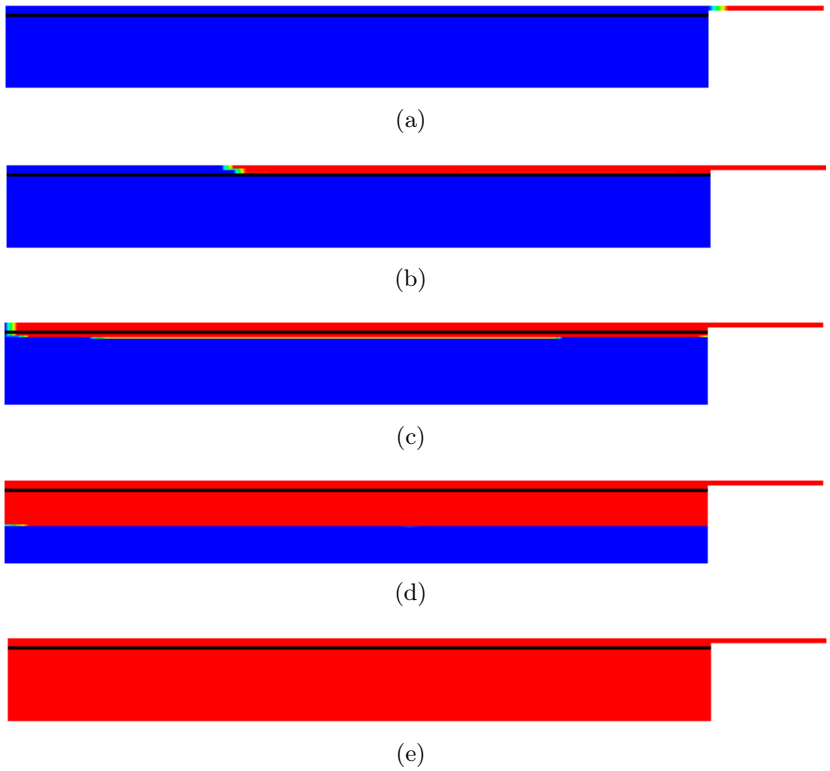

(a)

(b)

(c)

(d)

(e)

Figure 6.12: 2D simulation of resin injection with filling the distribution medium for $k = 10^{-14}m^2$, and a distribution medium thickness equal to $3mm$. The resin is represented in red and the air is represented in blue.

Influence of the distribution medium thickness on the filling time of the preforms

Figure 6.13 shows the filling of the distribution medium and of the preforms for a permeability $k = 10^{-14}\mathrm{m}^2$, for a thickness of distribution medium equal to 30 mm and for a thickness of preforms equal to 30 mm.

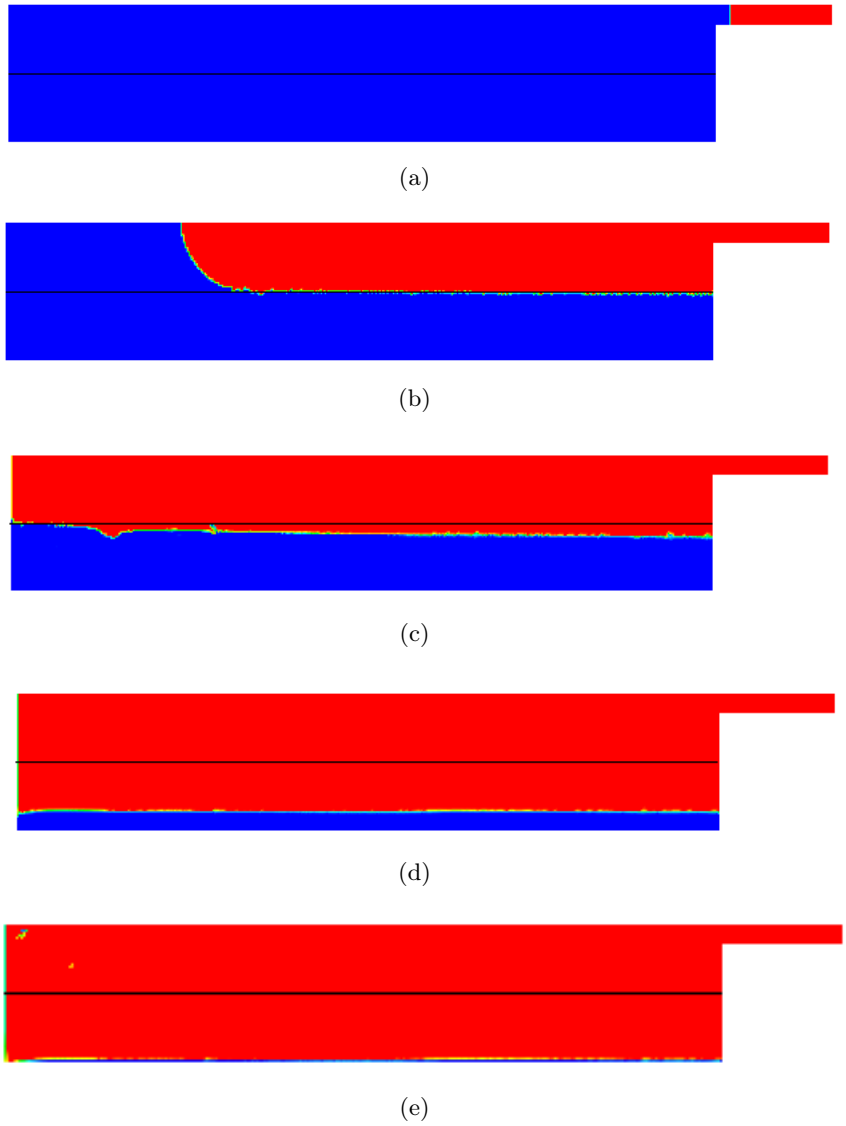

(a)

(b)

(c)

(d)

(e)

Figure 6.13: 2D simulation of resin injection with filling the distribution medium for $k = 10^{-14}m^2$, and a fluid medium thickness equal to 30 mm. The resin is represented in red and the air is represented in blue.

When the thickness of the distribution medium is high (which does not correspond to the real physical reality of LRI processes), the time for filling preforms is 12000s which is lower then 13870s, the time of filling preforms when the thickness of distribution medium is 3 mm.

Influence of the preform permeability

As we have mentionned before, when permeability is of order $10^{-14}\mathrm{m}^2$, the resin is impregnated after the total filling of the distribution medium. Figure 6.14 shows a 2D simulation of resin injection for a permeability equal to $10^{-8}\mathrm{m}^2$. We deduce that for a permeability of the order

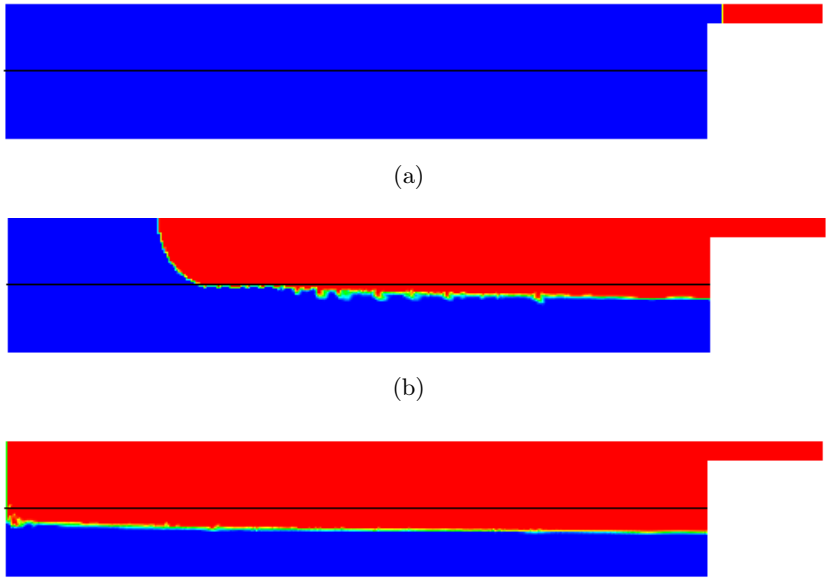

(a)

(b)

(c)

Figure 6.14: 2D simulation of resin injection with filling the distribution medium for $k = 10^{-8}m^2$, and a fluid medium thickness equal to 30 mm. The resin is represented in red and the air is represented in blue.

$10^{-8}\mathrm{m}^2$, the resin begins its impregnation into preforms before the total filling of the preforms, contrary to the low permeability cases. This has a great influence in turning the injection strategy.

6.3.2.3 3D extension

A similar 3D simulation is carried out. Geometry is the same as in 2D case, extruded along the **z** axis. The thickness of distribution medium is $10\,mm$ and the thickness of preforms is $30\,mm$. The filling time of preforms is $3150s$ which corresponds to a logical physical time corresponding to filling a preform with a permeability of $10^{-13}\mathrm{m}^2$. The time step used when filling Darcy is $\Delta t = 10s$. The mesh is made up by 10000 nodes and the CPU time is $120mn$. All the results and validated hypotheses for 2D cases are valid for this simulation. Results for this simulation are presented in Figure 6.15 for $p_{ext} = 10^5 Pa$, $k = 10^{-13}\mathrm{m}^2$ $\mu = 1Pa.s$.
In addition, the time step used is $1s$ during the filling of the distribution medium and $10s$ when filling the preforms. We remark that in Figure 6.15, the air is imprisoned in the right side of the piece, this is due to the little difference between the inlet and Darcy's domain.

6.3.3 Complex piece

To validate the model used to simulate the LRI process, we will simulate a complex piece with particular geometrical form. The aim of this simulation is to realize a flow in a complex piece for very low permeabilities. The technical difficulty in this simulation, is the initialization of the interface between Stokes and Darcy's domains. The details of this initialization will be presented in Appendix B.

6.3.3.1 2D case

The geometry and boundary conditions of this simulations are presented in figure 6.16. A pressure of $10^5 Pa$ is imposed on the inlet of injection. Zero pressure is imposed on the bottom of the domain. On the other sides of the domain, zero normal velocity is imposed. The mesh is realized with gmsh and the number of nodes is 3200 (Figure 6.17).

Numerical results

We will present the results of the simulation in $2D$ for two values of permeability ($k = 10^{-7}\mathrm{m}^2$ and $k = 10^{-14}\mathrm{m}^2$) to study the influence of the preform permeability on the resin flow.

Figure 6.18 shows the flow of the resin in a $2D$ case for a permeability $k = 10^{-7}\mathrm{m}^2$. We conclude that the resin flows into preforms before the total filling of the distribution medium. This is due to the high permeability of preforms which allows an easy impregnation of resin. We observe also a radial flow of the resin. The total filling time of this simulation is $0.0068s$. This

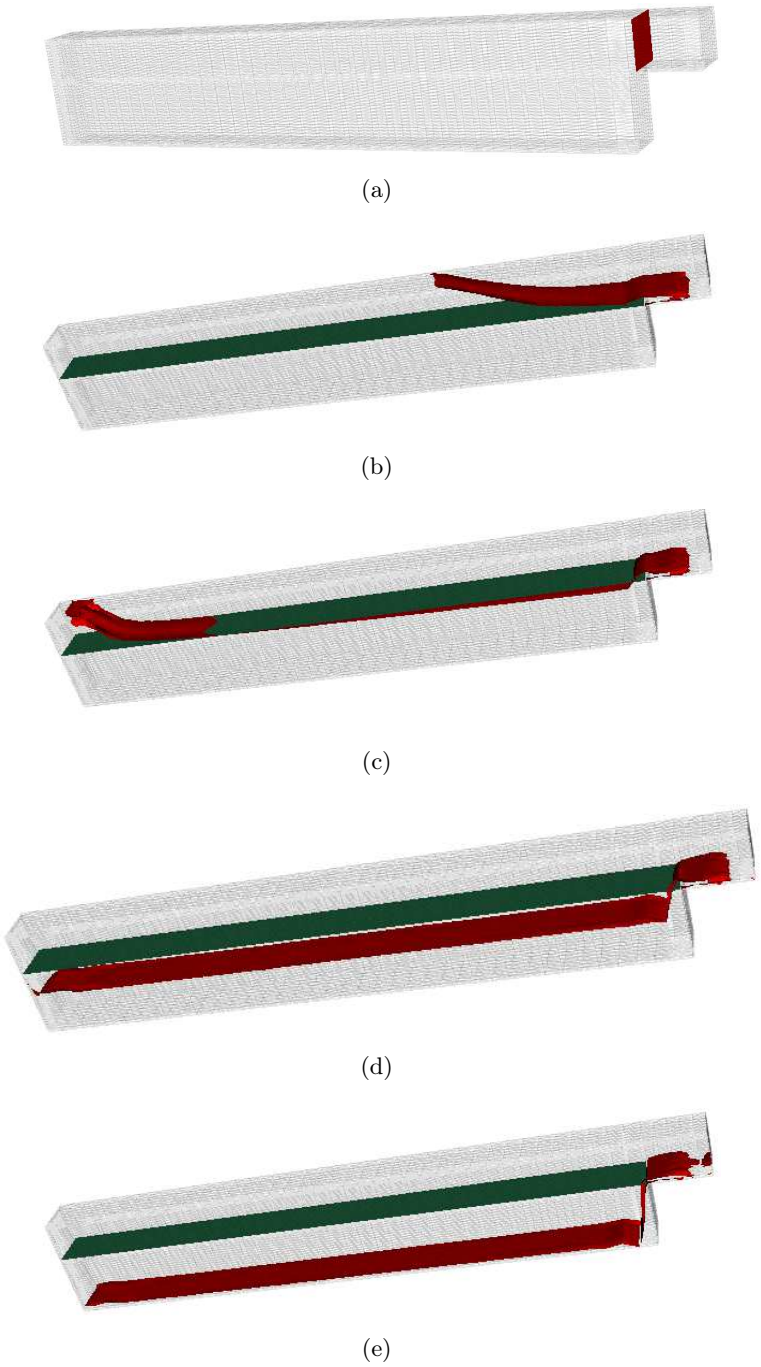

(a)

(b)

(c)

(d)

(e)

Figure 6.15: 3D simulation of resin injection with filling the distribution medium for $k = 10^{-13}m^2$. The resin is represented in red and the air is represented in blue.

time is quick compared with the real cycle times of resin infusion process. It is a consequence of the high permeability used in this case. The time step is $\Delta t = 0.002s$ and the CPU time is

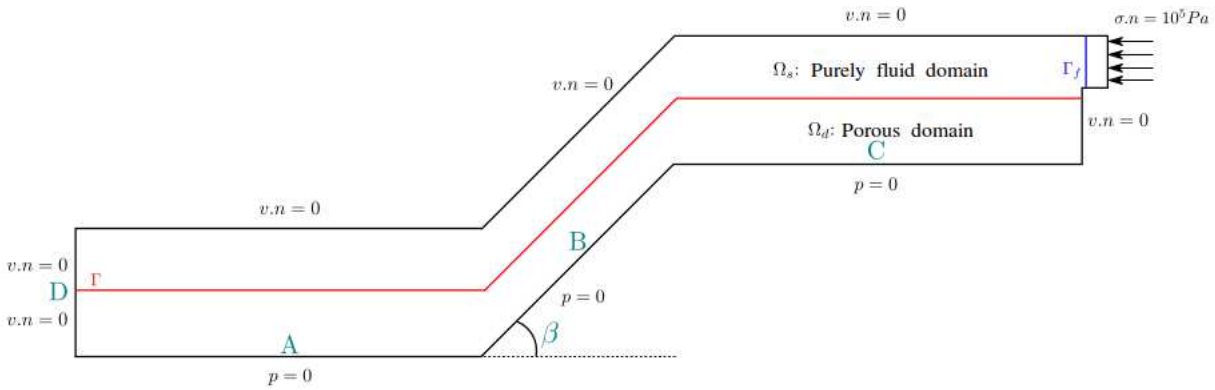

Figure 6.16: Geometry and boundary conditions of a $2D$ complex piece with $A = 0.1\,m$, $C = 0.1\,m$, $D = 0.04\,m$ and $\beta = \frac{\pi}{4}$

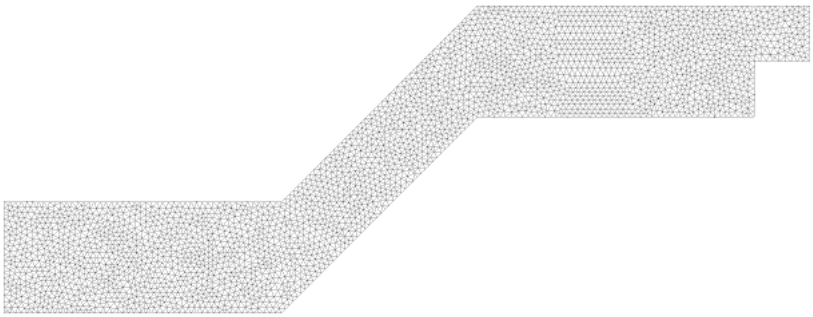

Figure 6.17: mesh of the 2D complex piece made up of 3213 nodes

$70s$. Figure 6.19 shows the flow of the resin in $2D$ case for a permeability $k = 10^{-14}\mathrm{m}^2$. We deduce that the resin fills the distribution medium first, and then the impregnation of preforms begins. The filling time of this simulation is $3570s$, the time step $\Delta t = 10s$ when we fill the distribution medium and $\Delta t = 100s$ when we fill the preforms. The CPU time is $120s$.

These simulations allow to verify the hypothesis of the prefilled layer for low permeabilities ($k < 10^{-9}\mathrm{m}^2$). We conclude on the robustness of our simulations, first because we dont have any oscillations around the interface for both pressure (Figure 6.20(a)) and velocity (Figure 6.20(b)) for very low permeabilities, second because we use coarse meshes with high time step which reduce a lot the CPU time of the simulation without affecting the results significantly. We deduce also that for the low permeabilities ($10^{-14}\mathrm{m}^2$) the filling time corresponds to the cycle time of resin infusion process used in industry [P.Wang 2010].

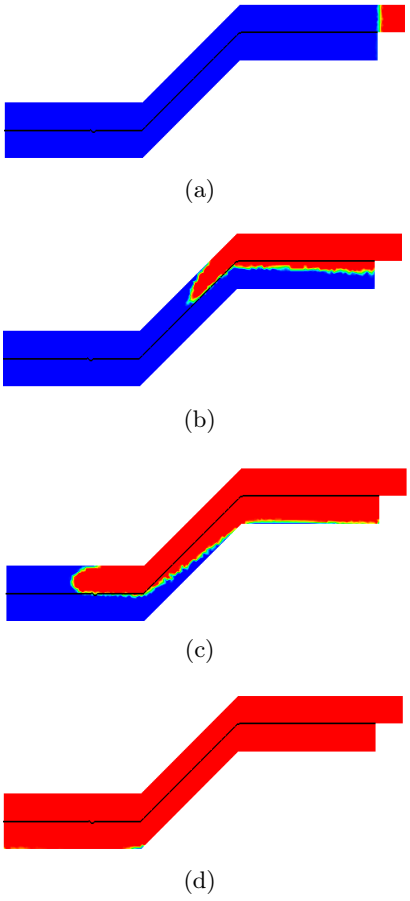

(a)

(b)

(c)

(d)

Figure 6.18: 2D simulation of resin injection with filling of the distribution medium for $k = 10^{-7}m^2$. The resin is represented in red and the air is represented in blue.

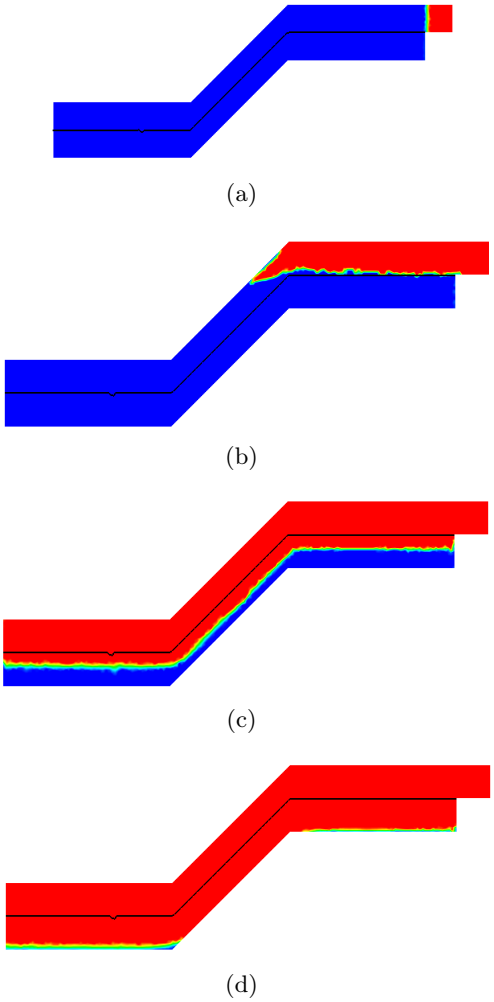

(a)

(b)

(c)

(d)

Figure 6.19: 2D simulation of resin injection with filling the distribution medium for $k = 10^{-14}m^2$. The resin is represented in red and the air is represented in blue.

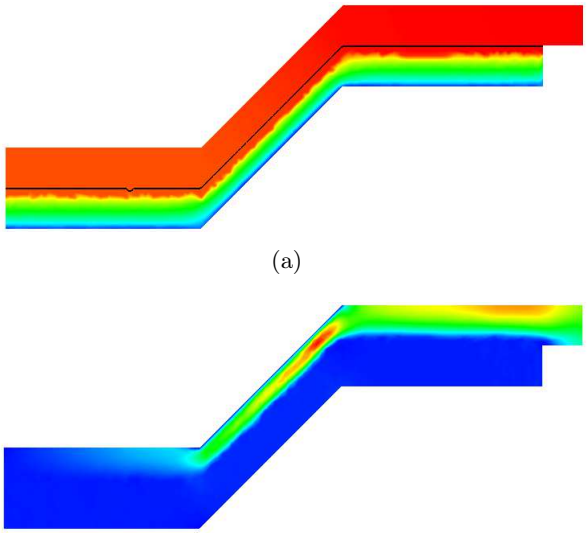

(a)

(b)

Figure 6.20: (a) Pressure distribution and (b) velocity distribution for a 2D simulation of a complex piece

6.3.3.2 3D case

The 3D complex geometry is the same as in 2D case, extruded along the **z** axis. The mesh of this 3D piece is realized by gmsh and is made up of 23 000 nodes (Figure 6.21).

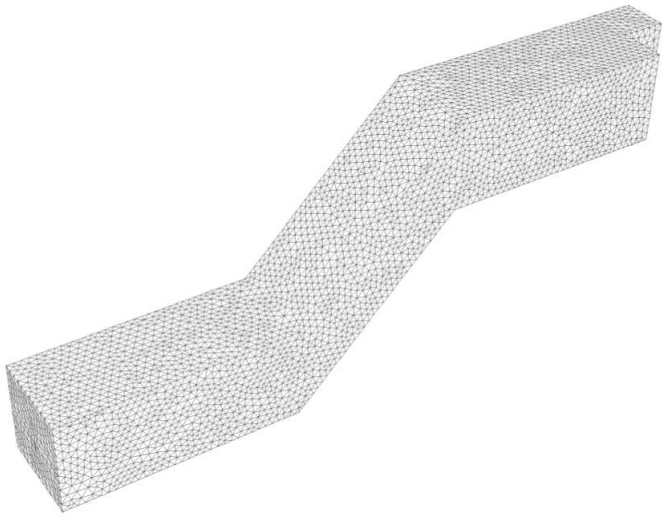

Figure 6.21: 3D mesh of complex piece

As in 2D cases, the technical difficulty in this simulation is the initialization of the interface which separates Stokes and Darcy because it has a particular form, this initialization will be detailed in appendix B. The initial fluid front is simply initialized by a plane. Boundary conditions are the same as in 2D case. Permeability is $k = 10^{-13}\mathrm{m}^2$ and the filling time is of $900s$. As for all our simulations, our model shows also its robustness in this case, for all the time steps and for all the permeabilities. Figure 6.22 shows the resin position during its injection in the complex piece for a permeability equal to $10^{-13}\mathrm{m}^2$. In this case the time step is $1s$ when filling Stokes' domain and it increases to $10s$ when filling Darcy's domain which reduces the CPU time to 120 minutes even if we are in a 3D case and the mesh contains a considerable number of elements.
On the top of the piece, the front of the resin disappear because we have a numerical diffusion which make $\phi_f = +\varepsilon$ (very small positive value) instead of $\phi_f = 0$.
We remark also that in the bottom of the piece, the flow is radial and we can have a filling default (see Figure 6.23)

There is no oscillations of velocity around the interface (Figure 6.24(a)) and for pressure (Figure 6.24(b)) despite the low permeability and the complex geometry of the piece.

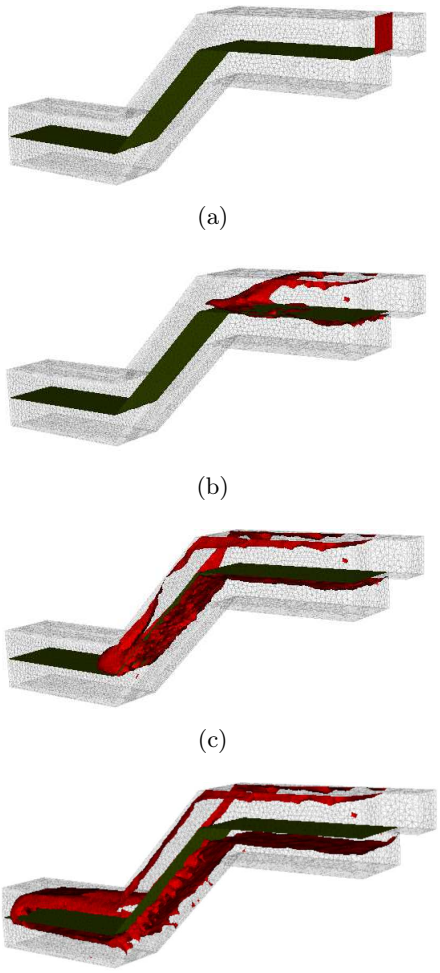

(a)

(b)

(c)

(d)

Figure 6.22: 3D simulation of resin injection with filling the distribution medium for $k = 10^{-13}m^2$. The resin is represented in red and the air is represented in blue.

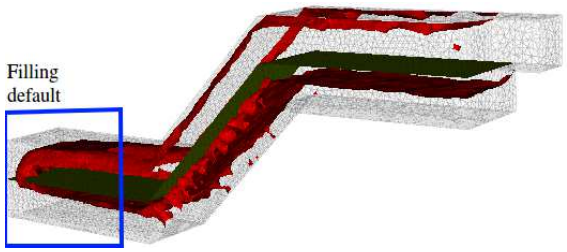

Figure 6.23: Zoom on the filling default located in the bottom of the complex piece where the resin has a radial flow

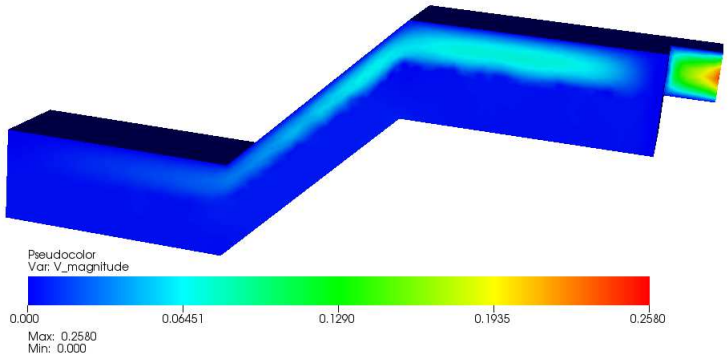

(a)

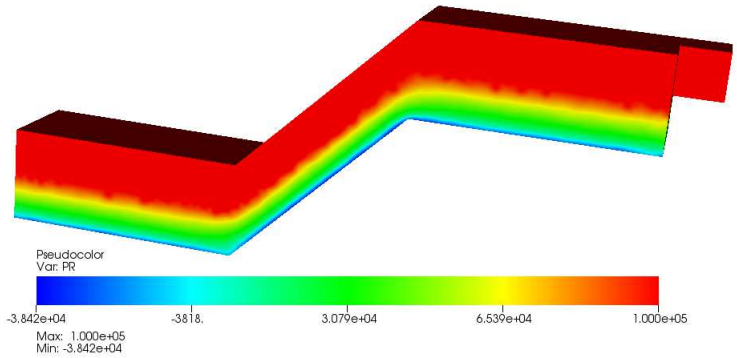

(b)

Figure 6.24: (a) velocity distribution, (b) pressure distribution for a 3D simulation of a complex piece with a permeability $k = 10^{-13}\mathrm{m}^2$

6.4 Simulation of the transient flows with the deformations of preforms

In the infusion tests, the numerical constants of stabilization are taken as $c_1 = 1$, $c_p = 2$, $c_u = 2$ and $L_0 = \sqrt[m]{meas(\Omega_d)}$. As for transient flow, the thickness E in the filtered level set function is $E = 20\,h_K$ where h_K is the size of mesh. Concerning the solid mechanis problem, in distribution medium where we have an elastic linear behavior, the Young modulus E_p is equal to $200\,kpa$ and the Poisson coefficient ν is equal to 0.4. While the behavior of preforms in transverse direction (the direction of deformations) is described by the elastic non linear of NC2 preforms given by experiments.

6.4.1 Infusion of plate

In these simulations, we will take into consideration the deformation of preforms. For that we will validate the weak coupling between the solid mechanics and the fluid mechanics problems. To validate the robustness of our approach and its application in real physical case, we will do a comparison between our results and the experimental results obtained by P. Wang [P.Wang 2010].

6.4.1.1 Definition of the problem: geometry and boundary conditions

Resin infusion simulation is carried out on a plate preform of thickness 0.01m and of width 0.385m. The geometry and boundary conditions are presented in Figure 6.25. In this case, we have two types of boundary conditions: the boundary conditions corresponding to the solid mechanics problem (Figure 6.25(a)) and the boundary conditions corresponding to the fluid mechanics problem (Figure 6.25(b)).

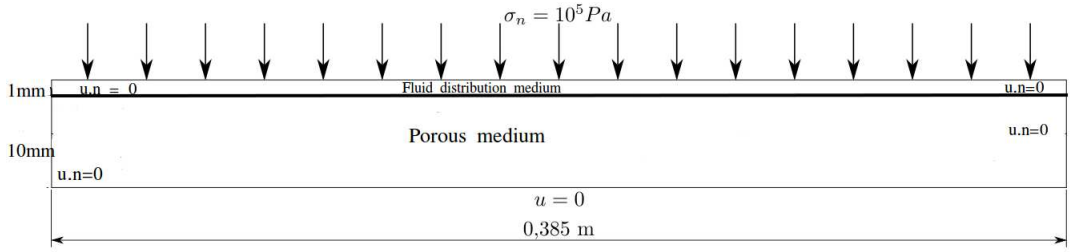

(a)

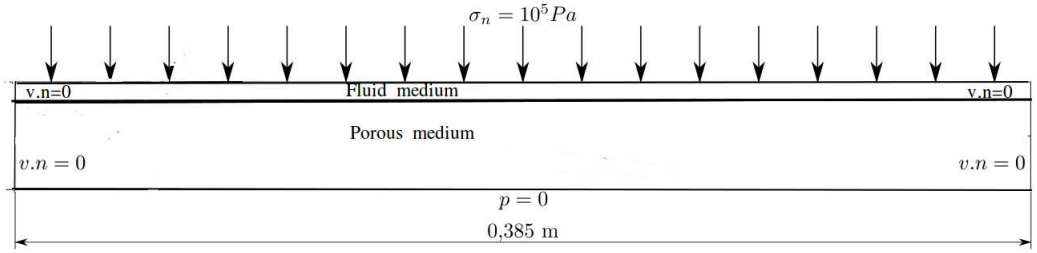

(b)

Figure 6.25: Boundary conditions of a plate infusion with filled distribution medium for the solid mechanics problem (a) and for the fluid mechanics problem (b)

– For the solid part, a pressure of $1bar$, applied by the vacuum bag, is imposed on the top of the domain. On the bottom of the domain, zero displacement is imposed because the stacking of resin and preforms lies on a rigid mould. On the other sides of the domain, zero displacement conditions are imposed.

– For the fluid part, an injection pressure of $1bar$ is imposed on the top of the domain and zero pressure is applied on the bottom of the domain to have a pressure gradient between the top and the bottom of the domain and to allow to the air to be pulled out, air is considered as a Newtonian icompressible fluid of very low viscosity relatively compared the resin. To avoid the outflow of the resin on the boundaries, zero normal velocity is imposed.

The mesh is realized with gmsh and is made up by $2,400$ nodes (Figure 6.26). An infusion test of a plate with 24 and 48 plies of quasi-UD G1157 is carried out.

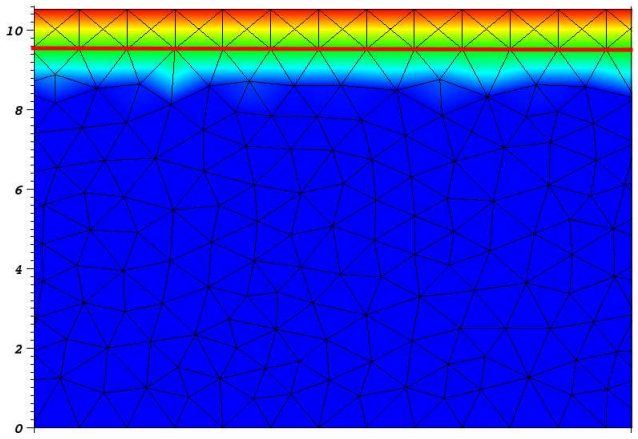

Figure 6.26: A zoom on the coarse mesh of this plate with the Stokes-Darcy interface in black color

For the stacking of 24 UD G1157 plies, the thickness of the preforms is about 10mm and for the stacking of 48 UD G1157 PLIES, the thickness of preforms is of about 20mm [P.Wang 2010]. The initial porosity is 61%, the diameter of the carbon fiber is $5\,10^{-6} meter$ and the constant of Cozeny is then equal to 10 which corresponds to an initial permeability equal to $3\,10^{-14}\mathrm{m}^2$. In this case, we consider the resin **RTM6**, its viscosity is considered constant equal to $0.058Pa.s$ which corresponds to the estimated value during the first 30 minutes of the process. The parameters of these two simulations are summarized in Table 6.4. The time step is $\Delta t = 4s$.

Resin viscosity	Initial permeability	Initial porosity	thickness of preform
$0.058Pa.s$	$3 \times 10^{-14}\mathrm{m}^2$	61%	10 mm

Table 6.4: Physical parameters of the numerical simulation

6.4.1.2 Numerical results and comparison with experimental results

Figure 6.27 shows the flow of the resin into the 24 plies stacking. The resin is represented in red and the air is represented in blue. The distribution medium is already filled by resin.

Our aim in these two simulations is to compare the filling time of preforms, the change of the porosity and in the thickness of preforms after compaction and after the infusion of resin, with the experimental results realized by [P.Wang 2010]. We have two steps in the numerical simulation.

- The first step corresponds to the preform compaction (Figure 6.27 (a) and Figure 6.27 (b)). The vacuum bag imposes an external pressure on the top of the domain, which leads to a compaction of preforms.
- The second step corresponds to the infusion of the resin into preforms, Figure (6.27 c). This step begins after the end of the compaction step.

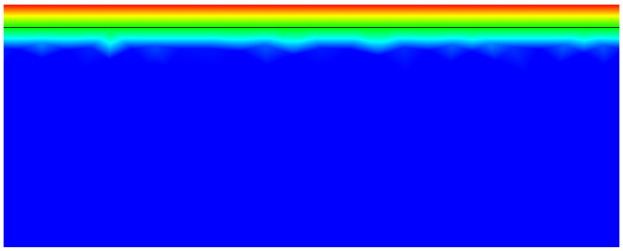

(a)

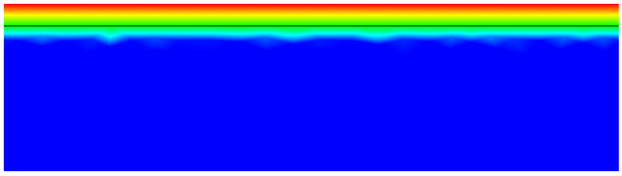

(b)

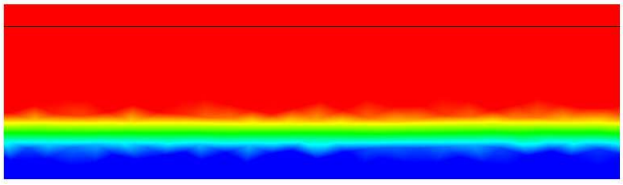

(c)

Figure 6.27: A zoom on the compaction of the plate with filled distribution medium, (a): before compaction, (b): after compaction, (c): during resin infusion

Table 6.6 shows the results of the infusion after compaction, the thickness of the preforms

decreases from 10mm to 6.3 mm numerically (Figure 6.28 (b)) and to 6.2 mm experimentally. The porosity decreases from 0.61 to 0.38 (Figure 6.29 (a)) numerically and from 0.61 to 0.39 experimentally. Table 6.7 shows that the inflation of preforms during the resin infusion is of 0.61 mm (Figure 6.28(c) where the thickness of preforms increases from 6.3 mm to 6.9 mm) similarly to the experiments where the inflation is of 0.6 mm. This inflation is present due to the pressure applied by the resin into the pores during its infusion. Consequently, the porosity increases from 0.38 to 0.43 (Figure 6.29 (b))numerically and from 0.39 to 0.44 experimentally. As for the time required to fill the preforms only, experimental and numerical results perfectly match.
Figure 6.30 shows the evolution of preforms thickness as a function of time during compaction and during resin infusion.

These results for the 24 plies of UD G1157 show a very good correlation between the numerical results of our model and the experiments which confirms the relevance of our model to simulate LRI process in real and severe physical cases.

Parameters	Numerical	experimental
Thickness of preforms	10 mm	10 mm
Porosity	0.61	0.61

Table 6.5: Initial conditions of experimental and numerical simulation of 24 plies infusion

Parameters	Numerical	experimental
Thickness of preforms	6.3 mm	6.2 mm
Porosity	0.38	0.39

Table 6.6: Comparison between numerical and experimental results obtained after the compaction of 24 plies

Parameters	Numerical	experimental
Thickness of preforms	6.9 mm	6.8 mm
Inflation of preforms	0.6 mm	0.6 mm
Porosity	0.43	0.44
Filling time of preforms	500 s	500s

Table 6.7: Comparison between analytical and experimental results obtain after the infusion of 24 plies

Simulations have also been done for a 48 plies case, according to the cases reported in [P.Wang 2010]. Results also correlate well in this second case, they are reported in Appendix C.

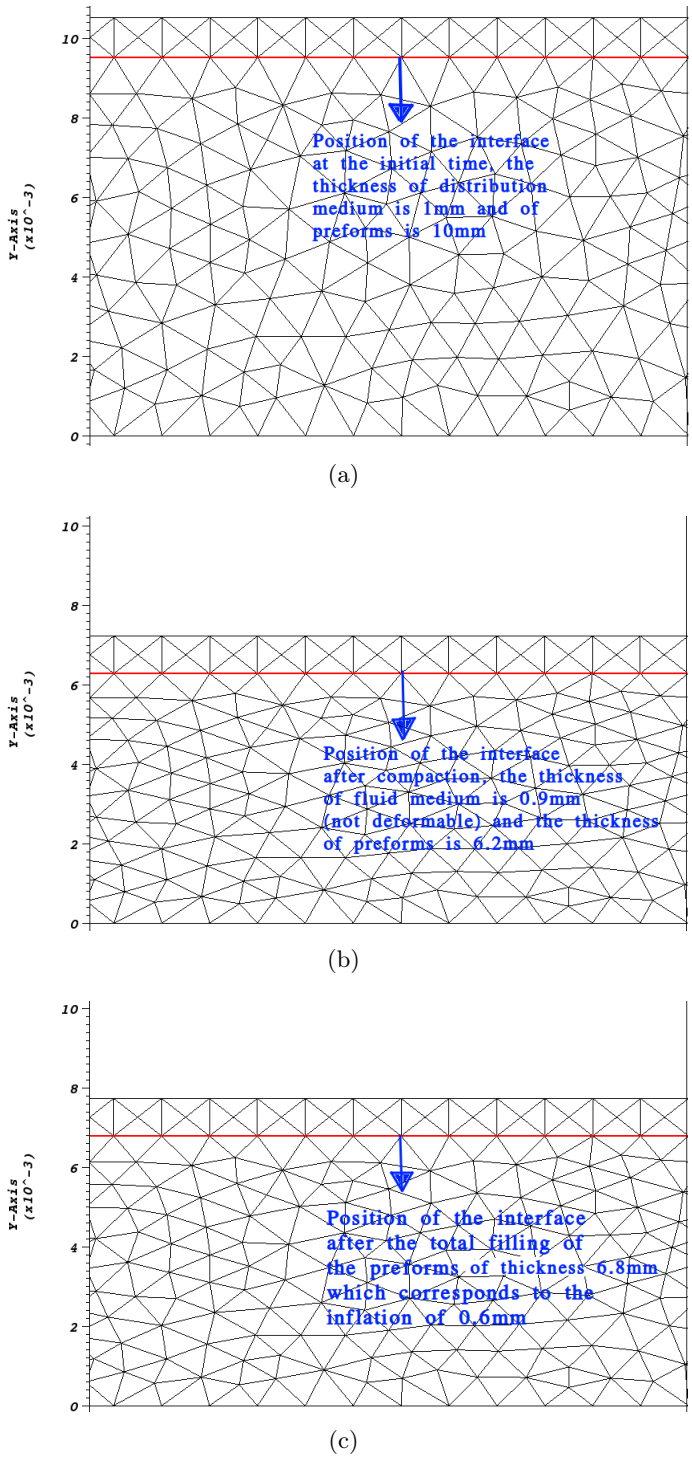

Figure 6.28: Change of the preforms thickness after compaction (b) and after infusion (c)

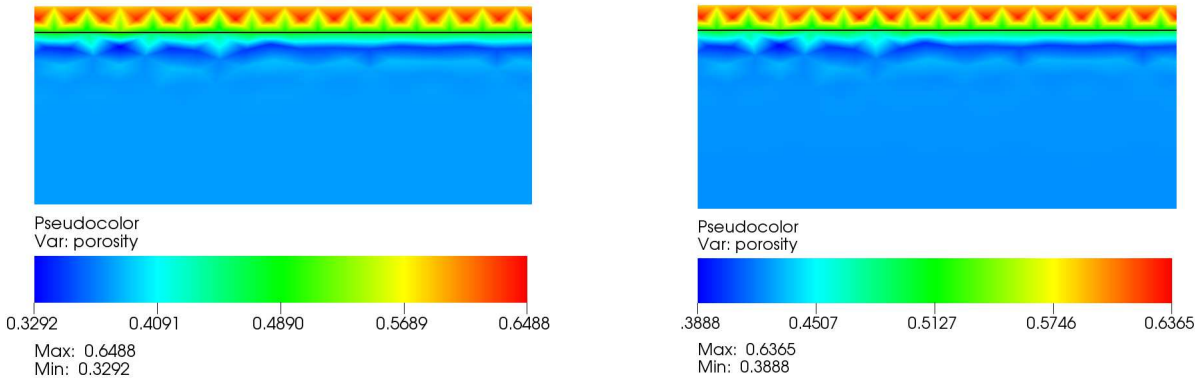

Figure 6.29: Change in the porosity after preforms compaction (a) and after resin infusion (b)

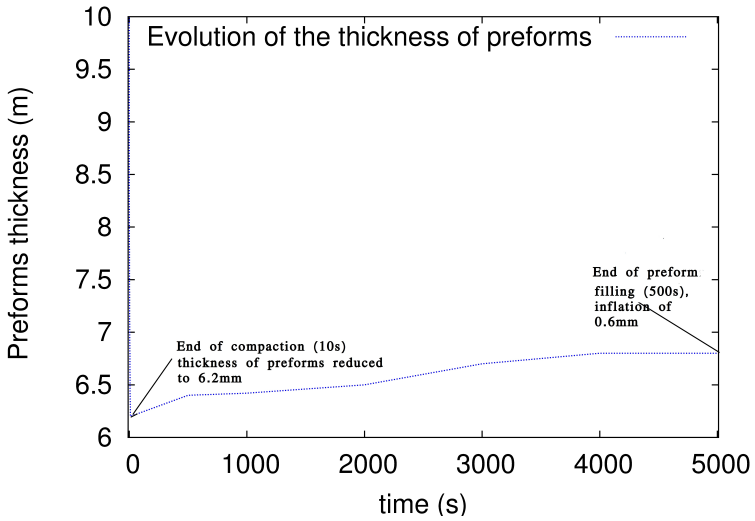

Figure 6.30: Evolution of preforms thickness after compaction and after resin infusion

6.4.2 Infusion of plate with the filling of the distribution medium

In this simulation, we will take into consideration the filling of the distribution medium during the infusion of preforms. The distribution medium taken into consideration is not deformable (it stiffness is high). This simulation allows us to follow the complete LRI process (Figure 6.31).

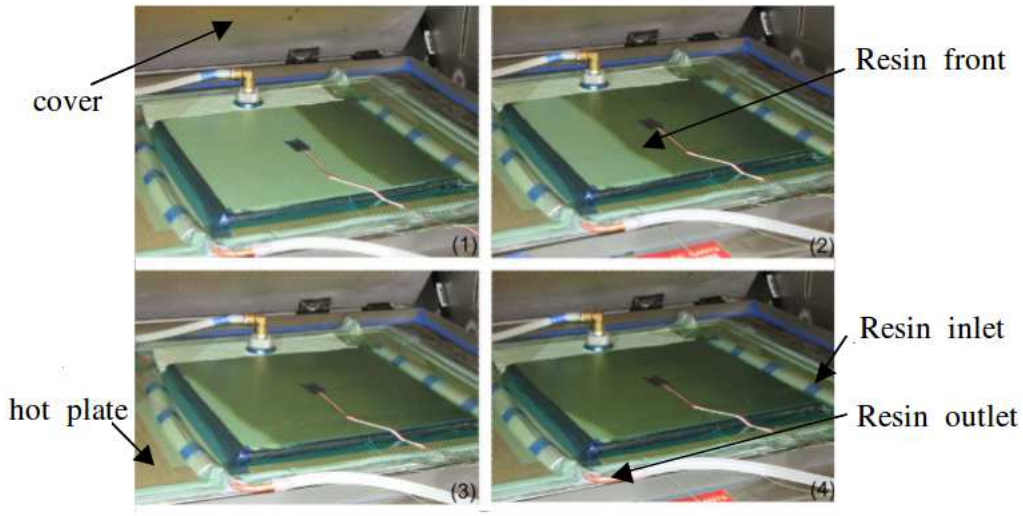

Figure 6.31: Infusion of a plate with LRI process

6.4.2.1 Definition of problem and boundary conditions

The domain of computation is a rectangle of dimensions $0.033 \times 0.292\, mm^2$ with an inlet for injection. The thickness of preforms is $30\, mm$ and the thickness of distribution medium is 1/10 of the preforms thickness, $3mm$. The mesh is made up by 2300 nodes (Figure 6.32). Two types of boundary conditions are used. The boundary conditions for the solid part (Figure 6.33 (a)) and the boundary conditions for the fluid part (Figure 6.33(b)). For the solid part, a pressure of $10^5 Pa$ is imposed on the top of the domain. A zero displacement is imposed on the bottom of the domain. And on the other boundaries of the domain, a zero normal displacement is imposed. For the fluid part, an injection pressure of $10^5 Pa$ is imposed on the top of the domain and a zero pressure is imposed on the bottom of the domain. On the other boundaries

of the domain, zero normal velocity is imposed. The diameter of the fibers is $5\,10^{-6}\mathrm{m}^2$, the Cozeny's constant is 10 and the initial porosity is 0.61 which corresponds to a permeability equal to $3\,10^{-14}\mathrm{m}^2$.

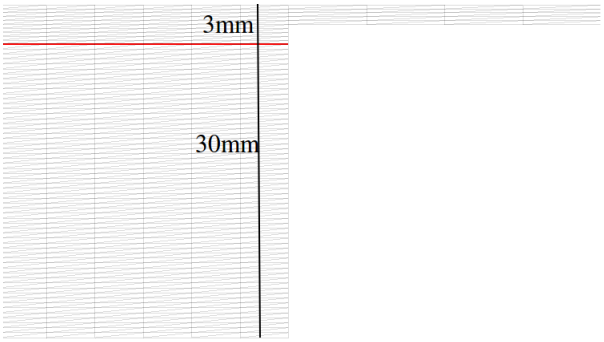

Figure 6.32: The mesh of the domain made up of 2300 nodes

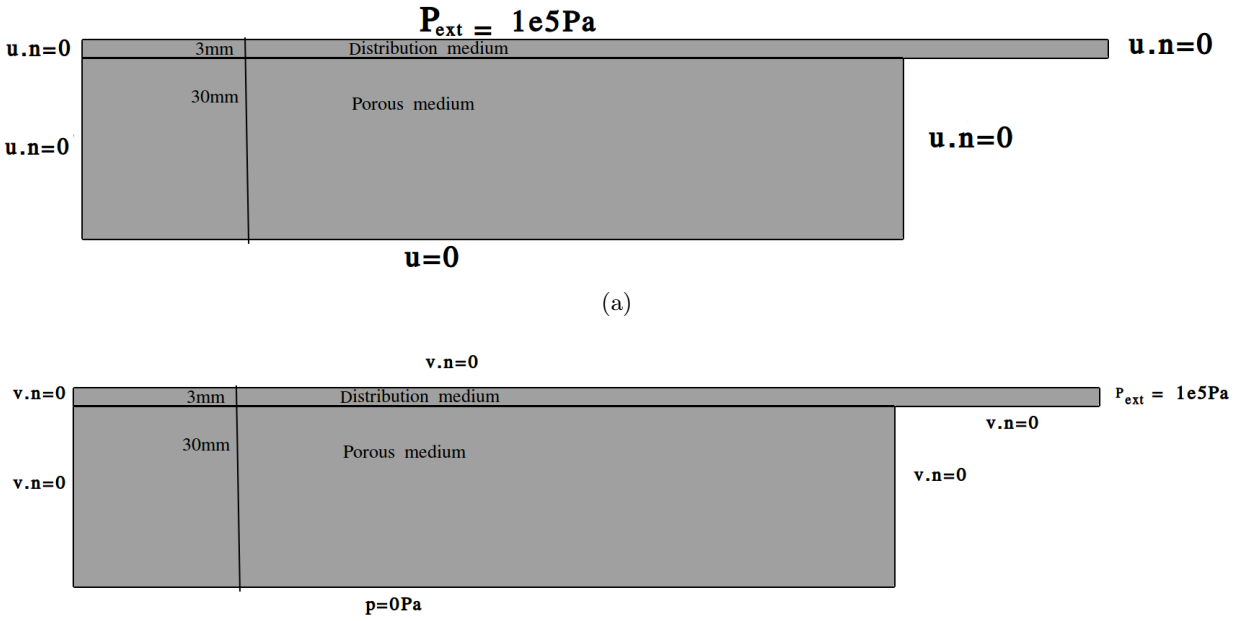

Figure 6.33: Boundary conditions of the solid mechanics problem (a) and of the fluid mechanics problem (b)

6.4.2.2 Numerical results

Figure 6.34 shows the results of this simulation after compaction, after the filling of the medium and after the total filling of preforms. This simulation corresponds to the real simu-

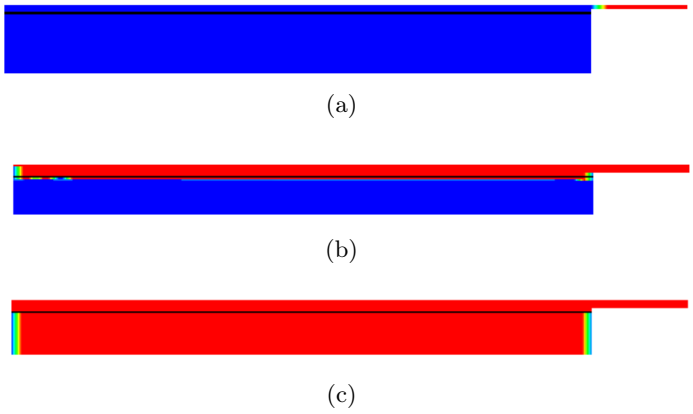

(a)

(b)

(c)

Figure 6.34: 2D simulation of preform infusion at the initial time, (a) after compaction, (b) after a total filling of distribution medium and (c) after the total filling of preforms

lation of the LRI processes. The filling time of fluid medium is $120s$ and the filling time of preforms is $3000s$ which corresponds to a real physical time of preform filling under compaction of initial thickness $20\,mm$. In addition, the time step used is $1s$ during compaction and during the filling of the distribution medium and $10s$ when filling the preforms. For this high time step and coarse mesh, the CPU time of this simulation is 20 minutes.
Defaults on the side of the piece are just due to the thickness of the level set ϕ_f of the fluid front where we have a mixed law between fluid and air.

6.4.2.3 3D extension

We did the same simulation in $3D$. Figure 6.35 shows the compaction of the preform and the evolution of the resin flow front for this case corresponding to the 2D case extruded along **z**axis. The boundary conditions are the same as in $2D$ for the solid mechanics problem and the fluid mechanics problem, except the boundary condition corresponding to the velocity on the top of the domain for the fluid mechanics problem taken as $\mathbf{v} = 0$ instead of $\mathbf{v}.\mathbf{n} = 0$. All the remarks for the $2D$ case corresponds also to the $3D$ case. Our simulations ensure that the model which couples the deformation of preforms and the resin flow front allows to characterize the parameters of the final piece (thickness, fiber volume fraction). In addition, the time step used is $1s$ during compaction and during the filling of the distribution medium and $10s$ when

filling the preforms

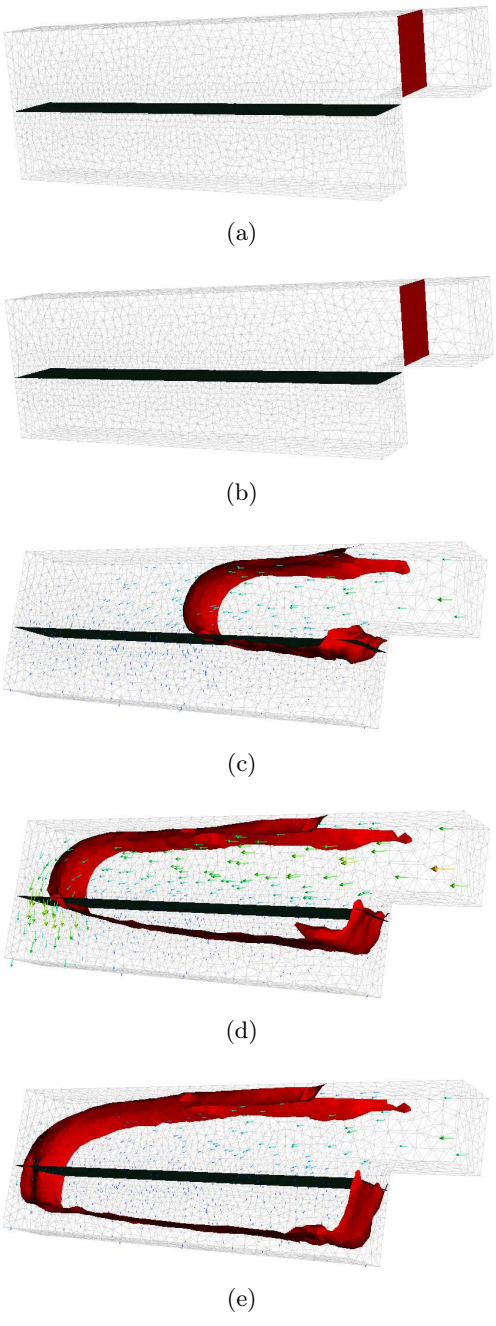

(a)

(b)

(c)

(d)

(e)

Figure 6.35: 3D simulation of resin infusion process with filling distribution medium, Stokes-Darcy interface is shown in green and the fluid flow front in red. (a): Initial state (b): after compaction (c) $\longrightarrow$ (e): evolution of resin flow front

Figure 6.36(a) shows the pressure during the compaction before the impregnation of resin

into preforms (the pressure of the resin is zero). Figure 6.36(b) shows the pressure during the resin infusion and confirms the absence of oscillations around the interface for a low physical permeability equal to $3\,10^{-14}\mathrm{m}^2$ corresponding to a diameter of fibers equal to $5\,10^{-6}$ *meter*.

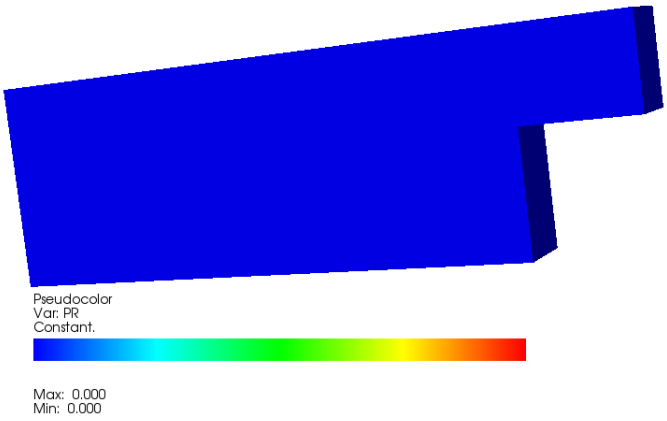

(a)

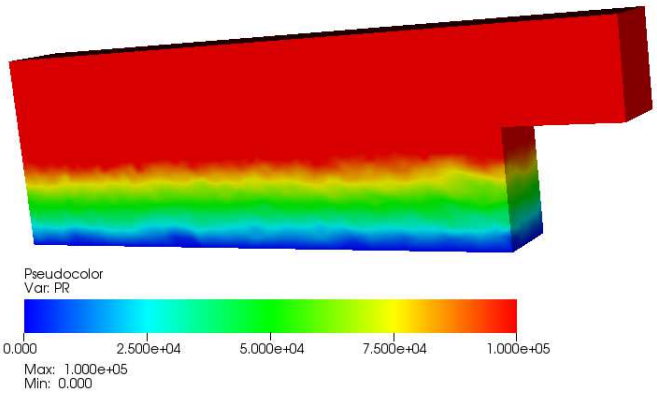

(b)

Figure 6.36: (a) pressure distribution during compaction (b) pressure distribution after resin infusion

6.5 Conclusions

In this chapter, transient flows without and with preforms deformations were validated with different numerical simulations in $2D$ and $3D$ cases. In addition, our simulations corresponds to the real physical reality of LRI processes as we shown in some illustrations. We take a low thickness of distribution medium, low permeabilities, complex geometries and some results were compared to experimental results realized by P.Wang [P.Wang 2010]. Consequently, with our model, we are able to predict the real filling time of preforms, the initial and final thickness of the stacking and the initial and final fiber volume fraction. Moreover, these simulations show the efficiency of the level set method to describe the resin flow front and to separate Stokes-Darcy domain, the efficiency of the ASGS method used for the Stokes-Darcy problem in severe regime and the efficiency of the solid mechanics problem. Particulary, another advantage is the high performance of the model for high time step and coarse meshes which implies a low CPU time.

Finally, all the numerical simulations conducted here, show the robustness and the ability of our approach to model resin infusion processes in a real industrial and physical context.

Conclusions

Liquid Resin infusion processes, used for manufacturing composite materials, parts with high quality, allow to investigate new designs for large dimensions pieces. However, despite numerous advantages, the control of these processes is difficult, especially for the most critical properties related to the final piece like its dimensions and its fibre volume fraction.

The aim of this work is to propose a numerical methodology to simulate these processes in order to provide parameters such as the filling time, the final dimensions of the piece, the volume fraction... In an isothermal framework, simulating LRI processes requires the coupling between fluid mechanics and solid mechanics problems. The fluid mechanics problem describes the flow of the resin into the distribution medium and then into the fibrous preforms assimilated to a porous medium. Hence we have to deal with the coupling of Stokes and Darcy equations. Furthermore, a specificity of this modelling is the order of the permeability which is very low ($10^{-14}\mathrm{m}^2$). The solid mechanics problem describes the finite deformations undergone by the preforms. These deformations are due to both an external mechanical pressure applied during the compaction stage and to the resin pressure.

This Stokes-Darcy coupled problem is considered here by using a monolithic approach which consists in considering one single mesh to discretize both Stokes' and Darcy's problems. Following this approach, the same pair of finite element is chosen to discretize velocity and pressure in Stokes and Darcy domains. In this work, linear-linear pair has been investigated. In order to fulfill the stability conditions of the Brezzi-Babũska theory, a Variational MultiScale method has been used to stabilize the Stokes-Darcy discrete problem. This method is called Algebraic SubGrid Scale method and involves stabilization terms for both velocity and pressure. The Stokes-Darcy interface is represented by a level set function. Many cases of validation have been performed, including manufactured solutions to study the convergence rates, comparisons with analytical solutions and comparisons with another approach called decoupled method. These cases have shown the efficiency of this stabilized finite element approach in severe regimes (low permeabilities, complex geometries, small thickness of distribution medium). Particularly, there is no significant oscillations of the velocity in the vicinity of the interface which was the problem met in the previous work of G.Pacquaut conducted in our laboratory. An important point which has to be outlined is that one single numerical parameter has significant importance

on the stability of the method. This parameter L_0 is related to the domain measure (surface area or volume measures).

The solid mechanics problem is solved in the finite strains context, using an Updated Lagrangian approach where the dry preforms have a non linear orthotropic elastic behavior. The transverse response of the preforms is given by experimental results on NC2 preforms. Fluid and solid mechanics problems are subsequently solved incrementally with weak coupling algorithms. The coupling is carried out, on one hand through the resin pressure which is involved in the constitutive law of preforms by the Terzaghi's model. On the other hand, the deformations of preforms induce a change in porosity of the medium and in turn a change of permeability which affects the resin flow. Finally, the flow front is captured by using a level set method. This method is slightly modified compared with the literature. We have used a hyperbolic tangent filter to truncate the level set function outside a neighbourhood of the interface. This filtered function is then transported in classical way using SUPG method and reinitialized in an appropriate way.

The numerical methodology developed in this work conducts to important results. First, the results provided by our monolithic approach are successfully comparable with results obtained by the decoupled approach performed with an industrial software (PAM-RTM). Furthermore, we can expect time saving with our approach due to the monolithic Stokes-Darcy coupling (no iterations have to be performed). Second, the oscillations of the velocity were a blocking point in the previous work of G. Pacquaut, especially with real values of permeability. This problem has been removed by our approach. Furthermore in this previous work, the distribution medium was deformable like the fibrous preforms. In our work we are able now to compact a stacking of distribution medium and preforms without any significant deformation of the distribution medium supposed not to be deformable under the mechanical state prevailing in infusion processes. Moreover, the thickness of the distribution medium can be taken of the order of a few millimetres as the real polyester grid used in LRI processes. Finally, all these developments and improvements allowed us to present comparisons between simulations and experiments in unidirectional flow with physical and process parameters typically used in LRI processes. Filling time, final dimensions, fibre volume fractions ... have been predicted with success. This represents an important step in simulating of LRI process and more generally of composite materials manufacturing processes.

As outlook, we have direct and long-range improvements for the physical and numerical

context of this work.
Concerning the physical context, we can take into consideration the thermo-physico chemical of the resin. Because resin viscosity is a function of the temperature and the crosslinking of resin. This will allow to compare the results with more exhaustive experimental results.
Concerning the numerical aspect, 3D more complex cases can be considered. A method to perform theses cases is the adaptation of the mesh which allows us to improve the description of variables (level set, velocity and pressure) in the vicinity of the flow front while keeping coarse meshes away from the critical zones.
Despite the fact that our simulations were performed using a low CPU time for 2D and 3D cases and show performance in complex and severe 3D flows, some improvements can be realized to reduce more the CPU time and maintaining the robustness of the model. Until now, we use a direct solver while the use of an iterative solver is possible. In Zebulon, the choice of iterative solver is available to solve finite element problems. But, we were limited on the choice of direct solver because iterative solvers diverge in our case. This technical point has to be improved. In additional, parallel computation can be used to reduce the CPU time.

In the long term, the permeability in the LRI processes is orthotropic, for that we have to extend our stabilization method to deal with this type of permeabilities. This work is in progress in a current PHD realized in our school By M.Blaise.
Finally, we can reduce the modelling scale. The hydro-mechanical interactions with mesoscopic and microscopic scales can describe more finely the physical reality. For example at the mesoscopic scale, we will consider the flow into tows thanks to the developments presented in this PHD work. And if we consider the microscopic scale, the flow around the fibers can be described by Navier-Stokes equations for example. But in this case, the fluid front will have to account for cappilarity issues involved in a 3 phases flow (air, resin, solid), including geometrical (curvature) as well as physical (surface tension, static and dynamic contact angles) characteristics. This outlook will be taken into consideration in an on-going PHD.

Appendix A

Lax-Miligram Theorem

Lax-Miligram theorem

- H is a hlibert real or complex space with a product scalar denoted by $< .,. >$ and an associated norm $||.||$.
- $a(.,.)$ is a bilinear form:
  - **Continuous** on $H \times H$:
    $\exists c > 0, \forall (u,v) \in H \times H, |a(u,v)| \leqslant c||u||\,||v||$
  - **Coercive** on H (or H elliptic):
    $\exists \alpha > 0, \forall u \in H, a(u,u) \geqslant \alpha||u||^2$
- L is a linear continuous form on H.

$\exists$ a unique $u \in H$ such that $a(u,v) = L(v)$ verified for all $v \in H$
In addition, if the bilinear form a is symmetric, then u is the unique element of H which minimize $J : H \longrightarrow \mathcal{R}$ defined by $J(v) = \frac{1}{2}a(v,v) - L(v),\ \forall v \in H$. This means that:

$$\text{it exists}\, u \in H,\ J(u) = \underset{v \in H}{min} J(v)$$

.
Lax-Miligram can be applied to another general problems:

By application of the Riesz theorem on the continuous linear forms, it exists a unique vector $\mathbf{f} \in H$ such that:

$$\forall v \in H, L(v) =< f, v >$$

And by applying Riesz theorem on bilinear continuous forms, it exists a unique continuous linear endomorphism $A \in L(H)$ such that:

$$\forall u, v \in H, a(u,v) =< Au, v >$$

Then, the result of the Lax-Miligram theorem writes:

$$\exists\, \text{a unique u} \in H,\ \text{such that}\ Au = f$$

Appendix B

Initialization of the level set function for 2D and 3D complex pieces

For the simulation of complex pieces, an additional difficulty is related to the initialization of the level-set functions which represent the interfaces. In this appendix, we will present the method used to initialize the level set functions for the 2D and 3D complex pieces.
First, to initialize this function, we will compute the minimum distance between every node of the mesh and the three rectangles represented in Figure B.1. These rectangles are shown in blue and correspond to the Stokes-Darcy interface.

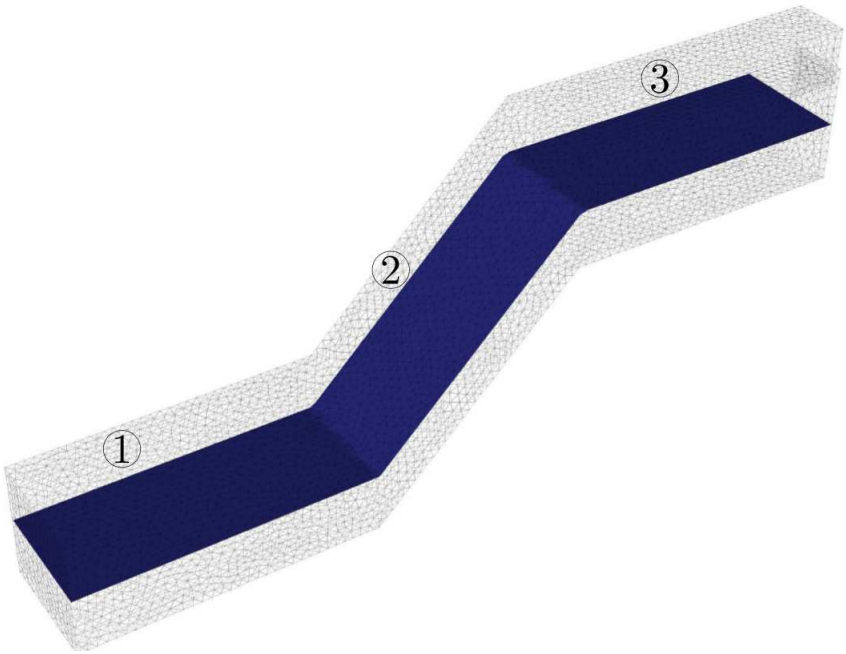

Figure B.1: Representation of three rectangles

Let us define a rectangle defined by four vertices P_0, P_1, P_2 and P_3. If we take $e_0 = P_1 - P_0$ and $e_1 = P_3 - P_0$, the rectangle can be defined by $R(s,t) = P_0 + se_0 + te_1$ where $(s,t) \in [0,1]^2$ as we show in Figure B.2.

Let us define M a node and R a rectangle (Figure B.3). The smallest distance between M and the rectangle R corresponds to the distance which separate the node M and its orthogonal

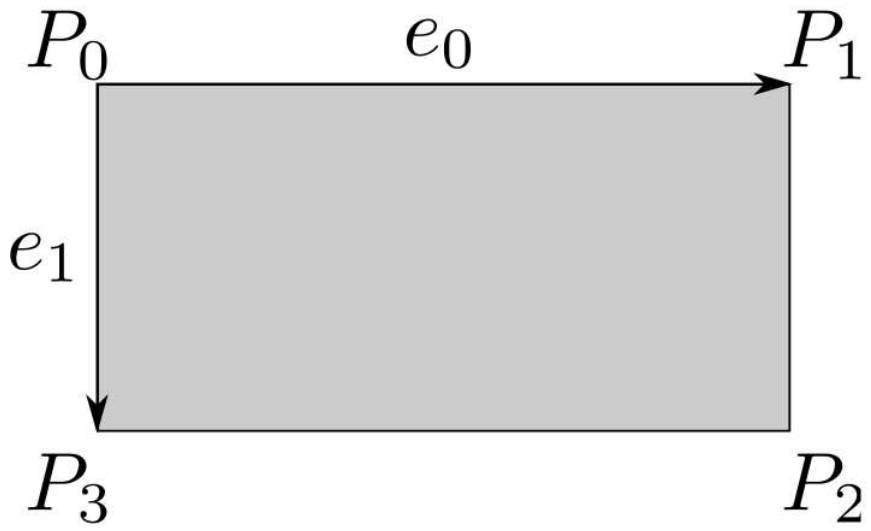

Figure B.2: Definition of a rectangle R

projection $M^{'}$ on the plane defined by the equation $a\,x + b\,y + c\,z + d = 0$:

$$d = \frac{|a\,x + b\,yc\,z + d|}{\sqrt{a^2 + b^2 + c^2}}$$

Different cases are possible. If $M^{'}$ is inside the rectangle R, then $M^{'}$ is the nearest to M. However, if $M^{'}$ is outside of the rectangle R, then the nearest point is a vertex of R or a point on an edge of R.
We identify 9 areas (Figure B.4). If the projected point is in the area 0, then it is the nearest point to M. Instead this, if this projected point is in the areas 2, 4, 6 or 8, then the nearest point is respectively the point P_1, P_0, P_3 or P_2. If the projected point is in the areas 1, 3, 5, 7, then the nearest point is its projection on P_1P_2, P_1P_0, P_0P_3, P_3P_2.

After the computation of the smallest distance relatively to the three rectangles, we can initialize the level set function which separate Stokes and Darcy.
Figure B.5 shows isovalues of the level set function in 2D, Figure B.6 shows isovalues of the level set function in 3D.

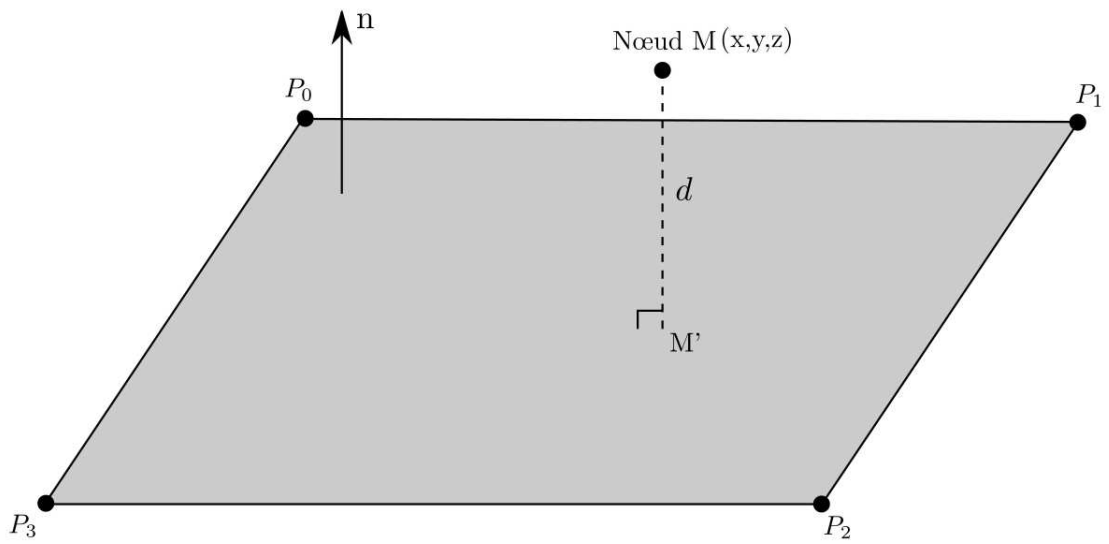

Figure B.3: Distance from a node M to a rectangle R

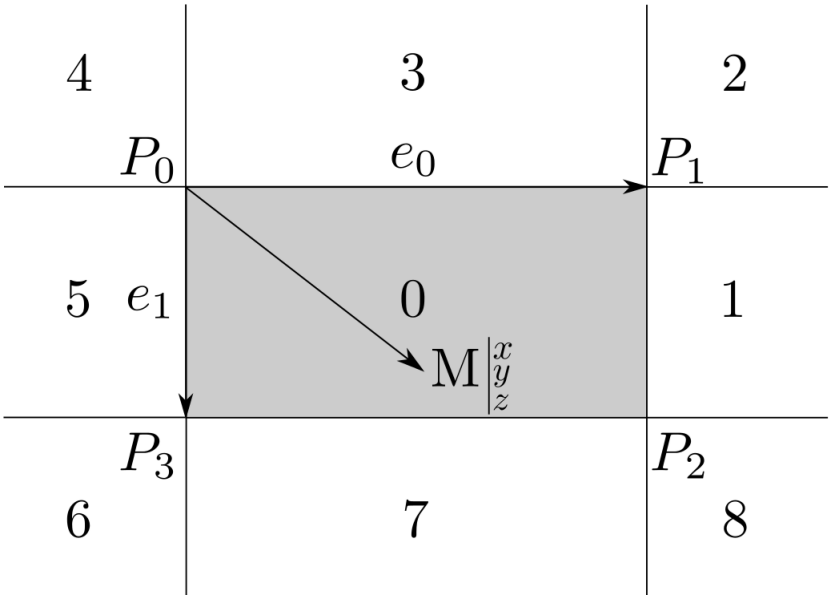

Figure B.4: Different possible areas

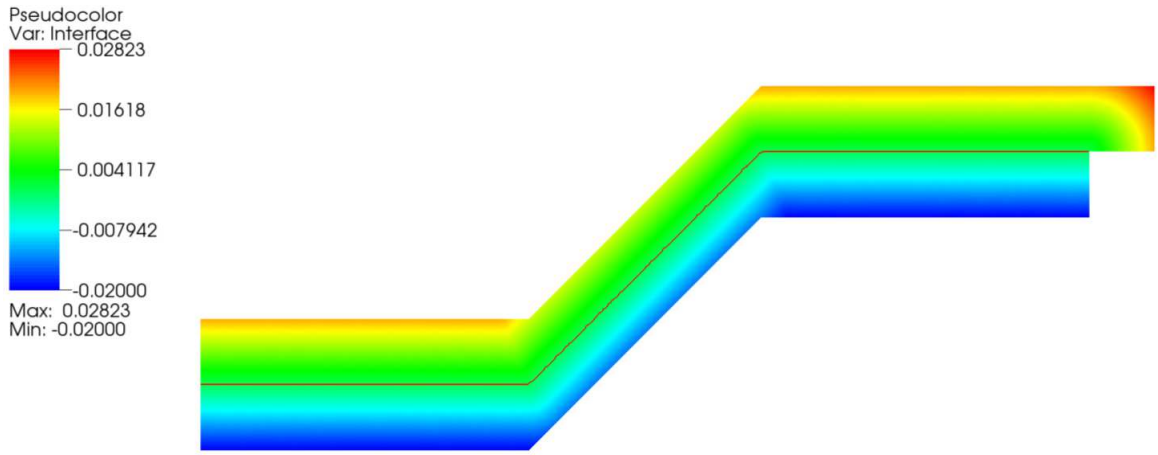

Figure B.5: Isovalue of the level set function which represents Stokes-Darcy interface in 2D. The Stokes-Darcy interface is represented in red

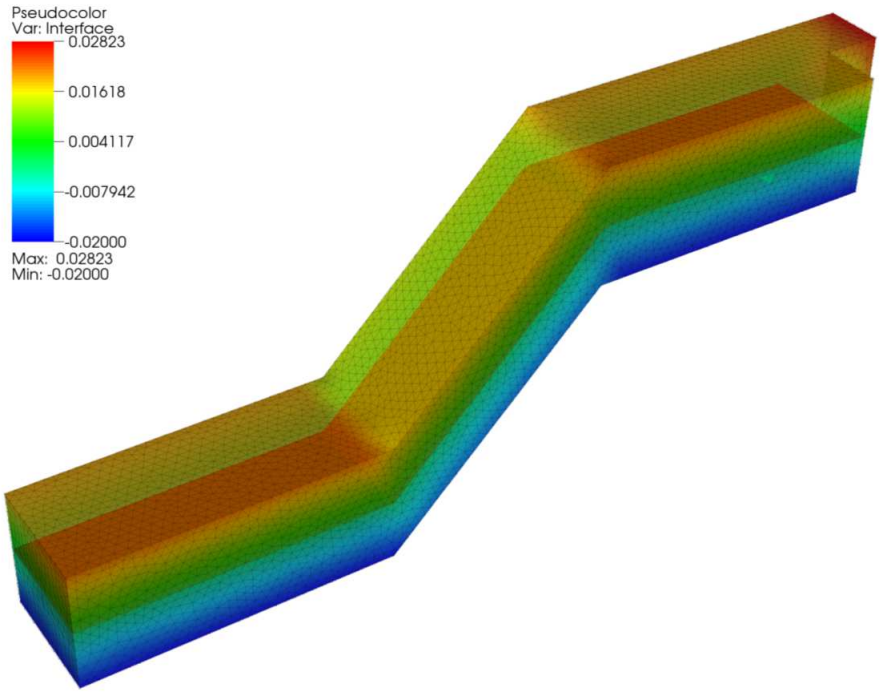

Figure B.6: Isovalue of the level set function which represents Stokes-Darcy interface in 3D. The Stokes-Darcy interface is represented in red

Appendix C

Infusion of 48 plies of NC2 preforms

Resin infusion simulation is carried out on a preform of thickness 0.02 m and of width 0.385 m. The thickness of the distribution medium is 2 mm. The distribution medium does not undergo deformations as the porous medium. It has a linear elastic behavior and its Young's modulus is 200 kPa. The 48 plies of preforms are deformable and follows the constitutive law of NC2 preforms in transverse direction (given by experiments). The geometry and boundary conditions are presented in Figure C.1. In this case, we have two types of boundary conditions: the boundary conditions corresponding to the solid mechanics problem (Figure C.1(a)) and the boundary conditions corresponding to the fluid mechanics problem (Figure C.1(b)).

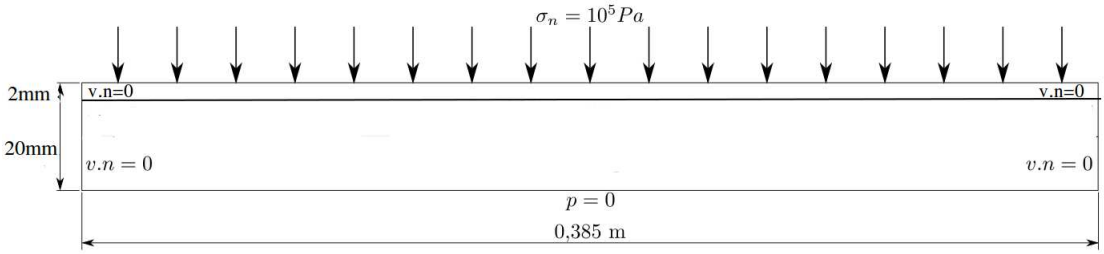

(a)

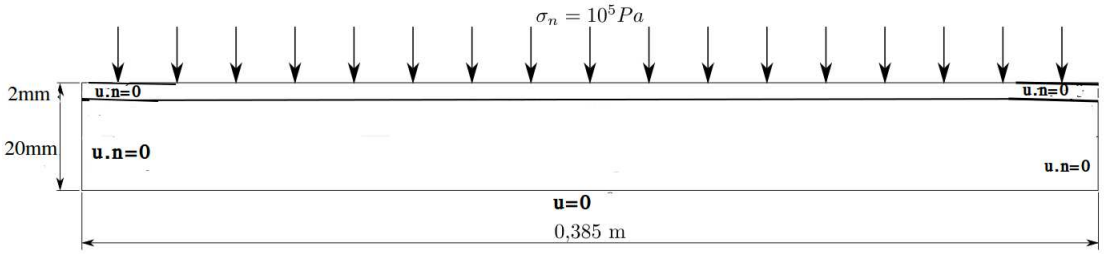

(b)

Figure C.1: Boundary conditions of a plate infusion with filled distribution medium for the solid mechanical problem (a) and for the fluid mechanical problem (b)

- For the solid part, a pressure of 1bar, applied by the vacuum bag, is imposed on the top of the domain. On the bottom of the domain, zero displacement is imposed because the stacking of resin and preforms lies on a rigid mould. On the other sides of the domain, zero displacement conditions are imposed.
- For the fluid part, an injection pressure of 1bar is imposed on the top of the domain and zero pressure is applied on the bottom of the domain to have a pressure gradient

between the top and the bottom of the domain and to allow to the air to be pulled out, air is considered as a Newtonian icompressible fluid of very low viscosity compared with the resin. To avoid the outflow of the resin on the boundaries, zero normal velocity is imposed.
The parameters of these two simulations are summarized in Table C.1. The time step is $\Delta t = 4s$.

Resin viscosity	Initial permeability	Initial porosity	thickness of preform
$0.058 Pa.s$	$3 \times 10^{-14} \mathrm{m}^2$	61%	20 mm

Table C.1: Physical parameters of the numerical simulation

C.0.0.4 Numerical results and comparison with experimental results

Figure C.2 shows the flow of the resin into the 48 plies stacking. The resin is represented in red and the air is represented in blue. The distribution medium is already filled by resin.

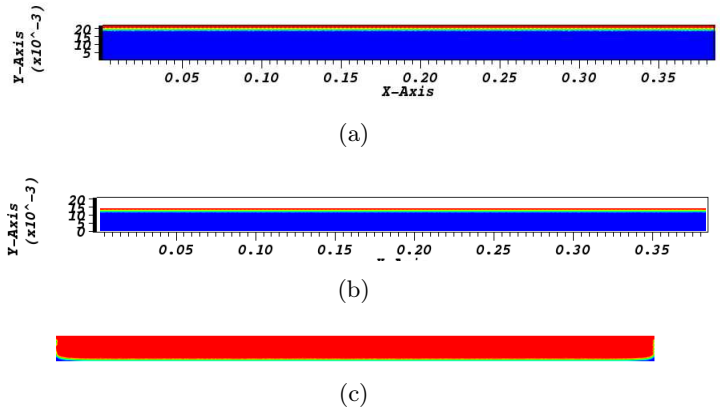

(a)

(b)

(c)

Figure C.2: 2D simulation of NC2 preforms with 48 plies. The resin is shown in red and the air is shown in blue

Table C.2 shows the results of the infusion after compaction, the thickness of the preforms decreases from $20mm$ to $13\,mm$ numerically and to $12.7\,mm$ experimentally. The porosity decreases from 0.61 to 0.4 numerically and from 0.61 to 0.39 experimentally. After infusion, the porosity increases from 0.4 to 0.57 numerically and from 0.39 to 0.56 experimentally. The time of preforms filling is $1500s$ numerically while it is $1000s$ experimentally. We dont compare the inflation of preforms after resin infusion because it was not measured by experiments. Table C.3 shows the numerical and some experimental results after resin infusin into preforms. We conclude a good correlation between experimental and numerical results for 48 plies of preforms.

Parameters	Numerical	experimental
Thickness of preforms	13 mm	12.7 mm
Porosity	0.4	0.39

Table C.2: Comparison between numerical and experimental results obtained after the compaction of 48 plies of NC2 preforms

Parameters	Numerical	experimental
Thickness of preforms	14.2 mm	...
Inflation of preforms	1.2 mm	...
Porosity	0.57	0.56
Filling time of preforms	1500 s	1000s

Table C.3: Comparison between experimental and numerical results obtained after the infusion of resin into 48 plies of NC2 preforms

Bibliography

[A.Dereims 2013] A.Dereims. *Simulation industrielle des procédés d'élaboration des pièces composites par infusion de résine: couplage fluide/solide poreux trés faiblement pérméable en grandes déformations.* PhD thesis, Ecole Nationale Supérieure des Mines de Saint-Etienne, juillet 2013. (Cited in page 108.)

[A.Ern 2005] A.Ern. Aide-mémoire des éléments finis. Dunod/L'usine Nouvelle, 2005. (Cited in pages 93 and 98.)

[A.Masud & Hughes 2002] A.Masud and T.J.R Hughes. *A stabilized mixed finite element method for Darcy flow.* Comput. Methods Appl. Mech. Engrg., vol. 191, pages 4341 – 4370, 2002. (Cited in pages 48 and 50.)

[Araya *et al.* 2006] R. Araya, G. R. Barrenechea and F.Valentin. *Stabilized Finite Element Methods Based on Multiscale Enrichment for the Stokes Problem.* SIAM J. Numer. Anal., vol. 44, Issue 1, pages 322 – 348, 2006. (Cited in pages 45, 46, 47 and 48.)

[Arbogast & Brunson 2007] T. Arbogast and D.S. Brunson. *A computational method for approximating a Darcy-Stokes system governing a vuggy porous medium.* Computational geosciences, vol. 11, no. 3, pages 207–218, 2007. (Cited in pages 26 and 57.)

[Arnold *et al.* 1984] D.N. Arnold, F.Brezzi and M.Fortin. *A stable finite element for Stokes equations.* Calcolo, vol. 21, pages 337 – 344, 1984. (Cited in pages 38 and 39.)

[Baiocchi *et al.* 1993] C. Baiocchi, F. Brezzi and L. Franca. *Virtual bubbles and Galerkin least squares type methods.* Comput. Methods Appl. Mech. Engrg., vol. 105, pages 125 – 141, 1993. (Cited in page 45.)

[Barrenechea & Valentin 2002] G. Barrenechea and F. Valentin. *An unusual stabilized finite element method for a generalized Stokes problem.* Numer. Math, vol. 92, pages 653 – 677, 2002. (Cited in page 45.)

[Bear 1990] J. Bear. *Dynamics of Fluids in Porous Media.* Dover Publications, 1990. (Cited in page 23.)

[Berthelot 2005] J.M Berthelot. Matériaux composites : Comportement mécanique et analyse des structures. Tec & Doc Lavoisier, Paris, 2005. (Cited in page 7.)

[B.J.Daly & W.E.Pracht 1968] B.J.Daly and W.E.Pracht. *Numerical Study of Density-Current Surges.* Physics of FLuids, vol. 11, page 15, 1968. (Cited in page 132.)

[Bochev & Gunzburger 1998] P. Bochev and M. Gunzburger. *Least-squares finite element methods for elliptic equations.* SIAM J. Numer. Anal, vol. 40/4, pages 789 – 837, 1998. (Cited in pages 48 and 53.)

[Bramble & Xu 1989] J. H. Bramble and J. Xu. *A local post-processing technique for improving the accuracy in mixed finite-element approximations.* SIAM J. Numer. Anal., vol. 26, pages 1267–1275, 1989. (Cited in page 44.)

[Brinkman 1947] H.C. Brinkman. *A calculation of the viscous force exerted by a flowing fluid on a dense swarm of particules.* Applied science research, pages 27 – 34, 1947. (Cited in pages 23 and 24.)

[Bruchon *et al.* 2009] J. Bruchon, H. Digonnet and T. Coupez. *Using a signed distance function for the simulation of metal forming processes: Formulation of the contact condition and mesh adaptation. From a Lagrangian approach to an Eulerian approach.* International Journal for Numerical Methods in Engineering, vol. 78, no. 8, pages 980 – 1008, 21 May 2009. (Cited in page 127.)

[Celle *et al.* 2008] P. Celle, S. Drapier and J-M. Bergheau. *Numerical modelling of liquid infusion into fibrous media undergoing compaction.* European Journal of Mechanics, vol. 27, no. Issue 4, pages 647–661, 2008. (Cited in pages viii, 12, 56, 88, 108, 123 and 162.)

[Chamberland *et al.* 2010] E. Chamberland, A. Fortin and M. Fortin. *Comparison of the performance of some finite element discretizations for large deformation elasticity problems.* Computers and Structures, vol. 88, no. 11-12, pages 664–673, 2010. (Cited in page 92.)

[Codina & S.Badia 2010] R. Codina and S.Badia. *Stabilized continuous and discontinuous Galerkin techniques for Darcy flow.* Computer Methods in Applied Mechanics and Engineering, vol. 199, no. 25-28, pages 1654–1667, 15 May 2010. (Cited in pages 48, 61, 64, 67, 68, 69, 70, 97 and 98.)

[Codina 2002] R. Codina. *Stabilized finite element approximation of transient incompressible flows using orthogonal subscales.* Computer Methods in Applied Mechanics and Engineering, vol. 191, pages 4295–4321, 2002. (Cited in page 62.)

[Cottet & E.Maitre 2006] G.H. Cottet and E.Maitre. *A level set method for fluid-structure interactions with immersed surfaces.* Mathematical Models and Methods in Applied Sciences, vol. 16, no. 3, pages 415–438, 2006. (Cited in page 81.)

[Crouzeix & Raviart 1973] M. Crouzeix and P.A. Raviart. *Conforming and nonconforming finite element methods for solving the stationary Stokes equations.* RAIRO Num.Anal., vol. R-3, pages 33–75, 1973. (Cited in page 38.)

[C.Taylor & P.Hood 1973] C.Taylor and P.Hood. *A numerical solution of the Navier-Stokes equations using the finite element.* Computers and Fluids, vol. 1, no. 1, pages 73–100, 1973. (Cited in page 38.)

[C.W.Hirt & B.D.Nichols 1981] C.W.Hirt and B.D.Nichols. *Volume of fluid (VOF) method for the dynamics of free boundaries.* Journal of computational physics, vol. 39, no. 1, pages 201–225, 1981. (Cited in pages 134 and 135.)

[Darcy 1856] H. Darcy. Les fontaines publiques de la ville de dijon. Dalmont, 1856. (Cited in page 23.)

[D.J.Silvester & N.Kechkar 1990a] D.J.Silvester and N.Kechkar. *Stabilized bilinear-constant velocity-pressure finite elements for the conjugate gradient solution of*

the Stokes problem. Comput. Methods Appl. Mech. Engrg., vol. 79, pages 71–86, 1990. (Cited in page 41.)

[D.J.Silvester & N.Kechkar 1990b] D.J.Silvester and N.Kechkar. *Stabilized bilinear-constant velocity-pressure finite elements for the conjugate gradient solution of the Stokes problem.* Comput. Methods.Appl. Mech., vol. 79, pages 71–86, 1990. (Cited in page 44.)

[D.L.Youngs 1982] D.L.Youngs. *Time-dependent multi-material flow with large fluid distrotion.* Numerical methods for fluid dynamics, vol. 24, pages 273–285, 1982. (Cited in page 135.)

[Donea & Huerta 2003] J. Donea and A. Huerta. *Finite Element Methods for Flow Problems.* John Wiley and Sons Inc, vol. 13, 2003. (Cited in page 92.)

[Dullien 1979] F.A.L Dullien. *Porous Media: Fluid Transport and Pore Structure.* Academic press, vol. 21, 1979. (Cited in page 160.)

[Dursapt 2007] M. Dursapt. Mise en forme des matériaux composites. 2007. (Cited in pages xiii, 7 and 8.)

[E.A.Kempner & H.T.Hahn 1998] E.A.Kempner and H.T.Hahn. *A unified approach to manufacturing simulation for composites.* In Proceedings of the First Korea-U.S. Workshop on Composite Materials, 1998. (Cited in page 164.)

[E.Burmana & P.Hansbob 2007] E.Burmana and P.Hansbob. *A unified stabilized method for Stokes and Darcy equations.* Journal of Computational and Applied Mathematics, vol. 198, pages 35 – 51, 2007. (Cited in pages 26 and 57.)

[F.Brezzi & J.Douglas 1988] F.Brezzi and J.Douglas. *Stabilized mixed methods for Stokes problem.* Numer. Math., vol. 53, pages 225–236, 1988. (Cited in page 41.)

[F.Brezzi & J.Pitkaranta] F.Brezzi and J.Pitkaranta. *On the stabilization of finite element approximations of the Stokes problem.* Efficient Solutions of Elliptic Systems, Notes on Numerical Fluid Mechanics, 10 (Ed. by W. Hackbusch), Vieweg, Wiesbaden, pages 11–19. (Cited in page 41.)

[F.Brezzi & M.Fortin 1991] F.Brezzi and M.Fortin. Mixed and hybrid finite element methods. Springer-Verlag, 1991. (Cited in pages 35 and 71.)

[F.H.Harlow & J.E.Welch 1965] F.H.Harlow and J.E.Welch. *Numerical calculation of time dependent viscous incompressible flow for fluid with free surface.* Physics of FLuids, vol. 8, no. 12, pages 2182–2189, 1965. (Cited in page 133.)

[franca et al 1990] franca et al. *A convergence analysis of a stabilized method for the Stokes flow.* Report LNCC 19/90, Rio de Janeiro,Brazil, 1990. (Cited in page 44.)

[Franca *et al.* 1989] L.P. Franca, E.G. Dutra and E.Gomes. *Galerkin gradient least-squares method.* Comput.Methods Appl.Mech.Eng, vol. 74, pages 41–54, 1989. (Cited in pages 48, 53 and 55.)

[Gartling *et al.* 1996] D.K. Gartling, C.E. Hickox and R.C. Givler. *Simulation of coupled viscous and porous flow problems.* Computational Fluid Dynamics, vol. 7, no. 1-2, pages 23 – 48, 1996. (Cited in page 112.)

[Geuzaine & Remacle 2009] C. Geuzaine and J.-F. Remacle. *Gmsh: a three-dimensional finite element mesh generator with built-in pre- and post-processing facilities.* International Journal for Numerical Methods in Engineering, vol. 79, no. 11, pages 1309–1331, 2009. (Cited in page 179.)

[G.R.Barrenechea *et al.* 2007] G.R.Barrenechea, L.P.Franca and F. Valentin. *A Petrov-Galerkin enriched method: a mass conservative finite element method for the Darcy equation.* Computer Methods in Applied Mechanics and Eng., vol. 196, no. 21-24, pages 2449–2464, 2007. (Cited in page 48.)

[Hassanizadeh 1983] S.M. Hassanizadeh. *General conservation equations for multi-phase systems, Constitutive theory for porous media flow.* CML Publications, Southampton, pages 30 – 45, 1983. (Cited in page 23.)

[Hughes & L.Franca 1989] T.J.R Hughes and L.Franca. *A new finite element method for computation fluid dynamics: the Galerkin least squares method for advective diffusive equations.* Comput.Methods Appl.Mech.Eng, vol. 73, pages 173–189, 1989. (Cited in pages 48 and 53.)

[Hughes *et al.* 1986] T.J.R. Hughes, L.P. Franca and M.Balestra. *A new finite element formulation for computational fluid dynamics: Circumventing the babuska-brezzi condition: a stable Petrov-Galerkin formulation of the stokes problem accommodating equal-order interpolations.* Springer: Berlin, vol. 59, pages 85 – 99, November 1986. (Cited in pages 41, 43 and 44.)

[Hughes 1988] T.J.R. Hughes. *The variational multiscale method—a paradigm for computational mechanics.* Computer Methods in Applied Mechanics and Engineering, vol. 166, no. 1-2, pages 3–24, 13 November 1988. (Cited in page 45.)

[Hughes 1995] T.J.R. Hughes. *Multiscale phenomena: Green's functions, the Dirichlet-to-Neumann formulation, subgrid scale models, bubbles and the origins of stabilized methods.* Computer Methods in Applied Mechanics and Engineering, vol. 127, no. 1-4, pages 387–401, 1995. (Cited in pages 45 and 60.)

[Hyman 1984] James M. Hyman. *Numerical methods for tracking interfaces.* Computational methods, vol. 12, no. Issues 1-3, pages 396–407, 1984. (Cited in pages viii and 133.)

[I.Christie *et al.* 1976] I.Christie, D.f. Griffiths, A.R.Mitchell and O.C.Zienkiezicz. *Finite element methods for second order differential equations with significant first derivates.* Internat. J. Numer.Methods Engrg., vol. 10, pages 1389–1396, 1976. (Cited in page 144.)

[J.A.Sethian 1999] J.A.Sethian. *Level Set Methods and Fast Marching Methods: Evolving Interfaces in Computational Geometry.* Fluid Mechanics, Computer Vision,Computer-Aided Design, Optimal Control and Material Sciences. Cambridge University Press, no. ISBN-13, 1999. (Cited in page 137.)

[J.Bonet & D.R.Wood 1997] J.Bonet and D.R.Wood. *Nonlinear continuum mechanics for finite element.* Cambridge University Press, no. 13, 1997. (Cited in page 151.)

[J.Coirier 2001] J.Coirier. Mécanique des milieux continus: cours et exercices corrigés. Dunod, 2001. (Cited in pages 151 and 157.)

[J.Douglas & J.wang 1989] J.Douglas and J.wang. *An absolutely Stabilized Finite Element Method for the Stokes problem.* Mathematics of computation, vol. 52, no. 186, pages 495 – 508, April 1989. (Cited in pages 41, 43 and 44.)

[J.E.Aarnes *et al.* 2005] J.E.Aarnes, T.Gimse and K.-A.Lie. *An introduction to the numerics of flow in porous media using Matlab, Geometrical Modelling Numerical Simulation and Optimization, Industrial Mathematics at SINTEF.* Springer Verlag, 2005. (Cited in page 44.)

[J.J.Droux & Hughes 1994] J.J.Droux and T.J.R. Hughes. *A boundary integral modification of the galerkin leastsquares formulation for the Stokes problem.* Comput. Methods Appl. Mech. Engrg., vol. 113, pages 173–182, 1994. (Cited in pages 48 and 53.)

[J.M.Urquiza *et al.* 2008] J.M.Urquiza, D.N'Dri, A.Garon and M.C. Delfour. *Coupling Stokes and Darcy equations.* Applied Numerical Mathematics, vol. 58, no. 5, pages 525–538, 2008. (Cited in page 28.)

[J.Nitsche 1977] J.Nitsche. *L-convergence of finite element approximations.* Mathematical aspects of finite element methods,Springer, 1977. (Cited in page 41.)

[J.Park & M.K.Kang 2003] J.Park and M.K.Kang. *A numerical simulation of the resin infusion process.* Composite Structures, vol. 60, no. 4, pages 431–437, 2003. (Cited in page 160.)

[K.Terzaghi *et al.* 1967] K.Terzaghi, R.B.Peck and G.Mesri. *Soil Mechanics in Engineering Practice.* Jones Wiley & Sons, New york, 1967. (Cited in page 164.)

[L.Abouorm *et al.*] L.Abouorm, R.Troian, S.Drapier, J.Bruchon and N.Moulin. *Stokes/Darcy coupling in severe regimes using multiscale stabilization for mixed finite elements: monolithic appraoch versus decoupled approach.* submitted. (Cited in page 108.)

[Layton *et al.* 2003] W.J. Layton, F.Schieweck and I.Yotov. *Coupling fluid flow with porous media flow. SIAM Journal on Numerical Analysis.* SIAM on Numerical Analysis, vol. 40, no. 6, pages 2195–2218, 2003. (Cited in page 28.)

[L.Franca & T.J.R.Hughes 1988] L.Franca and T.J.R.Hughes. *Two classes of mixed finite element methods.* Methods Appl. Mech. Engrg., vol. 69, pages 89–129, 1988. (Cited in page 41.)

[L.P.Franca & R.Stenberg 1991a] L.P.Franca and R.Stenberg. *Error analysis of some Galerkin-least-squares methods for the elasticity equations.* SIAM J. Num. Anal, 1991. (Cited in page 44.)

[L.P.Franca & R.Stenberg 1991b] L.P.Franca and R.Stenberg. *Error Analysis of Galerkin Least Squares Methods for the Elasticity Equations.* SIAM J. Numer. Anal., vol. 28, no. 6, pages 1680–1697, December 1991. (Cited in pages 48 and 53.)

[L.P.Franca *et al.*] L.P.Franca, J.Karam Filho, A.F.D. Loula and R.Stenberg. *A convergence analysis of a stabilized method for the Stokes flow.* Report LNCC 19/90, Rio de Janeiro, Brazil. (Cited in page 41.)

[L.Ville *et al.* 2011] L.Ville, L.Silva and T.Coupez. *Convected level set method for the numerical simulation of fluid buckling.* International Journal for numerical methods in fluids, vol. 66, no. 3, pages 324–344, 2011. (Cited in page 145.)

[Masud & Hughes 2002] A. Masud and T. J. R. Hughes. *A stabilized mixed finite element method for darcy flow.* Computer Methods in Applied Mechanics and Engineering, vol. 191, no. 39-40, pages 4341–4370, 2002. (Cited in page 97.)

[M.discacciati *et al.* 2007] M.discacciati, A.Quarteroni and A.Valli. *Robin-Robin Domain Decomposition Methods for the Stokes-Darcy Coupling.* SIAM J. Numer. Anal, vol. 45, no. 3, pages 1246–1268, 2007. (Cited in page 56.)

[M.Rudman 1997] M.Rudman. *Volume-tracking methods for interfacial flow calculations.* International Journal for numerical methods in fluids, vol. 24, pages 671–691, 1997. (Cited in pages viii and 136.)

[M.Sussman *et al.* 1994] M.Sussman, P.Smereka and S.Osher. *A level set approach for computing solutions to incompressible two-phase flow.* Journal of Computational Physics, vol. 114, no. 1, pages 146–159, 1994. (Cited in page 140.)

[Nafa & Wathen 2008] K. Nafa and A. J. Wathen. *Local projection finite element stabilization for the general- ized Stokes problem.* Numerical Analysis report NA-08/17, Oxford University Computing Laboratory,Oxford University Computing Laboratory, Oxford, UK., vol. 196, 2008. (Cited in page 49.)

[Nafa & Wathen 2009] K. Nafa and A. J. Wathen. *Local projection stabilized Galerkin approximations for the gen- eralized Stokes problem.* Comput. Methods. Appl. Mech. Engrg., vol. 198, no. Issues 5-8, pages 877–883, 2009. (Cited in page 49.)

[Nafa 2009] K. Nafa. *Improved local projection for the generalized Stokes problem,SCPDE 08, Hong Kong, China.* Adv. in Appl. Math. and Mech., vol. 1, no. 6, pages 862–873, 2009. (Cited in page 49.)

[Nakshatrala *et al.* 2006a] K.B Nakshatrala, D.Z. Turner and K.D. Hjelmstad. *A stabilized mixed finite element method for Darcy flow based on a multiscale decomposition of the solution.* Comput. Methods Appl. Mech. Engrg., vol. 195, pages 4036 – 4049, 2006. (Cited in pages 45, 51 and 52.)

[Nakshatrala *et al.* 2006b] K.B. Nakshatrala, D.Z. Turner, K.D. Hjelmstad and A. Masud. *A stabilized mixed finite element method for Darcy flow based on a multiscale decomposition of the solution.* Computer Methods in Applied Mechanics and Engineering, vol. 195, no. 33-36, pages 4036–4049, 2006. (Cited in page 61.)

[O.Basset 2006] O.Basset. *Simulation numérique d'écoulements multi fluides sur grille de calcul.* Thèse de doctorat, Ecole Nationale Supérieure des Mines de Paris, 2006. (Cited in page 140.)

[Pacquaut *et al.* 2012] G. Pacquaut, J. Bruchon, N. Moulin and S. Drapier. *Combining a level set method and mixed stabilized p1/p1 formulation for coupling stokes-darcy flows.* International Journal for Numerical Methods in Fluids, vol. 69, no. Issue2, pages 459–480, 2012. (Cited in pages 57, 88, 101, 111, 113 and 130.)

[Pacquaut 2009] G. Pacquaut. *Couplage Stokes/Darcy dans un cadre Level-set en grandes déformations pour la simulation des procédés par infusion de résine.* PhD thesis, Ecole Nationale Supérieure des Mines de Saint-Etienne, 2009. (Cited in pages 12, 13, 88 and 164.)

[P.A.Raviart & J.M.Thomas 1977] P.A.Raviart and J.M.Thomas. *A mixed-finite element method for second order elliptic problems.* Springer, New York, vol. Mathematical aspects of the finite element method, Lecture Notes in Mathematics, 1977. (Cited in pages 49 and 50.)

[P.Celle 2006] P.Celle. *Couplage fluide/milieu poreux en grandes déformations pour la modélisation des procédés d'élaboration par infusion.* PhD thesis, Ecole Nationale Supérieure des Mines de Saint-Etienne, 2006. (Cited in page 158.)

[P.Wang 2010] P.Wang. *Étude numérique et expérimentale de procédé d'élaboration des matériaux composites par infusion de résine.* thèse de doctorat, École Nationale supérieure des Mines de Saint-Étienne, 2010. (Cited in pages 168, 187, 194, 195, 196, 198 and 206.)

[R.Duran & R.Notchetto 1989] R.Duran and R.Notchetto. *Pointwise accuracy of a stable Petrov-Galerkin approximation of the Stokes problem.* SIAM J. Num. Anal, vol. 26, no. 186, pages 1395 – 1406, 1989. (Cited in page 44.)

[Riviere & I.Yotov 2005] B. Riviere and I.Yotov. *Locally conservative coupling of Stokes and Darcy flows.* SIAM on Numerical Analysis, vol. 42, no. 5, pages 1959–1977, 2005. (Cited in page 26.)

[Russo 1996] A. Russo. *Bubble stabilization of finite element methods for the linearized incompressible Navier-Stokes equations.* Comput. Methods Appl. Mech. Engrg., vol. 132, pages 335 – 343, 1996. (Cited in page 45.)

[Salari & Knupp 2000] K. Salari and P. Knupp. *Code verification by the method of manufactured solutions.* Rapport technique, Sandia National Laboratories, 2000. (Cited in page 92.)

[S.Badia & R.Codina 2008] S.Badia and R.Codina. *Unified stabilized finite element formulation for the Stokes and the Darcy problems.* SIAM journal on Numerical Analysis, vol. 47, no. 3, pages 1971–2000, 2008. (Cited in pages 61, 68, 69, 70, 73, 75, 78, 79, 88, 95 and 98.)

[S.Badia & R.Codina 2010] S.Badia and R.Codina. *Stabilized Continuous and discontinuous Galerkin techniques for Darcy flow.* Computer Methods in Applied Mechanics and Engineering, vol. 199, no. 25-28, pages 654–667, 2010. (Cited in pages 45, 51 and 66.)

[S.Osher & J.A.Sethian 1988] S.Osher and J.A.Sethian. *Fronts propagating with curvature-dependent speed: Algorithms based on hamilton-jacobi formulations.* Journal of Computational Physics, vol. 79, no. 1, pages 12–49, 1988. (Cited in page 136.)

[S.Osher & R.P.Fedkiw 2001] S.Osher and R.P.Fedkiw. *Level set methods: an overview and some recents results.* Journal of computational physics, vol. 169, no. 2, pages 436–502, 2001. (Cited in page 137.)

[S.Toll & Manson 1994] S.Toll and J.a.E Manson. *An analysis of the compressibility of fibre assemblies.* In Proceedings of the FRC Conference, Newcastle upon Tyne, 1994. (Cited in page 161.)

[T.Coupez 2006] T.Coupez. *Réinitialisation convective et locale des fonctions level set pour le mouvement des surfaces et d'interfaces.* In Journées Activités Universitaires de Mécanique, 2006. (Cited in page 140.)

[T.G.Gutowski 1987] T.G.Gutowski. *Consolidation experiments for laminate composites.* Journal of Composite Materials, vol. 21, no. 1, pages 650–669, 1987. (Cited in page 161.)

[T.J.R.Hughes & A.N.Brooks 1979] T.J.R.Hughes and A.N.Brooks. *A multidimensional upwind scheme with no crosswind diffusion.* Finite Element Methods for Convection Dominated Flows (Ed. by T.J.R. Hughes), ASME, New York,, vol. 32, pages 19–35, 1979. (Cited in pages 41 and 144.)

[T.J.R.Hughes *et al.* 1989] T.J.R.Hughes, L.P.Franca and G.M.Hulbert. *A new finite element formulation for computational fluid dynamics: VIII. The Galerkin-least-squares method for advective- diffusive equations.* Comput. Methods Appl. Mech. Engrg., vol. 73, pages 173–189, 1989. (Cited in page 41.)

[T.J.R.Hughes 1982] T.J.R.Hughes. *Streamline upwind/Petrov-Galerkin formulations for convective dominated flows with particular emphasis on the incompressible Navier- Stokes equations.* Comput. Methods Appl. Mech. Engrg., vol. 32, pages 199–259, 1982. (Cited in page 41.)

[T.J.R.Hughes 1987] T.J.R.Hughes. *The Finite Element Method. Linear Static and Dynamic Analysis. Prentice-Hall.* Linear Static and Dynamic Analysis. Prentice-Hall., pages 173–189, 1987. (Cited in page 41.)

[T.J.R.Hughes 1995] T.J.R.Hughes. *Multiscale phenomena: Green's function, the Dirichlet-to-Neumann formulation, subgrid scale models, bubbles and the origins of stabilized formulations.* Computer Methods in Applied Mechanics and Engineering, vol. 127, pages 387–401, 1995. (Cited in page 61.)

[T.Karper *et al.* 2009] T.Karper, K.A.Mardal and R.Winther. *Unified finite element discretizations of coupled Darcy-Stokes flow. Numerical Methods for Partial Differential Equations.* SIAM on Numerical Analysis, vol. 25, no. 2, pages 311–326, 2009. (Cited in page 26.)

[T.Y.Hou & X.-H.Wu 1997] T.Y.Hou and X.-H.Wu. *A multiscale finite element method for elliptic problems in composite materials and porous media.* Journal of Computational Physics, vol. 134, pages 169–189, 1997. (Cited in page 44.)

[Vernescu 1990] B. Vernescu. *Asymptotic analysis for an incompressible flow in fractured porous media.* International Journal of Engineering Science, vol. 28, pages 959 – 964, 1990. (Cited in page 24.)

[Ville *et al.* 2011] L. Ville, L. Silva and T. Coupez. *Convected level set method for the numerical simulation of fluid buckling.* International Journal for numerical methods in fluids, vol. 66, no. 3, pages 324–344, 2011. (Cited in page 144.)

[Wang *et al.* 2010] P. Wang, S. Drapier, J. Molimard, A. Vautrin and P. Henrat. *Characterization of Liquid Resin Infusion (LRI) filling by fringe pattern projection and in situ thermocouples.* Flow Processes in Composite Materials, vol. 41, January 2010. (Cited in pages v, 11, 123 and 156.)

[W.J.Layton *et al.* 2003] W.J.Layton, F.schieweck and I.Yotov. *coupling fluid flow with porous media flow.* SIAM J. Numer. Anal, vol. 40, no. 6, pages 2195–2218, 2003. (Cited in pages 56, 57 and 58.)

[W.Noh & P.Woodward 1976] W.Noh and P.Woodward. *SLIC(simple line interface calculation.* In Proceedings of the Fifth International Conference on Numerical Methods in Fluid Dynamics. Twente University, Enschede. Springer, pages 330–340, 1976. (Cited in page 135.)

Résumé : Les procédés par infusion de résine consistant à infuser une résine liquide à travers un empilement de préformes fibreuses sous l'action d'une pression extérieure appliquée à cet empilement. Un drainant peut être utilisé pour créer un lit de résine sur ou sous cet empilement fibreux. Ces procédés sont utilisés pour fabriquer des pièces minces utilisées dans l'aéronautique par exemple. Les caractéristiques physiques et mécaniques des pièces obtenues sont difficiles à prévoir et à contrôler. La simulation numérique peut donc aider à la maîtrise de ces procédés. Dans ce travail, un modèle numérique éléments finis est proposé pour simuler les procédés par infusion de résine. L'écoulement de la résine, considérée comme un fluide Newtonien incompressible, est décrit par les équations de Stokes dans le drainant (milieu très perméable), et par les équations de Darcy dans les préformes fibreuses (milieu faiblement perméable). Ce couplage Stokes - Darcy est réalisé par une approche monolithique, consistant à utiliser un seul maillage pour les deux milieux. La formulation mixte en vitesse - pression, est alors discrétisée par des éléments finis linéaire - linéaire, et stabilisée par une méthode multiéchelle dite "ASGS". L'interface entre Stokes et Darcy et le front de la résine sont chacun représentés par une fonction "Level-Set", et des conditions de couplage sont imposées sur l'interface qui sépare les deux milieux. Au cours du procédé, les préformes subissent de grandes déformations, que ce soit durant la phase de compaction, ou durant l'infusion de la résine. La pression de la résine fait alors gonfler les préformes. Les déformations des préformes sont traitées par une formulation Lagrangienne réactualisée établie en grandes déformations. Les préformes sèches ont un comportement élastique non linéaire, donné dans le sens transverse par l'expérience. L'effet de la résine sur les préformes humides est représenté par le modèle de Terzaghi. Lorsque les préformes se déforment, leur porosité et donc la perméabilité du milieu varient, affectant ainsi l'écoulement. La formule de Carman-Kozeny est utilisée pour relier porosité et perméabilité. Après avoir validé le couplage Stokes - Darcy par de nombreux cas tests et par la méthode des solutions manufacturées, diverses simulations 2D et 3D de procédés par infusion de résine sont présentées, incluant la déformation des préformes. Des comparaisons sont finalement faites avec succès entre simulation numérique et résultats expérimentaux dans un cas de géométrie simple. Des extensions à des cas tridimensionnels présentant des courbures et des variations d'inertie sont proposées en guise de perspectives.

Abstract: Resin infusion-based processes are good candidates for manufacturing thin composite materials parts such as those used in aeronautics for instance. These processes consist in infusing a liquid resin into a stacking of fibrous preforms under the action of a mechanical pressure field applied onto this stacking where a stiff- distribution medium is also placed to create a resin feeding. Both physical and mechanical properties of the final pieces are rather difficult to predict and control. Numerical simulation are perfectly suited to master these processes. In the present work a numerical finite element modeling framework is proposed to simulate infusion processes. The flow of the assumed newtonian resin is described in the distribution medium, a highly porous medium, through Stokes' equations and through Darcy's equations in the fibrous preforms, very low permeability media. This coupled Stokes-Darcy flow is modeled in a monolithic approach which consists in using a single mesh for both media. The mixed velocity- pressure formulation is then discretized by linear-linear finite elements, stabilized by a so-called ASGS multiscale approach. Both Stokes-Darcy interface and fluid front are represented individually thanks to "Level-Set" functions, and some specific coupling conditions are prescribed on the interface separating both fluid and porous media. During the process, orthotropic preforms undergo finite strains, either during the compaction stage when resin is not yet present, or during resin infusion. Resin pressure then tends to make the preforms swell. Preforms deformations are represented through an updated Lagrangian formulation for finite deformations. Dry preforms possess a non-linear elastic behaviour in their transverse direction - across their thickness- given by existing experimental measurements. The effect of the presence of resin in the wet preforms is accounted for using a Terzaghi's equivalent model. Also, when preforms deform their porosity will change, and so will their permeability, modifying the resin flow. A Carman-Kozeny model is then used to relate porosity and permeability. After the Stokes-Darcy coupling is validated both on numerous tests cases and using the method of manufactured solutions, various 2D and 3D simulations of injection and infusion-based processes are analyzed.The latter including preform deformations along with resin flow. Comparisons with existing experimental measurements permit to validate the approach on a simple geometry. Last, some extensions to more complex 3D cases are proposed as outlooks, including curvatures and thickness variations.